

# **3D INVERSE HEAT TRANSFER METHODOLOGIES FOR MICROELECTRONIC AND GAS TURBINE APPLICATIONS**

by

**David Gonzalez Cuadrado**

**A Dissertation**

*Submitted to the Faculty of Purdue University*

*In Partial Fulfillment of the Requirements for the degree of*

**Doctor of Philosophy**



School of Mechanical Engineering

West Lafayette, Indiana

December 2018

**THE PURDUE UNIVERSITY GRADUATE SCHOOL  
STATEMENT OF COMMITTEE APPROVAL**

Dr. Guillermo Paniagua, Co-Chair

School of Mechanical Engineering

Dr. Amy Marconnet, Co-Chair

School of Mechanical Engineering

Dr. Nicole Key

School of Mechanical Engineering

Dr. Carl Wassgren

School of Mechanical Engineering

Dr. John Clark

Propulsion Directorate, Air Force Research Laboratory, Wright-Patterson AFB

**Approved by:**

Dr. Jay Gore

Head of the Graduate Program

*To my grandparents Donato, Matilde, Jose, and Dionisia: without their sacrifices throughout  
life, I would not be able to write these lines.*

## ACKNOWLEDGMENTS

This can be a chapter by itself, and a lengthy one, but I will make it short.

I would like to thank my advisors Guillermo Paniagua and Amy Marconnet, for all their technical contributions, personal support and trust through the whole PhD adventure. Also, I would like to express my gratitude to the Cooling Technologies Research Center for the financial support and all its members for the valuable advices and suggestions to improve the quality of this work.

Also, I would like to show my appreciation towards all the members of the jury for the valuable advice and suggestions for improvement on the work and final dissertation: Prof. Nicole Key, Prof. Carl Wassgren and Dr. John Clark.

I feel very grateful to the research teams I have been a part of in the last four years. Each and every one of the members of the MTEC and PETAL laboratories have made me a better researcher and a better person; thanks to their advice, constructive criticism, and suggestions through the countless meetings we have had.

None of this would have been the same without my “battle-mates” that have been around giving support, advice, and disagreements since the day I arrived at Purdue: Pramod, Calvin and Hiral.

A more than special thanks goes to all my friends at Purdue and inside of the research team, especially to James, Francisco, Cis, Jorge Saavedra and Jorge Sousa, who shared my journey from Europe to discover the wonders of America with good and bad moments through these years.

Also, I would like to thank my friends from Spain, who now are all around the world and I want them to know that the travel towards this objective would have been more painful and less enjoyable without their continuous presence in my life.

I would like to express my gratitude to my family, especially to my brother Miguel, and my parents Miguel Angel and Maria de los Angeles. Fifty years ago, my family was a rural family, struggling



to survive and to provide a future to the following generations. Now, I am here writing these lines thanks to their effort, tears, sweat and values. I worked to complete this document, but they worked more to give me the opportunity to do it. And I want everyone that reads this to know that what is achieved within this document is more than just four years of David's work, it is an achievement of more than fifty years of sacrifice and selfless efforts from my grandparents and parents.

Finally, I cannot complete this thesis without mentioning Valeria, who in a way is part of the previous paragraph since she is family to me. She has stood by me in the bad and worse moments and she has laughed and enjoyed with me the good and better ones. I look forward to continuing like this, and I would like to thank her for being there for me; not only for the support during the PhD years, but for her support throughout life.

There are countless other names I could wish I had time to mention who have helped me a great deal over the years. I hope you all know that you are in my mind and I am grateful for all you have done for me.

## TABLE OF CONTENTS

TABLE OF CONTENTS.....	vi
LIST OF TABLES.....	ix
LIST OF FIGURES .....	x
NOMENCLATURE .....	xviii
ABSTRACT.....	xxii
CHAPTER 1. INTRODUCTION .....	1
1.1 Research Objectives.....	1
1.2 Research Methodology .....	4
1.3 Dissertation Guideline .....	6
CHAPTER 2. A REVIEW OF INVERSE HEAT CONDUCTION METHODS.....	9
2.1 Sensitivity Coefficient Definition.....	12
2.2 Challenges of the Inverse Heat Transfer Methods.....	18
2.3 Inverse Heat Transfer Classifications .....	21
2.4 Fitting Methodologies.....	25
2.4.1 The Levenberg-Marquardt Method & Digital Filter Method .....	26
2.4.2 Transfer Function Methods.....	32
2.5 Optimization Methodologies .....	35
2.5.1 Deterministic Optimization Methods .....	37
2.5.2 Stochastic Optimization Methods.....	37
2.5.3 Hybrid Optimization Methods.....	40
2.6 Comparison Between Fitting Methods And Optimization Methods .....	41
2.7 Conclusions.....	45
CHAPTER 3. DEVELOPMENT OF TRANSIENT 3D IHT METHODOLOGIES .....	47
3.1 Conjugate Gradient Method with the Adjoint Problem.....	47
3.1.1 Whole Domain Estimation .....	52
3.1.2 Sequential Estimation .....	54
3.1.3 Noise Effect in Conjugate Gradient Method .....	57
3.1.4 Uncertainty Evaluation .....	59
3.2 Digital Filter Method .....	60

3.2.1	Non-iterative Non-linear Digital Filter Method Improvement .....	66
3.2.2	Uncertainty Evaluation .....	68
3.3	Conclusions .....	70
CHAPTER 4. SENSOR OPTIMIZATION IN MICROELECTRONICS USING IHTM .....		72
4.1	Conductive Heat Transfer Numerical Evaluation .....	73
4.1.1	Conjugate Gradient Method Evaluation .....	76
4.1.2	Digital Filter Method Evaluation .....	78
4.2	Conjugate Heat Transfer Numerical Evaluation .....	80
4.2.1	Conjugate Gradient Method Evaluation .....	82
4.2.2	Digital Filter Method Evaluation .....	83
4.3	Experimental Validation .....	85
4.3.1	Conjugate Gradient Method Validation .....	97
4.3.2	Digital Filter Method Validation .....	98
4.3.3	Digital Filter Method with Non-iterative Non-linear Correction .....	99
4.4	Sensor Location Optimization Technique .....	103
4.4.1	Kriging Interpolation Combined with Genetic Algorithm Optimization .....	103
4.5	Conclusions .....	112
CHAPTER 5. DIGITAL FILTER INVERSE METHOD APPLIED TO GAS TURBINE		
CASING .....		114
5.1	Numerical Evaluation .....	115
5.1.1	High Frequency Phenomena Retrieval .....	125
5.1.1.1	Numerical Analysis .....	125
5.1.1.2	Practical Implementation .....	131
5.1.2	Prediction of the Upstream Conditions Based on IHTM .....	132
5.2	Experimental Evaluation of the IHTM in Turbine Casing .....	134
5.2.1	Blowdown Wind Tunnel Design .....	135
5.2.2	Facility Calibration Strategy .....	139
5.2.3	Annular Test Section Design .....	145
5.2.4	Infrared Thermography Experimental Setup .....	152
5.2.4.1	Instrumentation .....	154
5.2.5	Experimental campaign .....	159

5.2.6 Digital Filter Method Validation .....	166
5.3 Conclusions.....	178
CHAPTER 6. CONCLUSIONS.....	180
REFERENCES .....	185
APPENDIX A. UNCERTAINTY ANALYSIS PROCEDURE.....	205
APPENDIX B. EXPERIMENTAL DATA IN MICROELECTRONICS APPLICATION.....	208
APPENDIX C. INVERSE METHOD AND KRIGING INTERPOLATION OPTIMIZATION MATLAB GUI FOR SIMPLE 3D GEOMETRIES.....	219
APPENDIX D. INFRARED WINDOW MATERIAL SELECTION .....	228
APPENDIX E. EXPERIMENTAL DATA IN GAS TURBINE APPLICATION.....	233
VITA .....	254
PUBLICATIONS.....	255

## LIST OF TABLES

Table 3-1. Conjugate Gradient Method uncertainty analysis based on the numerical assessment.....	59
Table 3-2. Uncertainty analysis of the Digital Filter Method .....	69
Table 4-1. Uncertainty analysis of the heat flux computation using the non-linear inverse method.....	102
Table 4-2. Uncertainty calculation of the power in the experiments.....	103
Table 5-1. Uncertainty analysis for the turbine casing inverse heat transfer analysis .....	124
Table 5-2. Root Mean Square Error (RMSE) relative to the two non-dimensional numbers using the different sampling distributions.....	144
Table 5-3. Turbine application experimental campaign tests. ....	160
Table A-1. Uncertainty analysis of the heat flux computation using the non-linear inverse method.....	206

## LIST OF FIGURES

Figure 1-1. Schematic of the research directions.....	4
Figure 1-2. Research methodology for microelectronic application. ....	6
Figure 2-1. Sensitivity coefficient for the temperature increase with respect to the heat flux. At a particular point, there is a delay in the temperature response due to the finite speed of thermal diffusion. The peak magnitude shifts depending on the time of application of the heat flux pulse. Also the peak magnitude and location is modified with the size of the non- dimensional timestep, since at smaller timesteps the energy provided to the system is smaller. .....	15
Figure 2-2. Classification of inverse heat transfer methods based on the methods used to solve the inverse problem. ....	23
Figure 2-3. Schematic of the digital filter method and Levenberg-Marquardt method procedures to solve non-linear inverse problems and the relation between them. The DFM can be used to provide an initial value of heat flux for the Levenberg-Marquardt Method, but the computation of the direct problem will provide new values of temperature and the sensitivity coefficients can be re-computed till we reach convergence. ....	29
Figure 2-4. (a) Four imposed transient heat flux profiles and (b) predictions of the heat flux profiles using analytical estimation of the sensitivity coefficients using the Digital Filter Method. Note that the imposed heat flux is input into a 2D analytical solution to extract temperatures that are fed into a 1D solution with the Digital Filter Method. Reproduced from [89] with permission. ....	31
Figure 2-5. Schematic of the transfer function method in frequency domain procedure to determine the heat flux in inverse heat transfer problems. ....	34
Figure 2-6. Application of the transfer function method using a) a 1D numerical model of a flat plate using the simulated temperature readings from three different planes as input to the inverse method and b) a 3D inverse heat flux estimation using a temperature reading from an experimental setup consisting of a cutting tool of high speed steel during machining. Reproduced from [93] with permission. ....	35

Figure 2-7. Genetic algorithm optimization procedure to calculate the heat flux in inverse heat transfer problems. ....	39
Figure 2-8. Example of hybrid optimization methodology procedure [62]. ....	41
Figure 2-9. Comparison between steepest descent method and conjugate gradient method. Reproduced from [80] with permission. ....	42
Figure 3-1. Conjugate gradient method with the adjoint problem procedure to determine the heat flux for an inverse heat transfer problem. ....	49
Figure 3-2. Whole domain estimation solution when applying a sinusoidal heat flux input into a stack of slabs of different materials. ....	53
Figure 3-3. Temperature response to a pulse of heat flux in a slab (top). Whole domain estimation schematic (bottom left) and Sequential estimation schematic (bottom right). ....	55
Figure 3-4. Calculated heat flux with the inverse heat transfer methodology using whole estimation method (left), sequential method with 3 future steps(center) and 2 future steps (right). ....	56
Figure 3-5. a) Computation of the conjugate gradient method with 0.5K of random level of noise. b) Computation of the conjugate gradient method with 1K of random level of noise. ....	58
Figure 3-6. Results of the heat flux for a given distribution of temperature for different values of regularization coefficients. ....	65
Figure 3-7. Non-linear non-iterative process with temperature adaptive sensitivity coefficient estimation. ....	67
Figure 4-1. Sketch of the simulated microchip with the sources of heat flux and the temperature reading location. ....	72
Figure 4-2. (top) Schematic of the complete experimental test fixture and (bottom) the COMSOL model used for the inverse method and Kriging model. (bottom inset) Approximate verification model to prove the simplified geometry. ....	74
Figure 4-3. Sketch of the “reduced chip” structure including the geometry of the real microchip with 100 heaters. ....	75
Figure 4-4. Temperature distribution within the chip for the reduced chip and the simplified reduced chip model at $t=1.5s$ and $t=5s$ . ....	75
Figure 4-5. Analyzed model with the imposed heat flux in all the heaters. ....	77

Figure 4-6. Computed temperature (left) and estimated heat flux (right) by the conjugate gradient method after 2, 6 and 9 iterations in the center (top) and the corner (bottom) of the analyzed chip. ....	77
Figure 4-7(a) Imposed heat flux in the numerical experiment for the corner and center heaters. (b) Temperature increase over time at the top surface in the corner and center locations of the microchip.....	79
Figure 4-8. Comparison between the imposed heat flux and the heat flux estimated with the inverse 3D methodology. ....	80
Figure 4-9. Microchip with four heaters (left) velocity field in the fluid domain (top right) and temperature field in the solid and fluid domains (bottom right). ....	81
Figure 4-10. Imposed heat flux in ten timesteps in two of the heaters of the test article. ....	82
Figure 4-11. Computation of the heat flux in all the nodes of the heater 3 in the first four iterations of the conjugate gradient method.....	83
Figure 4-12. Location of the different heaters (left) and comparison between the imposed heat flux and computed heat flux (right) with the digital filter method.....	84
Figure 4-13. Microchip with 25 independent heaters used for the experimental validation of the inverse methodology. The system consists of a grid with 25 independently controlled heaters and 26 embedded temperature sensors. ....	85
Figure 4-14. a) Microchip in the experimental setup, b) COMSOL model of the microchip with subdivisions in the top surface marking the approximate size of the pixels for IR thermal measurements, and c) Fluent model of the microchip for conjugate heat transfer analysis. Divisions shown here outline the 25 different heaters elements.....	86
Figure 4-15. Numerical validation of the inverse methodology in Ansys Fluent including conjugate heat transfer. (a) The imposed and retrieved heat fluxes in selected four heaters agree well. (b) Top view of the 5x5 heater grid with the four selected heaters labeled. A heat flux is imposed on heater 1, while all remaining heaters are off for the duration of the simulations. ....	87
Figure 4-16. Experimental procedure. ....	88
Figure 4-17. Thermocouple calibration. ....	89
Figure 4-18. RTD calibration.....	90
Figure 4-19. Heaters calibration. ....	91



Figure 4-20. Experimental setup to measure the top surface temperature of the chip in the specified field of view of the IR microscope. ....	92
Figure 4-21. Different experiments performed with the 5x5 heaters test article. ....	93
Figure 4-22. Experiments performed to validate the methodology. Each small inset indicates which heat sources were on (red) for each experiment and the black box indicates the field of view of the infrared microscope. The thermal images are from one frame of the thermal movie and show the spatial variation in temperature of the die. ....	94
Figure 4-23. Infrared images of the experiment 4 and experiment 6 at second 50 of the transient experiment. ....	95
Figure 4-24. Thermal response during Experiment 1 with a 15x15 grid of sensors in order to validate the data with the inverse methods. ....	96
Figure 4-25. Comparison of the imposed heat flux and the computed heat flux with the Conjugate Gradient Method after 11 iterations in the center(top) and corner (bottom) of the experimental chip. ....	97
Figure 4-26. Comparison of the imposed heat flux and the computed heat flux using Digital Filter Method. ....	99
Figure 4-27. Validation of the inverse methodology for the experiment 1. (a) Temperature maps at selected times. Note that the temperature is fairly uniform at each time step. (b) Sketch of the 5x5 heater grid with the 9 active heaters indicated in red. The black outline indicates the field of view. (c - d) Heat flux in the center (blue) and (red) corner heater within the field of view as extracted from the inverse method. Panel (c) shows the results for natural convection with the Comsol model and panel (d) shows the results under forced convection using the Fluent model. ....	100
Figure 4-28. Experimental validation for experiments 3 and 4 at t=40s demonstrating ability to spatially resolve heat flux. (a) Schematic of active heaters and observed temperature map at t = 40s. (b) Imposed and retrieved heat fluxes in each heater at t=40s. ....	101
Figure 4-29. Temperature maps in the plane where the temperature sensors should be located at t=1.5s and t=2.7s. ....	108
Figure 4-30. Location of the optimal points inside of the microchip envelope for the case run with 8 sensors. ....	108

Figure 4-31. Kriging interpolation results for the temperature maps using the optimal location for the sensors. ....	109
Figure 4-32. Number and location sensor optimization strategy coupled with an inverse method assessment. ....	110
Figure 4-33. Example of the scatter sensor optimization technique using the experimental data from the Experiment 1.....	111
Figure 5-1. Schematic of the inverse heat transfer procedure applied to the turbine casing. ....	116
Figure 5-2: Computational domain with details of solid and fluid domain. ....	117
Figure 5-3. Numerical domain used in Numeca for the computation of the conjugate heat transfer in the casing of the turbine blade. ....	118
Figure 5-4. a) Transient evolution of the heat flux applied in the conjugate heat transfer simulation in two different points of the domain. b) Spatial distribution of heat flux at $t=4.5s$ in the overtip region in the conjugate heat transfer calculation. ....	120
Figure 5-5. Temperature distribution in the outer wall of the casing at $t=3s$ and $t=5s$ for the baseline case of casing thickness (0.5mm) and tip clearance (1% of the blade span). ....	121
Figure 5-6. a) Comparison between the transient evolution of imposed heat flux and the retrieved heat flux. b) Spatial distribution of the imposed heat flux at $t=1s$ in the simulation. c) Spatial distribution of the retrieved heat flux at $t=1s$ in the simulation. ....	122
Figure 5-7. a) Imposed heat flux extracted from the conjugate heat transfer simulation with a clearance of 0.25% the blade span. b) Retrieved heat flux from the inverse method in the case of 0.25% of the blade span. c) Imposed heat flux extracted from the conjugate heat transfer simulation with a clearance of 0.55% the blade span. d) Retrieved heat flux from the inverse method in the case of 0.55% of the blade span. ....	123
Figure 5-8. Numerical heat transfer simulation imposing fluctuations of heat flux in a thin layer of aluminum. ....	127
Figure 5-9: Temperature fluctuation damping through Aluminum (dashed lines) and Copper (solid lines) for different thicknesses and frequencies. ....	128
Figure 5-10. Inner and outer T vs time signals for a frequency of 1 kHz (a) Al, 500 $\mu m$ thickness and (b) Al 0.5 cm thickness .....	130
Figure 5-11. Averaged heat flux evolution at different upstream pressure conditions. ....	133
Figure 5-12. Pressure prediction based on the inverse heat transfer procedure. ....	133

Figure 5-13. Schematic of the layout of the Purdue Experimental Turbine Aerothermal Laboratory.....	135
Figure 5-14 . Temperature achieved after the mixer with several hot to cold flow ratios.....	136
Figure 5-15. Min-max temperature difference along the length of the piping downstream of the mixer. ....	138
Figure 5-16. a) Reynolds number per meter and b) Mach number maps achieved in the test section in all the span of the sonic valve and with a maximum massflow of 15 kg/s. ....	140
Figure 5-17. a) Comparison between the Re/m map and the Kriging meta-model in function of the massflow and the throat area with the representation of the points resulted from the optimization methodology. b) Comparison between the Mach number map and the Kriging meta-model in function of the massflow and the throat area with the representation of the points resulted from the optimization methodology. c) Root mean squared error of the Mach number and Re/m number using 20, 36 and 50 points in the Kriging interpolation optimization methodology. ....	143
Figure 5-18. a) Sampling comparison between the Kriging optimization result and the Latin Hypercube approach. b) Re/m error comparison between the surface generated with the Latin Hypercube sampling and the Kriging interpolation optimization. c) Mach error comparison between the surface generated with the Latin Hypercube sampling and the Kriging interpolation optimization. ....	145
Figure 5-19. a) Annular test section measurement planes. b) Velocity profile at two axial locations. c) Stage velocity triangles. d) Absolute-relative velocities of a rotor row with a pre-swirler; e) Velocity triangle in a stationary rotor row with rotating pre-swirler; f) Reverse rotation. ....	147
Figure 5-20. Annular test section: a) Overall layout of the optical windows; b) frontal view of the test section; c) meridional view; d) supersonic configuration. ....	150
Figure 5-21. Left) Mach-Re limits in subsonic operation. Right) Operational range in subsonic conditions.....	151
Figure 5-22. Left) Mach-Re limits in supersonic operation. Right) Operational range in supersonic conditions.....	152
Figure 5-23. Meridional cut of the annular test section under investigation. ....	153

Figure 5-24. Infrared access in the turbine annular cascade to perform infrared thermography of the inner casing of the rotor. ....	154
Figure 5-25. Measurement planes in the experimental setup of the annular the test section. ..	155
Figure 5-26. a) Instrumented annular test section ready to be set into the wind tunnel. b) Detail of the thermocouple probe already in the test section. c) Detail of the total pressure probe already in the test section. d) Total pressure rake and e) Total temperature rake. ....	156
Figure 5-27. Instrumentation used for the validation of the inverse heat transfer methodology composed by a) surface thermocouples in the inner surface of the measured intake and b) Infrared camera configuration to measure the outer temperature of the same turbine intake. ....	157
Figure 5-28. Test section instrumented, installed and ready for the experiments. ....	158
Figure 5-29. a) Gas temperature measured by one of the total pressure probes in the test section during the baseline experiment and b) gas to wall temperature ratio during the same experiment.....	161
Figure 5-30. a) Total pressure measurement in the annular test section in plane 1 during the experiment 5. b) Massflow measurement during the same experiment in the venturi located upstream of the test section.....	162
Figure 5-31. a) Static pressure readings in the plane 1 in the hub of the flowpath. b) Static pressure readings in the plane 2 in the shroud of the flowpath. c) Uniformity in the circumferential direction of the static pressure in the hub of the plane 1. ....	164
Figure 5-32. a) Surface thermocouples located inside of the test section. b) Temperature comparison between the Thermocouple 6 and the thermocouple 10 located in the same axial position in the experiment 1. c) Temperature comparison between the thermocouple 6 and the thermocouple 10 located in the same axial position in the baseline case. ....	165
Figure 5-33. Comsol model with the boundary conditions applied during the calculation. ....	166
Figure 5-34. a) Surface thermocouples in the inner flowpath and b) inner metal temperature in the different axial locations over the measured surface.....	168
Figure 5-35. Calibration IR camera and IR transparent window set up. ....	169
Figure 5-36. IR images taken during the experiment 1. ....	170

Figure 5-37. a) IR image of the region of interest. b) Spatial behavior of the temperature in the region inside the window. c) Temperature measured in the inner and outer surface of the shroud, used to compute the heat flux with the 1D heat conduction code.....	171
Figure 5-38. a) Temperature map in time and space for the calculation of the 1D heat conduction with the thermocouples in location 1. b) Heat flux computed with the 1D heat conduction code with the temperature from the thermocouple at location 1.....	172
Figure 5-39. Comparison between the heat flux computed by the inverse heat conduction method and the heat flux through the casing. ....	174
Figure 5-40. a) Heat flux comparison between the inverse method solution and the imposed heat flux in the upstream axial location in function of the difference between the gas temperature and the wall temperature. b) Heat flux comparison between the inverse method solution and the imposed heat flux in the downstream axial location in function of the difference between the gas temperature and the wall temperature. ....	175
Figure 5-41. a) Heat flux comparison between the inverse method solution and the imposed heat flux in the upstream axial location in function of the gas to wall temperature ratio. b) Heat flux comparison between the inverse method solution and the imposed heat flux in the downstream axial location in function of the gas to wall temperature ratio. ....	176
Figure 5-42. a) Heat flux comparison between the inverse method solution and the imposed heat flux in the upstream axial location in function of the convective heat transfer coefficient. b) Heat flux comparison between the inverse method solution and the imposed heat flux in the downstream axial location in function of the convective heat transfer coefficient. ....	177
Figure 5-43. a) Heat flux comparison between the inverse method solution and the imposed heat flux in the upstream axial location in function of the massflow. b) Heat flux comparison between the inverse method solution and the imposed heat flux in the downstream axial location in function of the massflow.....	177
Figure 6-1. Comparison summary of the different analyzed methodologies.....	182

## NOMENCLATURE

### Roman Symbols

$ATM$	Atmospheric
$C$	Covariance
$C_p$	Heat capacity [J/kg K]
$d$	Model order
$E$	Error
$F$	Temperature factor
$G$	Green Function
$h$	Tip gap height [m]
$H$	Hessian matrix
$k$	Number of independent variables
$k$	Conductivity [W/m K]
$M$	Mach number
$P$	Pressure [Pa] [bar]
$q$	Heat flux [W/m <sup>2</sup> ]
$R$	Radius [m]
$Re$	Reynolds Number
$t$	Time [s]
$t$	t-statistics
$T$	Calculated temperature [K]
$u$	Rotational velocity magnitude [m/s]
$v$	Absolute velocity magnitude [m/s]

$w$	Relative velocity magnitude [m/s]
$X$	Sensitivity coefficient matrix
$Y$	Measured temperature [K]

### Greek symbols

$\alpha$	Regularization parameters
$\alpha$	Thermal diffusivity [m <sup>2</sup> /s]
$\alpha$	Absolute flow angle
$\beta$	Relative flow angle
$\rho$	Density [kg/m <sup>3</sup> ]
$\lambda$	Weights in Kriging method
$\sigma$	Standard deviation
$\gamma$	Required precision
$\omega$	Angular velocity [rad/s]

### Subscripts

$0$	Total quantity
$1$	Plane 1: stator inlet
$2$	Plane 2: rotor inlet
$3$	Plane 3: rotor outlet
$i$	Particular time step
$j$	Particular space location
$m$	Total number of temperature measurements

$M$	Particular sensor measurement
$n$	Total number of time steps
$p$	Total number of heat sources
$r$	Relative
$s$	space
$t$	time

### Acronyms

<i>BFGS</i>	Broyden-Fletcher-Goldfarb-Shanno method
<i>CFV</i>	Critical Flow Venturi
<i>CGM</i>	Conjugate Gradient Method
<i>DFM</i>	Digital Filter Method
<i>FOV</i>	Fast Opening Valve
<i>GA</i>	Genetic Algorithm
<i>HP</i>	High Pressure
<i>IHCP</i>	Inverse Heat Conduction Problem
<i>IHTM</i>	Inverse Heat Transfer Method
<i>IR</i>	Infrared
<i>LHS</i>	Latin Hypercube Sampling
<i>LP</i>	Low Pressure
<i>PETAL</i>	Purdue Experimental Turbine Aerothermal Laboratory
<i>RMS</i>	Root Means Square
<i>RPM</i>	Revolutions Per Minute
<i>RTD</i>	Resistance Temperature Detector



<i>SWG</i>	Shock Wave Generator
<i>TC</i>	Thermocouple
<i>TRL</i>	Technology Readiness Level

## ABSTRACT

Author: Gonzalez Cuadrado, David. PhD

Institution: Purdue University

Degree Received: December 2018

Title: 3D Inverse Heat Transfer Methodologies for Microelectronic and Gas Turbine Applications

Committee Chair: Guillermo Paniagua, Amy Marconnet

The objective of this doctoral research was to develop a versatile inverse heat transfer approach, that would enable the solution of small scale problems present in microelectronics, as well as the analysis of the complex heat flux in turbines. An inverse method is a mathematical approach which allows the resolution of problems starting from the solution. In a direct problem, the boundary conditions are given, and using the governing physics principles and equations you can calculate the solution or physical effect. In an inverse method, the solution is provided and through the physical equations, the boundary conditions can be determined. Therefore, the inverse method applied to heat transfer means that we know the variation of temperature (effect) over time and space. With the temperature input, the geometry, thermal properties of the test article and the heat diffusion equation, we can compute the spatially- and temporally-varying heat flux that generated the temperature map.

This doctoral dissertation develops two inverse methodologies: (1) an optimization methodology based on the conjugate gradient method and (2) a function specification method combined with a regularization technique, which is less robust but much faster. We implement these methodologies with commercial codes for solving conductive heat transfer with COMSOL and for conjugate heat transfer with ANSYS Fluent.

The goal is not only the development of the methods but also the validation of the techniques in two different fields with a common purpose: quantifying heat dissipation. The inverse methods were applied in the micro-scale to the dissipation of heat in microelectronics and in the macro-scale to the gas turbine engines.

In microelectronics, we performed numerical and experimental studies of the two developed inverse methodologies. The intent was to predict where heat is being dissipated and localized hot spots inside of the chip from limited measurements of the temperature outside of the chip. Here, infrared thermography of the chip surface is the input to the inverse methods leveraging thermal model of the chip. Furthermore, we combined the inverse methodology with a Kriging interpolation technique with genetic algorithm optimization to optimize the location and number of the temperature sensors inside of the chip required to accurately predict the thermal behavior of the microchip at each moment of time and everywhere.

In the application for gas turbine engines, the inverse method can be useful to detect or predict the conditions inside of the turbine by taking measurements in the outer casing. Therefore, the objective is the experimental validation of the technique in a wind tunnel especially designed with optical access for non-contact measurement techniques. We measured the temperature of the outer casing of the turbine rotor with an infrared camera and surface temperature sensors and this information is the input of the two methodologies developed in order to predict which the heat flux through the turbine casing. A new facility, specifically, an annular turbine cascade, was designed to be able to measure the relative frame of the rotor from the absolute frame. In order to get valuable data of the heat flux in a real engine, we need to replicate the Mach, Reynolds, and temperature ratios between fluid and solid. Therefore, the facility can reproduce a large range of pressures and flow temperatures. Because some regions of interest are not accessible, this research

provides a significant benefit for understanding the system performance from limited data. With inverse methods, we can measure the outside of objects and provide an accurate prediction of the behavior of the complete system. This information is relevant not only for new designs of gas turbines or microchips, but also for old designs where due to lack of prevision there are not enough sensors to monitor the thermal behavior of the studied system.

## CHAPTER 1. INTRODUCTION

### 1.1 Research Objectives

While numerous numerical solvers have been developed to predict temperature distributions and heat flows in real systems given boundary conditions and material properties for a given geometry (*i.e.*, the forward problem), experimental characterization often relies upon limited temperature sensors and boundary conditions, material properties, or geometrical parameters may not be well characterized. In this case, the unknown information (*e.g.*, boundary conditions) can be retrieved from limited data (*e.g.*, temperature measurements) given with inverse methods algorithms.

Inverse methods applied to heat transfer are particularly interesting for fields where the dissipation of heat constitutes a problem for placement of the sensors or their survivability. On one hand, in fields such as microelectronics, due to compactness of the current and future generation of microprocessors, inverse heat transfer methods can predict the thermal behavior of the chips using few temperature measurements outside of the system. This prediction can be used for design purposes, optimizing the location of the temperature sensors for instance, or during operation using real-time inverse methods, it can be used for active thermal management of the complete system.

On the other hand, in propulsion applications the survivability of the sensors is compromised due to the harsh environments they are subjected to. Inverse heat transfer methodologies allow the determination of the internal conditions of the flow, based on measurements from outside of

the system. It ensures the survival of these instruments and prevents aerothermal distortion caused by routing the instrumentation into the test article.

This thesis addresses the following key points:

a) **Evaluation of the feasibility of using inverse methods applied to heat transfer in complex**

**3D geometries:**

Many studies have been performed using inverse methodologies applied to different fields, including heat transfer research. The objective of this part of my thesis is to evaluate different algorithms that can be applied to solve inverse problems for complex 3D geometries. This means that not only analytical solutions are applied in the methodology, but we combine the inverse methods with numerical models to solve the heat conduction equation.

b) **Development of two different inverse methodologies for heat transfer problems for conductive heat transfer and for conjugate heat transfer:**

Two different methods were selected and developed based on the evaluation of past research: (1) the conjugate gradient method with a whole domain estimation algorithm and a sequential time estimation and (2) a function specification method with a regularization technique. The objective of this method development is to test the robustness and computation efficiency of both methods. The first method was selected for its robustness and the second, for its computational efficiency. At the same time, they were evaluated with two different commercial solvers for the forward problem providing a pure conductive routine and a conjugate heat transfer routine.

c) **Application of the inverse methodologies to microelectronics:**

In this phase, we apply to our inverse methods to a microscale application. The goal is to verify if the inverse methods based on a model of a real microchip can accurately predict the hotspots happening inside of the chip. All this evaluation is made at the microchip card scale.

Finally, with the information provided with the inverse methodology about hotspots inside of the chip, we optimize the number and location of the temperature sensors for any kind of chip required to predict the complete thermal behavior of the assessed microelectronic card in time and in space.

**d) Application of the inverse methodologies to gas turbine casing:**

In this application, we target macroscale systems. The ultimate goal is to predict the heat flux through the casing of the turbine rotor based on temperature measurements taken outside. This methodology can be used to retrieve other operating conditions inside of the engine based on the retrieved heat flux. The advantage of this technique is the use of external measurement techniques, which benefit the acquisition of data for two main reasons: the sensors are not intrusive, so they do not disturb the flow and the sensors are protected from the harsh conditions of the flow. An experimental validation of the methodologies for this application will be performed in a turbine test rig.

Figure 1-1 summarizes the complete research proposal starting with the development of the two methodologies based on the literature survey. Then we apply these methodologies to two different fields in which the heat management plays a major role. These objectives are related to the research methodology explained in the following subsection for each one of the parts.

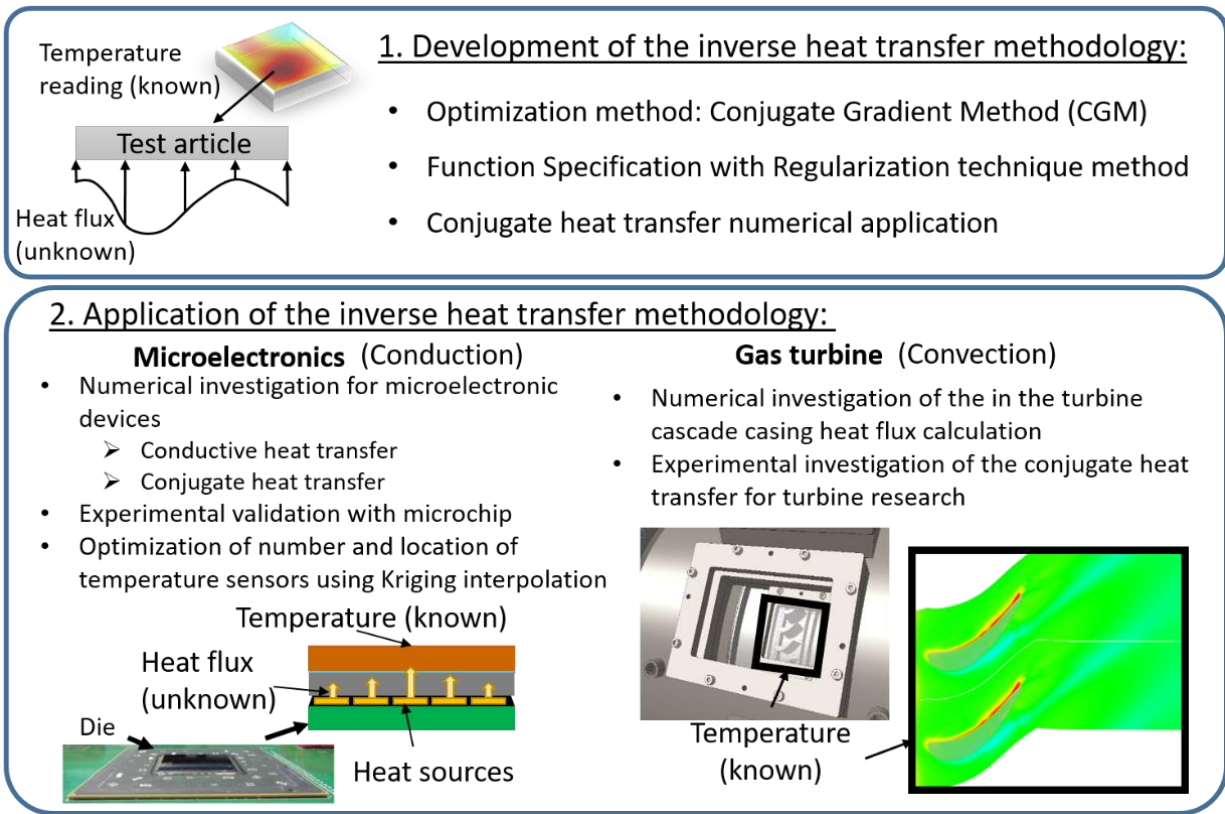


Figure 1-1. Schematic of the research directions.

## 1.2 Research Methodology

In order to accomplish the four objectives explained in the previous subsection we followed the following research approach.

### a) Development of 3D transient inverse methods:

An intensive literature survey through all the algorithms employed in the resolution of inverse heat transfer problems is conducted. The outcome is summarized in the implementation of two different methods based on (1) an optimization technique for robustness and (2) on a more computationally efficient function specification method combined with regularization techniques. For the implementation of these methodologies, we combined two commercial software programs: (1) Matlab for implementation of the inverse methods and (2) multi-



physics software to solve the heat transfer phenomena in complex 3D geometries. The specific multi-physics software depends on the type of heat transfer that needs to be solved and different approaches are needed in order to establish communication between Matlab and the solver. For conductive heat transfer, COMSOL Multiphysics is used for the heat transfer analysis. In the case of the conjugate (i.e., combined conduction and convection) heat transfer applications, the chosen software is ANSYS Fluent.

This development also includes an evaluation of the robustness and computational efficiency of the different methods. The evaluation was performed with a basic model of a microchip in order to couple it with the following section.

b) Inverse heat transfer methods applied to microchips:

Using the developed inverse methods, we evaluate the heat generation inside of the microchip based on external measurements of temperature and then optimize the location of the sensors inside of the microchip. The methodology to perform this work is summarized in the Figure 1-2. The inverse methodology is applied to find the heat generated inside of the microchip and the solution of the inverse method is the input for an optimization technique based on genetic algorithms that coupled with a Kriging interpolation is providing the optimize location of the temperature sensors. In this case, experimental data taken from a real microchip with heat generators is used for the validation of the methodology.

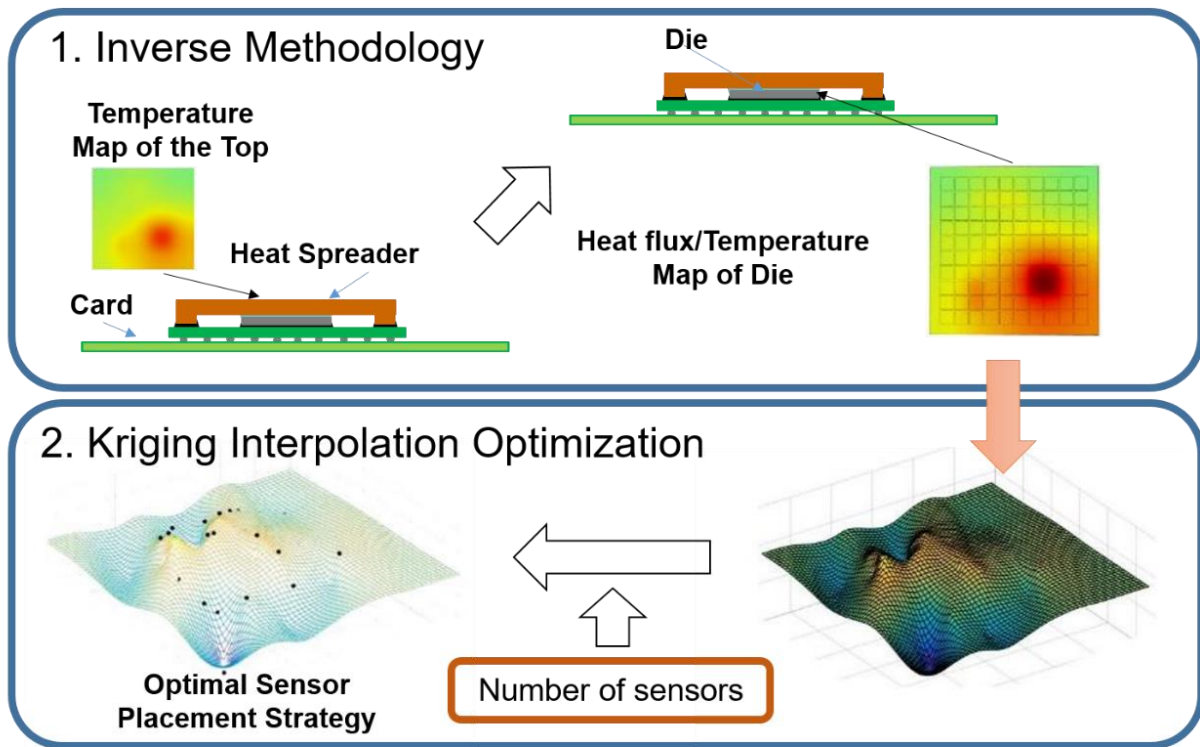


Figure 1-2. Research methodology for microelectronic application.

c) Inverse heat transfer method applied to gas turbines:

The validation of the method for a macroscale application is performed in the rotor casing of a turbine facility. For this, a turbine cascade wind tunnel was specially designed for optical measurements. The experimental validation of the methodology uses infrared thermography to measure the temperature of the outer casing of the turbine stage and with this information retrieve the heat flux through the casing of the turbine rotor.

### 1.3 Dissertation Guideline

This dissertation is divided in 6 chapters in which the methodology and application of the doctoral are detailed. Chapter 2 is an overview of the different inverse methodologies employed

for heat transfer research. It discusses and describes the most important and common methodologies, classifying them by solving methods.

Chapter 3 details the two methodologies that have been developed and applied in this work: the digital filter method and the conjugate gradient method with a sequential estimation. A comparison between the results obtained with the Digital Filter Method and with the Conjugate Gradient Method is included. Additionally, an explanation of an improved Digital Filter Method developed in this work to account for temperature dependent properties and boundary conditions is detailed in this paragraph with some preliminary results.

Chapter 4 emphasizes the application of the method in microelectronics, evaluating the robustness to noisy inputs, the comparison between the two methodologies, the implementation for conductive and conjugate heat transfer models, and the experimental validation of the methodologies. At the end of the chapter, Kriging interpolation optimization for limited sensor placement is detailed and the results are discussed and evaluated.

Chapter 5 focuses on the gas turbine application, with special attention to the design of the wind tunnel and test section developed for optical measurement techniques. The improved Digital Filter Method is evaluated using several numerical experiments. The inlet conditions of the experiments are retrieved only by measuring the heat flux in the outer surface of the engine. Also, the inverse method is validated with several experiments in the wind tunnel at different gas to wall temperature ratios and mass flows. A detailed analysis of the experiments and the results of the inverse methodology is included in this chapter, concluding that the inverse method can predict in time and in space the behavior of the heat flux, and it can be related to the inlet conditions of the experiment.

Chapter 6 contains all the conclusions extracted from the presented doctoral dissertation. Special remarks have been made in the effectiveness of each method for each type of application and

guidelines for the implementation of this inverse methodology in real machinery have been provided.

Additionally five different appendix have been included, divided by topics. In the Appendix A, the uncertainty evaluation is explained. Appendix B contains the complete experimental results used for the validation of the inverse methodologies. Appendix C details the Matlab GUI created for the combination of the inverse method with the sensor optimization technique. The selection of the Infrared transparent window is included in the Appendix D and the Appendix E itemizes all the experimental data gather during the gas turbine application measurement campaign.

## CHAPTER 2. A REVIEW OF INVERSE HEAT CONDUCTION METHODS

It is relatively straightforward to determine temperature distributions given information about geometry, boundary, conditions, and material properties by solving (analytically or numerically) the heat diffusion equation for conduction or coupled heat, mass, and momentum transfer problems for conjugate heat transfer problems. But the inverse problem, *i.e.*, determining an unknown heat transfer coefficient given a measured temperature, is ill posed and motivates the developments of computational algorithms to estimate the unknown parameters. Experimentally, numerous sensors exist ranging from thermocouples to infrared detectors to observe temperature profiles, but measuring heat fluxes, heat generation, and convection coefficients is not always as straight forward.

In any system, a “cause” (*e.g.*, distribution and magnitude of heat generation) under certain “conditions” (*e.g.*, specific material properties) give as a result a “change” or “effect” in the system (*e.g.*, increased temperatures). When one of these elements (the “cause”, “conditions”, or “effect”) is unknown and we want to know it, we have, literally, a “problem”. In the direct problems we know the “cause” and the “conditions” and our unknown is the “effect”. These problems, due to the nature of the physics behind them, are normally well-posed and have a unique solution, a unique “effect”. However, if the unknown is the “cause” or the “conditions”, the nature of the problem changes since the calculation is starting from the solution and it becomes an ill-posed problem. These are the so called inverse problems.

In the inverse problems we are not looking for the solution to the problem, *i.e.*, we are not looking for the effect. Instead, we measure the “effect” (*e.g.*, the temperature distribution) and use that

as the starting point of the inverse problems to retrieve the “cause” and “conditions” of the problem (*e.g.*, boundary conditions or material properties). For a well-posed problem [1]:

- a. the solution exists,
- b. the solution is unique,
- c. the solution's behavior changes continuously with the initial conditions.

But inverse problems are generally ill-posed, which means that they do not satisfy all these properties. Even though the solution always exists, it may be not unique and any small change in the “effect” can propagate numerically and change completely the solution. As an example, there are different combination of boundary conditions that can cause the same effect in the system. Thus, the solution of an inverse problem is not unique. Also, when there is noise involved in the measurements or any oscillation in the “effect” this is understood in the problem as something due to changes in the boundary conditions, which leads to non-continuous behavior of the initial conditions of the problem.

Methods to solve inverse problems have been used continuously in research in all fields, sometimes even without notice or classifying it as an inverse method. Any time that we are applying “reverse engineering”, we are applying some kind of inverse method to solve a problem. This technique was used, for example, in the definition of the International Gravity Formula and to compute the standard acceleration of gravity by Newton [2]. Based on observation and repetition of experiments, he could define a model with a constant that was previously unknown. Therefore, starting from the “effect” he could compute which were the “causes” and the “conditions” of the problem. But the field of solving inverse problems was truly opened after the Second World War when Swedish mathematicians found an article from the Soviet-Armenian physicist Viktor Ambartsumian published in 1929 [3][4][5]. In his article, Ambartsumian was

asking if based on the eigenvalues of a matrix, one could find the form of the equations that yielded the eigenvalues. Ambartsumian thoughts were more related with the definition of physical laws from the experimental data, *i.e.*, starting from observations of the phenomena, is it possible to define a physical law that explains the observed effect in the system? In the cases that are analyzed subsequently in this chapter, the physical law is defined (the heat diffusion equation) and the boundary conditions of the problems are unknown.

This literature review is focused in the application of the inverse methods in the particular field of heat transfer. Therefore, the physical law for how heat is spread through a solid is defined: the heat diffusion equation. But the boundary conditions or material properties are unknown, which is common and often due to inaccessibility or lack of relevant experimental data. In that case, the only option is the measure the temperature map and use inverse methodologies to retrieve the heat flux (“cause”) or thermo-physical properties of the material (“conditions”) of the heat problem. Inverse methods have been widely used for the following topics inside of the field of heat transfer:

- Estimation of thermo-physical properties of materials [6][7][8][9][10][11][12].
- Estimation of bulk radiation properties and radiation boundary conditions [13][14][15][16].
- Solidification and change of physical state [17][18][19].
- Estimation of heat flux in ducts [20][21][22].
- Conductance during solidification process [23][24].
- Contact resistance [25].
- Estimation of reaction function [26][27].

- Estimation of the boundary shapes of bodies [28][29].

These problems are solved using different inverse heat transfer techniques, which will be introduced and detailed in following sections of this chapter. All of them have something in common: they require the determination of a sensitivity coefficient which relates the effect with the cause. The sensitivity coefficient is the derivative of the computed parameter with respect to the parameter that is causing it. Therefore, in heat transfer, the sensitivity coefficient is the derivative of the temperature with respect to the heat flux that created that temperature increase. In the next section, we explain the term and we give insights about its calculation.

As we will detail in the Section 2.3, inverse methodologies can be classified in a variety of different ways. The classification and simplification that is introduced in this dissertation groups them by nature of the solving methodologies: optimization techniques and fitting techniques. All optimization methodologies can be used to compute the cause of an event, if the objective function of the optimization is well defined. The fitting techniques rely on the solution of a system of equations, in time domain or frequency domain, provided the relation between the cause (heat flux) and the effect (increase of temperature), which is the sensitivity coefficient or matrix of coefficients.

## 2.1 Sensitivity Coefficient Definition

The evaluation of the sensitivity coefficient provides a valuable knowledge about the performance of the inverse problem. The sensitivity coefficient can be understood in layman terms as the quantification of the effect in the measured parameter due to a variation in a “cause”. In this research, we use an unknown heat flux as the “cause” in order to simplify the formulation, but any other parameter such as thermal conductivity, density, or thermal diffusivity could be



the “cause” under evaluation. Therefore, in heat transfer terms for this problem, the sensitivity coefficient relate to the heat flux is the effect in the temperature due to variations in the heat flux, which is similar to the concept of thermal resistances but evaluated at every position and time within the domain. Mathematically it is expressed as the derivative of the temperature with respect to the heat flux at a particular location and for a 1D problem with a single heat source can be represented as:

$$X_{jM}(x_j, t_i) = \frac{\partial T(x_j, t_i)}{\partial q_M} \quad (1)$$

Therefore,  $X_{jM}$  represents the measured effect (temperature) at the location  $x_j$  at the time  $t_i$  due to the heat flux component  $q_M$ , where the subscript  $M$  represents the time step when the heat flux was applied.  $X_{jM}$  is the sensitivity coefficient that measures the sensitivity of the temperature measurement  $T(x_j, t_i)$  to changes in the value of  $q_M$ . Small values of the sensitivity coefficient imply that large changes in the heat flux yield small changes in temperature. This is one of the main challenges of the inverse methodologies, since the calculation of the heat flux is highly dependent on the temperature measurement. Note that equation 1 is a simplified version of the coefficient assuming 1D temperature locations and only one heat source in transient operation. If we add a 2D grid of temperature sensors and more than one heat source the matrix size grows exponentially, as well as the number of unknowns in the problem. Considering the whole structure of a real system, equation 1 generates a Jacobian matrix known as Sensitivity Matrix [30].

In problems where the parameters or boundary conditions values differ in orders of magnitude, the effect of the searched parameter can vary over orders of magnitude as well. This creates difficulties in the evaluation of the linear dependence between the cause and the effect. A

solution for this is to use dimensionless sensitivity coefficients (Equation (2)) and dimensionless distance and time constants (Equation (3) and (4), respectively).

$$X^+ = T^+ = \frac{T - T_0}{q_c L / k} = \frac{k}{L} \frac{\partial T}{\partial q_c} \quad (2)$$

$$x^+ = \frac{x}{L} \quad (3)$$

$$t^+ = \frac{\alpha t}{L^2} \quad (4)$$

Here,  $k$  is the thermal conductivity,  $L$  is a characteristic length scale for the problem,  $t$  is the characteristic time for the problem,  $\alpha$  is the thermal diffusivity of the material,  $q_c$  is the heat flux applied in the pulse and  $T_0$  is the initial temperature of the system.

These are the expression of the common non-dimensional numbers in the inverse heat transfer problem evaluated using sensitivity coefficients, but they can vary depending on the analytical solution of the problem, since, for example, for lumped capacitance problems they can be expressed in a different way [6]. Also, we can define a dimensionless timestep similar to Equation (4) but substituting the time  $t$  by the timestep  $\Delta t$ . It is remarkable that the dimensionless time is the same as the well-known Fourier number (Fo) that characterizes the transient behavior in heat conduction.

The shape and value of the sensitivity coefficient changes with the problem, boundary conditions, and length scales of the time step. The location of the peak is influenced by the size of the timestep. In order to obtain the sensitivity coefficient represented in Figure 2-1, we need to apply a pulse of heat flux in a particular timestep. When dealing with smaller timesteps, the amount of

energy transmitted to the test article (or model) is smaller and therefore the peak is lower. At the same time, due to the adimensionalization in time, the peak appears before, only because it is expressed in terms of  $t^+$ . In terms of  $t$ , the peak would appear before for larger timesteps.

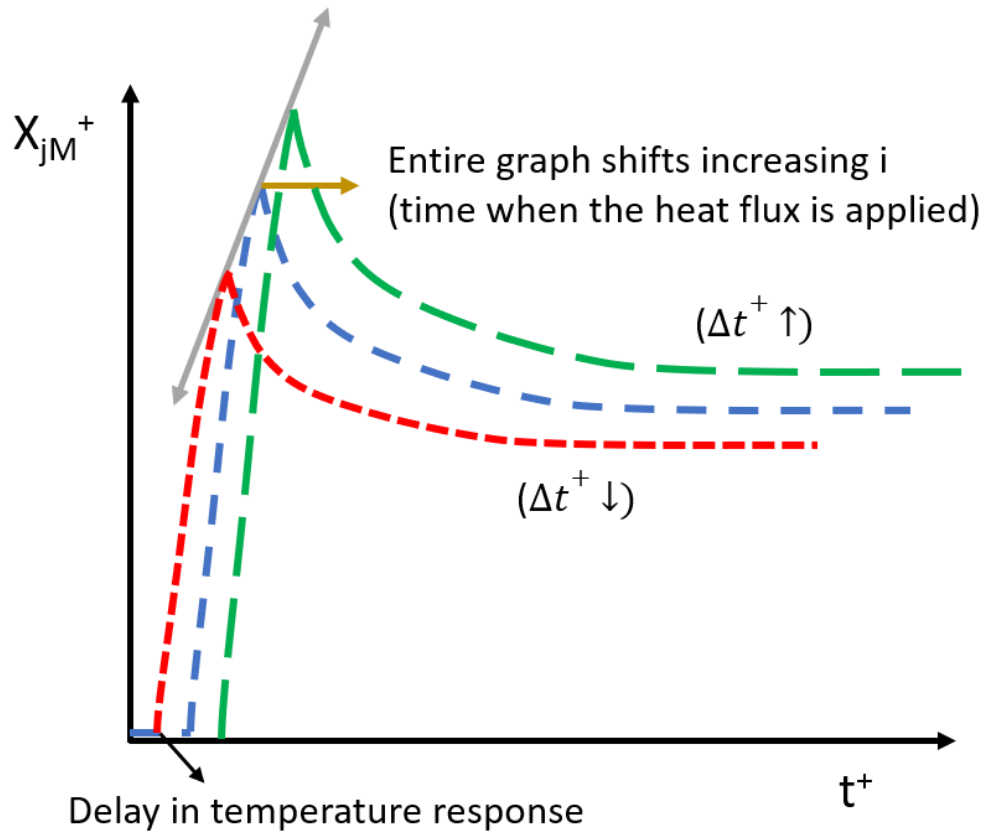


Figure 2-1. Sensitivity coefficient for the temperature increase with respect to the heat flux. At a particular point, there is a delay in the temperature response due to the finite speed of thermal diffusion. The peak magnitude shifts depending on the time of application of the heat flux pulse. Also the peak magnitude and location is modified with the size of the non-dimensional timestep, since at smaller timesteps the energy provided to the system is smaller.

There are different ways to compute the sensitivity factor depending on the complexity of the system. The first method is based on the analytic solution. This method works well for conductive problem with simple geometries and with information about the boundary conditions. We solve the temperature distribution by solving heat diffusion equation with the known

boundary conditions and then we derive the temperature result with respect to the unknown parameter (boundary condition or any thermal property) to get the sensitivity coefficient with respect to the aforementioned parameter.

To illustrate the calculation using the analytic solution method we have chosen the solution of the semi-infinite solid in which we apply a uniform heat flux  $q''_s$  [31]:

$$T(x, t) - T_0 = \frac{2 q''_s \left(\frac{\alpha t}{\pi}\right)^{\frac{1}{2}}}{k} \exp\left(\frac{-x^2}{4 \alpha t}\right) - \frac{q''_s x}{k} \operatorname{erfc}\left(\frac{x}{2\sqrt{\alpha t}}\right). \quad (5)$$

The sensitivity coefficient is calculated deriving the Equation (5), so the sensitivity coefficient with respect to the boundary condition  $q''_s$  at the any location  $x$  and at a time  $t$  is

$$X_{q_s}(x, t) = \frac{\partial T(x, t)}{\partial q''_s} = \frac{2 \left(\frac{\alpha t}{\pi}\right)^{\frac{1}{2}}}{k} \exp\left(\frac{-x^2}{4 \alpha t}\right) - \frac{x}{k} \operatorname{erfc}\left(\frac{x}{2\sqrt{\alpha t}}\right) \quad (6)$$

The sensitivity coefficient depends on position and time after the applied heat flux. We can observe that this coefficient does not depend on the magnitude of  $q''_s$  and therefore the inverse problem is linear.

A second methodology involves solving the Boundary Value problem. It consists in deriving the heat diffusion equation with respect to the searched parameter or function and adapting the boundary conditions to the differentiation. Normally, the result is a PDE of the same kind as the heat diffusion equation and, therefore, we can solve it in the same way [30]. The Conjugate Gradient Method uses this approach to compute the sensitivity problem. The following problem (in the left column) considers a slab of thickness  $L$  with a planar heat source in the middle of the

slab that yields the sensitivity coefficient problem (in the right column) where the subscript  $j$  counts the number of parameters to be determined by the inverse method.

Forward problem definition

Sensitivity coefficient definition

$$\frac{\partial T(x, t)}{\partial x^2} + C_j q_j(t) \delta(x - 0.5) = \frac{\partial T(x, t)}{\partial t} \quad 0 < x < L, t > 0 \quad (7) \quad \frac{\partial X_j(x, t)}{\partial x^2} + C_j(t) \delta(x - 0.5) = \frac{\partial X_j(x, t)}{\partial t} \quad (11)$$

$$\frac{\partial T(0, t)}{\partial x} = 0 \quad x = 0, t > 0 \quad (8) \quad \frac{\partial X_j(0, t)}{\partial x} = 0 \quad (12)$$

$$\frac{\partial T(L, t)}{\partial x} = 0 \quad x = L, t > 0 \quad (9) \quad \frac{\partial X_j(L, t)}{\partial x} = 0 \quad (13)$$

$$T(x, 0) = 0 \quad 0 < x < L, t = 0 \quad (10) \quad X_j(x, 0) = 0 \quad (14)$$

Another method to compute the sensitivity coefficient is using the finite difference approximation. Using different schemes to compute the derivative with respect to the searched parameter, we can compute the sensitivity coefficient. For instance, using the forward difference scheme the sensitivity coefficient would be computed as

$$X_{ij} = \frac{T_i(q_1, q_2, q_j, \dots, q_N + \gamma q_1, q_2, q_j, \dots, q_N) - T_i(q_1, q_2, q_j, \dots, q_N)}{\gamma q_j} \quad (15)$$

where  $N$  is the total number of parameters to estimate and  $\gamma$  is a parameter that oscillates between  $10^{-5}$  and  $10^{-6}$ , obtained empirically [6], that increments the heat fluxes a small step. This method is the computationally most expensive of the three approaches since it requires  $N$  additional

direct solutions for the forward and backward schemes and  $2N$  additional direct solutions for more complex schemes like the central differences scheme.

The first two methodologies to compute the sensitivity coefficient can be applied in 1D and 2D simple problems in which the analytical solution is known. If complex 3D problems are targeted the only way to compute the sensitivity coefficient is the finite difference approximation.

All these methods can be extended to problems with multiple temperature sensors and multiple unknown parameters.

## 2.2 Challenges of the Inverse Heat Transfer Methods

The main challenge related with inverse methodologies for heat transfer is related to the ill-posed nature of the problem. Recall that Hadamard [1] defined a well-posed problem as the one that (a) has solution, (b) this solution is unique and (c) the behavior of the solution changes continuously with the boundary and initial conditions. The inverse problem has several solutions for the same boundary conditions and it is extremely sensitive to the errors in the measurements, therefore it is ill-posed. Understanding this concept is central to properly analyzing inverse method solutions, keeping in mind the limitations that these facts imply.

Particularly in conductive heat transfer, we have to take into account two other concepts for the inverse calculation of the boundary conditions or inverse parameter. First, the effect of the boundary conditions damps and lags through the solid. Specifically, the magnitude of the temperature increase diminishes with the distance from the source (damping) and this temperature increase is delayed in time depending on the distance from the boundary conditions (lagging). Thus, the sensitivity coefficient depends on space and time. These effects are mainly related with the thermal properties of the material. Materials with larger thermal diffusivity have

smaller damping and lagging. This has implications in the selection of location of the sensors. If the sensor is too far away from the point of applied heat flux, the temperature increase will fall within the uncertainty of the measurements and, therefore, it will be practically impossible to have reliable information of the solution to the inverse problem. In heat transfer problems with oscillating thermal transients, higher frequencies of oscillation yield smaller the depths at which the effect of the oscillating heat source is felt within the solid. To give an order of magnitude from the analytical solution in a semi-infinite body [6], for a steel slab, applying heat fluxes at a frequency of 1Hz, the metal slab will not experience any significant temperature fluctuation beyond 0.82 cm from the heating source. If we increase the frequency even further to 100 Hz, this distance is reduced by one order of magnitude to 0.08 cm. This effect can be observed not only on the damping, but also on the lagging. For the case of the 1 Hz heat frequency the time lag at  $x=0.82$  cm is 0.73 s. Hence, lagging and damping constitute a major limitation for these kinds of problems.

The sensitivity coefficients are another important source of uncertainty in inverse heat transfer calculations due to the important role they play in the computation. This coefficient measures the effect in the measured temperature due to variations in the searched parameter. If its value is too small, the inverse calculation will be extremely difficult since we have  $|X^T X| \approx 0$ , which is an ill-conditioned matrix and thus any column of  $X$  can be expressed as a linear combination of different columns in the system [7]. Physically, this means that there will be a large range of values of the parameter (or function) that you want to estimate that will give the same temperature response. It is recommended to maximize  $|X^T X|$  and have linearly independent rows in the matrix to reduce the range of the solution.

Close related to the previous problem, we find that the computation and sensitivity matrix module are very sensitive to the size of the timestep. Timewise variations of the sensitivity coefficient should be analyzed in order to choose the best temperature measurement location and measurement time steps to apply the inverse method. Normally, they will be correlated to the maximization of  $|X^T X|$  and the larger independent sensitivity coefficients.

Taking into account all these challenges, the objective function that must be minimized when searching for an unknown parameter,  $q_c$ , in order to properly solve the heat diffusion equation is related to the measured temperature  $Y$  and the calculated temperature  $T$ :

$$S(q_c) = \sum_{i=0}^M (T_i(q_c) - Y_i)^2. \quad (16)$$

In this function, the  $Y_i$  is the measured temperature at time  $i$ , and  $M$  is the total number of measurements in time. By varying the unknown parameter,  $q_c$ , we modify the value of the calculated temperature  $T_i(q_c)$  at time  $i$  using the sensitivity coefficients to minimize the objective function  $S(q_c)$ . If we consider that  $N$  is the total number unknown parameters (heat flux in time and space in this case), then  $M \geq N$  in order to have enough equations to solve all the unknowns. This objective function can also be expressed in matricial form as

$$S(q_c) = [Y - T(q_c)]^T [Y - T(q_c)]. \quad (17)$$

As the superscript  $T$  denotes transpose matrix, Equations (16) and (17) are equivalent and are used interchangeably.



### 2.3 Inverse Heat Transfer Classifications

Inverse methods can be classified in different ways depending on the purpose of the calculation. These classifications help to identify which method or methods are suitable for a particular problem, since the computational time can be greatly reduced knowing the characteristics of the problem. Figure 2-2 illustrates a simplification of the different numerical methods that are used to solve the inverse problems.

The first classification the solution method for the heat diffusion equation. Broadly speaking, solution methods include using Duhamel's Theorem [6] or difference methods (including finite difference approaches, finite element methods, and control volume approaches)[32][33]. The difference approaches can handle easily non-linear solutions of the heat diffusion equation, while solutions based on Duhamel's Theorem is restricted to linear solutions. In linear problems, the properties of the materials and boundary conditions do not depend on the temperature of the test article, while in non-linear problems there is a dependency on temperature. Not all the inverse heat conduction algorithms are suitable to calculate non-linear problems. Particularly, solutions based in the Duhamel's Theorem and the solutions performed using Laplace transforms fail to handle non-linear problems. Other methods based on function specification and regularization methods can be applied to both non-linear and linear heat diffusion equations. But solutions based on Duhamel's Theorem are typically faster since they do not require an iterative calculation.

Next, we can classify the methodology depending on the algorithm used to solve the problem. Many algorithms have been used to solve inverse problems: integral equation approaches ([34]-[41]), series solution approaches ([42]-[45]), polynomial approaches ([46]-[48]), space marching techniques with noise filtering ([49]-[51]), hyperbolization methods of the heat equation ([52]-

[54]), iterative filtering techniques [55], and regularization techniques ([56]-[70]) amongst them the Tikhonov's regularization technique ([4],[71]-[75]). Since the number of methods is so large, we group them in two main groups: problems solved using *fitting techniques* (*i.e.*, calculating the best estimator of a system of equations) and *optimization techniques* [66][62], where we minimize an objective function based in the difference between the measured and the calculated temperature map. Fitting methodologies can be iterative or simple calculations solving a system of equations once, while the optimization methods involve always an iterative procedure. The function specification method [6][7] and the Marquardt-Levenberg methodologies [81][82][83] are in the first group. These methods can be combined with a regularization technique in order to reduce the divergence of the method and converge in a more physical solution. The second group, optimization techniques, include deterministic and stochastic methods and includes the Conjugate Gradient Method coupled with Adjoint and Sensitivity problems [109][131][132][133] which it is one of the most robust methods to solve complex 3D inverse heat transfer problems. Recently, there has been a tendency to use approaches with more complex mathematical methodologies such as using lattice-Boltzmann approaches combined with Proper Orthogonal Decomposition (POD) ([76]-[79]). These methods can produce low-order, high quality approximations of the field under certain assumptions and have been applied for estimation of estimation of both boundary heat flux [20][21][22] and thermal properties [6][7][8][9][10][11][12]. The following sections explain in more detail the two main categories of algorithms.

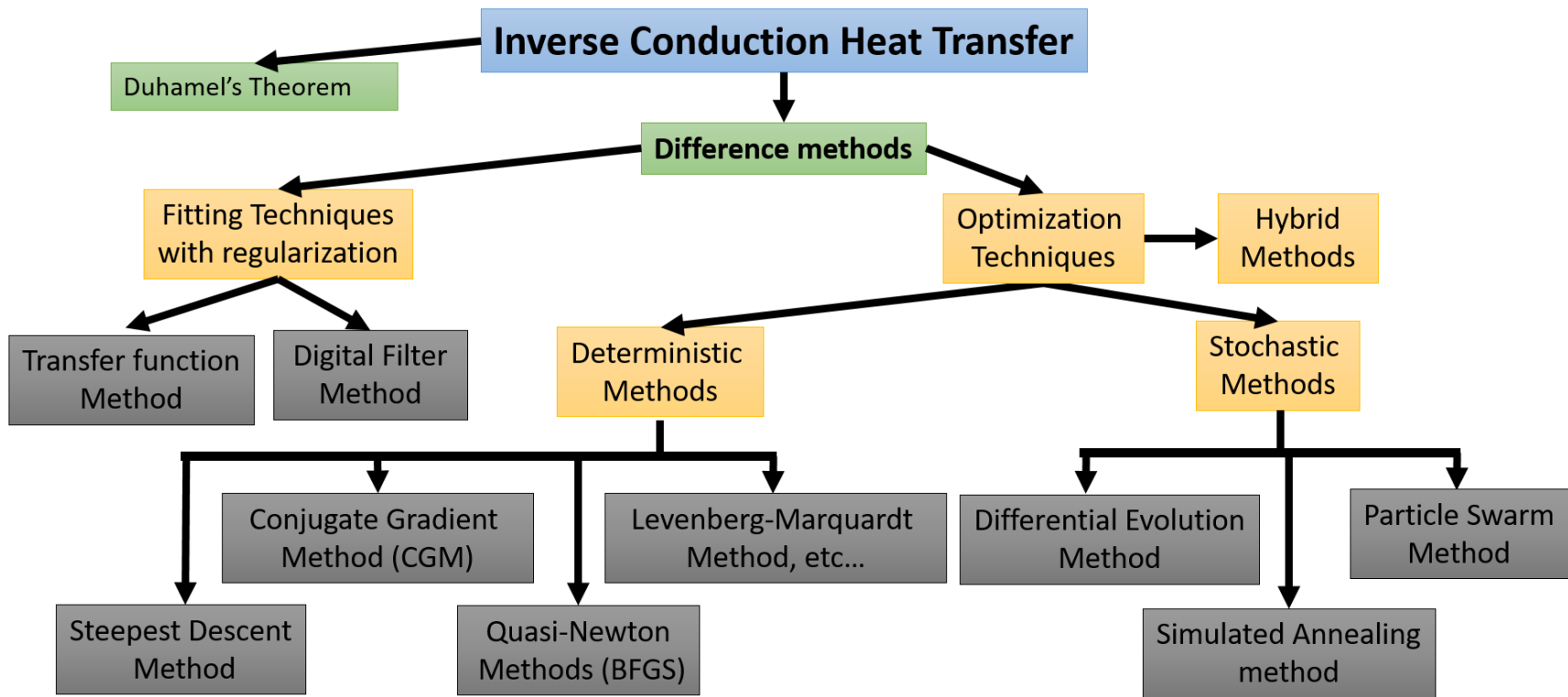


Figure 2-2. Classification of inverse heat transfer methods based on the methods used to solve the inverse problem.

Further, the method of solution of the Inverse Heat Conduction Problem (IHCP) can be also classified depending on the use of the time domain during the calculation. The calculation of the inverse method can be performed using the information of the temperature in the sensors (a) in the same moment when the heat flux is applied (*i.e.*, Stolz method [32]), (b) in the moment when it is applied plus some of the future time steps (*i.e.*, sequential methods)[33], or (c) using the whole domain estimation, in which all the time steps are considered in the calculation of the heat flux at a particular time. The first method, called Stolz method [32], is extremely sensitive to measurement errors since it is based in a direct correspondence between the measurement of the sensor at the present time and the value of the heat flux at the same time. Sequential methods use only few of the future time steps are typically more robust, being less sensitive to the effect of the error in the measurements. Therefore, we can compute the inverse calculation with much smaller time steps. The whole domain methods are suitable for even smaller time steps since they are even less sensitive to the measurement error, but we are penalized in the computational cost with respect to the “sequential” methods. Most of the algorithms introduced in this research can be modified for use in both sequential and whole domain estimations.

In order to evaluate the inverse heat conduction methods, Beck [6] and Ozisik [24] [30] established a set of criteria for evaluating methods to solve IHCPs:

1. Low difficulty of programming and moderate computational cost
2. Easy to adapt to different geometries using different coordinate systems.
3. Calculated temperatures and heat flux must be accurate if the temperature measurement is accurate.
4. Insensitive to measurement errors.

5. The stability of the method must be guaranteed for small and large time steps.
6. The starting time of the application of the heat flux should not be required prior knowledge for the calculation.
7. Handle all kind of materials including isotropic and anisotropic thermal properties.
8. The method can allow for more than one heating plane within the system.
9. Temperature distribution measured with one or more temperature sensors.
10. Contact resistances can be included in the calculations.
11. Errors need to be evaluated on a statistical basis.

## 2.4 Fitting Methodologies

As described in the previous section, we broadly classify inverse methods into two categories: fitting methods and optimization methods. Fitting methods typically fit for the temperature difference between the calculated and the measured temperatures in one calculation, without the need of any iterative process. However, when there are non-linear features in the heat conduction calculation we can implement an iterative procedure based in a least square estimation as well. All the methodologies based on fitting require a definition of the sensitivity coefficient. We summarize three fitting methods: the Levenberg-Marquardt method, the digital filter method, and the transfer function method. These methods were selected as they are the most commonly used in the literature. They are completely different one from each other, giving a great diversity of in the example of the fitting methods

### 2.4.1 The Levenberg-Marquardt Method & Digital Filter Method

The basic algorithm that describes this approach was introduced by Levenberg and Marquardt [81][83] for parameter and function estimation. This algorithm was initially developed to solve non-linear estimation problems, but it is used in this case to solve ill-conditioned linear problems. The estimation of the heat flux for this method is based on the minimization of the ordinary least squares norm:

$$S(q_c) = \sum_{i=1}^M (Y_i - T_i(q_c))^2, \quad (18)$$

where  $S$  is the objective function,  $Y_i$  is the measured temperature,  $T_i(q_c)$  is the estimated temperature, and  $M$  is the number of measurements. We can highlight the correlation between the Equation (16) and the Equation (18), which therefore can be written in matricial form in the same way that Equation (17).

In order to minimize the above objective function, we need to compute the derivatives with respect to all the parameters we need to estimate and equate this to zero. The gradient of the objective equation with respect to the vector of heat flux needs to be equal to zero:

$$\nabla S(q_c) = -2 \underbrace{\left[ \frac{\partial T^T(q_c)}{\partial q_c} \right]}_{X^T} [Y - T(q_c)] = 0. \quad (19)$$

The sensitivity matrix  $X$ , also known as Jacobian matrix, is the transpose of the first term between brackets in the Equation (19), so that equation can be expressed using the sensitivity matrix as

$$-2 X^T [Y - T(q_c)] = 0 \quad (20)$$

If the sensitivity matrix of coefficients does not depend on the temperature, *i.e.*, we are solving a linear problem, the solution for the Equation (20) can be expressed as

$$q_c = (X^T X)^{-1} X^T Y. \quad (21)$$

Equation (21) constitutes the main core of this method and provides the best estimator of the linear problem solution using least squares.

There have been two main expansions of this equation over the years in order to accommodate the solution for non-linear problems and to avoid the non-singularity of the matrix  $X^T X$  due to the ill-condition nature of the problem. The non-linear estimation of the heat flux requires an iterative procedure. For this iterative process, the temperature vector is linearized using a Taylor series expansion around the solution of the heat flux at the previous iteration. The Equation (22) linearizes the temperature behavior under non-linear conditions, where  $k$  is the current iteration.

$$T(q_c) = T(q_c^k) + X^k(q_c - q_c^k) \quad (22)$$

When we substitute the new value of  $T(q_c)$  described in Equation (22) into Equation (20), the best estimator of the  $q_c$  is written as the iterative Gauss method which is an approximation of the Newton-Raphson method.

$$q_c^{k+1} = q_c^k + [(X^k)^T X^k]^{-1} (X^k)^T [Y - T(q_c^k)] \quad (23)$$

The stopping criteria for this iterative estimation can follow different standards. Three criteria widely accepted were introduced by Dennis and Schanabel [86]:

$$S(q_c^{k+1}) < \varepsilon_1, \quad (24.a)$$

$$\|(X^k)^T [Y - T(q_c^k)]\| < \varepsilon_2, \text{ and} \quad (24.b)$$

$$\|q_c^{k+1} - q_c^k\| < \varepsilon_3. \quad (24.c)$$

The parameters  $\varepsilon_1, \varepsilon_2, \varepsilon_3$  are tolerances set by the user based in the uncertainty of the temperature measurements and the standard deviation of the estimated heat flux [87]. These

criteria is not always suitable for any problem and it may be adapted depending on the problem and the degree of accuracy required in the solution. For example, the criteria described in the Equation (24.b) will fail when the function describes a maximum or a saddle point and criteria in Equation (24.c) may not give the final solution if the calculation stalls for few iterations before advancing to a minimum [7][85]. This iterative procedure can be understood as well as an optimization methodology, as described in the next section.

The second modification of the Levenberg-Marquardt method consists of eliminating or minimizing the ill-condition of the matrix  $(X^T X)^{-1}$  that needs to be transposed. If the determinant of that matrix is 0 or very small we are not able to use the procedure to determine the desired parameter. A regularization term is included inside of the ill-conditioned matrix to alleviate this problem, especially in the first guess of the unknown parameters in the iterative process when the matrix is very ill-posed:

$$q_c^{k+1} = q_c^k + [(X^k)^T X^k + \mu^k \Omega^k]^{-1} (X^k)^T [Y - T(q_c^k)], \quad (25)$$

where  $\mu^k$  is the damping parameter and  $\Omega^k$  is a diagonal matrix. A common practice is to start with large values of  $\mu^k$  in comparison with the determinant of the matrix  $(X^k)^T X^k$  and then reduce it as the iteration process advances. In this way, the method migrates from a Steepest Descent Method to the above described Gauss Method.



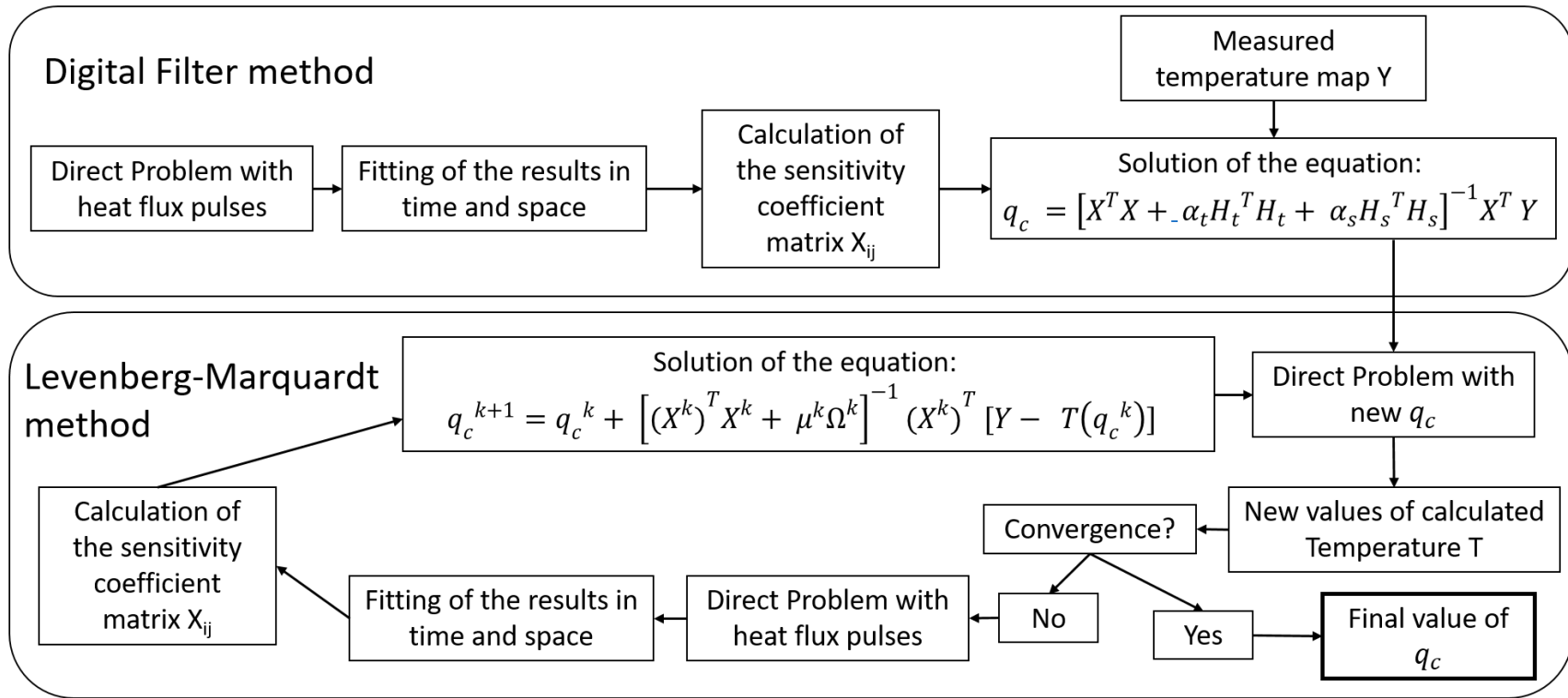


Figure 2-3. Schematic of the digital filter method and Levenberg-Marquardt method procedures to solve non-linear inverse problems and the relation between them. The DFM can be used to provide an initial value of heat flux for the Levenberg-Marquardt Method, but the computation of the direct problem will provide new values of temperature and the sensitivity coefficients can be re-computed till we reach convergence.

Figure 2-3 illustrates the steps to complete the estimation of the heat flux using the Levenberg-Marquardt method, in its direct approach and in its iterative approach. The direct approach is the Digital Filter Method and the iterative method approach takes into account the temperature computed in the previous iteration in order to compute the non-linearity provided by the temperature dependent thermal properties.

As aforementioned, the Levenberg Marquardt Method is called by some researchers Digital Filter Method and this is the nomenclature that we have adopted in this doctoral dissertation. In this method the sensitivity coefficients in the  $X$  matrix can be obtained as explained in the previous section. The solution proposed in the Digital Filter Method is a non-iterative solutions that combines the Levenberg-Marquardt method with a regularization divided in a spatial term and a time term [88][89]. Therefore, the equation that needs to be fit is

$$S = (Y - T)^T(Y - T) + \alpha_t[H_t q]^T[H_t q] + \alpha_s[H_s q]^T[H_s q]. \quad (26)$$

The solution to this is obtained applying the same principles that in the Levenberg-Marquardt method:

$$q_c = [X^T X + \alpha_t H_t^T H_t + \alpha_s H_s^T H_s]^{-1} X^T Y. \quad (27)$$

The expressions  $\alpha_t H_t^T H_t$  and  $\alpha_s H_s^T H_s$  are the transient and spatial regularization terms, respectively. Inside of these terms, the coefficients  $\alpha_s$  and  $\alpha_t$  are the regularization parameters with values between 0 and  $10^{-4}$ . The solution is very sensitive to the value of these regularization coefficients, which depend on the geometrical features and the previous information of the transient and spatial distribution of heat flux. The matrix  $H_s$  and  $H_t$  are the structures that define

the order of the regularization and modifying its internal arrangement adjusts the regularization order based on the geometrical relations between the analyzed points:

$$H_t = \begin{bmatrix} -I & I & 0 & \dots & 0 \\ 0 & -I & I & \dots & 0 \\ \vdots & \vdots & \vdots & \ddots & \vdots \\ 0 & 0 & \dots & \dots & 0 \end{bmatrix}, \text{ where } I = \begin{bmatrix} 1 & 0 & 0 & \dots & 0 \\ 0 & 1 & 0 & \dots & 0 \\ \vdots & \vdots & \vdots & \ddots & \vdots \\ 0 & 0 & \dots & \dots & 1 \end{bmatrix} \quad (28)$$

$$H_s = \begin{bmatrix} h_s & 0 & 0 & \dots & 0 \\ 0 & h_s & 0 & \dots & 0 \\ \vdots & \vdots & \vdots & \ddots & \vdots \\ 0 & 0 & \dots & \dots & h_s \end{bmatrix}, \text{ where } h_s = \begin{bmatrix} -1 & 1 & 0 & \dots & 0 \\ 0 & -1 & 1 & \dots & 0 \\ \vdots & \vdots & \vdots & \ddots & \vdots \\ 0 & 0 & \dots & \dots & 0 \end{bmatrix}.$$

a,b,c,d)

The distributions shown in the Equation (28), correspond to first order regularization terms, both in space and in time. Najafi *et al.* [89] used this method to retrieve distributions of heat flux in a simple 2D geometry. He calculated the sensitivity matrix analytically which allows a quick estimation of the imposed heat flux.

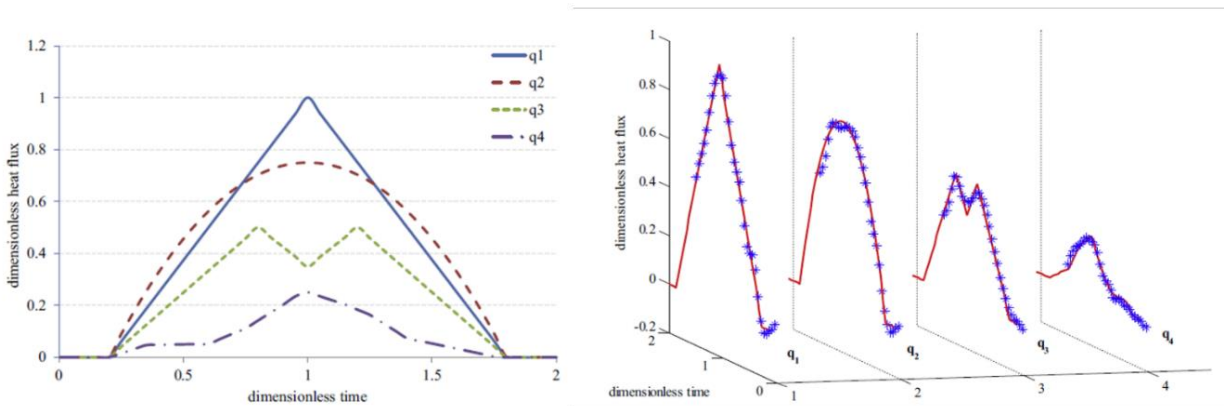


Figure 2-4. (a) Four imposed transient heat flux profiles and (b) predictions of the heat flux profiles using analytical estimation of the sensitivity coefficients using the Digital Filter Method. Note that the imposed heat flux is input into a 2D analytical solution to extract temperatures that are fed into a 1D solution with the Digital Filter Method. Reproduced from [89] with permission.

Computational efficiency is the main benefit of using the Levenberg-Marquardt method. Since we simply have to solve a system of equations described by the sensitivity coefficient matrix, using

the non-iterative procedure with regularization and preconditioning, the problem can be evaluated in nearly real time with a good accuracy.

#### 2.4.2 Transfer Function Methods

Transfer function methods solve the heat conduction equation in the frequency domain, so the equation needs to be transformed in order to solve it. They are used broadly in problems with analytical solution.

Analytically, the heat diffusion equation can be solved in different ways including using Fourier transforms, Laplace transforms, or Green functions based on the response of the system to a pulse of heat. In the last few decades, the evolution of fast inverse methods has shifted towards the frequency domain ([90]-[93]). Calculations in the frequency domain may be easier for complex problems since convolution in the time domain transforms in a simple multiplication in the frequency domain.

First consider a transfer function method based on Green Functions and Laplace transforms (therefore limited to linear problems). Briefly, the effect on the temperature due to a heat pulse at a particular location and time is evaluated for the future timesteps giving as a result that the temperature is the convolution of the effect (sensitivity coefficients) with the applied heat flux.

This approach is well described by Fernandes *et al.* [93] for both 1D and 3D cases.

Describing the method in more detail for a 1D case, we need to solve the heat diffusion equation, knowing the boundary or boundaries where the heat flux is applied. The integral solution of the direct problem based on the Green's function approach corresponds to

$$T(x, t) = T_0 + \alpha \int_0^t G(x, t|0, \tau) \frac{q(\tau)}{k} d\tau, \quad (29)$$

where  $G(x, t|0, \tau)$  is the Green function at the initial time that solve the equation. For a flat plate with heat one heat source, based on the analytical solution of the Green's function, we can substitute  $G(x, t|0, \tau)$  in Equation (29) and the solution of the temperature is

$$T(x, t) = T_0 + \frac{\alpha}{kL} \int_0^t q(\tau) d\tau + \frac{2\alpha}{kL} \sum_{m=1}^M e^{-\left(\frac{m\pi}{L}\right)^2 \alpha t} \cos\left(\frac{m\pi x}{L}\right) \int_0^t e^{\left(\frac{m\pi}{L}\right)^2 \alpha \tau} q(\tau) d\tau. \quad (30)$$

This is the direct solution of the variation of temperature in a flat plate, where  $M$  is the number of eigenvalues needed to converge. In order to use this analytical solution in an inverse procedure, we need to analyze the response of the system to the application of an impulse of heat. Based on the theory of dynamic systems, the response (temperature rise) is related to the input (heat flux) by the convolution integral (Equation (31)). Then the transfer function is expressed as the Laplace transform of the response taking into account that the impulse is stated as the Dirac Delta function,  $q(t) = \delta(t)$ .

$$T(x, t) = h(x, t) * q(t) = T_0 + \alpha \int_0^t h(x, t - \tau) q(\tau) d\tau \quad (31)$$

$$T(x, t) = h(x, t) * \delta(t) = T_0 + \alpha \int_0^t h(x, t - \tau) \delta(\tau) d\tau = h(x, t) \quad (32)$$

The transfer function  $h(x, t)$  is related to the Green's function by the factor  $\frac{\alpha}{k}$ . As we can solve the problem in the frequency domain by taking the Laplace transform, the computation of the heat flux is simplified to

$$q(s) = \frac{1}{H(x, s)} \cdot T(x, s) \quad (33)$$

in the frequency domain and is

$$q(t) = \frac{1}{h(x, t)} * T(x, t) \quad (34)$$

in the time domain.

Therefore, solving these simple equations, we estimate the heat flux that generates the temperature increase. The transfer function  $h(x, t)$  is similar to that of the Digital Filter Method. They are based on the same principles, but in this case, the calculation is entirely in the frequency domain before inverting the Laplace transform to the time domain. Moreover, this method is purely linear, without a possibility to include any non-linearity in the heat diffusion equation. Figure 2-5 shows an outline of the Transfer Function Method for solving IHCPs.

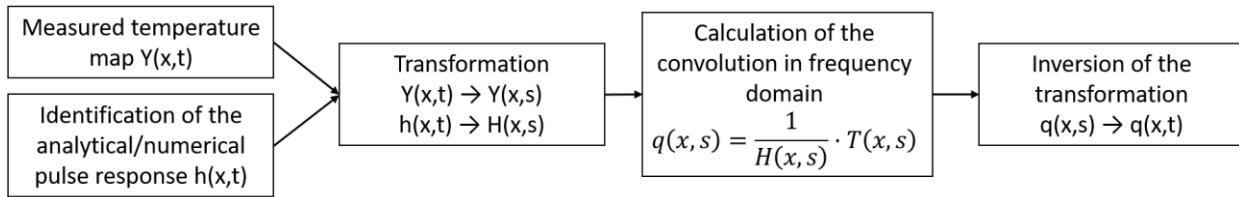


Figure 2-5. Schematic of the transfer function method in frequency domain procedure to determine the heat flux in inverse heat transfer problems.

Figure 2-6 shows examples of the 1D and 3D solutions provided by this method. Note that the agreement between the simulated heat flux and that computed by the 1D analytical solution is better when using data from measurement planes closer to the heat source. In experimental applications (Figure 2-6b), the estimation is noisier due to the noisy nature of the input temperature signal. There are some corrections that can be made in the method to reduce the error in the estimated heat flux using the temperature sensors further from the heat source. Specifically, this

correction uses the negative gradient of the sensitivity coefficient in time, neglecting the contribution of the positive gradient at the as a result of the application of the pulse.

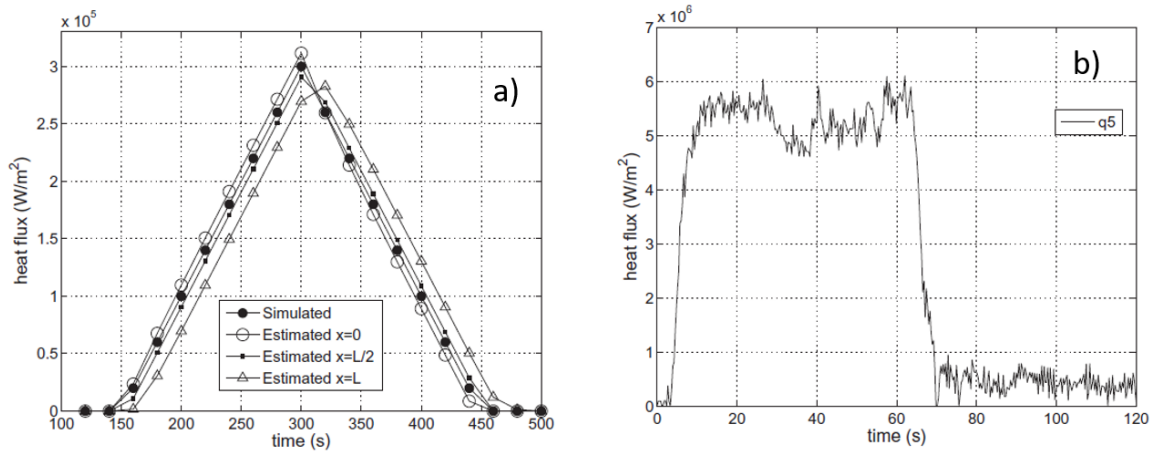


Figure 2-6. Application of the transfer function method using a) a 1D numerical model of a flat plate using the simulated temperature readings from three different planes as input to the inverse method and b) a 3D inverse heat flux estimation using a temperature reading from an experimental setup consisting of a cutting tool of high speed steel during machining. Reproduced from [93] with permission.

The Levenberg-Marquardt, digital filter, and transfer function methods are all fitting methodologies that are completely different amongst them. The fitting methodologies can go from iterative to non-iterative solved in the frequency domain. There is a large diversity of method that fall in the fitting methodologies. Beyond these approaches, the next section focuses on iterative methods for solving the IHCPs which are equivalent to optimization methodologies.

## 2.5 Optimization Methodologies

Nowadays, many methods used to solve inverse heat transfer methods are adaptations of optimization techniques ([62], [94]-[107]). Colaço *et al.* [62] recently reviewed optimization methodologies applied in inverse problem for heat transfer. Even though the algorithms of inverse problems and the optimization problems are similar, the problems are conceptually different, and

several key differences exist. While inverse methods are focused on the estimation of unknown parameters or functions for a physical problem, optimization techniques only consider minimization of a cost function, looking for the values of the inputs that result in the minimum value of the objective function and this can yield non-physical solutions. Additionally, for general optimization problems, the stability and uniqueness of the solution is not an important issue as long as the solution is feasible and of practical implementation. However, in inverse problems, the application of regularization techniques to minimize the instabilities generated by noisy data is common and, in most of cases, necessary due to the ill-conditioned nature of the problem. The link between inverse problems and optimization problems is the objective function itself (defined by Equation (16)). Since it should be minimized, researchers and mathematicians saw a niche for the application of optimization techniques in this field.

Optimization methods are divided in three categories depending on the mathematical algorithm used to compute the heat flux (or the parameter of interest): deterministic methods, stochastic methods, and hybrid methods. In this literature, we introduce some of the most used optimization techniques in inverse problems emphasizing the Conjugate Gradient Method due to its robustness as a deterministic method and the Genetic Algorithm and Particle Swarm as stochastic methods. Many other approaches exist and there is extensive literature detailing the different methods [112][113][114].

Deterministic methods apply an iterative procedure in order to achieve a minimum in the objective function. Basically, all deterministic methods use the gradient of the function to search for the minimum in the objective function and ensure convergence.



### 2.5.1 Deterministic Optimization Methods

This category includes all the methodologies that use the computation of the temperature gradient in space and time, and therefore the gradient of the objective function of an iteration to compute the value of heat flux in the following iteration. As aforementioned, deterministic methods apply an iterative procedure in order to achieve a minimum in the objective function. Basically, all deterministic methods use the gradient of the function to search for the minimum in the objective function and ensure convergence. The relation between one iteration and the next is based on identifying the ideal direction of descent and choosing the size of the step to follow in this direction. The Levenberg-Marquardt iterative method (described in the previous section), the Newton-Raphson method, a variation of this method called Broyden-Fletcher-Goldfarb-Shanno (BFGS) method ([104]-[108]), other Quasi-Newton Methods [110][111], the Steepest Descent Method, and the Conjugate Gradient Method belong to this category of deterministic methods.

The simplest method is the Steepest Descent Method. In this method we compute the gradient of the objective function by transforming the function to find the saddle point. It uses the Laplace method to deform an integral contour in the complex plane to find the saddle point and therefore the gradient of the objective function. The mathematical procedures used to calculate the gradient, the direction of descent, and the step size vary between these methods.

### 2.5.2 Stochastic Optimization Methods

The main difference between the deterministic and stochastic optimization methods is that the deterministic methods are based on the relation of the objective function with the parameter that we are estimating, while the stochastic methods do not have a mathematical basis behind the calculation. Amongst the stochastic optimization methods, genetic algorithm optimization [112][113][114][115], the differential evolution algorithm [116], the Particle Swarm

algorithm[117][118][119], and the Simulated Annealing algorithm[120][121] are commonly used in IHCPs. The second and third are variations of the genetic algorithm based on the behavior of nature and Darwin's Theory of Evolution of Species. On the other hand, the simulated annealing algorithm is based on the thermodynamic cooling of a material transitioning from a liquid state to a solid state. If the cooling is too fast or too slow the crystals formed during the solidification will have a high internal energy state. We could argue that in the case of the deterministic methods, the liquid is cooling too fast and may be falling in a local minimum of the equation. The simulated annealing algorithm allows the movement in all regions and directions of the objective function, being slower, but avoiding solution that fall in a local minimum. In this review, we will describe the basics of the genetic algorithm optimization technique as an example of a stochastic method.

Genetic algorithms are based on the way a population of individuals would reproduce or mutate. It is a global optimization method where natural selection is applied to an initial population of individuals obtained normally using design of experiments. Each one of the individuals is defined by a collection of finite parameters called genes. Each gene is unique and therefore each individual is unique. The individuals perform better or worse for the objective function and based on the suitability of each individual to minimize the objective function, there are three different processes that may happen to the population in the next generation: selection, crossover, and mutation. The process of selection is basically the selection of the individuals that are going to reproduce. The selection is based on the fitness of each individual, which is directly related to the value of the objective function for each individual. The smaller the value of the objective function, the larger the fitness parameter and the higher the probability of reproduction for the given individual. Based on this fitness parameter, individuals are paired and they reproduce to create new individuals for the next generation. Once the individuals are chosen for reproduction, we apply crossover. It

consists of combining the “genes” of the parent individuals. The level of crossover is generally determined by the user by setting a crossover coefficient between 0 and 1. If the coefficient is larger than 0.5, the gene is replaced by the gene of the parent. We can introduce more randomness in the process and, at the same time, avoid that the good individuals of previous iterations disappear. The last step is mutation where the bits in the gene are changed from 0 to 1 or vice versa. Thanks to the mutation, more randomness is included in the population in order to avoid local minimums. The main drawback is that if we abuse the mutation step, the process will need a lot of iterations/populations to reach convergence. The process to run inverse methods using genetic algorithm optimization is detailed in Figure 2-7.

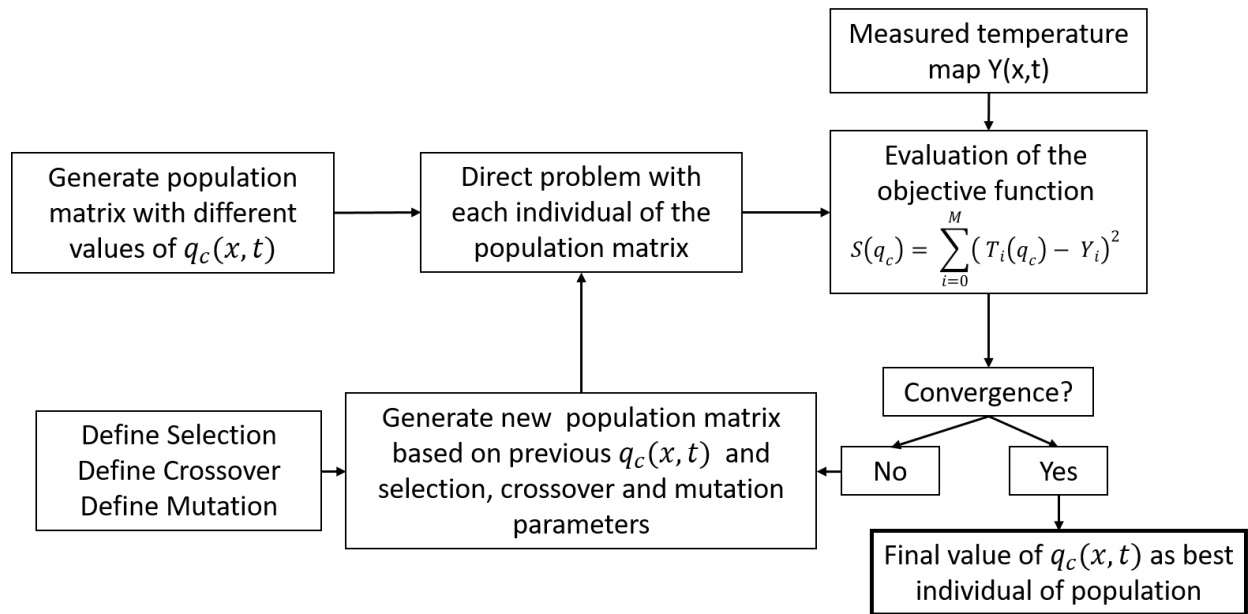


Figure 2-7. Genetic algorithm optimization procedure to calculate the heat flux in inverse heat transfer problems.

Inverse problems are ill-posed problems, which means that there are matrices used for the objective function that are very ill-conditioned. In these cases of very ill-conditioned matrix, the solution of the genetic algorithm optimization is highly dependent on the design of experiments or the

individuals of the first population. So it is extremely important to include the widest range of individuals in the initial population.

### 2.5.3 Hybrid Optimization Methods

Hybrid methods combine stochastic and deterministic method for better and faster convergence of the inverse method. The process tries to combine the strong points of each of the methodologies, using the stochastic methods to avoid falling in local minimums, looking for the global minimum, and, once it is localized, switching to a deterministic method for a faster convergence.

Few researchers have used hybrid methods due to the difficulty of the combination of the approaches and because two or more optimization methodologies (combined) need to be programmed. Colaço and Dulikravich [122], [123], [124], [125] developed different methodologies to optimize different aspects during the solidification of composite materials. Their method combines three different optimization methods for inverse methods: almost all the optimization is carried out with a Particle Swarm method that then is combined with a Differential Evolution method and finished with a BFGS method. The optimization starts with the Particle Swarm method and when some percentile of the particle finds a minimum, it switches to the Differential Evolution method to check if there is any improvement in the objective function. If any improvement is detected, the algorithm returns to the Particle Swarm method since that means that there is another region that could be a global minimum. If there is no improvement through the differential evolution method, the algorithm switches to a BFGS method to determine in a faster and more precise way where the minimum is located inside of the evaluated region. Finally, the solution is checked with the Particle Swarm method in order to determine if there is any modification of the location of the minimum and the procedure is repeated in an iterative way to

verify. Figure 2-8 depicts the global procedure of the hybrid method combining a Particle Swarm method, a Differential Evolution method and a BFGS deterministic method.

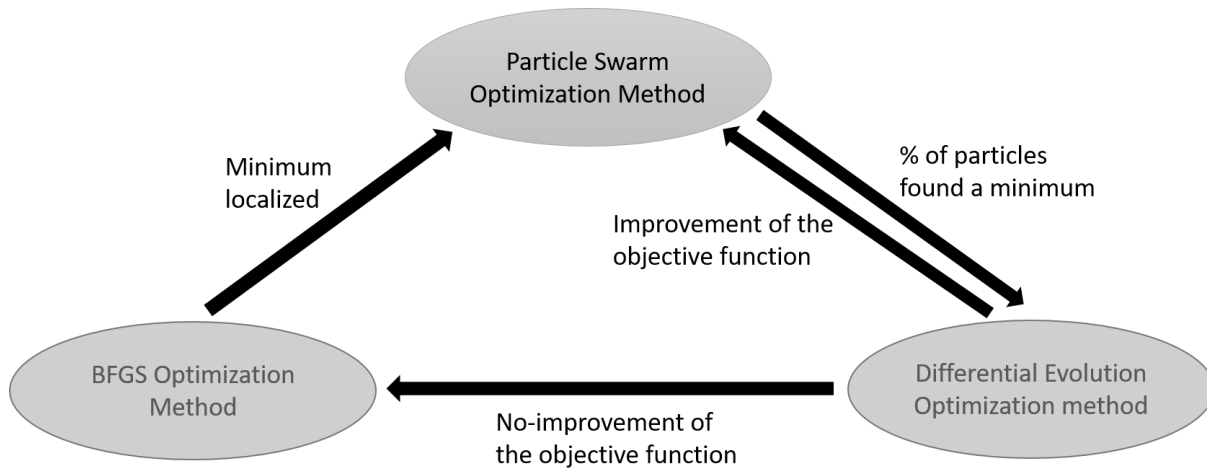


Figure 2-8. Example of hybrid optimization methodology procedure [62].

## 2.6 Comparison Between Fitting Methods And Optimization Methods

After describing the most important methods that have been used in inverse methods, it is remarkable to say that there is not a single method that overcomes all the problems derived from the ill-posed nature of IHCPs and out-performs the rest of the methods. Different methods are appropriate depending on the characteristics of the problem, the boundary conditions which are applied in the studied case, and the expected computational time versus precision that is demanded in the solution. In this section, we detail some comparisons found in the literature between the different methods described above and we draw conclusions about which methods are more suitable for each inverse problem. The conjugate gradient method seems to be the most common method in literature due to its robustness and fast convergence. Generally, it is combined with an adjoint problem and a sensitivity problem in order to compute the direction of search and the search

step. It is computationally more expensive than the steepest descent method, but it typically gives more accurate results for the same number of iterations.

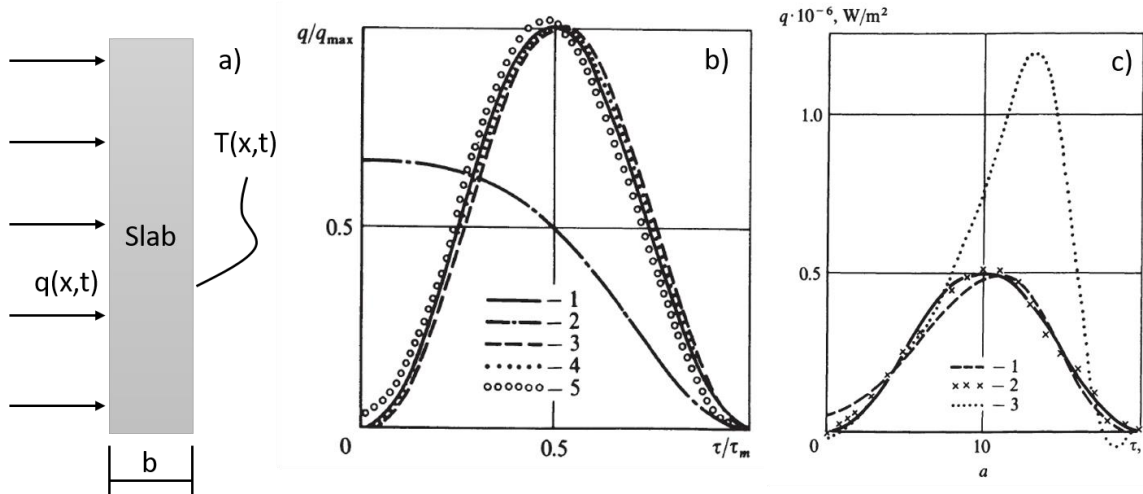


Figure 2-9. Comparison between steepest descent method and conjugate gradient method. Reproduced from [80] with permission.

The work of Alifanov [80] compares the steepest descent method with the conjugate gradient method for the case of a slab of material with a sinusoidal heat flux in time applied on one side and the temperature distribution measured on the opposite side. Figure 2-9b) depicts the results in a slab of  $b = 2\text{ mm}$  and the measurements taken at a distance  $b$  of the application of the heat flux. The Fourier number ( $Fo$ ) at the location of measurement is 0.01 and the real analytical solution is represented in the legend with 1. The first guess is made with null heat flux and then after the 1<sup>st</sup>, the 9<sup>th</sup>, and the 50<sup>th</sup> iteration with the conjugate gradient method we obtain what is depicted in 2, 3, and 4, respectively. The solution 5 is the 50<sup>th</sup> iteration using the steepest descent method. Clearly, the conjugate gradient methods offers a more precise approximation to the exact value than the steepest descent method for the same number of iterations.

Figure 2-9c) shows the results of the same problem now in absolute values and including varying thermo-physical properties of the material of the slab. In this case, 1 is the solution of the steepest

descent method after the 50th iteration, 2 is the solution of the conjugate gradient method after the 50th iteration, and 3 is the solution of the conjugate gradient method after 50 iterations assuming that the thermal diffusivity of the material is constant at every temperature. From this result, we can extract two main conclusions: 1) with temperature dependent properties, the steepest descent method requires more iterations to get good agreement than with constant material properties and 2) the effect of any variation of the thermal properties is important for the calculation since if it is not taken into account the calculation diverges and the estimation of the heat flux is wrong.

Ozisik [30] also compared different inverse techniques applying a square function of heat flux to a slab and using errorless temperature measurements in the computation ( $\sigma = 0.0$ ). In this case, the Levenberg-Marquardt method is compared with the conjugate gradient method combined with the adjoint problem. Ozisik shows the comparison where we observe that with the Levenberg-Marquardt method, we cannot retrieve the imposed heat flux accurately, showing a sinusoidal wave as a solution of the problem. However, the conjugate gradient method tracks the magnitude and the shape of the imposed heat flux with some spurious oscillations due to the effect of the applied regularization technique. In the case of the Levenberg-Marquardt method, the regularization obscures fast changes in heat flux.

The conjugate gradient method do not deal with the regularization and it can predict better sudden changes in heat flux. As it would be demonstrated in the following sections the regularization parameters play an important role in the retrieval of the time and spatial distribution of heat flux.

Colaço [62] developed both stochastic and deterministic techniques and compared them under the same conditions. In this case, they focused on the spatial variation more than on temporal variations of the searched parameters, which are the diffusivity and the source term in the heat

diffusion equation for a control volume approach. The exact values of temperature are also obtained using analytical solutions. Colaço shows the results the inverse calculation for the conjugate gradient method and the hybrid method combining the Particle Swarm method, the Differential Evolution method, and the BFGS method, respectively. The calculation was performed in the same way that Ozisik made the comparison between the Conjugate Gradient Method and the Levenberg Marquardt Method. A square function of heat flux was tried to be retrieved using both methodologies. We observe that for small number of sensors, the conjugate gradient method works better, but for larger number of sensors, there is a significant improvement in the solution with the hybrid method. Also we observe that sudden changes of heat flux are very difficult to retrieved with any of the assessed methodologies, therefore in the analysis of the selected methodologies the assessment is done with sinusoidal functions of heat flux, in time and in space.

It is remarkable that all these methods need to include a regularization technique inside of the objective function in order to drive the solution to a physical solution of the heat flux.

The conjugate gradient method is the most used method in literature for its robustness and the capability of computing large number of parameters in time and in space in an accurate way. It has been compared with different methods including deterministic, stochastic, and hybrid approaches, and, in most cases, it outperforms the other methods even though the application of the adjoint and sensitivity problems is not the most efficient computationally, since it can take 10% more of time than the steepest descent method [126].



## 2.7 Conclusions

Inverse methods have been used throughout history to solve for unknowns in physical laws. They have been applied to different fields and this literature review focuses on different techniques that have been developed for the determination of unknown parameters in heat transfer problems, commonly heat flux distribution. The sensitivity coefficient is used by all methods in order to compute the unknown parameters. Based on how the sensitivity parameter varies, some of the inverse methodologies are more attractive and robust than others.

We have divided these methods in two main branches depending on the nature of the evaluated methods: fitting methodologies and optimization methodologies. Optimization methodologies are normally iterative and therefore they can include non-linearity in the equation, while fitting methodologies can be solved in one iteration, are able to handle linear approximations, and are considerably faster than any iterative procedure. Optimization methodologies applied to inverse methods are commonly used for its flexibility and because they are studied in depth in other field. Any optimization technique can be used as an inverse method if the objective function is well defined. This is a very robust technique that provides very accurate and physical solutions when combining the objective function with a regularization technique.

In the fitting methodologies, the digital filter method and the transfer function method are highlighted in this chapter. The most important feature of these methods is the reduced computational effort required to get realistic and accurate results.

This chapter explains key aspects of the fundamentals of the several inverse methods applied to heat transfer problems and highlights the pros and cons of each one of them based on different applications. Based on the assessment performed by other researchers and the classification of the methodologies performed in this chapter, a fitting methodology and a deterministic optimization

methodology were selected to be modified and improved through the work presented in this doctoral dissertation. The fitting inverse methodology chosen is the Digital Filter Method and the Optimization Technique adopted is the Conjugate Gradient Method with Adjoint Problem to solve the direction of descent.

## **CHAPTER 3. DEVELOPMENT OF TRANSIENT 3D IHT METHODOLOGIES**

The criteria to select the investigated methodologies is based on the requirements of the different applications. On one hand, the methodology needs to be very robust when different temperature distributions and noise conditions are applied. On the other hand, for some applications, such as active thermal management in microchips, we need methods that are fast, even if some accuracy is sacrificed, and can predict general distributions of heat flux given the temperature maps. Therefore, based on the literature, we investigate the Conjugate Gradient Method, which is a very robust optimization method, and the Digital Filter Method, a fitting methodology that is combined with a regularization technique in order to improve the ill-condition nature of the solved system of equations.

### 3.1 Conjugate Gradient Method with the Adjoint Problem

One of the most robust and computationally efficient deterministic methods is the Conjugate Gradient Method (CGM). There are different ways to solve inverse problems using conjugation coefficients. The main difference of the conjugate gradient method compared to the steepest descent method is the use of the directions of descent from previous iterations to determine the direction and the step of the next iteration in the objective function. In this method we use an adjoint problem to compute the gradients. The adjoint equation is a linear differential equation derived from the main equation we need to minimize, from which the gradient or direction of descent can be efficiently calculated. Therefore, the calculation of the new direction of descent is based on

$$q^{k+1} = q^k + \beta^k d^k \text{ and} \quad (35)$$

$$d^k = -\nabla(q^k) + \gamma^k d^{k-1}, \quad (36)$$

where  $\gamma^k$  is the conjugation coefficient and  $\beta^k$  is the step in the direction of descent and  $k$  is the iteration number. These coefficients vary with each iteration and are expressed as:

$$\gamma^k = \frac{\int_{t=0}^{t_f} \int_{S_1} (d^k)^2 dS_1 dt}{\int_{t=0}^{t_f} \int_{S_1} (d^{k-1})^2 dS_1 dt} \text{ and} \quad (37)$$

$$\beta^k = \frac{\int_{t=0}^{t_f} \sum_{m=1}^M [T_m(t) - Y_m(t)] \Delta T_m(t) dt}{\int_{t=0}^{t_f} \sum_{m=1}^M [\Delta T_m(t)]^2 dt}, \quad (38)$$

where  $m$  is the timestep when the heat flux has been applied and the  $M$  is the total number of timesteps.  $Y_m(t)$  is the temperature measured with the sensor and the  $T_m(t)$  is the temperature computed by the inverse method with the boundary conditions applied in the previous iteration. In these equations, we established that the surface where we apply the heat flux is  $S_1$  and the surface of the test article where we measure is  $S_2$ . This is the main structure of the conjugate gradient algorithm. Different methods using the conjugate gradient vary in the specifics of the computation of the direction of descent and the gradient of the objective function, but all of them follow the same basic structure as outlined here and illustrated in Figure 3-1:

1. Solve the direct problem: With an initial guess of heat flux, the heat diffusion equation is solved (forward or direct problem) to determine the initial difference between the computed temperature map and the measured temperature map.

2. Evaluate convergence: Based on the comparison between the measured and the calculated data, we evaluate the convergence criteria determine if another iteration is required. The convergence criteria (discussed in previous sections) varies depending on the judgment of the researcher and the conditions of the experiment.
3. Solve the adjoint problem: We compute the direction of descent in this step by solving the aforementioned Equations (41)-(47). The solution of this adjoint problem provides the input to the sensitivity problem.
4. Evaluate the sensitivity problem: Applying the increment of heat flux provided by the adjoint problem, we evaluate the search step needed for the next iteration of heat flux, as it can be observed in Equations (48)-(52).
5. Begin next iteration of the heat flux calculation: With the direction of descent and the search step identified, we compute the new value of heat flux and return to step 1.

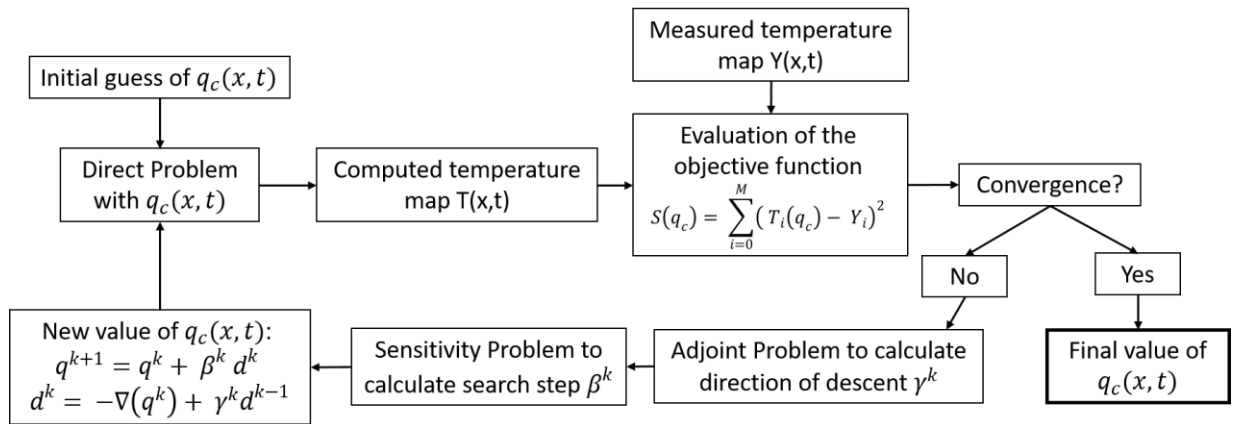


Figure 3-1. Conjugate gradient method with the adjoint problem procedure to determine the heat flux for an inverse heat transfer problem.

The adjoint problem combined with the sensitivity problem can provide the information needed to compute the coefficients  $\gamma^k$  and  $\beta^k$  and therefore calculate the new heat flux in each iteration. The

adjoint problem is based in the multiplication of the heat diffusion equation by a Lagrange multiplier  $\lambda$  and then the resulting formula is integrated in time and in space. The direction of descent is calculated with the following equations:

$$\begin{aligned} d^k[q(S_1, t)] &= \int_{t=0}^{t_f} \int_{S_2} [T - Y]^2 \delta(x - x_m) \delta(y - y_m) \delta(z - z_m) dS_2 dt \\ &+ \int_{t=0}^{t_f} \int_{\Omega} \lambda \left[ \frac{d^2 T}{dx^2} + \frac{d^2 T}{dy^2} + \frac{d^2 T}{dz^2} - \frac{dT}{dt} \right] d\Omega dt \end{aligned} \quad (39)$$

$$\begin{aligned} \Delta d^k[q(S_1, t)] &= \int_{t=0}^{t_f} \int_{S_2} 2[T - Y] \delta(x - x_m) \delta(y - y_m) \delta(z - z_m) dS_2 dt \\ &+ \int_{t=0}^{t_f} \int_{\Omega} \lambda \left[ \frac{d^2 \Delta T}{dx^2} + \frac{d^2 \Delta T}{dy^2} + \frac{d^2 \Delta T}{dz^2} - \frac{d\Delta T}{dt} \right] d\Omega dt \end{aligned} \quad (40)$$

where Equation (40) is the derivative of Equation (39). If we allow the derivative  $\Delta d^k$  to go to zero, the integrands will vanish and the remaining adjoint problem to be solved to get the values of  $\lambda$  becomes the following set of equations.

$$\frac{d^2 \lambda}{dx^2} + \frac{d^2 \lambda}{dy^2} + \frac{d^2 \lambda}{dz^2} - \frac{d\lambda}{dt} = 0 \quad (41)$$

$$\frac{d\lambda}{dn} = 2[T - Y] \delta(x - x_m) \delta(y - y_m) \delta(z - z_m) \text{ on } S_2, t > 0 \quad (42)$$

$$\frac{d\lambda}{dn} = 0 \text{ on } S_n \quad n = 1, 3, 4 \dots N \quad (43)$$

$$\lambda = 0 \text{ in the whole domain when } t = t_f \quad (44)$$

As we can observe the equation and the boundary conditions of the problem are of the same type that a common heat conduction problem with the exception that we are imposing the final

conditions and not the initial conditions. Therefore, we can use the same techniques to solve it by including a transformation of variable to invert the time:  $\tau = t_f - t$ . The increment in the step can be related to the increment of heat flux as

$$\Delta d = \int_{t=0}^{t_f} \int_{S_1} \lambda \Delta q(S_1, t) dS_1 dt \quad (45)$$

$$\Delta d = \int_{t=0}^{t_f} \int_{S_1} d' [q(S_1, t)] \Delta q(S_1, t) dS_1 dt. \quad (46)$$

Therefore, we can conclude that the Lagrange multiplier has a direct relation with the direction of descent:

$$d' [q(S_1, t)] = \lambda(x, y, z) \parallel \text{on } S_1. \quad (47)$$

The sensitivity problem (Equations (46)-(49)) is the next step to calculate the heat flux for the next iteration. In this problem, we solve exactly the same equation that in the direct problem, but imposing an increment of heat flux that will translate to an increment of temperature. From there, we can calculate the coefficient  $\beta^k$ .

$$\frac{d^2 \Delta T}{dx^2} + \frac{d^2 \Delta T}{dy^2} + \frac{d^2 \Delta T}{dz^2} - \frac{d \Delta T}{dt} = 0 \quad (48)$$

$$\frac{d \Delta T}{dn} = \Delta q(S_1, t) \text{ on } S_1, t > 0 \quad (49)$$

$$\frac{d \Delta T}{dn} = 0 \text{ on } S_n \quad n = 1, 3, 4 \dots N \quad (50)$$

$$\Delta T = 0 \text{ in the whole domain when } t = 0 \quad (51)$$

So, we obtain the following solution linearizing the temperature solution obtained in the previous iteration using a Taylor expansion:

$$d[q^{k+1}] = \int_{t=0}^{t_f} \sum_{m=1}^M [T_m(q^k) - \beta^k \Delta T_m(d^k) - Y_m]^2 dt . \quad (52)$$

Then the search step  $\beta^k$  is obtained by minimizing the Equation (50) with respect to the  $\beta^k$ , the solution to which is already shown in equation 36. Here, this method is described as a whole domain estimation (*i.e.*, all time steps included), but it can be modified to use sequential estimation. Whole domain estimation is very robust, and it uses the whole time domain in order to estimate the heat flux in each timestep. In the sequential estimation, only a given number of future timesteps are used to estimate the heat flux in a particular timestep [111].

### 3.1.1 Whole Domain Estimation

The regularization used in this methodology can be associated to time in two different ways: the whole domain estimation and the sequential estimation. The whole domain estimation is defined with the aforementioned equations, where the whole-time domain is taken into account in order to compute the heat flux in each time step. This is observed in all the integrations over time in the Equations (39), (40), (45), (46) and (50). In these integrations, the minimization is performed over the whole-time domain from  $t = 0$  to  $t = t_f$ . This way to compute the minimization and the step of descent minimize the computational time and effort of the methodology since it has to be computed only once for the whole-time domain. Therefore, the results at each time are more related with the whole behavior of the heat flux, acting like a regularization technique for the solution of the final heat flux. This technique is not very flexible since there is no parameter that can be changed in order to modify the solution that it is obtained. With this methodology the same solution is always obtained and normally tends to be the one that it is most likely to happen taken into account that the temporal gradient is limited by the integration. In this procedure, the heat flux solution is very unlikely to be discontinuous, and when there are extreme peaks appearing, the computation has diverged escaping of the local minimum of the objective function.



The results shown in the following pictures are connected with the microelectronics application. We used the case of the microelectronics application to test the different aspects of the code, since it is a simple case which major complication is the small size and the large number of different materials.

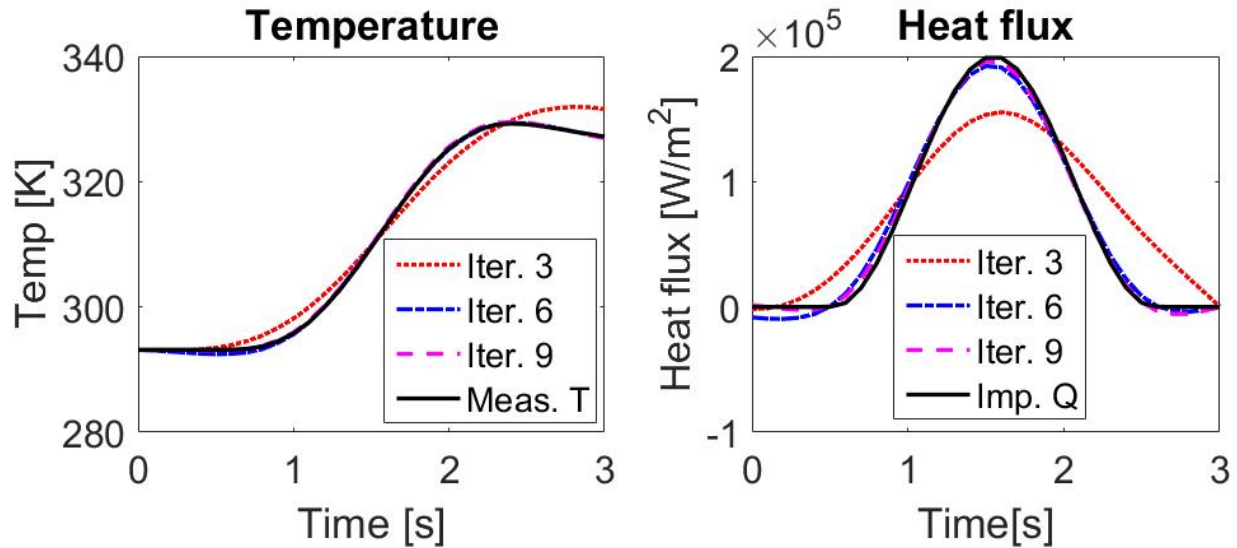


Figure 3-2. Whole domain estimation solution when applying a sinusoidal heat flux input into a stack of slabs of different materials.

Over a stack of different materials, we applied a sinusoidal heat flux in time and space as shown in the solid line of the right graph in the Figure 3-2. The response in terms of increment of temperature is plotted in the left figure. The objective function tries to minimize the difference between the measured temperature and the computed temperature, and as it can be depicted in the figure, the convergence is achieved when this difference is below a certain threshold. As observed in the previous results, the conjugate gradient method with whole domain estimation provides accurate results after 9 iterations, but the number of iterations is highly dependent on the gradient of the temperature in the input data as well as how are the gradients in the imposed heat flux, that for the method are unknown.

### 3.1.2 Sequential Estimation

In the sequential estimation, the domain in time is limited in the regularization in order to improve the convergence and minimize the computational resources needed to compute the heat flux with the Conjugate Gradient Method. To explain the difference between the two estimations, we have represented in the Figure 3-3, the temperature response of one surface of a slab to a heating pulse in space and time located in the opposite surface of the slab. This can be translated as the sensitivity coefficient of that particular geometry. First, the temperature has a delay in the answer due to the thickness of the slab and then reaches a maximum of temperature increase before decreasing exponentially and asymptotically due to the diffusivity of the material and the boundary conditions. This is the complete effect of a pulse of heat flux over the temperature. In the whole domain estimation for every heat flux timestep calculation, the effect over the temperature is considered over all the future timesteps. In the Sequential estimation, only a limited number of timesteps is considered. The number of future timesteps that are considered is a user choice, but there are some considerations to take into account about this number and it depends on the size of the timestep. As discussed in Chapter 1, the shape of the sensitivity coefficient changes in terms of location and magnitude of the peak depending on the non-dimensional timestep.

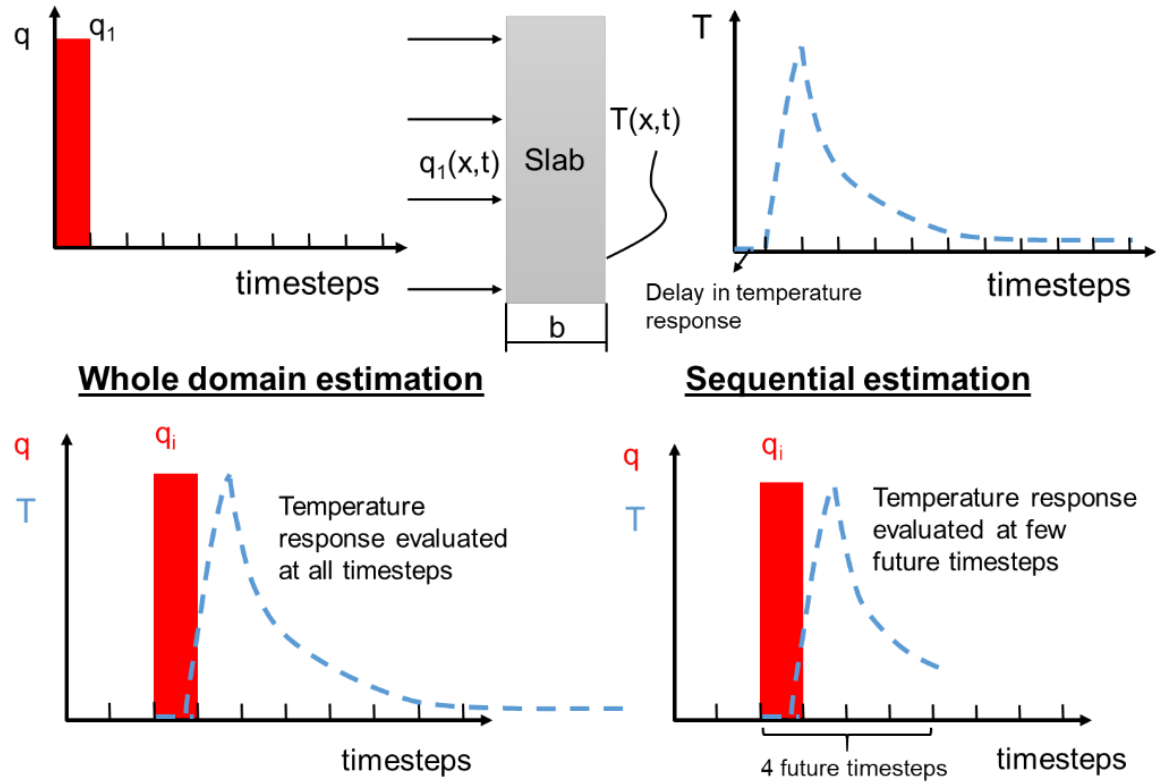


Figure 3-3. Temperature response to a pulse of heat flux in a slab (top). Whole domain estimation schematic (bottom left) and Sequential estimation schematic (bottom right).

Both techniques have been programmed to compare the results and their stability. Figure 3-4 illustrates the results for the whole domain estimation in the left, a sequential estimation using three future time steps in the center and a sequential estimation with two future timesteps in the right. We noticed that the case using the whole domain estimation is the most stable case, taking many iterations to blow up as observed in the literature, but at the same time is computationally more expensive. The case of the sequential estimation with 3 future timesteps converge faster to the searched value and the agreement is slightly better than in the case of the whole domain estimation, mainly in the regions when or where the heat flux suffer a strong variation (next to heat flux equal 0). It is less stable and less robust, and it blows up few iterations after it gets converged. In the case of the two future timesteps, the calculation blows up even before the solution converges.

This is because the heat does not travel through the solid in such a way that with only two timesteps we cannot assess all the heat provided to the surface by a pulse of heat flux in a particular timestep. This behaves like the Courant number in CFD and providing a small number of timesteps the convergence becomes more difficult and more unstable. More case with 5 and 10 future timesteps were analyzed with similar results to the ones shown in the whole domain estimation.

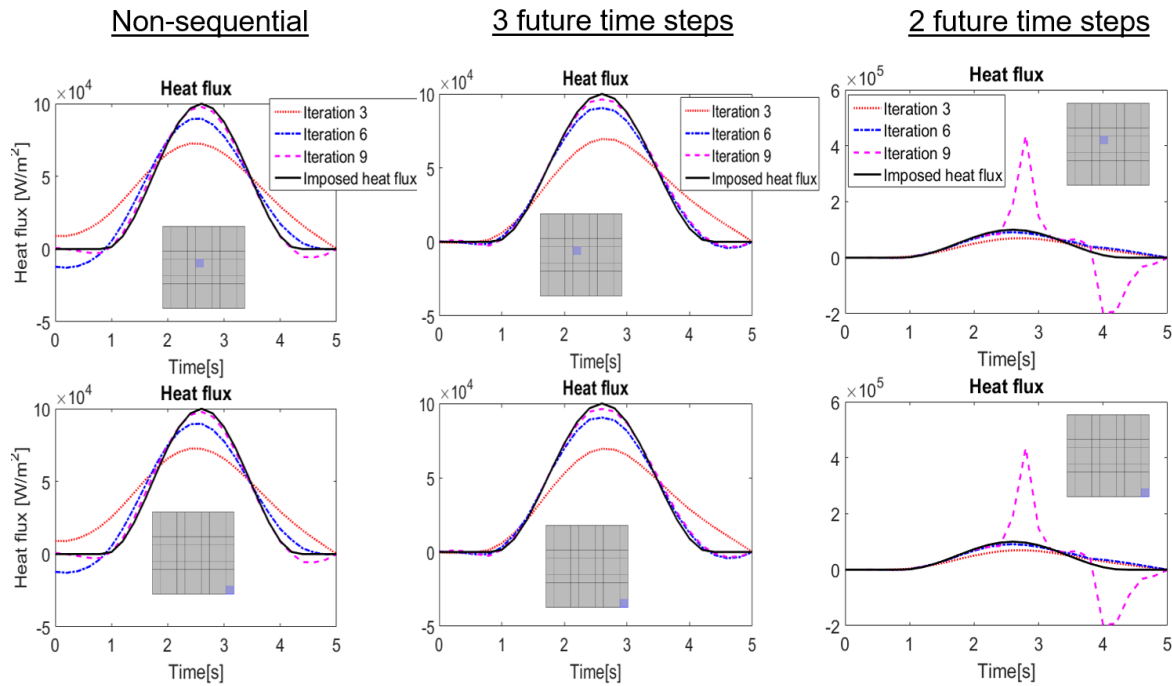


Figure 3-4. Calculated heat flux with the inverse heat transfer methodology using whole estimation method (left), sequential method with 3 future steps(center) and 2 future steps (right).

The overall difference in the computation between the whole domain estimation and the sequential estimation is small. There is an improvement in terms of computational time, but it is paid off in terms of robustness of the method. It is important to choose the right number of future timesteps in the evaluation of the sequential domain in order not to fall in unstable solutions. It is recommended that the number of timesteps is correlated with the behavior over time of the sensitivity coefficient. Checking this behavior, we observe that the sensitivity coefficient has a

large gradient at the beginning and then change the sign of the gradient descending in an exponential asymptotic way. It has been noticed that the convergence of the method improves when the number of timesteps is larger than the number of timesteps needed for the sensitivity coefficient to reach the 66% of the final value of the descending exponential function. If the number of future time steps is very low, even below the number of timesteps needed for the sensitivity coefficient to reach the peak, the results of the computation will be wrong and it will not converge in most of the cases. In fact, as demonstrated by Fernandes [93], it is more important to keep the trend in the exponential behavior of the function than the definition of the location of the peak. The magnitude of the peak and the final asymptotic value are important though.

### 3.1.3 Noise Effect in Conjugate Gradient Method

The effect of noise in the results of the CGM was evaluated numerically in order to test the robustness of the methodologies. We could not observe great differences between the whole domain estimation and the sequential estimation procedures. We add random noise numerically with a deviation of 0.5K and 1K to check how the behavior of the Conjugate Gradient Inverse method when the input signal is unstable. It is reasoned that the level of noise that makes the calculation unstable is directly related with the size of the gradient of temperature observed in the input of the method.

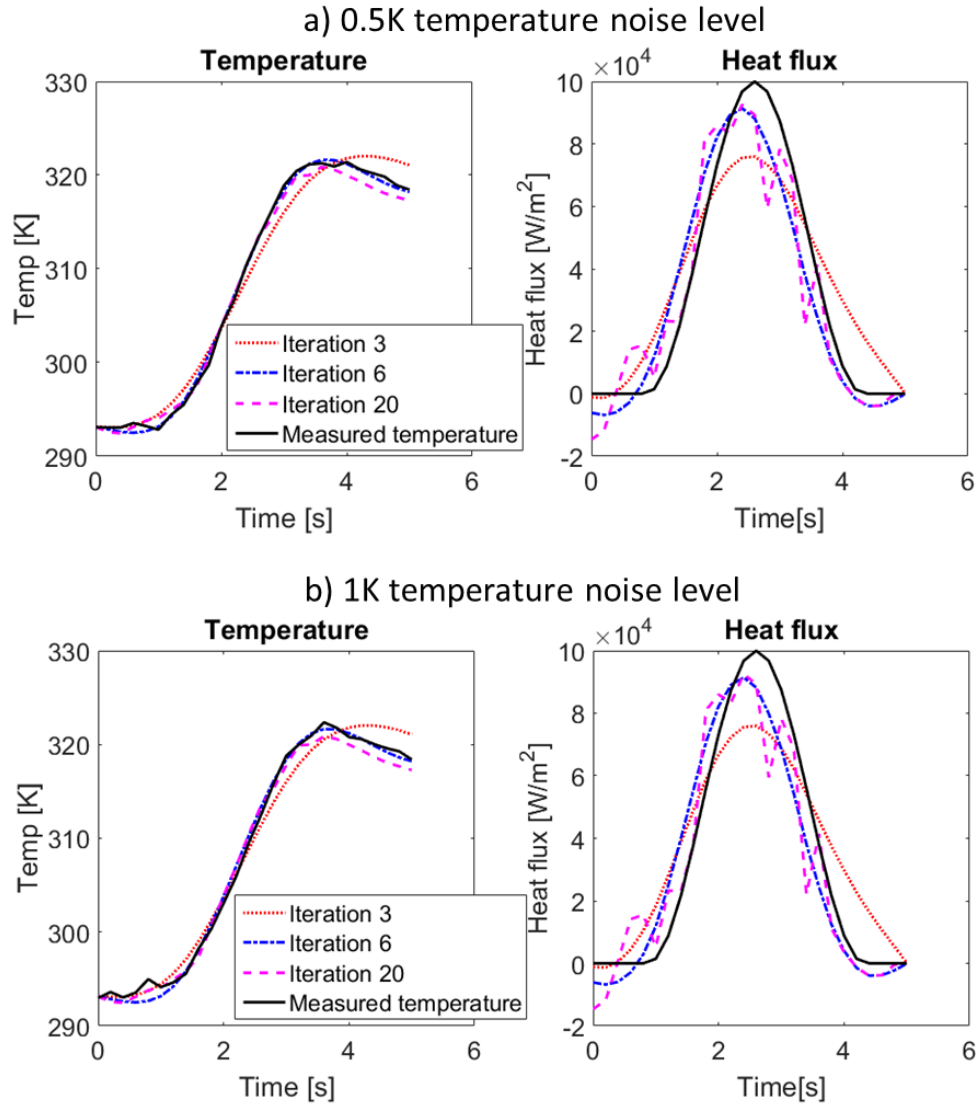


Figure 3-5. a) Computation of the conjugate gradient method with 0.5K of random level of noise.  
 b) Computation of the conjugate gradient method with 1K of random level of noise.

It is observed that introducing the noise, it takes more iterations in order to get to an approximate solution. As shown in Figure 3-5, after 6 iterations, even though the temperature is almost matched, the calculated heat flux do not match with the imposed heat flux with a large disagreement in the magnitude of the heat flux and in the temporal location of the peak. After 20 iterations, the heat flux has diverged and even though it is run for a lot of iterations, the solution has found another local minimum and it will not reach the solution giving the imposed heat flux.

Independently of the level of noise, and also on the distribution of the randomness of the noisy signal, the calculation always diverges in the same way. This is because the divergence depends on the general shape of the temperature input data.

### 3.1.4 Uncertainty Evaluation

For the case that we analyzed we computed the uncertainty using a linear approximation. The computation of the uncertainty with this methodology is described in the Appendix A.

Table 3-1. Conjugate Gradient Method uncertainty analysis based on the numerical assessment.

Quantity	Mean Value	Absolute Uncertainty	Heat flux variation relative to mean (%)	Sensitivity
<b>Temperature [K]</b>	314	1	4.31	13.65
<b>k single crystal silicon [W/mK]</b>	130	10	-0.52	-0.07
<b><math>\rho</math> single crystal silicon [kg/m<sup>3</sup>]</b>	2320	10	0.03	0.06
<b>Cp single crystal silicon [J/kgK]</b>	703	7	0.3	0.3
<b>k polycrystalline silicon [W/mK]</b>	100	10	-0.52	-0.7
<b><math>\rho</math> polycrystalline silicon [kg/m<sup>3</sup>]</b>	2330	10	0.09	0.21
<b>Cp polycrystalline silicon [J/kgK]</b>	678	7	0.15	0.15
<b>Thickness single crystal silicon [mm]</b>	1	0.05	1.98	0.40
<b>Thickness polycrystalline silicon [mm]</b>	0.5	0.05	2.06	0.21
<b>TOTAL</b>			<b>5.9</b>	

We have performed also for the conjugate gradient method the same uncertainty analysis that we performed for the digital filter method with all the parameters it depends on. From the results we

can see that this methodology is more sensitive to the temperature variations than the digital filter method. Also, the effect of the conductivity is higher in this method. Other parameters such as the thickness of the different materials, their density or the heat capacity seems to be invariants to the method and they play a smaller important role in the computation of the uncertainty. As in the digital filter method, the temperature measurement and the thickness of the different layers of materials are the main contributors to the uncertainty values of the methodology. In this case the total uncertainty calculated using the squared root of the sum of squares of the uncertainty of each one of the parameters is below 6%.

### 3.2 Digital Filter Method

In order to solve an ill-posed problem, we need to numerically reformulate the problem, including additional assumptions and enhancing the smoothness in a process called regularization [80]. There are different regularization techniques amongst which we highlight the widely used Tikhonov regularization method ([62], [130], [131], [132], [133]). Here, we have combined this regularization technique with the function specification method to minimize the number of operations needed to calculate the sensitivity coefficient of the geometry [89][88][93]. This method is based on the calculation of a sensitivity coefficient, which is the effect of a heat pulse on the temperature of the system at key points of interest. This sensitivity coefficient varies in space and time and, in order to simplify its applicability to the problem, is expressed as a matrix. Here the sensitivity coefficient is calculated with a finite element solver. COMSOL Multiphysics combined with Matlab, using the Livelink module between the two to communicate the data. The finite elements solver is run once with the selected 3D geometry. With the matrix sensitivity coefficients, we then apply Duhamel's Theorem to perform the regularization and solve the ill-



posed heat transfer problem. This approach is restricted to linear problems, but it is chosen here as computational time is a limitation. The main source of non-linearity is the temperature dependent thermal properties of the different materials. The temperature dependence of the thermal properties is taken into account in the modelling of the materials in COMSOL, through the calculation of a sensitivity coefficient, which is computed by applying a heat flux pulse at the heaters locations, and evaluating the increment of temperature in COMSOL. This is a precise methodology, which may yield inaccurate results only when the initial temperature of the test article is not the same that the one used in the sensitivity coefficient calculation in COMSOL.

Here, the temperature on the top of the chip from the forward solution (from COMSOL) is tracked numerically and is the only input to the inverse heat conduction method which is used to determine the unknown source of heat (as a function of space and time). Ultimately, the input to the inverse method will be experimentally determined temperature profiles.

To improve the computational efficiency of the method, we organize our inputs and unknowns in vectors discretized in time and space; therefore, the temperatures are

$$T = \begin{bmatrix} T(1) \\ T(2) \\ \vdots \\ T(n) \end{bmatrix} \quad and \quad T(i) = \begin{bmatrix} T_1(i) \\ T_2(i) \\ \vdots \\ T_m(i) \end{bmatrix}, \quad (53 \text{ a,b})$$

where  $n$  represents the total number of time steps, the index  $i$  is one particular time step, and  $m$  is the total number of sensors used to retrieve the temperature map. On the other hand, we can define our unknown heat fluxes in the same way.

$$q = \begin{bmatrix} q(1) \\ q(2) \\ \vdots \\ q(n) \end{bmatrix}, \quad q(i) = \begin{bmatrix} q_1(i) \\ q_2(i) \\ \vdots \\ q_p(i) \end{bmatrix}, \quad \text{and} \quad q_j(i) = q_{x_{j-1} \rightarrow x_j}(i), \quad (54 \text{ a,b})$$

where  $p$  is the number of sources of heat flux and  $q$  represents the heat flux at the time step  $i$ , taking into account the heat flux in the previous time steps. The relation between these vectors,  $T$  and  $q$ , is a simple multiplication by the sensitivity coefficient  $X$ :

$$T = X q. \quad (55)$$

In order to match the dimensions of  $q$  to  $T$ , the matrix  $X$  of the sensitivity coefficients must be [89]:

$$X = \begin{bmatrix} a(1) & 0 & 0 & \cdots & 0 \\ a(2) & a(1) & 0 & \cdots & 0 \\ \vdots & \vdots & \vdots & \ddots & \vdots \\ a(n) & a(n-1) & \cdots & \cdots & a(1) \end{bmatrix},$$

where

$$a(i) = \begin{bmatrix} a_{11}(i) & a_{12}(i) & \cdots & a_{1p}(i) \\ a_{21}(i) & a_{22}(i) & \cdots & a_{2p}(i) \\ \vdots & \vdots & \ddots & \vdots \\ a_{m1}(i) & a_{m2}(i) & \cdots & a_{mp}(i) \end{bmatrix}, \quad (56 \text{ a,b,c})$$

and

$$a_{jk}(i) = \frac{\partial T(x_j, t_i)}{\partial [q(1)]}.$$

Most of the error in a 3D inverse method calculation is induced through Equation (56.c), since we are calculating the effect on the temperature of a pulse of heat flux in a particular time and a

particular location in space. Therefore, we have to take into account that it is an approximation that will depend on the boundary conditions at the limits of the 3D geometry.

The matrix of measured temperatures,  $Y$ , comes from the experiments or the numerical “data”, and the coefficients  $a_{jk}(i)$  come from the direct finite element solution. Thus, to calculate the unknown vector of heat fluxes,  $q$ , we need to use a regularization technique for the objective function where we try to minimize the error between the measured temperature  $Y$  and the calculated temperature  $T$ . Combining the minimization with the regularization we obtain:

$$S = (Y - T)^T(Y - T) + \alpha_t[H_t q]^T[H_t q] + \alpha_s[H_s q]^T[H_s q], \quad (57)$$

where the variable  $S$  is the objective function that we try to minimize in our calculation. The suffix  $s$  and  $t$  define the regularization in space and in time respectively. The matrices  $H_s$  and  $H_t$  are the filter of the effect of each heat flux in space and in time, respectively. In our case, they are defined as

$$H_t = \begin{bmatrix} -I & I & 0 & \dots & 0 \\ 0 & -I & I & \dots & 0 \\ \vdots & \vdots & \vdots & \ddots & \vdots \\ 0 & 0 & \dots & \dots & 0 \end{bmatrix}, \text{ where} \quad (58 \text{ a,b,c,d})$$

$$I = \begin{bmatrix} 1 & 0 & 0 & \dots & 0 \\ 0 & 1 & 0 & \dots & 0 \\ \vdots & \vdots & \vdots & \ddots & \vdots \\ 0 & 0 & \dots & \dots & 1 \end{bmatrix}$$

$$H_s = \begin{bmatrix} h_s & 0 & 0 & \cdots & 0 \\ 0 & h_s & 0 & \cdots & 0 \\ \vdots & \vdots & \vdots & \ddots & \vdots \\ 0 & 0 & \cdots & \cdots & h_s \end{bmatrix}, \text{ where}$$

$$h_s = \begin{bmatrix} -1 & 1 & 0 & \cdots & 0 \\ 0 & -1 & 1 & \cdots & 0 \\ \vdots & \vdots & \vdots & \ddots & \vdots \\ 0 & 0 & \cdots & \cdots & 0 \end{bmatrix}.$$

The coefficients  $\alpha_s$  and  $\alpha_t$  are the regularization parameters with values between  $10^{-4}$  and 0 depending on the desired effect of the regularization in space or in time. The value of these coefficients depends on the characteristics of the geometry and the nature of the expected solution of heat flux.

Minimizing the sum of squares of the objective function, we obtain the least squares estimator of the heat flux:

$$\hat{q} = [X^T X + \alpha_t H_t^T H_t + \alpha_s H_s^T H_s]^{-1} X^T Y. \quad (59)$$

The inversion of the matrix in brackets can be performed with one of several functions in Matlab. After investigating several options, we found that the pseudo inverse (*pinv*) and the preconditioned conjugate gradient method (*pcg*) provide the most robust solution to our heat conduction problem. The difference on the solution between using one function or another are negligible, but as previously mentioned the solution is highly dependent of the value of the regularization coefficients. Figure 3-6 shows the solution of heat flux for the same input temperature varying the spatial and time regularization coefficients. In the figure on the left the time regularization coefficient is small so we are allowing large variations of heat flux in time, while in the figure on the right we have increased the value of the time regularization coefficient, limiting the gradient

between the value of the heat flux at one particular time and its value in the next timestep. As it is a zeroth order regularization we are only limiting the gradient of the heat flux, in first order and second order regularizations we could limit as well the first and second derivative of the solution.

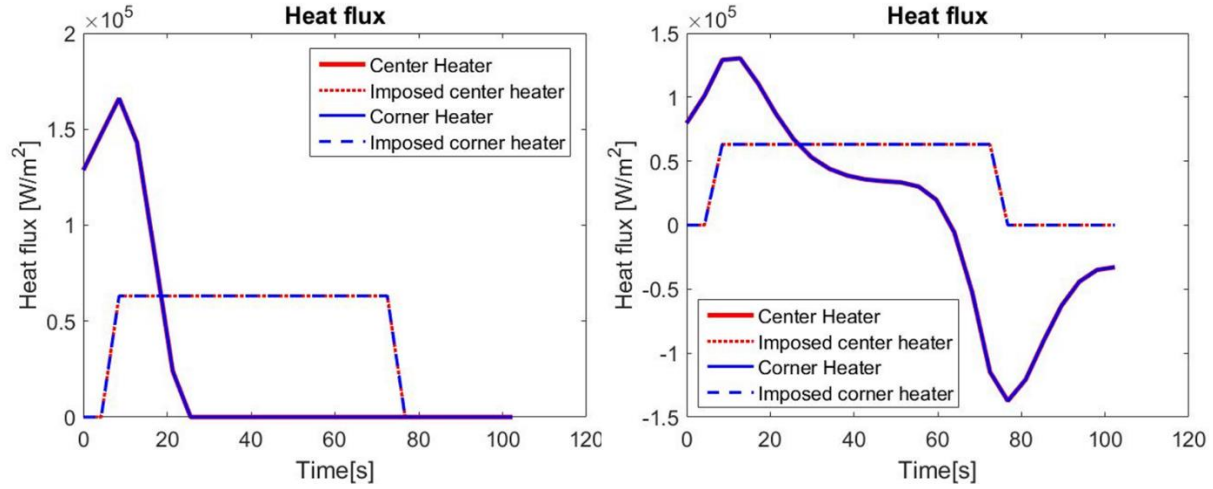


Figure 3-6. Results of the heat flux for a given distribution of temperature for different values of regularization coefficients.

The solution is considerably different in both cases. The prediction in the figure of the left shows a large pick of heat flux at the beginning that disappear towards the end. Based on the experience computing different cases, we have observed that this is the behavior predicted by the function when the system of equation is largely ill-conditioned in time. It modifies the value of the first columns of heat flux in order to match the required temperatures and in the last time steps it leaves it free in order to adapt the final value of the temperatures. The over prediction of heat flux in the initial steps is then compensated by negative or zero heat flux in the rest of the timesteps. The convergence in terms of temperature is not great in the final steps since it is normally higher than the input. When we increase the value of the regularization coefficient the value of heat flux becomes more reasonable as the ill-condition of the system of equations improves. Still in all the cases we observe large peaks when rapid changes in heat flux occur. This is also related with the

thickness of the material. In thin test articles, the response of the heat flux is not damped through the thickness of the object and the prediction of the heat flux is more sudden than the one obtained in a thick object where the temperature is damped due to the diffusivity of the material.

### 3.2.1 Non-iterative Non-linear Digital Filter Method Improvement

The Digital Filter Method as it is introduced in this section fails to solve non-linear problems where the thermal properties of the material depend on the temperature, since it is a linearization of the heat conduction equation. Also, in the real case where we have natural or forced convection, it under predicts the correct value of heat flux that have been input into the system. For this reason, we have included the following two corrections.

The improvement of the Digital Filter Method consists in the modification of two of the terms of the Equation (59): the temperature adjusted sensitivity coefficient ( $X_T$ ) and the inclusion of the convective heat losses ( $q_{conv}$ ). Therefore, the heat fluxes are defined by the Equation (60):

$$q_c = q_{imp} + q_{conv} = [X_T^T X_T + \alpha_t H_t^T H_t + \alpha_s H_s^T H_s]^{-1} X_T^T Y. \quad (60)$$

The unknown solved with this methodology is the imposed heat flux,  $q_{imp}$ . The temperature of the surface is an input of the method and hence, the convective heat flux can be computed beforehand. The convective heat flux is modeled based on the difference between the flow temperature and the solid temperature at each discretize location.

$$q_{conv} = C (Y_i - T_{amb}) \quad (61)$$

The coefficient  $C$  is a combination of the convective heat coefficient and the area where the temperature reading is averaged. This coefficient varies depending on the flow conditions and the studied geometry, therefore it needs to be calibrated before performing direct calculations at

different conditions. Once the value of the coefficient  $C$  is obtained, the subtraction of the convective heat flux from the computed heat flux,  $q_c$ , will give the imposed heat flux.

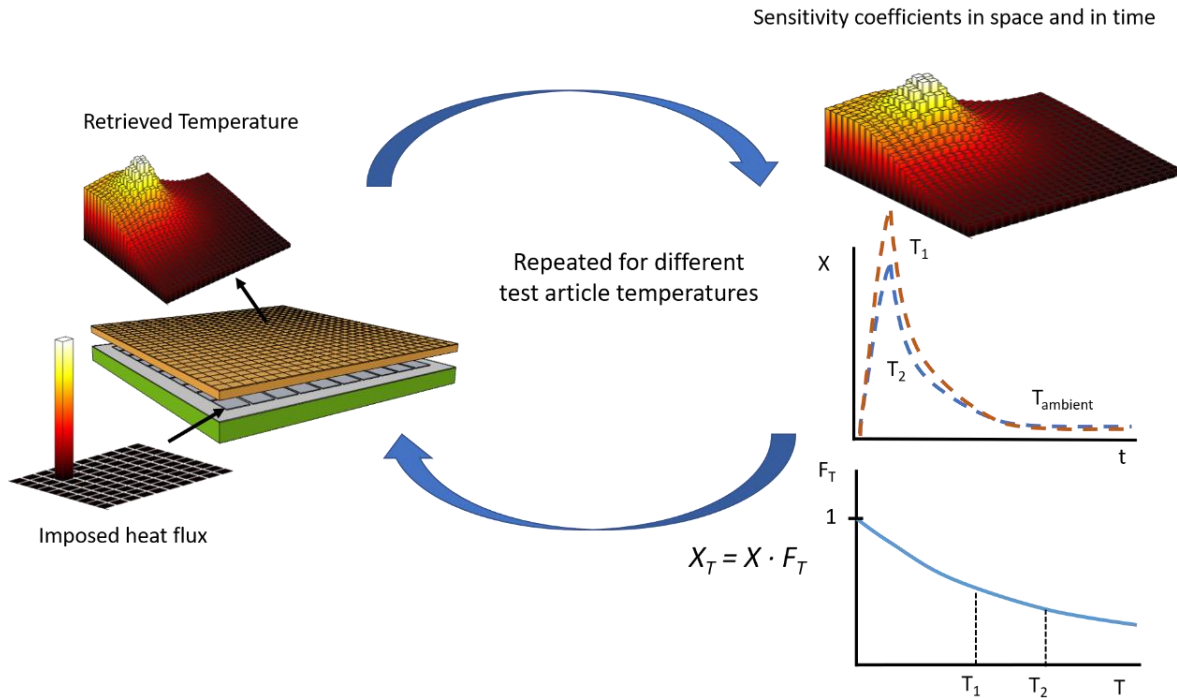


Figure 3-7. Non-linear non-iterative process with temperature adaptive sensitivity coefficient estimation.

The second improvement is the development of a new non-iterative methodology to include the non-linearity of temperature varying thermal properties in the inverse methodology. Most part of the methods that include this non-linear behavior are based on iterative processes that take into account the temperature obtained in the previous iteration in order to compute the new values of thermal properties, such as the Levenberg-Marquardt Method [81][82][83]. In the present study, the temperature is considered a known parameter since it is measured at each timestep, and the sensitivity coefficient can be adjusted based on the measured temperature before the inverse calculation is performed. The temperature adjustment of the sensitivity coefficients is made by

running direct simulations with heat flux pulses at different temperatures of the test article. These simulations provide the information needed to know how the temperature field reacts when the test article is already at higher temperatures and therefore with different thermal properties. Figure 3-7 represents the process followed to obtain the temperature adjusted sensitivity coefficients.

The results of the heat flux pulse simulations are compiled and a linear fitting with respect to the test article temperature between the coefficients is made, developing the concept of temperature factor,  $F_T$ . The corrected sensitivity coefficient is obtained by multiplying of the temperature factor by the sensitivity coefficient at ambient temperature.

$$X_T = F_T X_{amb} \quad (62)$$

With the temperature field at each timestep, the temperature factor  $F_T$  is computed using a linear fitting based in the data obtained with the heat flux pulses at different temperatures. Then the corrected sensitivity matrix  $X_T$  is obtained for each timestep. This improved methodology is used for the calculation of the heat flux in a microchip with 25 heaters independently controlled by measuring the temperature on the top surface with an infrared microscope.

### 3.2.2 Uncertainty Evaluation

The same uncertainty analyzed that we used for the CGM was applied for this new methodology. It is performed to evaluate the degree of convergence of the inverse heat transfer method. The parameters analyzed in the uncertainty calculation are based on the geometry, the materials used between the heaters and the top surface where the temperature was retrieved, and the measurement of the temperature itself. The uncertainty applied to each of the quantities is based on the accuracy of state of the art in measurement techniques. Therefore, measuring the temperature with infrared thermography, the absolute uncertainty is around 1K, the absolute uncertainty associated to the



thickness of the layers is 50 microns, and the relative uncertainties associated conductivity and heat capacity are predicted to be around 10%. In order to compute the effect of the thermal diffusivity of the materials, the uncertainty due to the density of the two silicon layers is added and expected to be around 0.5%. Table 3-2 shows the estimated uncertainty and sensitivity of each of the quantities involved in the inverse heat conduction combined with Kriging calculation.

Table 3-2. Uncertainty analysis of the Digital Filter Method

Quantity	Mean Value	Absolute Uncertainty	Heat flux variation relative to mean (%)	Sensitivity
<b>Temperature [K]</b>	314	1	3.21	10.08
<b>k single crystal silicon [W/mK]</b>	130	10	-0.13	-0.02
<b><math>\rho</math> single crystal silicon [kg/m<sup>3</sup>]</b>	2320	10	0.03	0.06
<b>Cp single crystal silicon [J/kgK]</b>	703	7	0.3	0.3
<b>k polysilicon [W/mK]</b>	100	10	-1.65	-0.16
<b><math>\rho</math> polysilicon [kg/m<sup>3</sup>]</b>	2330	10	0.09	0.21
<b>Cp polycrystalline silicon [J/kgK]</b>	678	7	0.15	0.15
<b>Thickness single crystal silicon [mm]</b>	1	0.05	1.98	0.40
<b>Thickness polycrystalline silicon [mm]</b>	0.5	0.05	2.06	0.21
<b>TOTAL</b>			<b>4.62</b>	

The total uncertainty associated with this methodology is less than 5%, as shown in Table 3-2. Most of this uncertainty is associated with the measurement of the temperature. Therefore, in order to achieve reliable results for heat flux, we need to measure the temperature as accurately as possible.

### 3.3 Conclusions

In this chapter, we have detailed the inverse methodologies employed in this doctoral dissertation. The base methodologies have been chosen based on the robustness and the computational efficiency. Two of them have been chosen, an optimization technique and a fitting technique.

The Conjugate Gradient Method is the optimization technique chosen because of its robustness and the Digital Filter Method is the chosen fitting technique because of its computational efficiency. From the analysis performed in this chapter we can extract the following conclusions:

- Both methodologies can predict the imposed heat flux for simple cases analyzed using numerical models. The Conjugate Gradient Method is more precise, and the Digital Filter Method is much faster.
- The Conjugate Gradient Method is an iterative procedure which converges slowly using as objective function the difference between the measured temperature and the computed temperature. Given the nature of the procedure, for a model with one million cells, the computation can take days on a computer with 64 GB of RAM memory and 12 cores.
- The Conjugate Gradient Method tends to diverge with levels of noise of 0.5K or higher. Very noisy signals are detrimental in the calculation of the heat flux using this method. It is important to remark that the diversion of the calculation is independent of the introduced noise, but it depends on the objective function and the location of the global and local minima of this equation. Therefore, when the computation diverges, it always diverges in the same way for the same model.
- An improvement to the CGM was then applied. The improvement consists of the use of sequential estimation in the computation of the direction of descent and the step of descent. Instead of computing the equations in the whole-time domain, we only consider few future timesteps. Sequential estimation improves the computational efficiency of the method, but

it becomes more unstable, especially if the number of future timesteps considered in the calculation is low.

- The Digital Filter Method is a non-iterative procedure based on the solution of an ill-conditioned system of equations. It consists of linearizing the heat conduction equation and introducing the concept of the sensitivity coefficient directly in the computation. In the equation, or system of equations, that needs to be solved, we then need to include regularization terms to drive the solution towards physical solutions of the heat conduction equation. The solution is highly dependent on the regularization terms in time and space that are required to improve the ill-condition nature of the system of equations. The solution takes seconds to compute using the same computer that for the CGM takes days.
- An improvement of the DFM has been introduced in this chapter, in order to include non-linearity of temperature dependent thermal properties and convective boundary conditions into the equation. This addition considerably improves the accuracy of the method as demonstrated in the next section. In this improved method, more computations of the direct problem are needed upfront in order to compute the corrected sensitivity coefficients, but this correction does not increase the time to solve the system of equations using the inverse method and retains the non-iterative nature of the DFM.
- An uncertainty analysis was performed for both methodologies analyzing the effect of the different measurable parameters on which the inverse method is dependent. The analysis assumes typical values of uncertainty for these parameters and is based on the numerical experiment created to develop the methodologies. For both methodologies, the main contributor is the uncertainty in temperature and the uncertainty in retrieved heat flux is 6% for the case of the CGM and 5% for the case of the DFM.

## CHAPTER 4. SENSOR OPTIMIZATION IN MICROELECTRONICS

### USING IHTM<sup>1</sup>

In microelectronics, once the chip is built there is some notion of where the heat sources are but the exact location of hot spots may not be exactly know due to difference in the fabrication or variations with the mode of operation. For this kind of problem, inverse methodologies can be used to find the location and magnitude of heat sources, as well as boundary conditions of the chip.

Figure 4-1 shows the basic schematic of the problem where the temperatures on the top are measured and the heat flux coming from individual heat generating sources inside of the chip are retrieved.

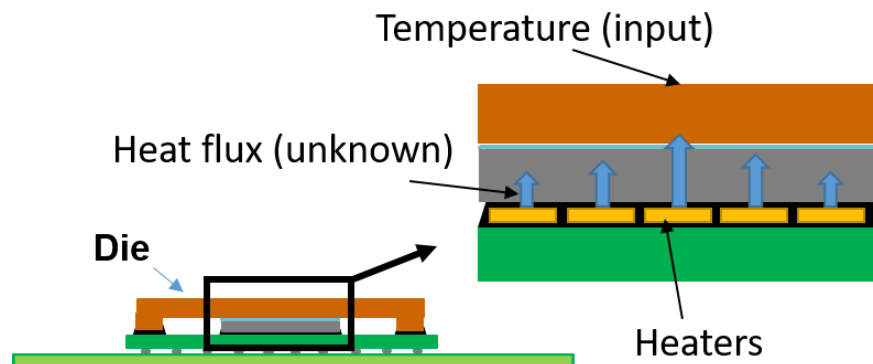


Figure 4-1. Sketch of the simulated microchip with the sources of heat flux and the temperature reading location.

<sup>1</sup> This chapter is partly based on:

D. G. Cuadrado, A. Marconnet, G. Paniagua, "Inverse Conduction Heat Transfer and Kriging Interpolation Applied to Temperature Sensor Location in Microchips", J. of Electronic Packaging, March 2018, doi: 10.1115/1.4039026. [169].

#### 4.1 Conductive Heat Transfer Numerical Evaluation

The case analyzed here is die with dimensions 21mm x 21mm. This die includes 100 heaters inside two layers of silicon. There is a temperature sensor embedded for every 25 heaters (one in each quadrant). Figure 4-2 shows the different layers of carrier, heaters, sensors and silicon with different thermal and mechanical properties. The model is a simplification of a real chip which contains 100 heaters and is attached to a board that has electrical circuitry to control the power of these heaters. Additionally, 625 (25x25 pixels) temperatures are calculated across the top of the chip, and the number of unknown heater flux levels is 100. The ratio of 6 to 1 was chosen in order to improve the results of the least squared method.

Simplifications are required to reduce the computational time of this method. The verification model consists of 1/25 of the final model and its modelling is illustrated in Figure 4-3. In the simplified domain, we have suppressed the connection balls to the carrier, the ball grid array (BGA), and underlying printed circuit board (*i.e.*, the card), as well as grouping some heaters together. The objective of the simplification is to reduce the size of the mesh and hence, reduce the computational time. Due to the simplifications made in the 3D domain, we first assessed the similarity of the results from the simple domain to those from the full model.

Thus, we have compared the “simplified reduced chip” with “reduced chip” structure that takes into account the BGA, card, and all the heaters, as shown in Figure 4-3 and Figure 4-4.

A direct heat transfer simulation is performed applying 0.2W to one corner heater with periodic boundary conditions on all side walls, adiabatic wall on the bottom and natural convection on the top surface. The temperature of a corner edge and centerline of the verification model for both the “reduced chip” and “simplified reduced chip” are shown in Figure 4-4. Evaluating the similarity

of the shape and the magnitude of the temperature variation, we establish that the simplified model represents the behavior of the real chip with good agreement.

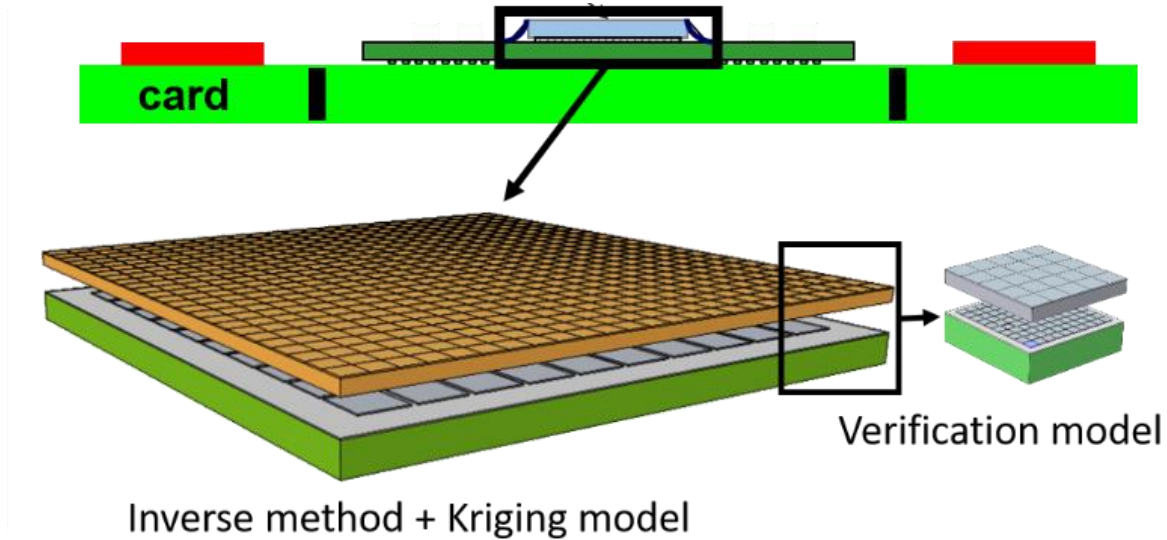


Figure 4-2. (top) Schematic of the complete experimental test fixture and (bottom) the COMSOL model used for the inverse method and Kriging model. (bottom inset) Approximate verification model to prove the simplified geometry

Regarding the computational efficiency, the reduced chip with 3.5 million cells takes 40 minutes to calculate a direct transient computation, while the simplified reduced chip with 0.9 million cells takes 13 min., reducing the computational time by a factor of 3.

The methodology can be applied to more complex geometry imported into or directly built in COMSOL Multiphysics with an increase in the computational time. The material properties are provided in the model inside COMSOL Multiphysics and they can be constant or temperature-dependent.

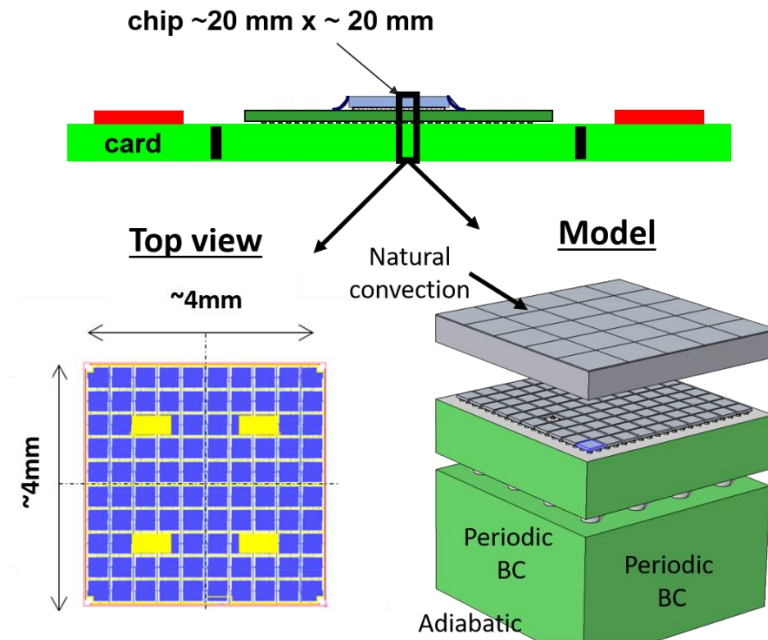


Figure 4-3. Sketch of the “reduced chip” structure including the geometry of the real microchip with 100 heaters.

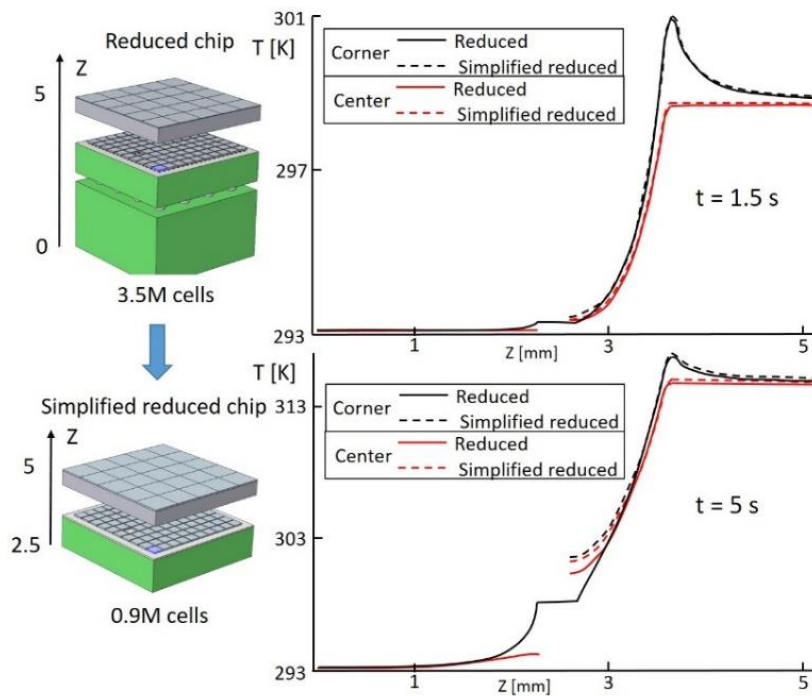


Figure 4-4. Temperature distribution within the chip for the reduced chip and the simplified reduced chip model at  $t=1.5 \text{ s}$  and  $t=5 \text{ s}$ .

The reduced model was only used for verification purposes, since we could not implement all the features in the complete chip for memory limitations. After all this analysis, the model that was used is the simplified model, which is in the Figure 4-2 bottom left. The boundary conditions were the same that the ones applied in the reduced model for verification, but the final size is around 21x21mm.

In order to compute the sensitivity coefficient in a first evaluation of the model, we used the model of the complete chip in COMSOL Multiphysics. The boundary conditions applied in this first evaluation of the model are the same boundary conditions than in the final inverse heat transfer computation and they are similar to the ones described in the Figure 4-3, but changing the periodic conditions on the sides for natural convection. In this way, the sensitivity coefficient is associated to the boundary conditions applied in each case and it varies depending not only on the geometry, but also on the boundary conditions applied to the system.

#### 4.1.1 Conjugate Gradient Method Evaluation

The conjugate gradient method was also tested in the same model under the same conditions that the digital filter method. So we are imposing a sinusoidal signal in all 100 heaters of the model. Figure 4-5 shows the model already evaluated in the previous case and with a surface of 21mmx21mm and 100 heaters embedded inside. For the analyzed case in COMSOL, sinusoidal wave with a peak of  $2e5W/m^2$  in 3seconds was applied and the measurements of temperature in the outer surface of the chip was recorded. This temperature is the input to the inverse conjugate gradient optimization methodology. The objective function that needs to be minimized is described in previous sections and is the square root of the sum of the squared difference of all the points that are evaluated in the inverse method. The conjugate gradient method is an iterative



methodology that need that the last point of the calculation goes to 0. Therefore in all the analyzed cases, the heat flux go to zero before stop recording data.

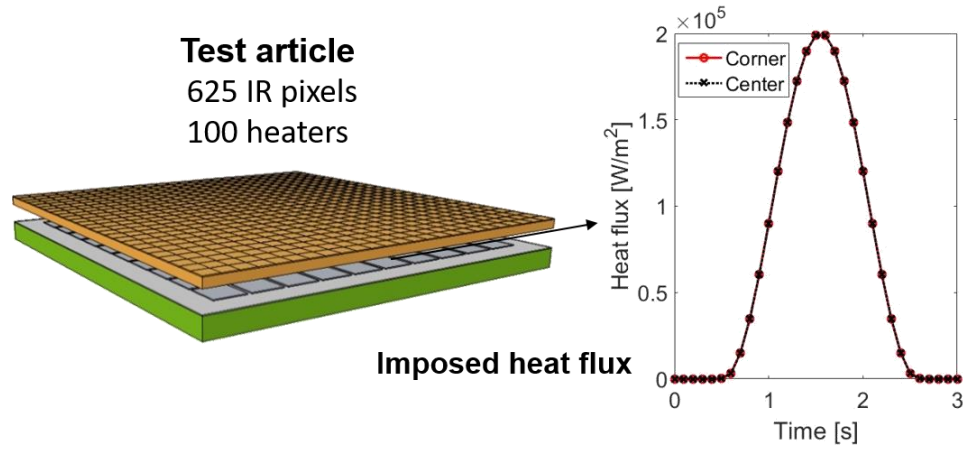


Figure 4-5. Analyzed model with the imposed heat flux in all the heaters.

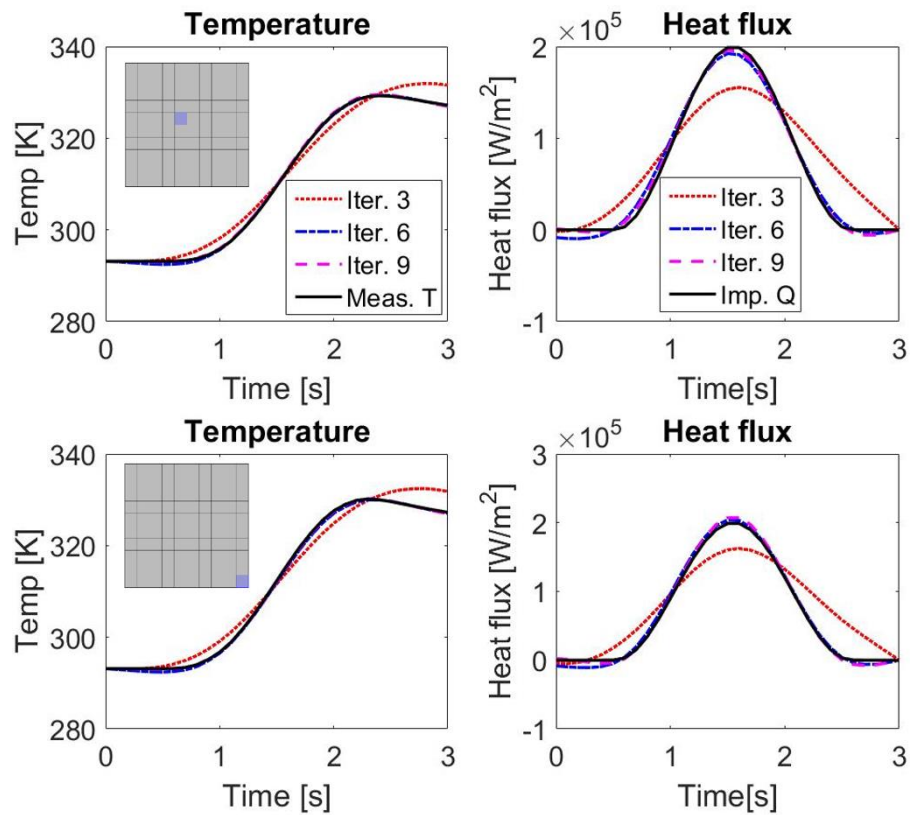


Figure 4-6. Computed temperature (left) and estimated heat flux (right) by the conjugate gradient method after 2, 6 and 9 iterations in the center (top) and the corner (bottom) of the analyzed chip.

The results of the inverse heat transfer method using the conjugate gradient method are shown in the Figure 4-6. It shows the temperature increase (input) of the surface temperature at two different locations, the center of the chip and one corner; and the imposed and estimated heat flux with the inverse method after 2, 6 and 9 iterations. We can observe that after 9 iterations the temperature is already matched and there is a good agreement between the imposed heat flux and the estimated heat flux, both in the center and the corner of the analyzed chip.

#### 4.1.2 Digital Filter Method Evaluation

The objective of this work is to define a proper location for the temperature sensors under any conditions. For this reason, the case that has been analyzed first is a constant heat flux in space and a sinusoidal shape in time. In order to compute the inverse method, we need measurements of the temperature on the top surface of the microchip. We perform a direct numerical experiment to retrieve the temperature distribution over this surface and use it as the input for the inverse methodology (rather than experimental data, for this validation). In the transient simulation, we imposed heat flux with a positive sinusoidal wave in time over 1.5 seconds with a maximum amplitude of  $2e5 \text{ W/m}^2$  as shown in Figure 4-7(a). This heat generation was applied in all of the 100 heaters in the interior of the model in this case. The boundary conditions were similar that the ones described in the simplified reduced model of verification: natural convection on the top and sides of the chip and adiabatic conditions on the bottom of the model. More complex cases can be analyzed spatially and timely distributed, but this case has been chosen to minimize the dependence of the solution of the optimization on the particular cases given when only few of the heaters are on. The temperature rise is tracked at each time step. Figure 4-7(b) depicts the temperature rise in the corner and center of the microchip, respectively.

With this numerical method, the calculated heat flux derived from the “measured” temperatures is shown in Figure 4-8. We observe a shift upstream in time compared to the imposed heat flux, as well as a slight under-prediction of the heat flux. This is due to the fact that the temperature is decreasing in the last time steps and therefore the model calculates a negative heat flux value. The same or very similar behavior is found at any heater location since the imposed heat flux is uniformly distributed in this case.

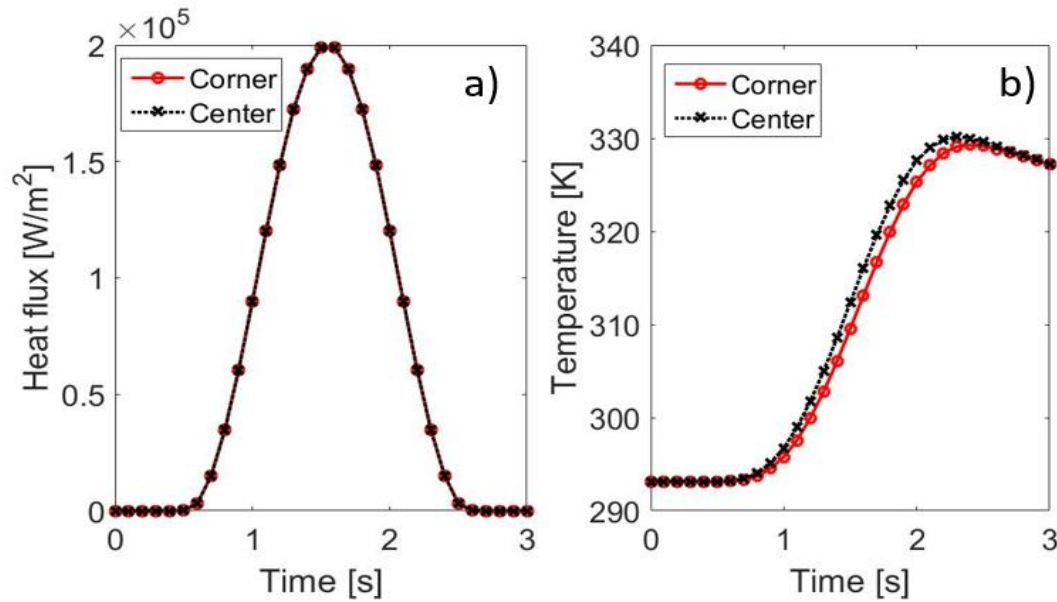


Figure 4-7(a) Imposed heat flux in the numerical experiment for the corner and center heaters. (b) Temperature increase over time at the top surface in the corner and center locations of the microchip.

The competitive advantage of this method with respect to other inverse methodologies such as the conjugate gradient method (CGM) is the computational efficiency. While the widely used CGM for 3D inverse problems is an iterative process and requires around 9 hours to give a suitable solution, the function specification method combined with the regularization problem is able to perform the same calculation with similar results in less than 15 minutes.

There is a good agreement in the magnitude of the heat flux prediction. This heat flux distribution is then used to predict the temperature distribution inside of the microchip where the temperature sensors are going to be located. This temperature distribution is used as an input of the second step of this methodology where the Kriging interpolation is implemented.

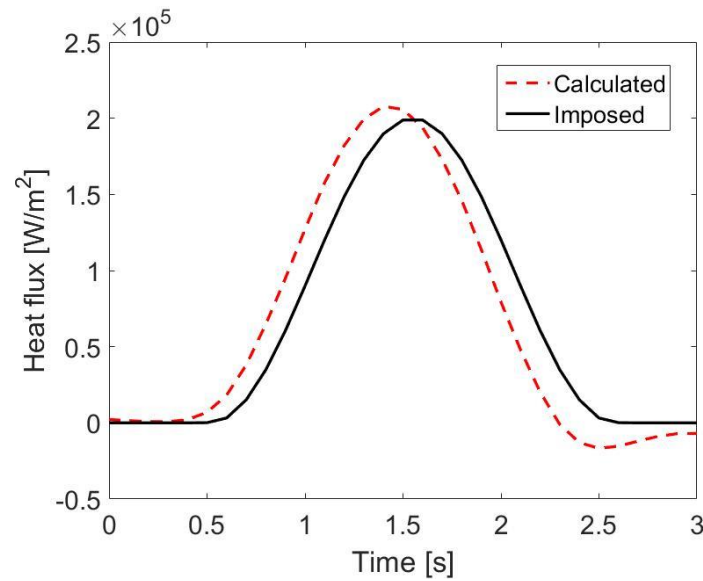


Figure 4-8. Comparison between the imposed heat flux and the heat flux estimated with the inverse 3D methodology.

#### 4.2 Conjugate Heat Transfer Numerical Evaluation

These two methodologies were programmed as well combining Matlab and Fluent in order to perform conjugate inverse heat transfer analysis. Fluent was chosen for its flexibility to create the links with other programs and because it is widely used in computational fluid dynamics, where the analysis of conjugate heat transfer plays an important role. The first step is to build a simple model which consists in the same number of layers of single crystal silicone and poly-crystal silicone and the same location of the heaters, but in this case only 4 heaters have been introduced in the chip. This simplification was made because for conjugate heat transfer we need to define

each one of the interfaces between the different solids and between the solids and the fluid. Figure 4-9 shows the model of the test article studied in Fluent. It is composed by four heaters equally spaced that can generate heat individually. The first step is to verify that the conjugation of heat is happening in our domain and for that in Figure 4-9 we show the velocity field and the temperature field. The temperature field shows that the fluid domain is clearly heated by one of the heaters since we observe an increase of temperature in the plane just downstream of the chip and also the footprint of the increase of temperature in the downstream exit plane of the domain. This confirms that there is conjugate heat transfer in the model between the solid domain and the fluid domain.

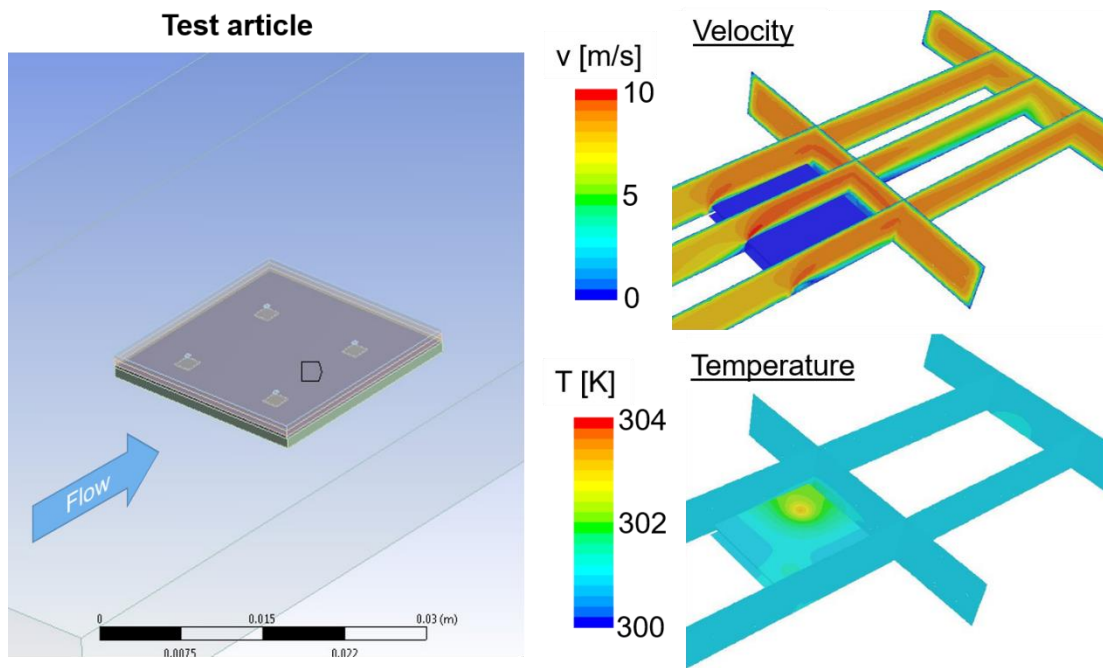


Figure 4-9. Microchip with four heaters (left) velocity field in the fluid domain (top right) and temperature field in the solid and fluid domains (bottom right).

The evaluation of the two different methods was done imposing different patterns of heat flux in the heaters. In this case we illustrate one of the numerical experiments where we imposed a peak of  $200000 \text{ W/m}^2$  in two of the heaters (heater 2 and heater 3) as shown in the Figure 4-10. We run the experiment during ten timesteps where we imposed a sinusoidal wave of heat flux in time.

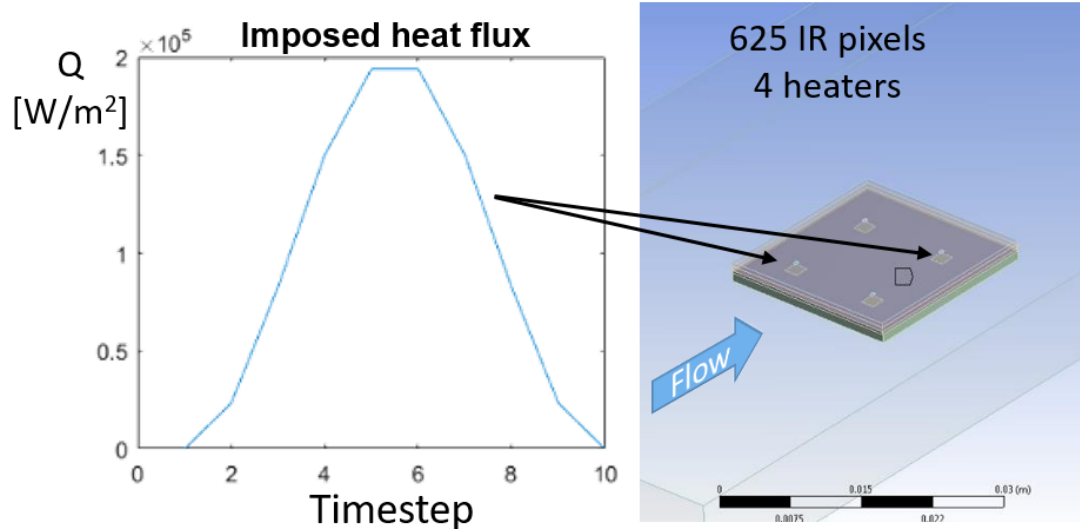


Figure 4-10. Imposed heat flux in ten timesteps in two of the heaters of the test article.

The temperature was measured in the top surface of the chip with a grid of 25x25pixels that represent the pixels of the infrared camera. Then the output of these measurements was introduced in the developed inverse methodologies in order to retrieve the imposed heat flux. In the following sections, the results of both methods are detailed.

#### 4.2.1 Conjugate Gradient Method Evaluation

The conjugate gradient method was predicting the values with good accuracy in the conductive heat flux calculation in COMSOL. The program was implemented in Fluent with the same algorithms that was programmed in the conductive application in COMSOL, both in the whole domain estimation and the sequential estimation. In the conjugate heat transfer estimation, the method is not behaving in the same way that expected based on the conductive calculation. The computational efficiency of this method was reduced considerably due to the fluid computation. The time to perform an iteration is increased by 5 times and the convergence is slower as demonstrate the Figure 4-11. In this figure, we plot the results in the first 4 iterations of the method in function of time and the nodes inside the heater. We can observe that even though with the

iterations the solution is approximating to the imposed heat flux, the calculated heat flux are far away from been converged based on the temperature measurements.

For this reason we can conclude that the conjugate gradient method needs a lot of iterations to get a converged solution and it may not be the most suitable method for the conjugate heat transfer computations.

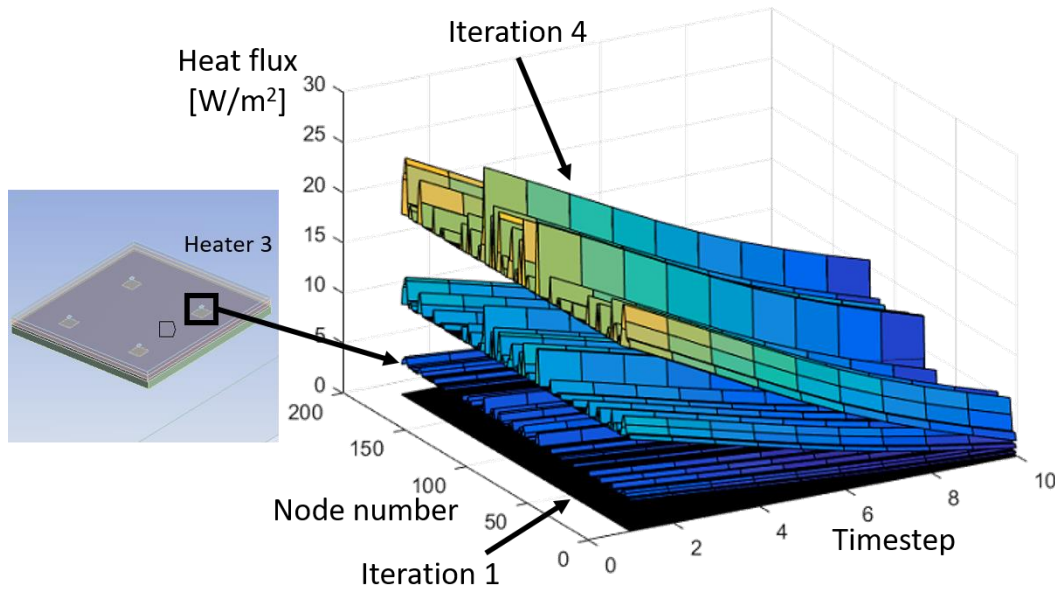


Figure 4-11. Computation of the heat flux in all the nodes of the heater 3 in the first four iterations of the conjugate gradient method.

#### 4.2.2 Digital Filter Method Evaluation

To demonstrate the accuracy and feasibility of this inverse methodology, we conduct a numerical “experiment” using the conjugate heat transfer model ANSYS Fluent. In this numerical experiment, first we compute the direct problem with known boundary conditions (*i.e.*, applied heat fluxes) in the heaters and measure the predicted temperature on the top surface of the silicon layer. In the inverse problem, we input the temperature measurement from the direct problem to compute the heat flux boundary conditions in space and time. The objective of this test is to validate if the

inverse methodology can predict the amplitude of the heat flux, its behavior through time and the spatial location of the heat source.

The digital filter method was able to predict successfully in the most part of the cases the imposed heat flux as shown in Figure 4-12. The aforementioned case with two heaters providing heat is represented as well as the comparison with the solution extracted from the Digital Filter Method. The method can predict the location of the heaters that are on and it predicts the magnitude and the shape of the heat flux that were imposed. The behavior of the heaters 2 and 3 is predicted based on the effect in the temperature in a transient. Also, the behavior of the heaters 1 and 4 is predicted, except for the last timesteps in the heater 1 where the method is predicting spurious positive heat flux.

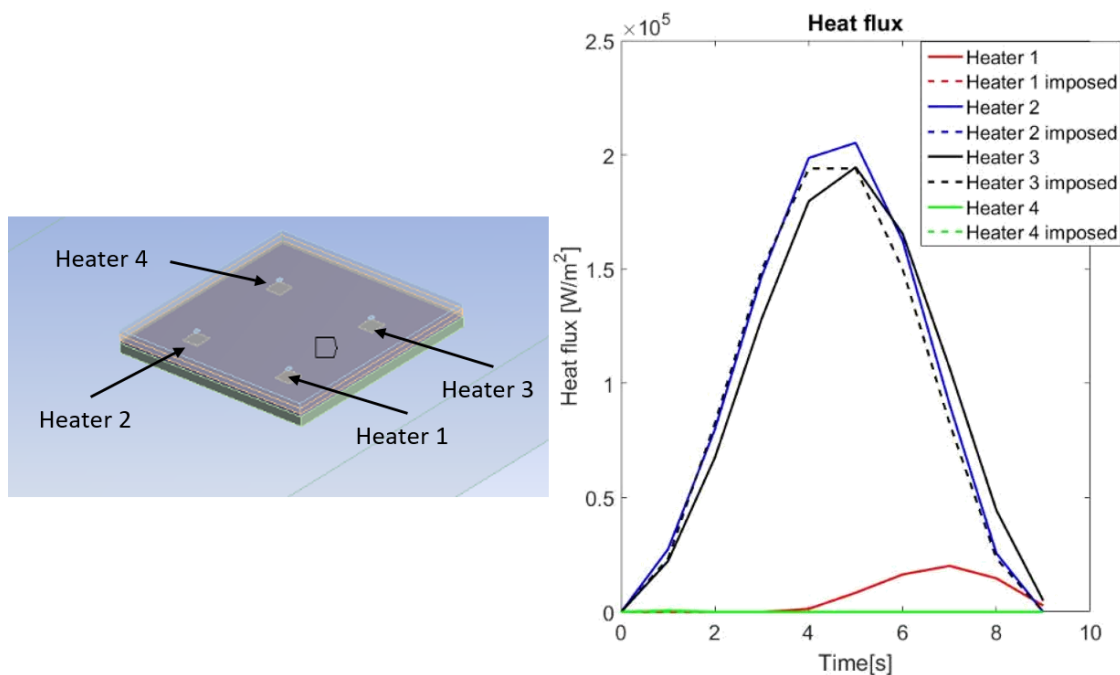


Figure 4-12. Location of the different heaters (left) and comparison between the imposed heat flux and computed heat flux (right) with the digital filter method.



### 4.3 Experimental Validation

The last step to validate the methodologies consists in the comparison of the results with experimental data. For this validation, we are using a squared chip of 21x21mm composed by several layers of silicone, 26 RTDs and 25 heaters that we can control individually.

Figure 4-13 shows the chip used during the experimental validation and a sketch of the location of the heaters inside the silicon layers.

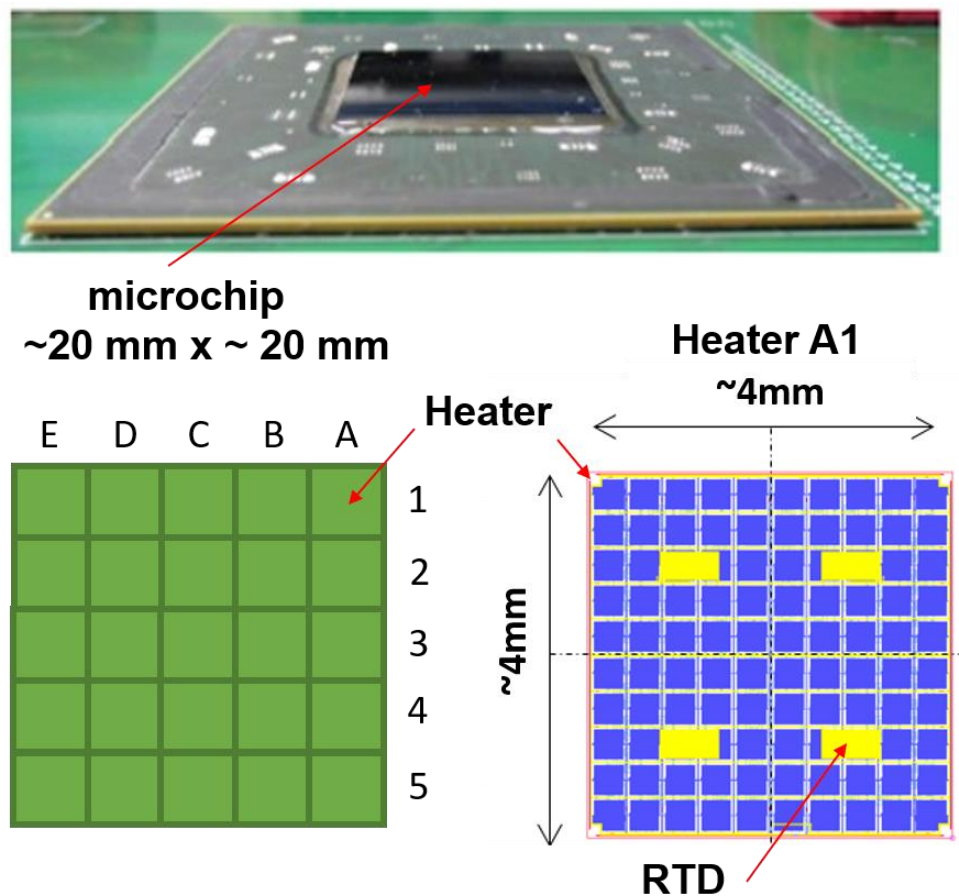


Figure 4-13. Microchip with 25 independent heaters used for the experimental validation of the inverse methodology. The system consists of a grid with 25 independently controlled heaters and 26 embedded temperature sensors.

Figure 4-14 depicts the two different models used for analysis of the microchip: (1) a pure conductive model using COMSOL Multiphysics® software and (2) a conjugate (*i.e.*, including convection and conduction) heat transfer model using ANSYS Fluent®. The COMSOL conduction model include the silicon microchip as described in the numerical analysis of the previous section, while the ANSYS Fluent conjugate heat transfer model includes the microchip, the printed circuit board (PCB), and the air in the enclosure surrounding the chip.

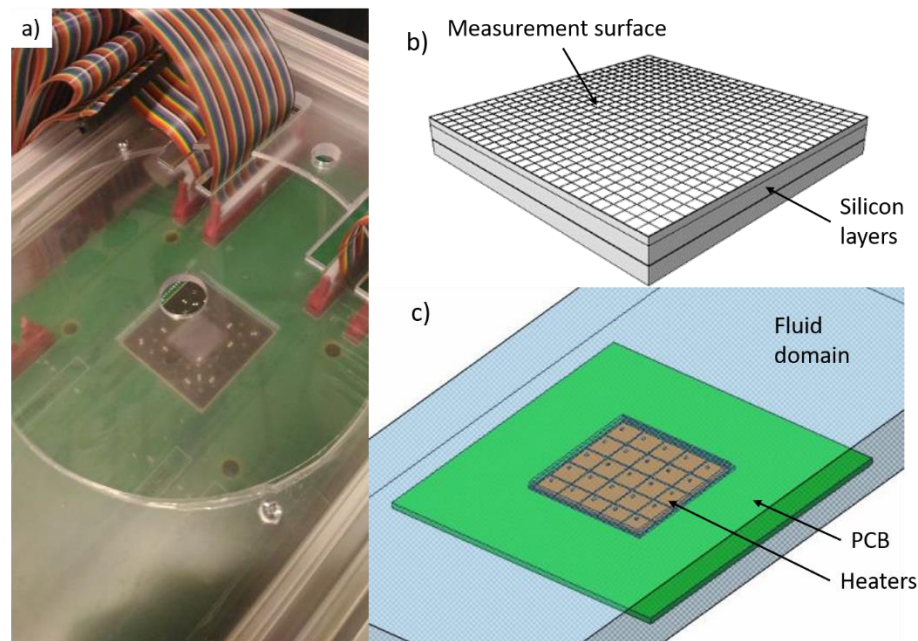


Figure 4-14. a) Microchip in the experimental setup, b) COMSOL model of the microchip with subdivisions in the top surface marking the approximate size of the pixels for IR thermal measurements, and c) Fluent model of the microchip for conjugate heat transfer analysis. Divisions shown here outline the 25 different heaters elements.

These models were tested numerically, specially the ANSYS Fluent model, since it is a complete different model with respect to the numerically aforementioned demonstration. Specifically, in the numerical experiment, a single heater provides a sinusoidal heat flux over 10 seconds with a maximum amplitude of  $2 \times 10^5 \text{ W/m}^2$ . The remaining heaters are off for the entire duration. Figure

4-15 depicts the imposed heat flux in four different heaters and the estimation of heat flux using the developed inverse methodology. Note that three heaters with no applied heat flux are shown for illustration and all the imposed and retrieved data for those heaters overlap at the  $0 \text{ W/m}^2$  axis. The method accurately predicts the location of the heat source, the time evolution of the imposed heating, and the magnitude of the heat flux with an error below 5% of its maximum, only providing the temperature measurement of the top surface of the test article.

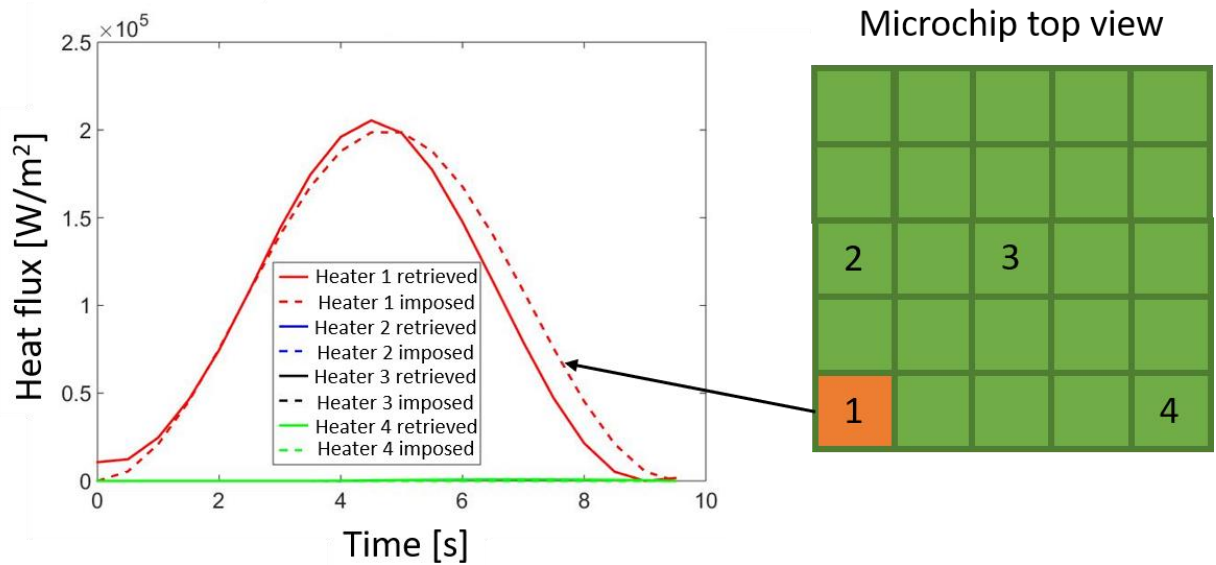


Figure 4-15. Numerical validation of the inverse methodology in Ansys Fluent including conjugate heat transfer. (a) The imposed and retrieved heat fluxes in selected four heaters agree well. (b) Top view of the 5x5 heater grid with the four selected heaters labeled. A heat flux is imposed on heater 1, while all remaining heaters are off for the duration of the simulations.

The procedure in order to make the experimental campaign is detailed in Figure 4-16. It starts with the design of the experimental setup. A controlled environment enclosure was designed in order to place the chip with heaters that we are using for the experimental validation. This enclosure helps in the acquisition of the infrared data reducing the error introduced by the convection and in acquisition of a stable reference temperature to calibrate the infrared measurements. This enclosure

has 4 walls in top bottom and sides, one open side and one side with fans in order to generate forced convection inside of the enclosure simulating a rack.

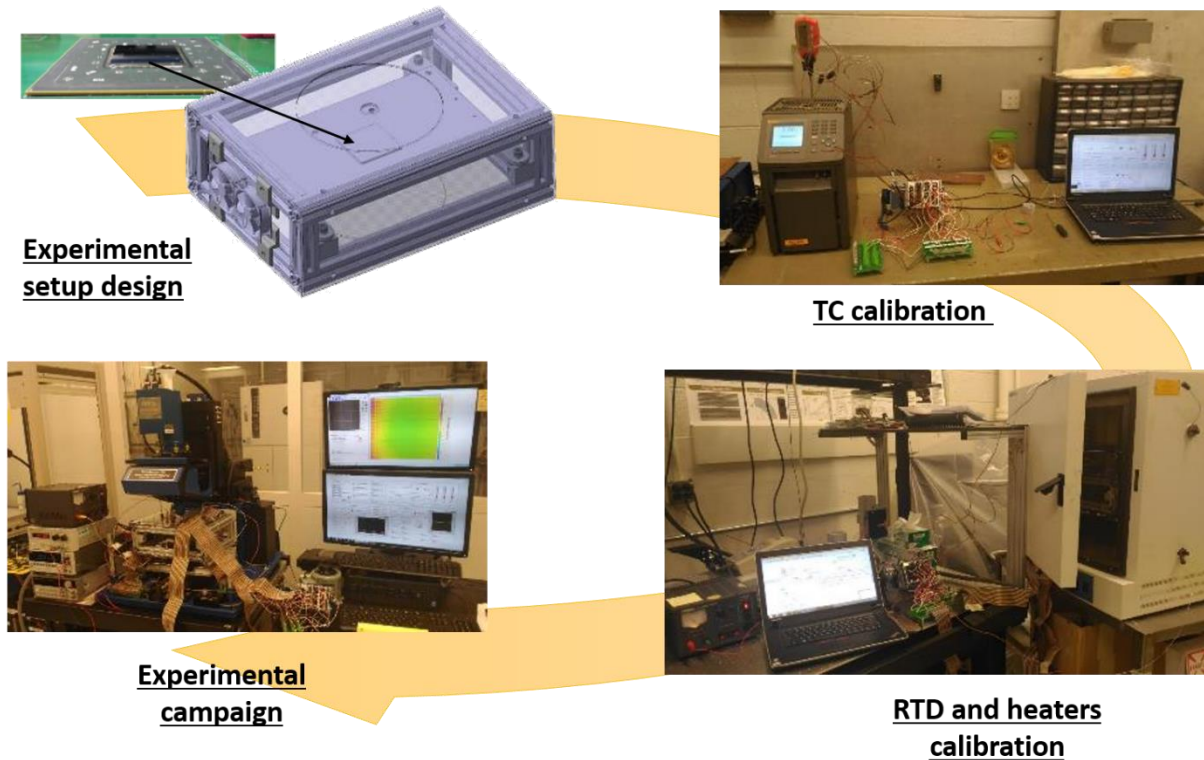


Figure 4-16. Experimental procedure.

Inside of the enclosure we perform different temperature measurements: thermocouples control the temperature of the air of the enclosure, the RTDs inside of the chip to measure the temperature near the surface of the chip and infrared thermography over the top surface of the chip which is going to be the measurement. These measurement techniques need to be calibrated before we perform the measurement campaign. The thermocouple probes specially designed for this application were calibrated in a first step using a Fluke thermocouple calibrator with an uncertainty of  $0.005^{\circ}\text{C}$ . They are thermocouples type K that were calibrated using 12 points of calibration in the thermocouple calibrator: eight of them increasing the temperature and four of them decreasing

the temperature from the previous calibration point. Figure 4-17 shows the result of the calibration of the three calibrated thermocouples.

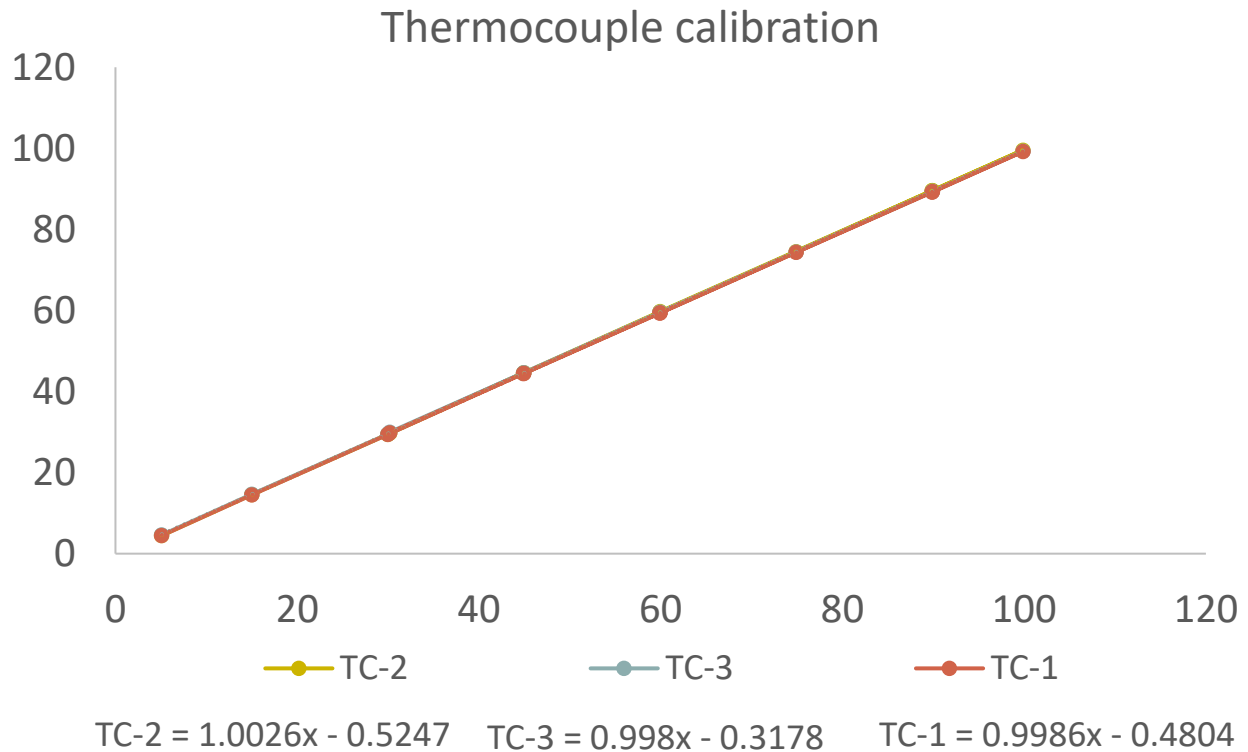


Figure 4-17. Thermocouple calibration.

These thermocouples, already calibrated, were used in the next step of the calibration procedure when we used an oven to calibrate the RTDs and the heaters inside of the chip. For this calibration, we used the same data acquisition system of the experimental campaign and the chip was placed inside of an oven together with the thermocouples to check which the internal temperature of the oven was. We placed one thermocouple next to the enclosure, one few centimeters over the enclosure and another at the bottom of the oven. In this case a 6 points calibration was performed, in order to calibrate all the heaters and all the heaters. Since we did not have channels to calibrate all together, we had to repeat the process several times.

The behavior of the RTDs, as expected, and the heaters is pretty linear with the temperature as shown in the Figure 4-18 and Figure 4-19. The RTDs are used to control the safety operation of the chip taking into account that they should not measure temperatures over 100°C. The temperature measured with eight of the RTDs is monitored to provide real time data about the status of the chip for a possible quick shut down of the experiment. The heaters instead are calibrated to know the total heat flux or power that they are providing including the effect of the temperature, since the resistance of the heaters varies with the temperature. Figure 4-18 and Figure 4-19 depict the effect of the temperature in the resistance of 8 of the RTDs and 8 of the heaters, but the complete chip with all the heaters are RTDs was characterized.

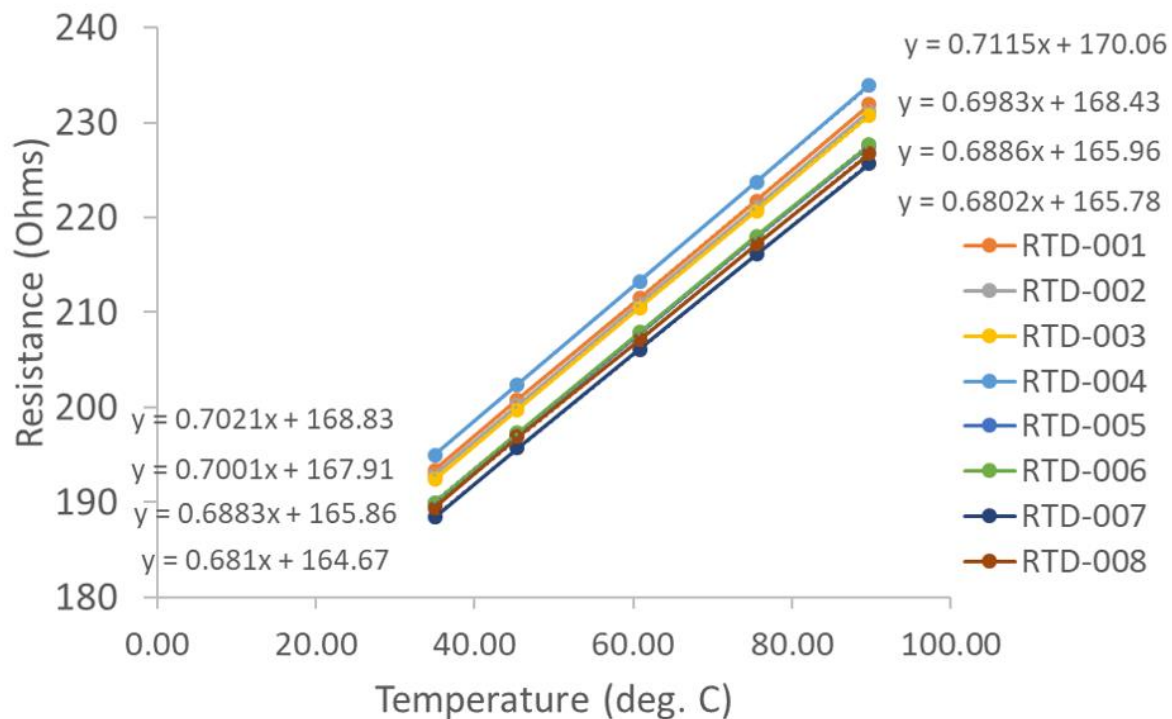


Figure 4-18. RTD calibration.



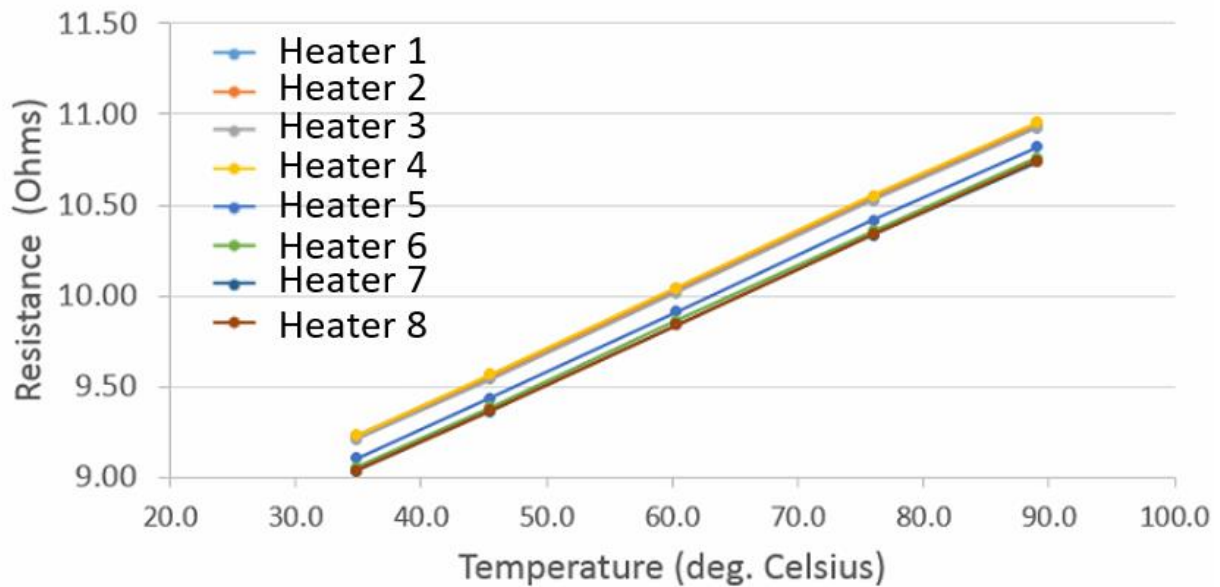


Figure 4-19. Heaters calibration.

Once all the measurement techniques and the heater chip were characterized, we could proceed with the experimental campaign using an infrared microscope. This infrared microscope measures the temperature at the top surface of the microchip as a function of space and time with  $\sim 18 \mu\text{m}$  spatial resolution and  $\sim 0.1 \text{ K}$  temperature resolution. Because silicon is IR transparent, we apply a layer of graphite paint on the measured surface. The lens used in this experiment had a field of view of  $12\text{mm} \times 12\text{mm}$ , therefore, the experimental campaign was carried out using a  $3 \times 3$  heaters array located in one of the corners of the test article, as shown in the Figure 4-20.

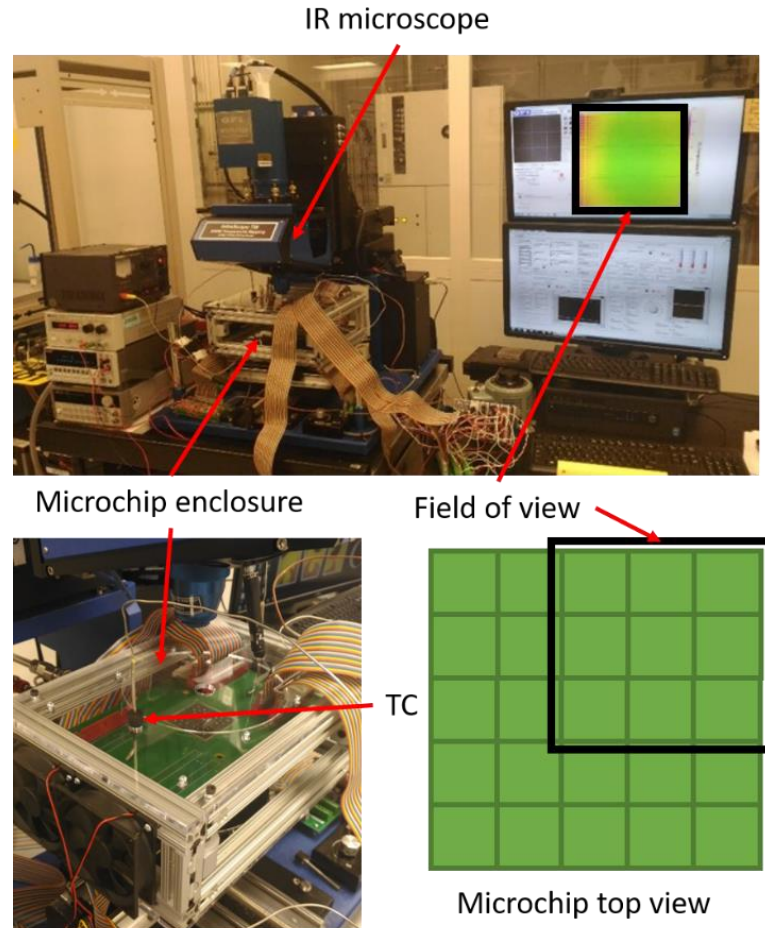


Figure 4-20. Experimental setup to measure the top surface temperature of the chip in the specified field of view of the IR microscope.

The experimental campaign was divided in 6 different experiments where we were providing different levels of heat flux in different heaters as shown in the Figure 4-21. The experiments were carried out for 100 seconds with a sampling frequency for the infrared camera of 1 Hz. The thermocouples and RTDs were sampled at 10Hz. The different heaters are represented as green squares and the heaters that are on in each one of the experiments are marked as an orange squared. The RTDs are located over the different heaters, except for the central heater with has 2 RTDs over it. The use of the microscope also provides a limitation to the setup since the field of view that we can target with the larger field of view lens is only a 3x3 matrix of heaters. For this reason,



we decided to limit the experimental campaign to the bottom right corner of the experimental chip and also reduce the number of experiments and the location of the heaters that are on to the particular field of view that we can observe. The six experiments depicted in the Figure 4-21 were performed in natural convection and in forced convection so we have a total of 12 experimental data which are validated in the case of the natural convection with the conductive model developed in COMSOL and the conjugate heat transfer using the model developed in Fluent. In experiment 1, we used the same strategy of the numerical experiment where we heat up all the heaters. In experiment 2, heat up the central heater of the chip and then it is combined with a corner heater for experiment 3. In experiment 4, we heat up the central heater of the field of view and then we evaluate what happens when we turn on the heaters in the same column and on the same row for experiments 5 and 6, respectively.

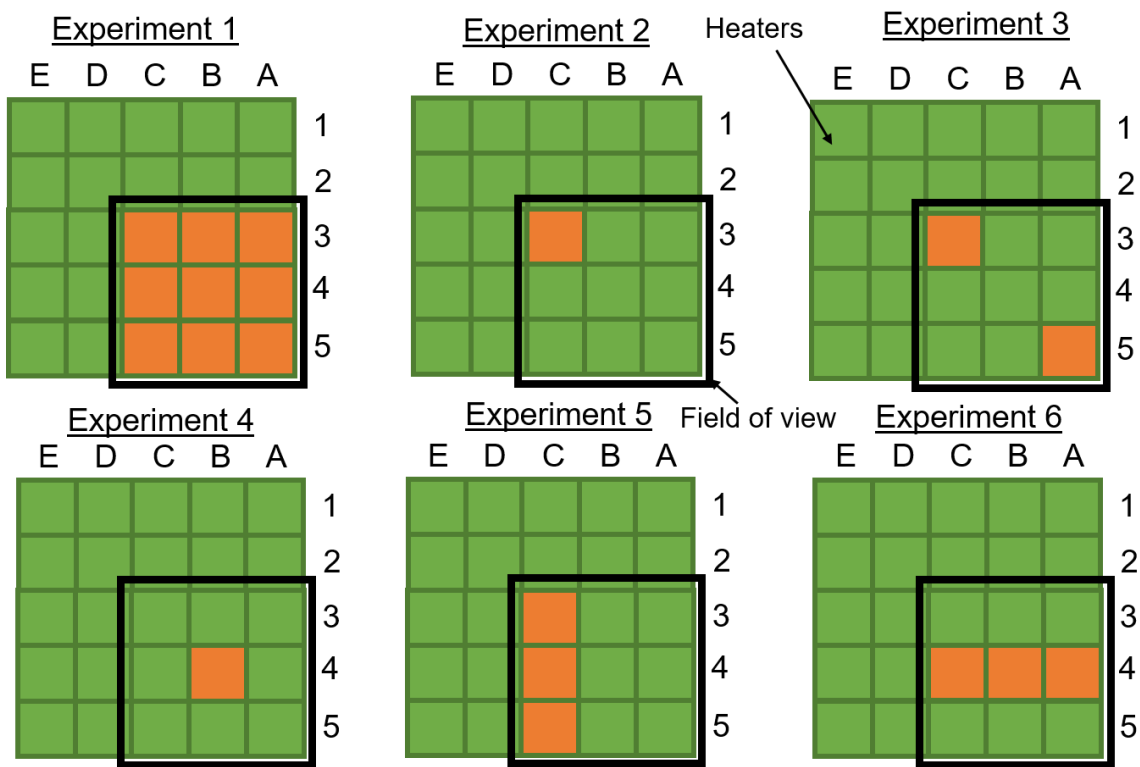


Figure 4-21. Different experiments performed with the 5x5 heaters test article.

Each experiment was run for 100 seconds recording one temperature map each second. In terms of time distribution of heat flux, the selected heaters for each of the cases were turned on between 2 s and 8 s after beginning the recording and they were switched off after 60 seconds of operation at constant heat flux. The heat flux generated by the heaters is controlled with a LabView program coupled with a Keithley sourcemeter, which is also used to record and save all the data. Figure 4-22 depicts the six experiments with variations in the heat flux maps and resultant temperature profiles. In this work we focus on experiments 1, 3, and 4 to validate the proposed inverse methodology.

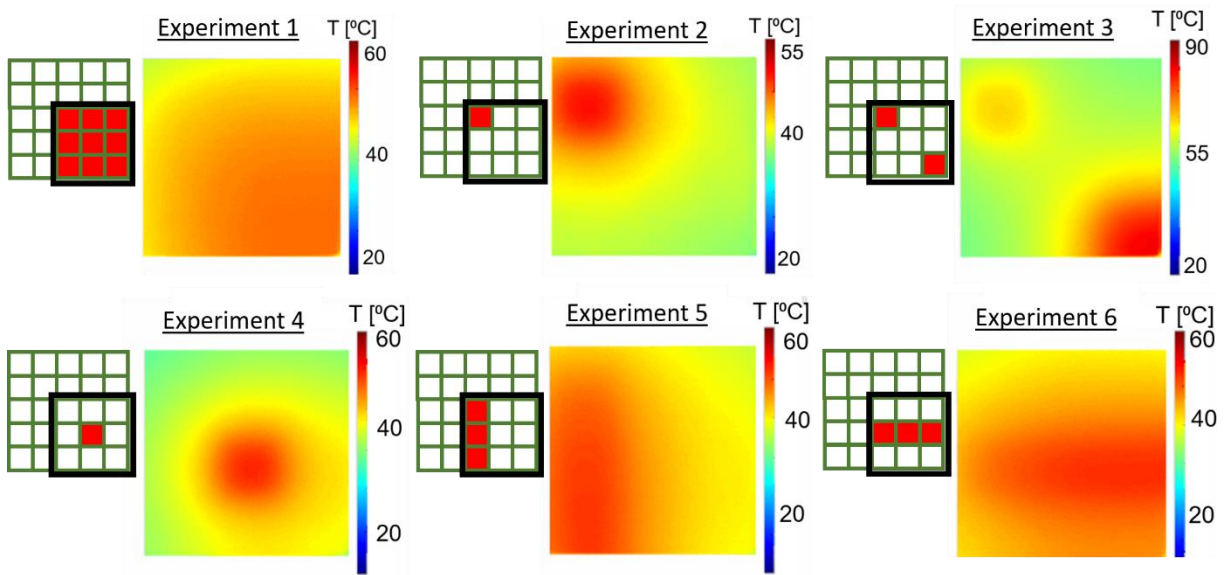


Figure 4-22. Experiments performed to validate the methodology. Each small inset indicates which heat sources were on (red) for each experiment and the black box indicates the field of view of the infrared microscope. The thermal images are from one frame of the thermal movie and show the spatial variation in temperature of the die.

As observed in the Figure 4-22, the spatial distribution of temperature varies considerably amongst the different experimental cases, and this helps in the determination of the location of the heat sources and the retrieval of the value of the applied heat flux. In experiment 1, we powered the 3x3 grid of heaters within the field of view of the microscope, while in experiments 2 and 4 we

only powered one heater but in different locations of our temperature map. In experiment 3, we used 2 heaters at the corners of the field of view. In the experiment 5 and 6, we turned on three heaters corresponding to a columns and a row of heaters of the field of view, respectively. The temperature map obtained with the IR microscope contains 1024x1024 measurements (pixels). To apply this methodology, which number of operations is directly proportional to the number of temperature measurements, we decided to reduce this number of measurements to a grid of 15x15 effective pixels. The temperature map was divided in the desired grid and all the nodes contained in the subdivisions were averaged at each time step to get the input temperature maps for the code.

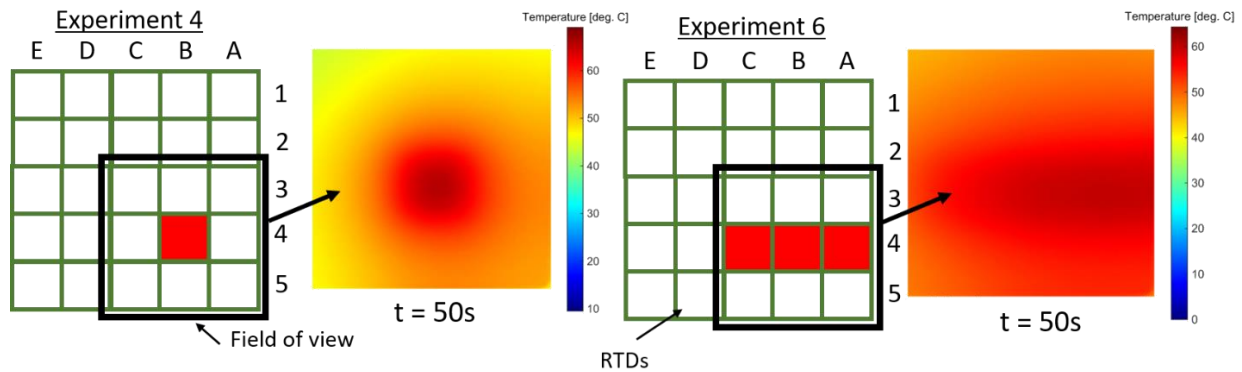


Figure 4-23. Infrared images of the experiment 4 and experiment 6 at second 50 of the transient experiment.

Figure 4-23 shows the experimental data measured in the experiment 4 and 6 after 50 seconds of experiment. The experimental procedure was similar for each one of the experiments only varying the times when the power was turned on and off to the heaters. First we start to sample with the infrared microscope and the other measurement techniques. After few seconds, we turn on the heaters and we observe the behavior of the temperature. At around the second 70 of each experiment we turn off the heaters in order to see how the temperature decays with time and if we are able to predict it with the inverse methods.

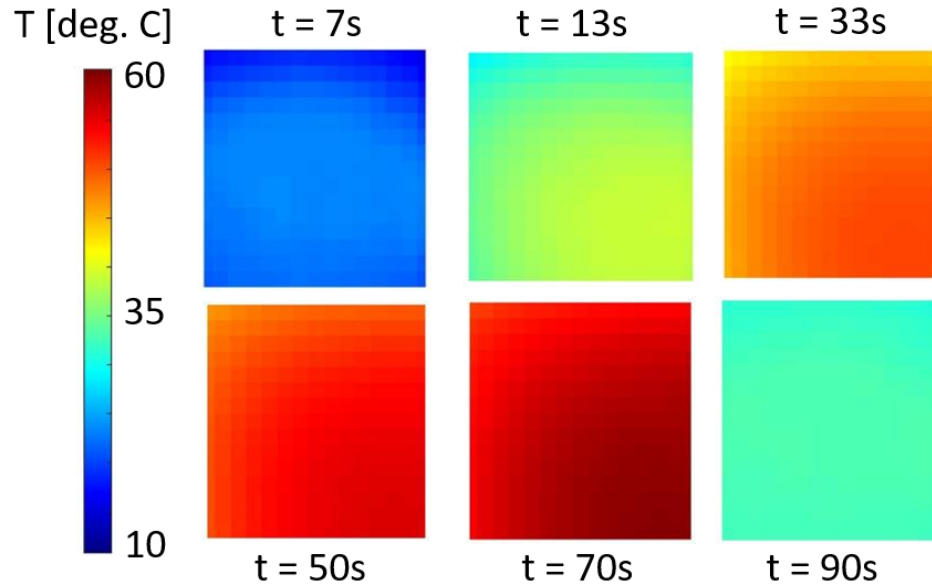


Figure 4-24. Thermal response during Experiment 1 with a 15x15 grid of sensors in order to validate the data with the inverse methods.

Figure 4-24 depicts the experimental data obtained with the infrared microscope at different timesteps during the experiment 1. It reaches a temperature of 60°C before we turned off the heaters. Also it can be observed that in this case the pixels are noticeable. We had to increase the size of the pixels applying an averaging technique in order to be able to apply it to the developed model where we have a 625 pixels where we can impose the temperature, step needed for the calculation of the heat flux with the inverse methods.

This experimental measured data was then used as input for the two inverse methods and we tested if we could predict the trends in time of heat flux, the magnitude of the heat flux that we are imposing in each one of the heaters and the location of the heaters that were on and off in each experiment.

#### 4.3.1 Conjugate Gradient Method Validation

The conjugate gradient method was validated for both experiment 1 and experiment 4. It is remarkable to observe that the solution of the conjugate gradient method and the digital filter method have several similitudes. It detects the same peak that in the previous model when we turn on the heaters and then stabilize around the value of heat that we have imposed. Then it detects or predicts the same negative value of heat flux (cooling) in the timestep when we turn off the heaters.

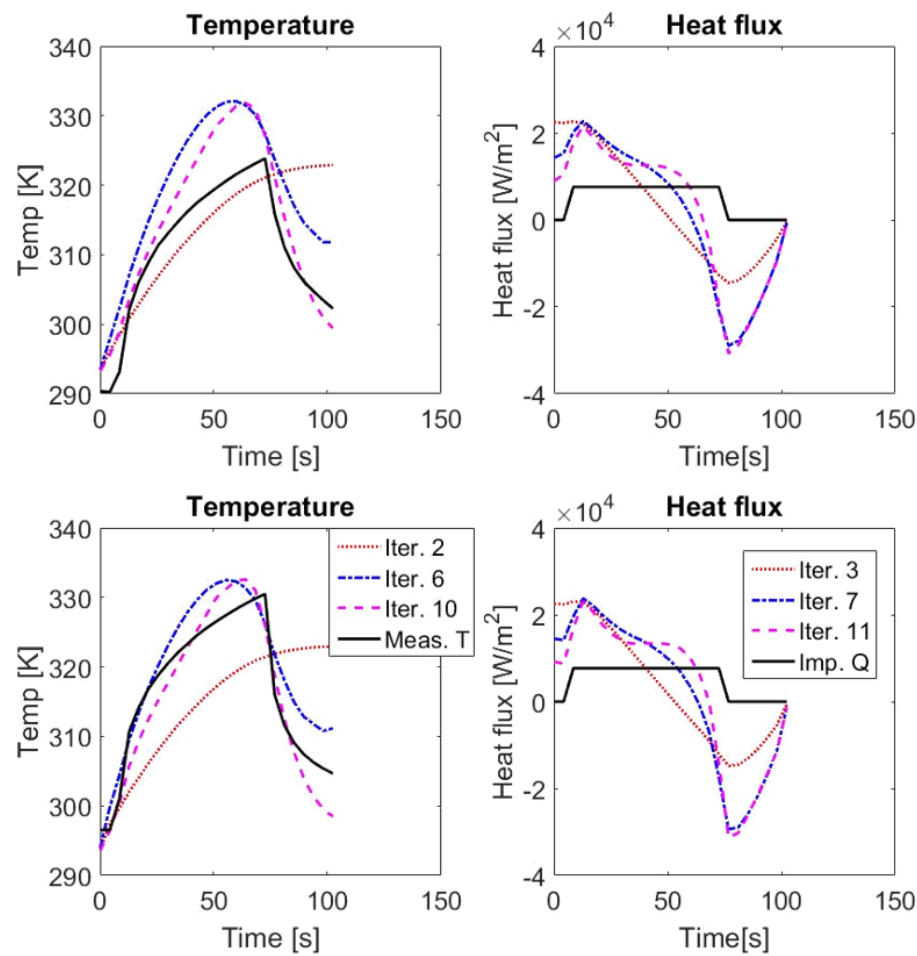


Figure 4-25. Comparison of the imposed heat flux and the computed heat flux with the Conjugate Gradient Method after 11 iterations in the center(top) and corner (bottom) of the experimental chip.

The dashed line, is the predicted heat flux after 11 iterations and we can observe that the temperature is not completely matched like in the numerical case, therefore for this case apart of the corrections that need to be implemented to minimize the peaks at the beginning and at the end of the application of the heat flux, we will need to let the process run for more iterations.

We used the same method to validate the other cases of heat flux imposed in the different experiments and we could observe that the conjugate gradient method is not the best method to identify hotspots in a small region with small gradients since it is not able to identify the location of the heaters that are on.

#### 4.3.2 Digital Filter Method Validation

The digital filter method was tested with the experiment 1 for the moment but it will be tested in the future with the other experiments. With the digital filter method, we have flexibility modifying three parameters to drive the solution to the most adequate solution of the heat flux based on previous knowledge. Figure 4-26 shows the comparison between the heat flux that we imposed in the central heater and the corner heater of the 3x3 array of heaters analyzed with respect to the solution extracted from the digital filter method. We can observe that it is not matching with the imposed heat flux due to the sudden changes in heat flux imposed since it is a squared step. The digital filter method is predicting which heaters are on and which ones are off and it gives the moment of time when we impose the heat flux and when we stop them. There is a peak in the predicted heat flux when the increase of heat flux is detected. This peak drives down the prediction of heat flux in the steady part of the heat flux and the sudden drop of temperature when the heat flux is stopped makes the method predict that there is cooling in our experimental setup which is true if we take into account that the dissipation for natural convection is larger than the one

predicted by the model. This feature can be minimize by applying the correction of the model already introduced but it will not disappear.

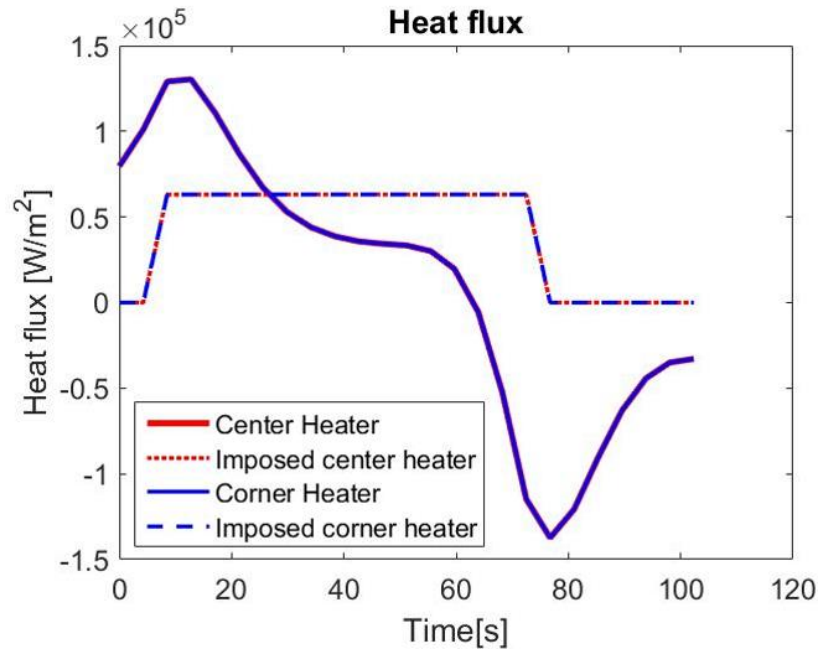


Figure 4-26. Comparison of the imposed heat flux and the computed heat flux using Digital Filter Method.

#### 4.3.3 Digital Filter Method with Non-Iterative Non-Linear Correction

All the tested experiments were analyzed using the inverse methodology. We focus on three of them: experiment 1 which is the most general case, and experiment 3 and 4 since they are the most challenging heat distributions of the experiments.

First, consider experiment 1 where all the heaters in the field of view are heating at the same rate. The temperature evolution in time is represented in the Figure 4-27 and we observe that we can predict the evolution in time of all the heaters. Also, the magnitude of the heat flux is captured well by the inverse methodology. The results show good agreement for both natural convection and conjugate heat transfer calculations.

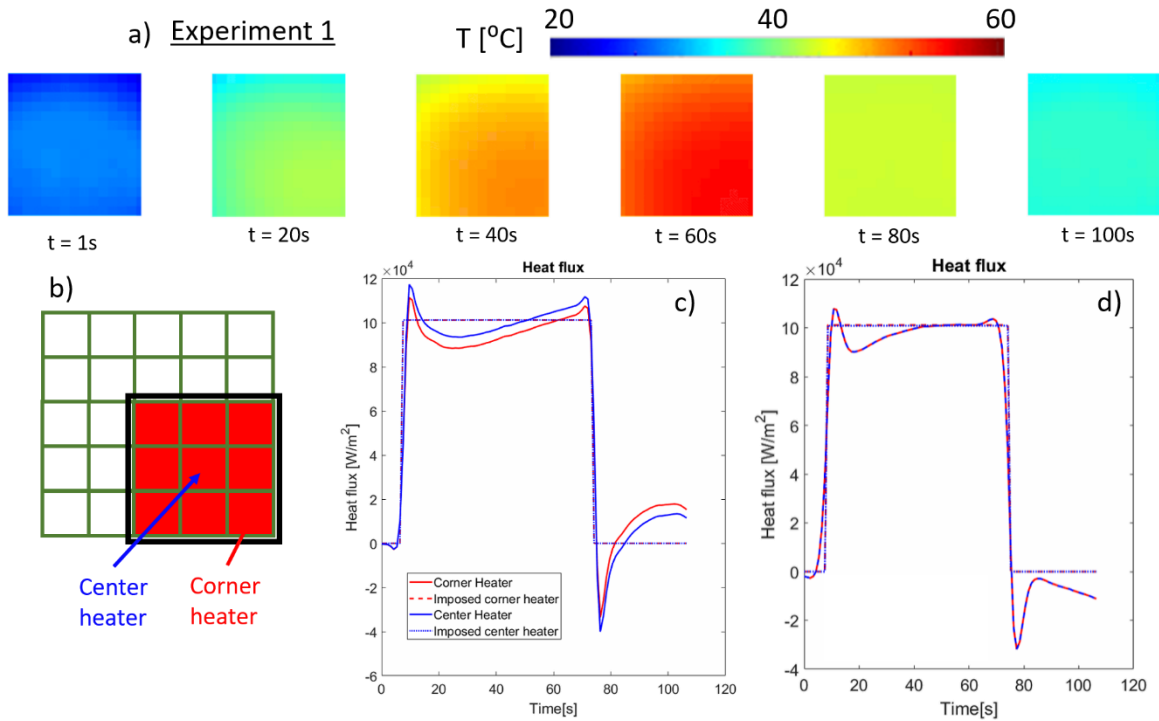


Figure 4-27. Validation of the inverse methodology for the experiment 1. (a) Temperature maps at selected times. Note that the temperature is fairly uniform at each time step. (b) Sketch of the  $5 \times 5$  heater grid with the 9 active heaters indicated in red. The black outline indicates the field of view. (c - d) Heat flux in the center (blue) and (red) corner heater within the field of view as extracted from the inverse method. Panel (c) shows the results for natural convection with the Coolsol model and panel (d) shows the results under forced convection using the Fluent model.

The new methodology can predict, not only the magnitude of the heat flux and the temporal behavior of the heat flux, but also spatially resolve the locations of applied heat flux as shown in Figure 4-28 which illustrates the imposed and retrieved heat flux at  $t=40s$  for experiments 3 and 4. We applied our methodology to the most complex case (experiment 3 where two heaters are active, while the rest do not provide any heat) and we obtained very good agreement in terms of the predicted magnitude of heat flux, the time when the heaters are turned on and turned off, and the location of the heat sources as can be observed in the Figure 4-28. The magnitude of the heat flux also varies from test to test and the methodology was able to compute the value of heat flux that



was imposed with a reasonable accuracy ( $< 10\%$  error) in all the heaters and at any moment of time.

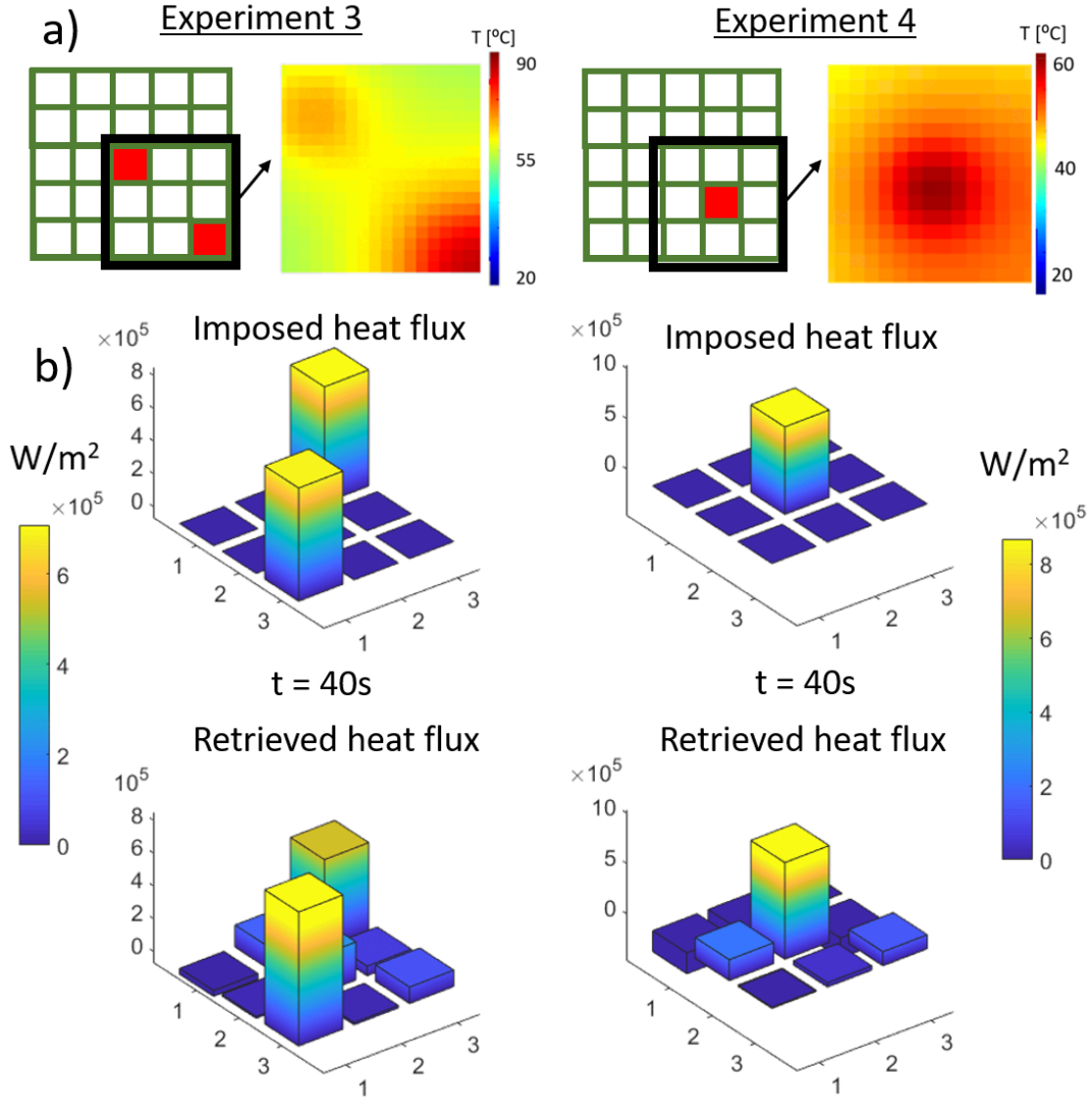


Figure 4-28. Experimental validation for experiments 3 and 4 at  $t=40s$  demonstrating ability to spatially resolve heat flux. (a) Schematic of active heaters and observed temperature map at  $t = 40s$ . (b) Imposed and retrieved heat fluxes in each heater at  $t=40s$ .

We performed an uncertainty analysis based on the uncertainty of the inputs to this method. For this case, we consider the uncertainty in the thermal properties of the different materials that

compose the microchip with the heaters, in the thickness of the materials (50 micrometers), and finally in the measured temperatures ( $\pm 2\text{K}$ , after the calibration of the thermocouples and the IR camera). Combining linearly all the contributions to the uncertainty, we observe that the uncertainty in temperature dominates the overall uncertainty. Also, as we take temperature measurements over all the surface as input to the method, this is logical. Based on the experimental setup, the overall uncertainty of the new non-linear non-iterative methodology is 7.1% for evaluating the value of predicted heat flux, as shown in Table 4-1.

Table 4-1. Uncertainty analysis of the heat flux computation using the non-linear inverse method.

Quantity	Absolute input uncertainty	Uncertainty in %	Variation in heat flux relative to mean in %	Sensitivity
Temperature [K]	2.0	0.64	6.35	9.98
k silicon [W/mK]	10	7.69	-0.15	-0.02
$\rho$ silicon [kg/m <sup>3</sup> ]	10	0.43	0.14	0.32
C <sub>p</sub> silicon [J/K kg]	7	0.99	0.30	0.30
k polycrystalline silicon [W/mK]	10	10.00	-1.66	-0.17
$\rho$ polycrystalline silicon [kg/m <sup>3</sup> ]	10	0.43	0.09	0.21
C <sub>p</sub> polycrystalline silicon [J/K kg]	7	1.03	0.15	0.15
thickness silicon [m]	0.00005	5.00	1.97	0.39
thickness polycrystalline silicon [m]	0.00005	10.00	1.97	0.20
<b>Overall Uncertainty in heat flux calculation</b>			<b>7.14</b>	

When comparing the heat flux extracted from our inverse method to that measured directly in the measurement rig, we must also consider the uncertainty in the power measurements. Specifically, the uncertainty of the experimentally measured heat flux is 4.6% as evaluated given the uncertainty in the voltmeter and sourcemeter measurements. Table 4-2 shows the uncertainty associated to the

power computed in each one of the heaters that we used as heat source during the different experiments.

Table 4-2. Uncertainty calculation of the power in the experiments.

Quantity	Absolute uncertainty	Uncertainty in %	Variation of power relative to mean in %	Sensitivity
Voltage [V]	0.005	0.152	4.591	30.30
Current [A]	0.00001	0.002	0.278	166.67
Overall uncertainty in power calculation			<b>4.600</b>	

#### 4.4 Sensor Location Optimization Technique

##### 4.4.1 Kriging Interpolation Combined with Genetic Algorithm Optimization

There are several methods to interpolate a surface from discrete data points: for example, polynomial interpolation, the radial basis function method, the inverse distance weighted methods, and Kriging interpolation. The first typically uses Taylor expansions to estimate the surface of the solution from the measurement points and it is one of the best estimators since it is based on the least squares solution. The Kriging methodology is based on a statistical method that uses a weighted variance, minimizing the error between the estimated and the actual values [134][135]. It was first proposed in the field of geo-statistics [136] to estimate three dimensional mineable deposits and it was adapted for other applications mainly related to optimization. The Kriging interpolation was applied recently in different optimization techniques in order to minimize the information needed to save and perform the optimization [137]. This method provides two main advantages since it provides anisotropy information (the direction and the ratio of anisotropy) and provides standard errors related with spatial data. If the desired quantity is  $T$  (in this case the temperature), the Kriging estimator is expressed linearly as  $T^*$  [138]:

$$T^*(x_0, y_0) = \sum_{i=1}^n \lambda_i T(x_i, y_i), \quad (60)$$

where the  $T(x_i, y_i)$  are the measurement points (*i.e.*, where the sensor is placed) and the  $\lambda_i$  are the weights of each one of the points. These weights are calculated in this method by evaluating the statistical properties of the data [139].

Additionally, we need to define a residual based on a model  $m(x, y)$ , which can even be the main level of the population  $\mu$ :

$$Y^*(x_i, y_i) = T(x_i, y_i) - m(x_i, y_i) \quad (61)$$

and

$$Y^*(x_0, y_0) = \sum_{i=1}^n \lambda_i Y(x_i, y_i). \quad (62)$$

The coefficients  $\lambda_i$  are calculated by minimizing the expected error variance of the estimate  $Y^*$ :

$$e^2 = E\{[Y^*(x_0, y_0)]^2\} - 2E\{Y^*(x_0, y_0)Y(x_0, y_0)\} + E\{[Y(x_0, y_0)]^2\}, \quad (63)$$

or, after substituting the estimate of  $Y^*$  from (62):

$$e^2 = \sum_{i=1}^n \sum_{j=1}^n \lambda_i \lambda_j E\{Y(x_i, y_i)Y(x_j, y_j)\} + 2 \sum_{i=1}^n \lambda_i E\{Y(x_i, y_i)Y(x_0, y_0)\} + C(0). \quad (64)$$

The covariance in the equation is defined as  $C(h)$ :

$$C(h) = \frac{1}{m} \sum_{i=1}^m [Y(x_i + h)] [Y(x_i)] . \quad (65)$$

Having previous information about the spatially distributed points, we calculate the covariance and the only remaining unknowns in Equation (64) are  $\lambda_i$ . We need to minimize the variance error to optimize the sensor placement; therefore, we derive the error by the weights and solve for when this derivative equals 0:

$$\frac{\partial e^2}{\partial \lambda_i} = 2 \sum_{j=1}^n \lambda_j C(x_i - x_j) - 2C(x_i - x_0) = 0 . \quad (66)$$

Therefore, the final equation is

$$\sum_{j=1}^n \lambda_j C(x_i - x_j) = C(x_i - x_0) . \quad (67)$$

There are different types of Kriging interpolators. The simple interpolator assumes a constant value of the expectation in all points. The ordinary Kriging method does not assume a constant expectation, but the statistical properties are function of the distance between the measured and the estimated points. It is the most commonly used method due to the accuracy of its estimate.

In this ordinary Kriging methodology, we need to impose another restriction on the weights in order to calculate them. Specifically, the sum of all the coefficients of the weights must be unitary.

Therefore, the system of equations to calculate the weights is defined as

$$\left\{ \begin{array}{l} \sum_{j=1}^n \lambda_j C(x_i - x_j) = C(x_i - x_0) \\ \sum_{j=1}^n \lambda_j = 1 \end{array} \right. \quad \text{for } i = 1, 2, 3, \dots, n \quad (68)$$

The outputs of this interpolation are the value of the function at the non-visited points and an estimation of the error variance, which is a way to measure the accuracy of the Kriging fitting. Since we do not have information regarding the distribution of the variance in space, this estimation of the error in variance is computed using a semi-variogram, which is a suitable model based in the distance between visited and non-visited points. Normally, a spherical function is used to express the semi-variogram in a 2D space:

$$C(h) = \left\{ \begin{array}{ll} c_0 \left( \frac{3}{2} \frac{h}{a_0} - \frac{1}{2} \left( \frac{h}{a_0} \right)^3 \right) & \text{for } h \leq a_0 \\ c_0 & \text{for } h > a_0 \end{array} \right. , \quad (69)$$

where  $h$  is the distance between the estimated point and the measured point in two-dimensional space and the coefficients  $a_0$  and  $c_0$  are 30 and 300, respectively, and they are chosen arbitrarily based on “trial and error” fitting.

In order to get the final location of interest we need to couple the Kriging interpolation method with an optimizer. In this case, a Genetic Algorithm optimizer is chosen due to its flexibility and robustness when programming any kind of spatial distribution data. The objective function is to minimize the sum of squares of the difference between the temperature value calculated by the Kriging interpolation and the temperature value obtained by COMSOL over all the points measured.

$$S(T) = \sum_{i=1}^p \sqrt{(T_i - Y_i)^2} . \quad (70)$$

Where  $S(T)$  is the objective function that we need to minimize,  $p$  is the total number of points that we have in the measurement surface and it varies with the surface discretization.  $T_i$  and  $Y_i$  are the calculated temperature by the Kriging interpolation in each point and the measurement temperature, respectively.

The optimizer was run for 100 generations with 50 specimens per generation with good convergence ratios for all the cases analyzed.

To estimate the optimal location of the points inside the microchip, we need to know the temperature map at different times and the number of sensors to be placed. The temperature map is the output of the inverse method and the number of sensors is an input from the design parameters. In this case, we have performed the GA optimization with 6 and 8 sensors inside of the chip. Figure 4-29 represents the temperature map at two different time steps. These temperature distributions have been included in the optimization using Kriging interpolation. The objective function of the optimization consists of the sum of the squares of the difference between the real distribution and the interpolated surface at each location.

In order to perform the optimization, we use the same heat flux that we imposed for the inverse heat transfer method. All the heaters are on, in a sinusoidal manner for 3 seconds and the boundary conditions shown in Figure 4-3. In the minimization we take two random timesteps and we apply the objective function detailed in Equation (70).

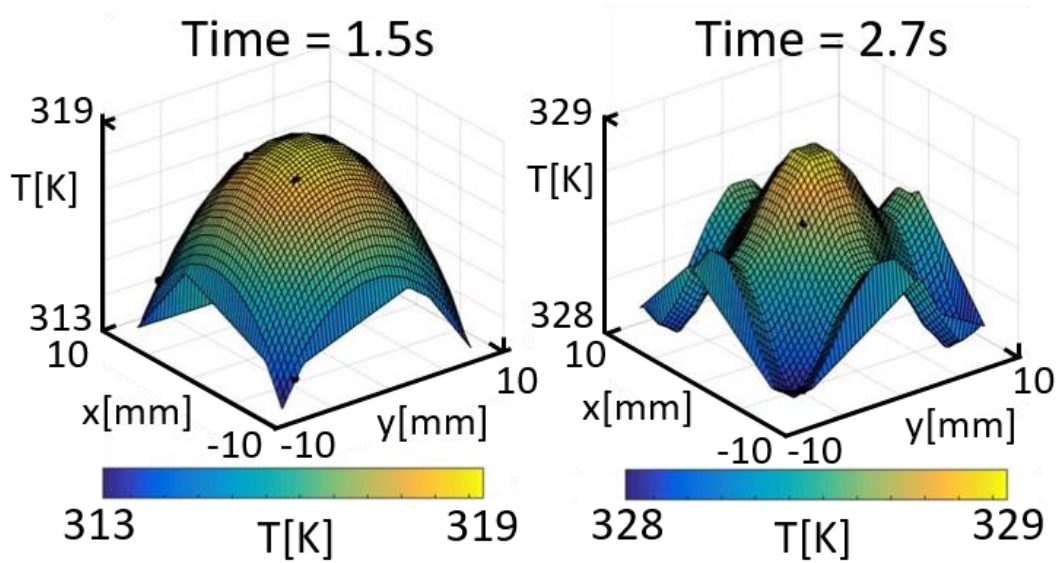


Figure 4-29. Temperature maps in the plane where the temperature sensors should be located at  $t=1.5s$  and  $t=2.7s$ .

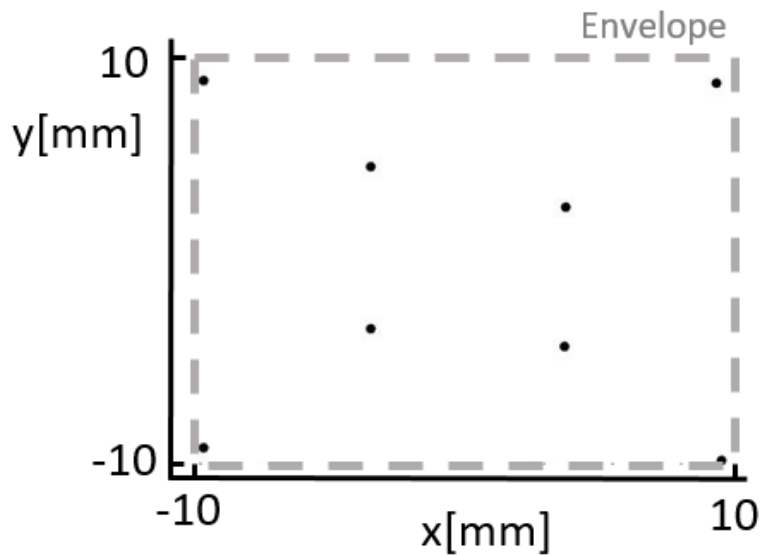


Figure 4-30. Location of the optimal points inside of the microchip envelope for the case run with 8 sensors.

Figure 4-30 shows the optimal location of the points after running the optimization with 100 individuals during 50 generations. The optimization parameters were the  $x$  and  $y$  positions of the points inside the spatial envelope of the chip. Due to the shape of the temperature profile (the



lowest temperature is located in the corners of the chip and the higher temperature is located in the center), the optimization algorithm locates one sensor in each corner and the other four sensors are placed in the center.

The Kriging interpolation is performed with the data of the optimal points and the solution surface is depicted in Figure 4-31. The goodness-of-fit of this surface to the input surface is lower than 70% for 6 optimal sensor locations, and higher than 80% for the two time steps evaluated when using 8 optimal sensor locations.

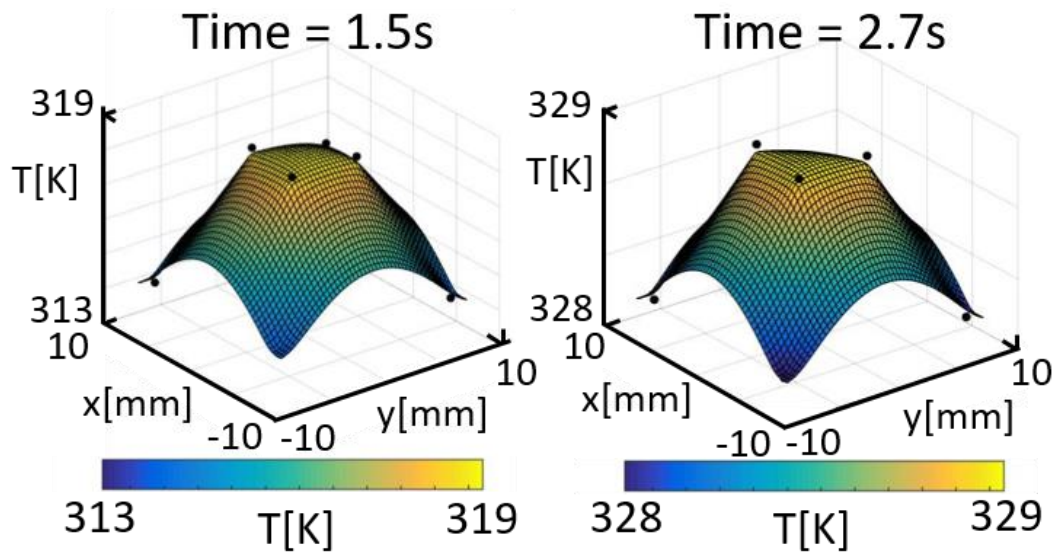


Figure 4-31. Kriging interpolation results for the temperature maps using the optimal location for the sensors.

This interpolation could be done using other models, such as a polynomial model, but the parameters will vary depending on the time the measurement is taken, which adds complexity to the meta-model used to recalculate the temperature map.

Finally, this methodology has been coupled with the inverse methodology following the strategy depicted in Figure 4-32.

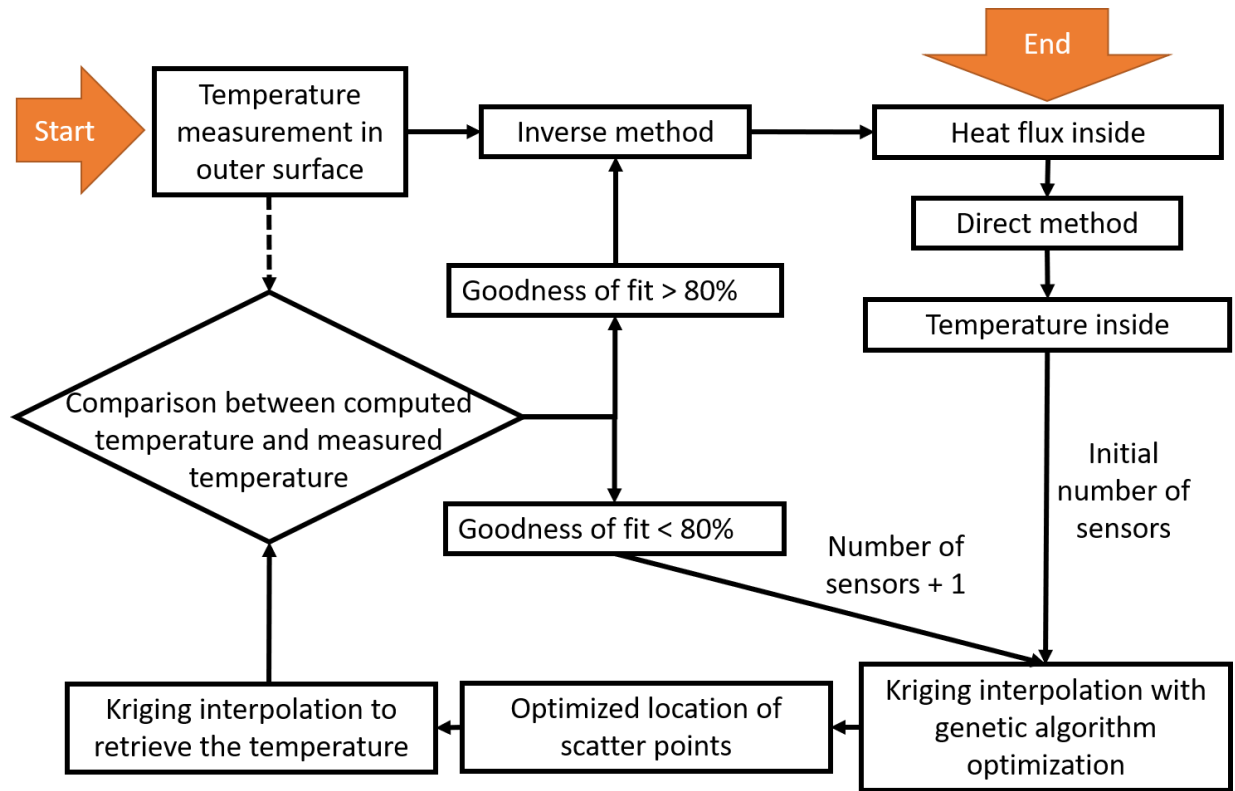


Figure 4-32. Number and location sensor optimization strategy coupled with an inverse method assessment.

Starting from the measured temperature and a model of the test article, we compute the inverse method. In this case, we have programed the Digital Filter Method due to its computational efficiency. Once the heat flux is obtained we can compute the temperature inside of the chip. Providing an initial number of sensors and a goodness of fit, we run the kriging interpolation optimization to optimize the location of the sensors inside of the chip. A temperature map can be derived from the scatter sensors that have been placed in the optimized locations and it is compared with the input infrared temperature map. From this comparison, we get the goodness of fit between the interpolated data and the measured data. If the goodness of fit is lower than certain assigned threshold the procedure add another sensor and recompute the location optimization. Once the

goodness of fit is larger than the threshold, we compute the heat flux again using the inverse methodology with the interpolated temperature map as an input.

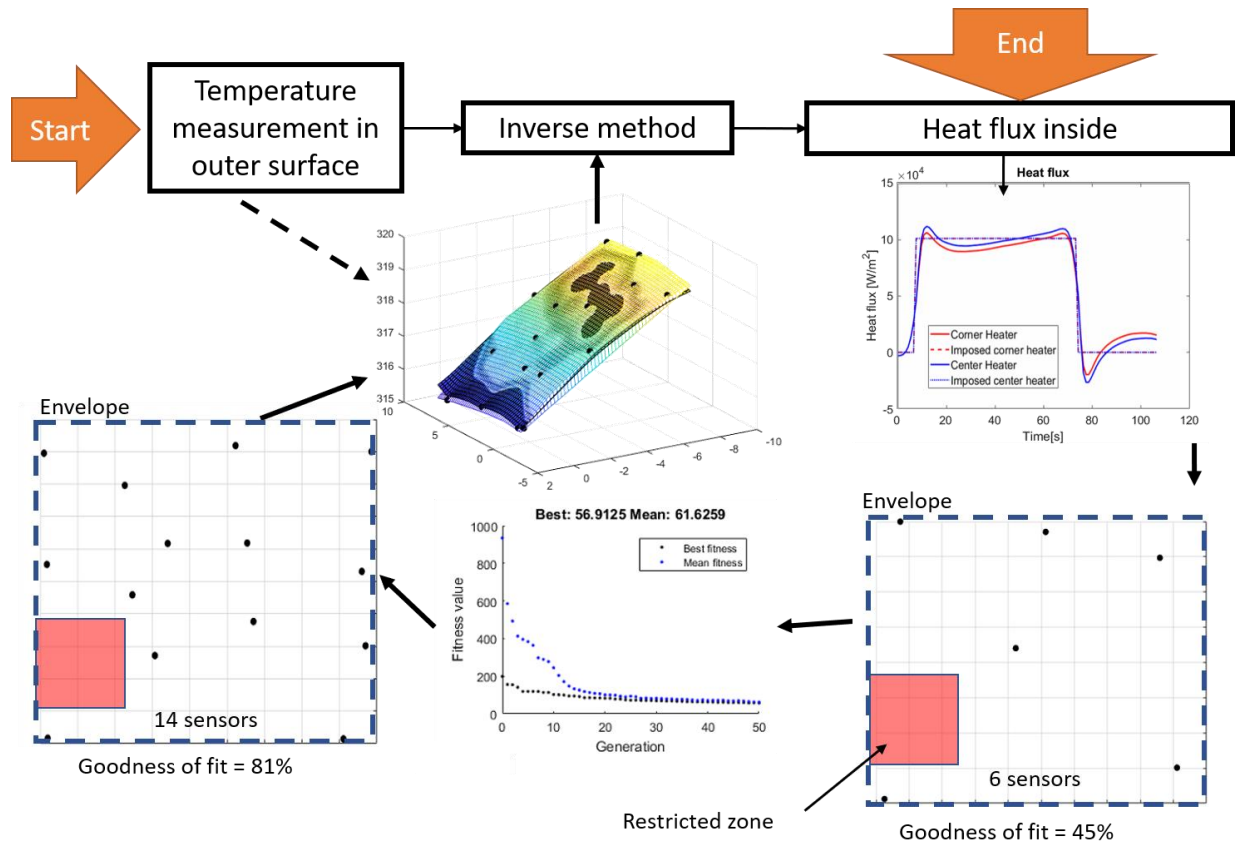


Figure 4-33. Example of the scatter sensor optimization technique using the experimental data from the Experiment 1.

Figure 4-33 shows an example of the complete method using experimental data. The initial number of sensors was 6 and the optimization with a prescribed goodness of fit of 80% gave a solution with 14 sensors scattered in the whole chip. Also an additional feature was implemented in which we add regions in which no sensor can be placed. This is done by increasing the penalty of the sensors located in that region in the minimization of the objective function.

#### 4.5 Conclusions

In this chapter, the inverse methods have been applied to a microscale problem, which is challenging given the limited thermal gradients observed in this application. The microscale field that has been targeted is the microelectronics application.

From the assessment performed in this chapter for this particular application, we can extract the following conclusions:

- The two developed methodologies (Conjugate Gradient Method and Digital Filter Method) have been assessed for this application. A numerical investigation followed by an experimental validation was conducted in order to bring light to the challenges faced in microscale applications. Additionally, the computation was performed using two different difference volume solvers, COMSOL Multiphysics and ANSYS Fluent, which evaluated the methodologies in pure conduction heat transfer and conjugate heat transfer, respectively.
- At the microscale, the spatial temperature gradients are small and, therefore, all of the methods based on the computation of gradients, such as all deterministic optimization methods, fail in the computation of the spatial location of the heat sources.
- The Conjugate Gradient Method is a gradient based methodology and, therefore, has problems predicting sudden changes of heat flux in space and time. The methodology was assessed numerically providing good agreement for simple and smooth changes of heat flux in time, failing to capture the spatial gradients due to the small spatial gradients. The experimental validation confirmed the difficulties of this method to perform track spatial gradients, leading to disagreements in the magnitude of the computed heat flux as well.
- The Digital Filter Method is recommended for this application, not only for its flexibility, but also for the accuracy of the results and the computational efficiency. The methodology

was assessed numerically and validated experimentally and was able to predict the magnitude, the location, and the temporal behavior of the imposed heat flux. Also, a comparison between the improved DFM and the basic DFM was performed, observing how the non-linear non-iterative methodology improves the prediction considerably.

- The methodology, if optimized to increase the computational efficiency, can be applied in real time and this makes it suitable for active thermal management of microelectronics.
- The number and location of the sensors inside of the microchip can be optimized using inverse methods. For this application of the inverse method, a Genetic Algorithm optimization combined with a Kriging interpolation method was developed. In this methodology, by controlling the goodness of fit of the interpolated temperature, the location of the sensors is optimized as a function of the number of sensors, which is directly dependent on the required goodness of fit.

## CHAPTER 5.     DIGITAL FILTER INVERSE METHOD APPLIED TO GAS TURBINE CASING<sup>2</sup>

The tip region of the turbine blade is responsible for more than 1/3 of the losses occurring in a turbine stage [140]. At the same time, the characteristics and flow topology of this part of the turbine strongly influences the convective heat transfer to the casing. Hence, the blade tip region is key in order to optimize the turbine performance as well as enhance its durability from the thermal perspective. For these reasons, an important part of past turbine research has focused on the optimization of the blade tip region aerothermodynamics [141]-[147].

The presence of a blade and the inclusion of cooling paths through this region, make the insertion of sensors in the rotor turbine casing a challenging task. In laboratory conditions, thin films, pressure taps, and capacitance probes [148][149] have been inserted in the casing to perform measurements of heat transfer, pressure, and clearance. However, at engine-like conditions these measurements are practically impossible. This makes turbomachinery researchers look for new options on how to characterize the turbine casing region, especially the overtip area. In this frame,

---

<sup>2</sup> This chapter is partly based on:

D. G. Cuadrado, F. Lozano, V. Andreoli, G. Paniagua, 2019. "Engine-scalable Rotor Casing Convective Heat Flux Evaluation Using Inverse Heat Transfer Methods", *Journal of Engineering for Gas Turbines and Power*, 141(1), p. 011012. [170]

Paniagua, G., Cuadrado, D., Saavedra, J., Andreoli, V., Meyer, T., Solano, J.P., Herrero, R., Meyer, S. and Lawrence, D., 2019. "Design of the Purdue Experimental Turbine Aerothermal Laboratory for Optical and Surface Aerothermal Measurements." *Journal of Engineering for Gas Turbines and Power*, 141(1), p.012601. [171]

V. Andreoli, D. G. Cuadrado, G. Paniagua, "Prediction of the Turbine Tip Convective Heat Flux Using Discrete Green Functions." *ASME. J. Heat Transfer*. 2018;(), doi:10.1115/1.4039182. [172]

D. G. Cuadrado, J. Saavedra, V. Andreoli, G. Paniagua, "Experimental Calibration of a High Speed Blowdown Tunnel". 2017 ISABE conference No 2017-22636. [173]

inverse heat transfer methodologies are indispensable since they allow the characterization of the heat transfer phenomena occurring inside the turbine based only on temperature measurements on the outer casing.

Inverse methods have been previously used in turbomachinery for design purposes [150]-[152]. In this case, we have focused the inverse method in the solution of the heat conduction equation through the casing. Therefore, in the proposed methodology, temperature measurements in the outer casing are the input parameters of the methodology in order to retrieve the heat flux in the inner turbine casing. This represents a non-intrusive technique for the retrieval of the heat transfer phenomena in the turbine casing. This avoids the intrusion of any measurement device that might modify the flow physics of the casing area, especially at the reduced tip clearance.

In the present work, inverse heat transfer methodologies have been applied in order to retrieve inner casing heat flux for various thicknesses using a Digital Filter Method [88][89]. This method uses the Duhamel's Theorem [6][153] to retrieve the response of the system to pulses in heat flux. It is a similar approach to the one used in the Green Functions convective heat transfer approach [154]-[159]. In the case of the Duhamel's Theorem, we observe the response of the solid while the Green Functions approach evaluate the fluid response.

## 5.1 Numerical Evaluation

In this application, providing the temperature map of one surface and a model with the geometrical and thermal properties, we compute the boundary conditions which is our unknown parameter. Therefore, measuring the temperature in the outer surface of the turbine casing we could retrieve the inner heat flux evacuated through the casing.

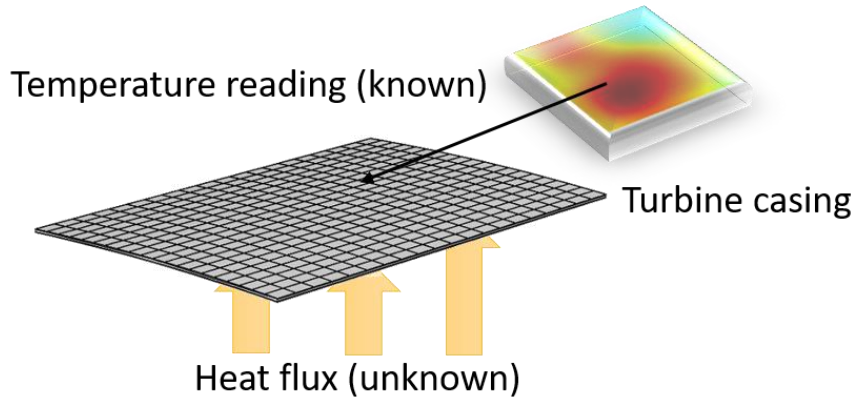


Figure 5-1. Schematic of the inverse heat transfer procedure applied to the turbine casing.

Equation (71) contains the solution of the heat flux with the spatial and temporal terms already included in the matrix.

$$\hat{q} = [X^T \psi X + \alpha_t H_t^T H_t + \alpha_s H_s^T H_s]^{-1} X^T Y, \quad (71)$$

In order to solve Equation (71), there are several methods that can be used, and all of them imply the use of a preconditioning technique of the sensitivity matrix of coefficients. Matlab functions already implemented such as *gmres*, *pinv* and *pcg* can be used to solve the ill-conditioned problem. For this case, and due to the extremely ill-condition of the matrix we have used the function *fmincon* of Matlab which is providing more accurate results without falling in large spatial and temporal variations of heat flux. To obtain more accurate results, it is recommendable to provide an initial iteration solution which has similar trends to the expected solution. This means that if you have a previous knowledge of where the blade is located, if it is specified at the beginning the results will improve with respect to the solution when no initial data is provided.

The methodology described in the previous section was applied in a numerical experiment performed in Numeca Turbo with conjugate heat transfer boundary conditions in the casing. The



solid domain was composed by a section of the outer wall and different thicknesses were tested. Figure 5-2 shows the computational domain with details of grid in the solid and the fluid regions. The mesh was generated using Numeca IGG/Autogrid5, maintaining the same grid characteristics used in [127]. In the previous work, a grid sensitivity study was performed to assess the correct characterization of the heat flux in the tip region of the same high-pressure turbine used for this work. Figure 5-2 shows the turbine stage, which is a scaled version of the geometry tested by Sieverding et al.[128]. In order to reduce the computational cost, only the steady Reynolds Averaged Navier-Stokes simulations are run with the complete stage.

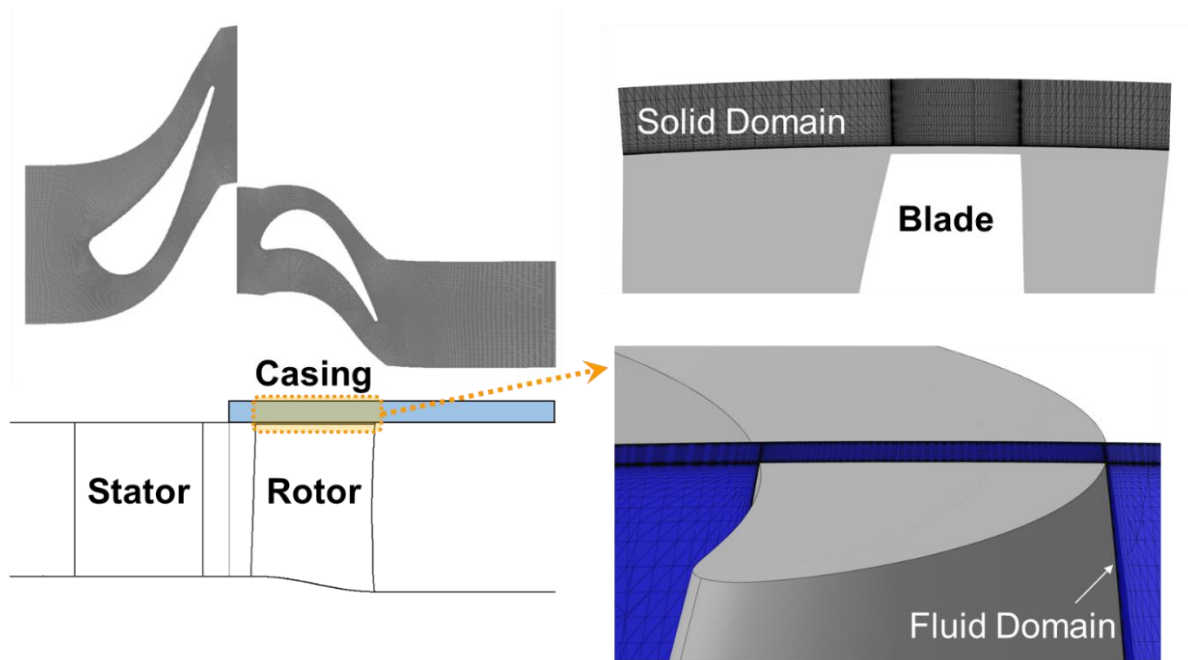


Figure 5-2: Computational domain with details of solid and fluid domain.

The pitchwise averaged quantities at the mixing plane between stator and rotor are extracted and imposed at the rotor inlet. The rotor only is then used for the full unsteady conjugate calculations. The first cell size was selected in order to guarantee a  $y^+$  lower than 1 everywhere. A ramp of total pressure was imposed at the rotor inlet in order to reproduce a time-variant increase of heat flux

on the internal casing. The temperature profile, function of radial location and time, is initialized with the profile extracted from the steady CFD and then increased uniformly of the 10% in an interval of 0.5s. After this ramp, the inlet total temperature achieves the 110% of the initial value and is kept constant until a steady state is achieved.

Figure 5-3 shows the boundary conditions used in the RANS simulations. At the rotor inlet, total pressure and temperature are imposed together with the velocity direction. The static pressure is imposed at the rotor outlet, applying the principle of radial equilibrium. The interface between fluid and solid domain allows the solution of the fully conjugate problem. On all the other solid walls, adiabatic boundary condition was imposed. On the side surfaces of the domain, periodic boundary conditions were imposed for both solid and fluid domains.

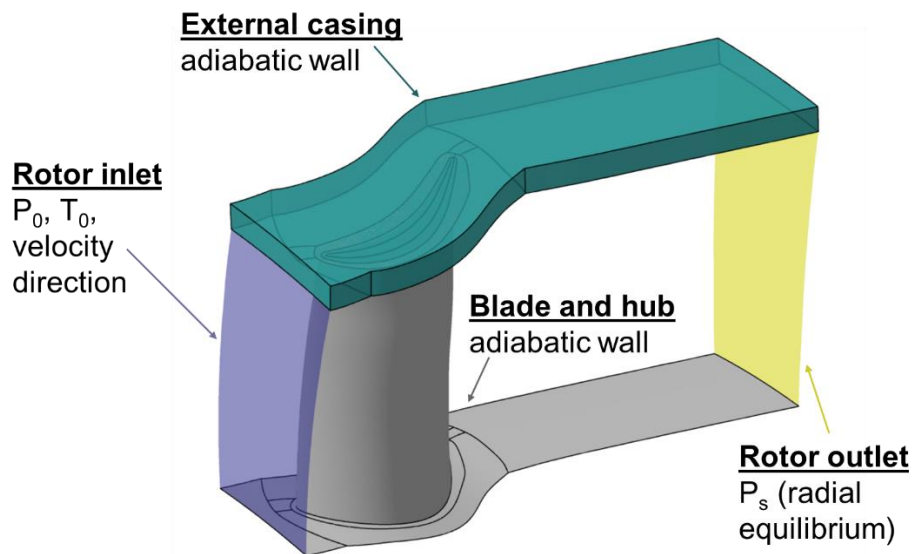


Figure 5-3. Numerical domain used in Numeca for the computation of the conjugate heat transfer in the casing of the turbine blade.

The output of the conjugate calculation is the input of the inverse methodology that has been programmed using COMSOL Multiphysics. The solid domain was reproduced in the same way that in the Numeca model and a direct calculation was performed to extract the temperature at the

outer side of the metallic block. The domain is discretized in squares (a grid of 20x20 in the outer wall of the casing and 15x15 in the inner wall) in order to retrieve the area-averaged value of the different discretized areas. The area evaluated is composed by the upper region of the turbine tip with a 25% of the axial chord upstream of the blade and 50% of the axial chord on the downstream part. The main purpose of the division of the surface in squares (or pixels) is the practical implementation using infrared thermography. Therefore, each one of the squares would be a pixel of the infrared camera and they would be the input data for the inverse methodology in order to retrieve the heat losses through the casing. This technique is not only restricted to the use of infrared thermography, but also any other temperature measurement technique can be used.

Figure 5-4 shows the heat trace of the blade in the relative frame during a transient operation where the mass flow through the turbine was increased. After running the numerical experiment the temperature of the outer part is represented in the Figure 5-5 for the case of 500 $\mu$ m casing thickness. This temperature distribution is the input of the inverse methodology.

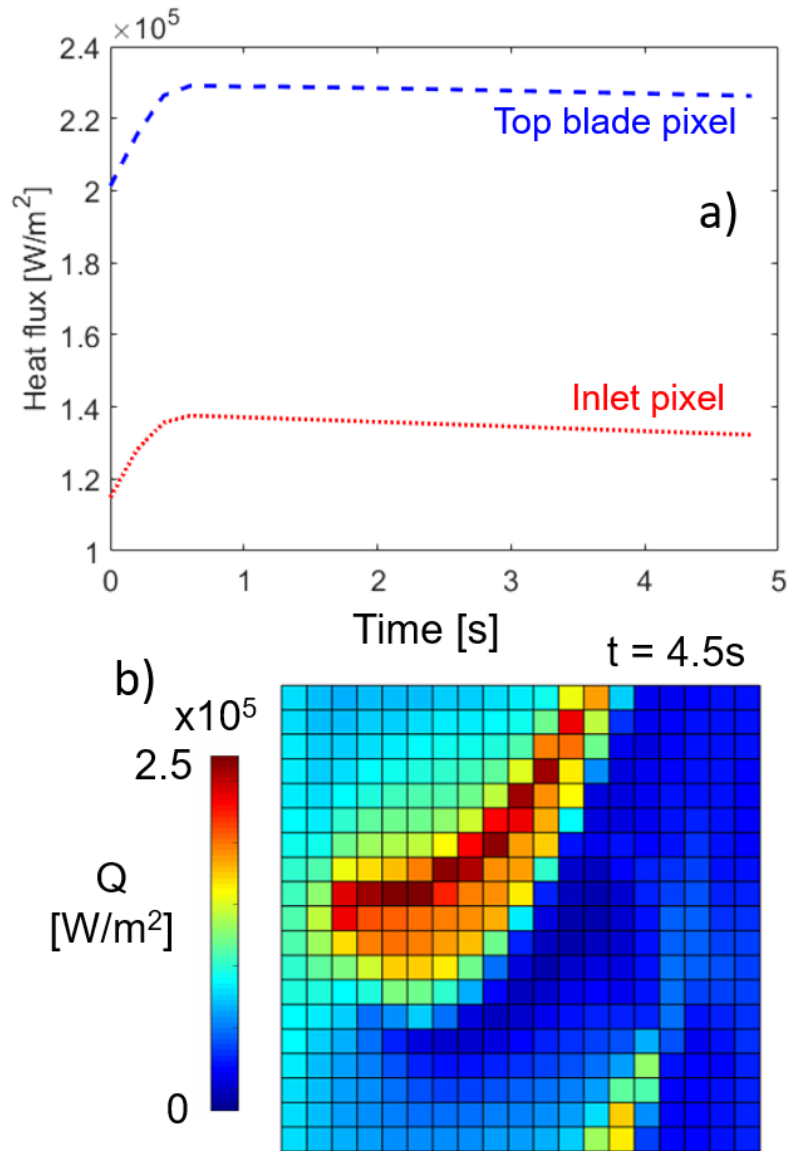


Figure 5-4. a) Transient evolution of the heat flux applied in the conjugate heat transfer simulation in two different points of the domain. b) Spatial distribution of heat flux at  $t=4.5$ s in the overtip region in the conjugate heat transfer calculation.

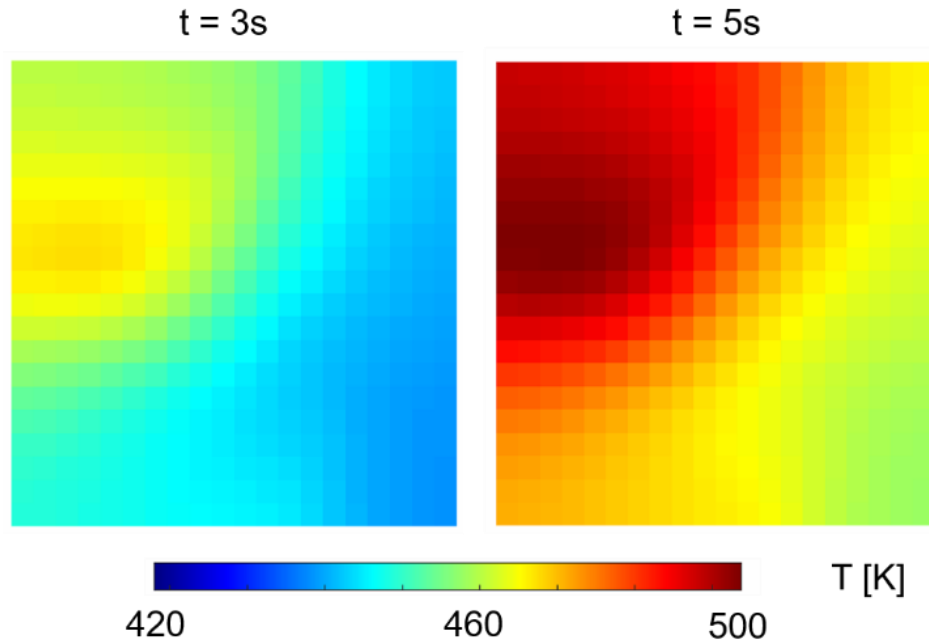


Figure 5-5. Temperature distribution in the outer wall of the casing at  $t=3s$  and  $t=5s$  for the baseline case of casing thickness (0.5mm) and tip clearance (1% of the blade span).

Three different thicknesses were evaluated:  $16\mu m$ ,  $500\mu m$  and 0.5cm. The temperature distribution at different thicknesses varies due to the diffusivity of the material, being more diffuse with larger thicknesses. However, the effect in the computation is not very large since the method uses a model of the plate or foil that already includes the thickness in the computation. The differences in retrieved heat flux between cases with different thicknesses is below 10%.

The results of the inverse calculation for the baseline case are shown in Figure 5-6. We can observe that the method is not able to predict accurately the value of heat flux along time since the sensitivity coefficient matrix is very ill-conditioned, but it predicts trends in the heat flux as well as provides a good estimate of the spatial distribution of heat flux. The over-prediction in the first timesteps is counteracted by an under-prediction of the heat flux in the last timesteps.

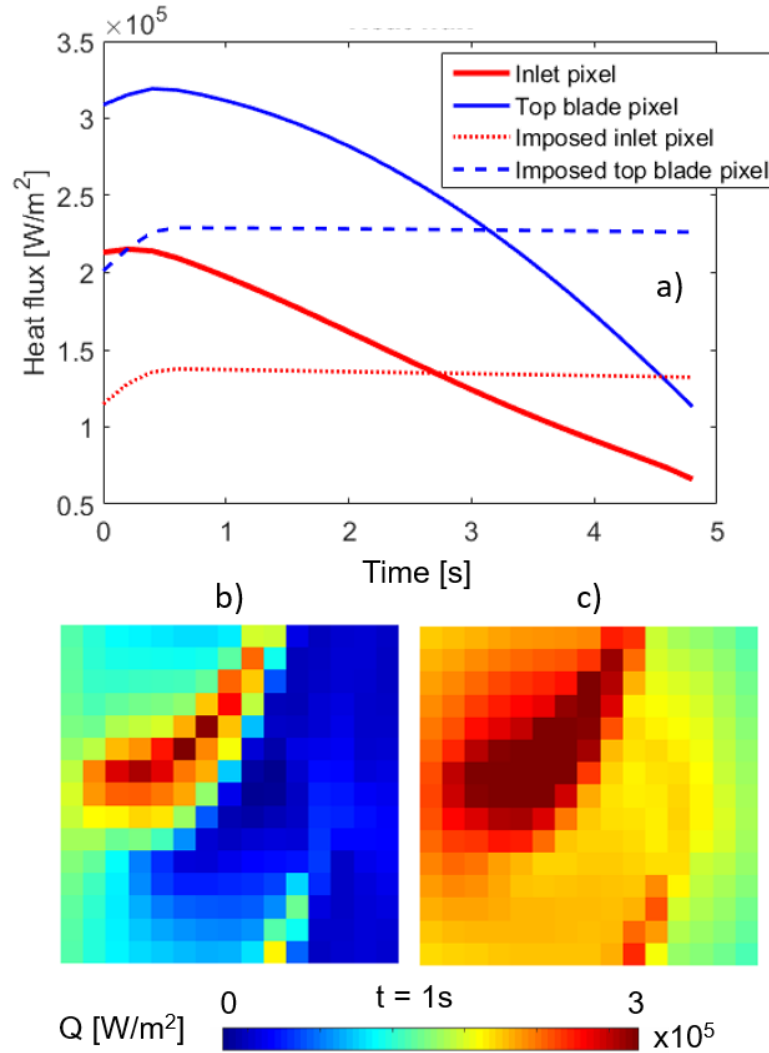


Figure 5-6. a) Comparison between the transient evolution of imposed heat flux and the retrieved heat flux. b) Spatial distribution of the imposed heat flux at  $t=1$ s in the simulation. c) Spatial distribution of the retrieved heat flux at  $t=1$ s in the simulation.

The same calculation was performed for different clearances. The trace of the blade in the casing varies considerably from one clearance to another due to the drastic changes of the aerodynamic phenomena in the tip flow. Figure 5-7 depicts the heat flux leaving the casing at two different clearances: 0.25%.and 0.55% of the blade span. If we compare the results with the case with a tip gap of 1% of the blade span, which is our baseline case for the calculations performed in this work, we observe that the heat transfer decreases when the tip gap reduces, and at the same time the hot

spots are moved from the top of the blade towards the leading edge of the blade. This may be counter intuitive since one may expect to have an increase in the heat losses through the casing in cases of tighter clearances. Instead, the adiabatic wall temperature is considerably increased due to the dominant role of the viscous forces in such cases and therefore the heat flux is reduced.

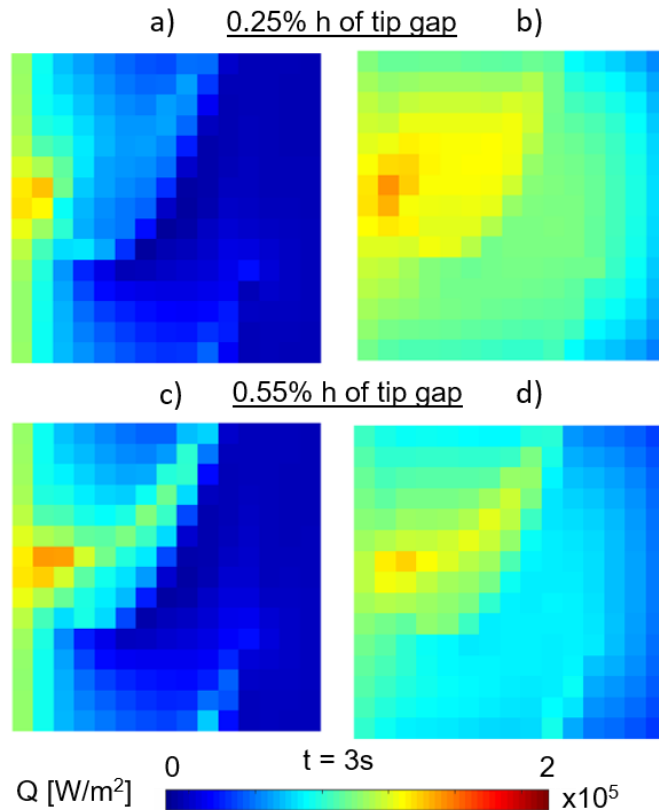


Figure 5-7. a) Imposed heat flux extracted from the conjugate heat transfer simulation with a clearance of 0.25% the blade span. b) Retrieved heat flux from the inverse method in the case of 0.25% of the blade span. c) Imposed heat flux extracted from the conjugate heat transfer simulation with a clearance of 0.55% the blade span. d) Retrieved heat flux from the inverse method in the case of 0.55% of the blade span.

The non-linear nature of the heat flux at different clearances, which depends not only on the upstream conditions of the flow but also in the geometrical shape of the turbine tip, makes impractical the implementation of the inverse heat transfer method to predict the tip clearance, but as described in the following section, it can be used to predict different parameters inside of the

turbine such as averaged upstream temperature or upstream pressure, since there is a clear relation between the heat flux in the casing and these quantities.

An uncertainty analysis of the developed inverse methodology was performed taking into account all the parameters that affect the calculation. They can be divided in geometrical and thermal properties. In the geometrical properties we took into account the thickness of the metallic window where we measure. The thermal properties of the material comprehend the thermal conductivity, the density and the thermal capacitance of the solid material. Also, the uncertainty in the measurement of the temperature has been taken into account. The approach used is based in a linearization of the uncertainty in which a mean value of each quantity has been taken and a variation equal to the uncertainty of each quantity has been added. As shown in Table 5-1, the main contributors in the total uncertainty are the temperature and the thickness. The total uncertainty of the method is below 4%.

Table 5-1. Uncertainty analysis for the turbine casing inverse heat transfer analysis

<b>Quantity</b>	<b>Mean Value</b>	<b>Absolute Uncertainty</b>	<b>Heat flux variation relative to mean (%)</b>	<b>Sensitivity</b>
<b>Temperature [K]</b>	500	0.5	3.18	31.7
<b>k [W/mK]</b>	130	10	-0.15	-0.02
<b><math>\rho</math> [kg/m<sup>3</sup>]</b>	2320	10	0.13	0.32
<b>Cp [J/kgK]</b>	703	7	0.3	0.3
<b>Thickness [mm]</b>	0.5	0.05	1.98	0.10
<b>TOTAL</b>			<b>3.8</b>	



All the previous calculations were performed under steady conditions of the rotor. This means that physically, the rotor will be located in an annular cascade and we are retrieving the heat flux in the relative frame of the rotor. In order to evaluate the effect in the absolute frame of reference the frequency retrieval was analytically and numerically evaluated.

#### 5.1.1 High Frequency Phenomena Retrieval

All the previous data was obtained in the relative reference frame, this means that it assesses the capability of the method to be used in an annular turbine cascade. However, in order to apply it to rotating machinery, we must evaluate the effect of the blade passing in the casing wall. In these environments, the heat flux is characterized by peaks occurring at the blade passing frequency. Due to high rotational speed, this results in high frequency fluctuations on the heat flux, as well as the temperatures induced in the casing.

##### 5.1.1.1 Numerical Analysis

The study has been done through an analytical solution [6], an in-house 1D conduction solver developed by Saavedra et al. [129] and the commercial finite element solver COMSOL. The object under consideration in this section is the conductive material layer that would be placed on the inner face of the facility's casing. Considering thermal properties and availability, two different materials have been studied, namely Al and Cu. In addition to frequency, another parameter that has been varied is the thickness of such layer. The values studied are:  $16\ \mu\text{m}$  (thin foil),  $100\ \mu\text{m}$ ,  $0.5\ \text{mm}$  and  $0.5\ \text{cm}$  (thick layer).

As mentioned before, when a fluctuating heat flux is applied on one of the boundaries of a slab, a fluctuating temperature field will be developed inside the solid. This is the principle applied herein.

By measuring those temperature fluctuations on the outer casing, the fluctuating heat flux on the inner casing can be retrieved.

The analytical solution considered herein [6] is based on a heat flux excitation as the one given in Equation (72). According to these authors, inside the solid, the fluctuations are damped as described in Equation (73). In this expression,  $x$  represents the distance penetrated in the material, with  $x = 0$  being the face where the fluctuating heat flux signal acts. For the present application, this represents the inner face of the casing (where it is intended to retrieve heat flux) and the opposite one the outer face of the casing (where temperature would be measured).

$$q(t) = \Delta q \cos(\omega t) \quad (72)$$

$$\frac{T - T_{t=0}}{(T - T_{t=0})_{x=0}} = \exp \left[ -x \left( \frac{\omega}{2\alpha} \right)^{1/2} \right] \quad (73)$$

From the expression above, it can be inferred that there are three parameters affecting the damping the temperature fluctuations suffer along the material's thickness:

- Thickness of the material ( $x$ ): higher thicknesses lead to higher damping.
- Frequency of the fluctuation ( $\omega = 2\pi f$ ): higher frequencies equally cause higher dissipation of the fluctuations along the thickness.
- Thermal diffusivity of the material ( $\alpha$ ): higher thermal diffusivities lead to lower damping of the fluctuations.

Therefore, in order to capture temperature fluctuations corresponding to high frequency inner heat flux fluctuations, as it will be shown, low thickness and high thermal diffusivity are required.

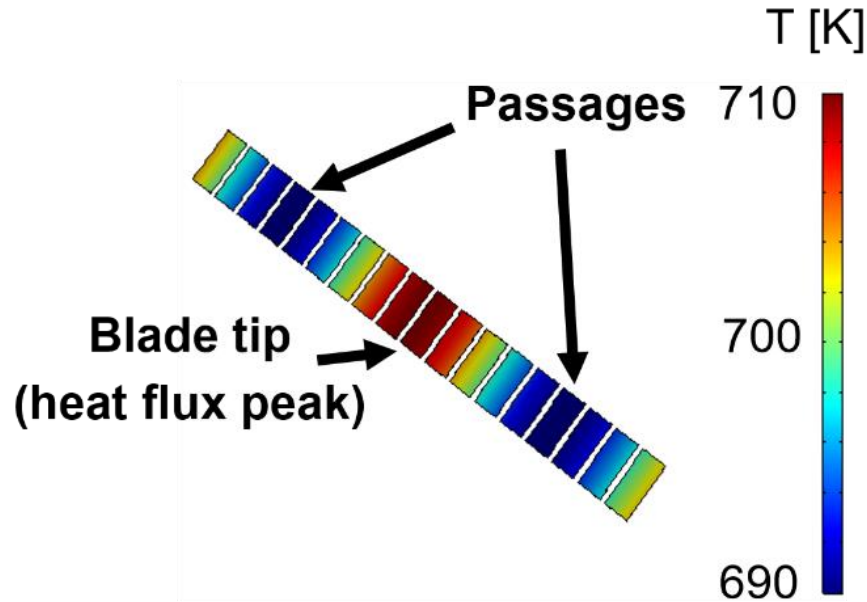


Figure 5-8. Numerical heat transfer simulation imposing fluctuations of heat flux in a thin layer of aluminum.

The effect of blade passing frequency and thickness on the damping of temperature fluctuations can be observed for Cu and Al in Figure 5-9. These data were computed with the finite elements solver COMSOL by imposing the corresponding heat flux signal on one of the faces and adiabatic boundary condition on the others. In both cases, the ratio of amplitudes of the temperature fluctuations for the outer to the inner face is given with respect to frequency of the imposed heat flux for different thicknesses.

For a thickness of  $16\ \mu\text{m}$ , a negligible damping occurs for both, Al and Cu. Only for a blade passing frequency of  $10\ \text{kHz}$  a damping slightly higher than 1 % appears.

However, as thickness is increased, higher damping appear, reducing the fluctuations amplitude at the outer part to approximately 40 % of those occurring on the inner face for a thickness of  $100\ \mu\text{m}$  and a blade passing frequency of  $10\ \text{kHz}$ . However, as thickness is increased, higher damping appears, reducing the fluctuations amplitude at the outer part to approximately 40 % of those

occurring on the inner face for a thickness of  $100\ \mu\text{m}$  and a blade passing frequency of  $10\ \text{kHz}$ . For Cu (solid lines), the damping suffered by the  $T$  fluctuations is slightly lower than for Al (dashed lines). Nevertheless, only approximately 40 % of the inner temperature signal can be retrieved on the outer face for  $10\ \text{kHz}$  of frequency.

For the thicker case depicted in Figure 5-9, the damping suffered by the temperature fluctuations are significantly increased. For a blade passing frequency of  $1\ \text{kHz}$ , the signal is damped over 80 % for both materials considered. Similarly, although the difference is minor, Al shows a higher damping of the fluctuations. For frequencies beyond  $2\ \text{kHz}$ , less than 10 % of the inner signal can be retrieved on the outer face of the material.

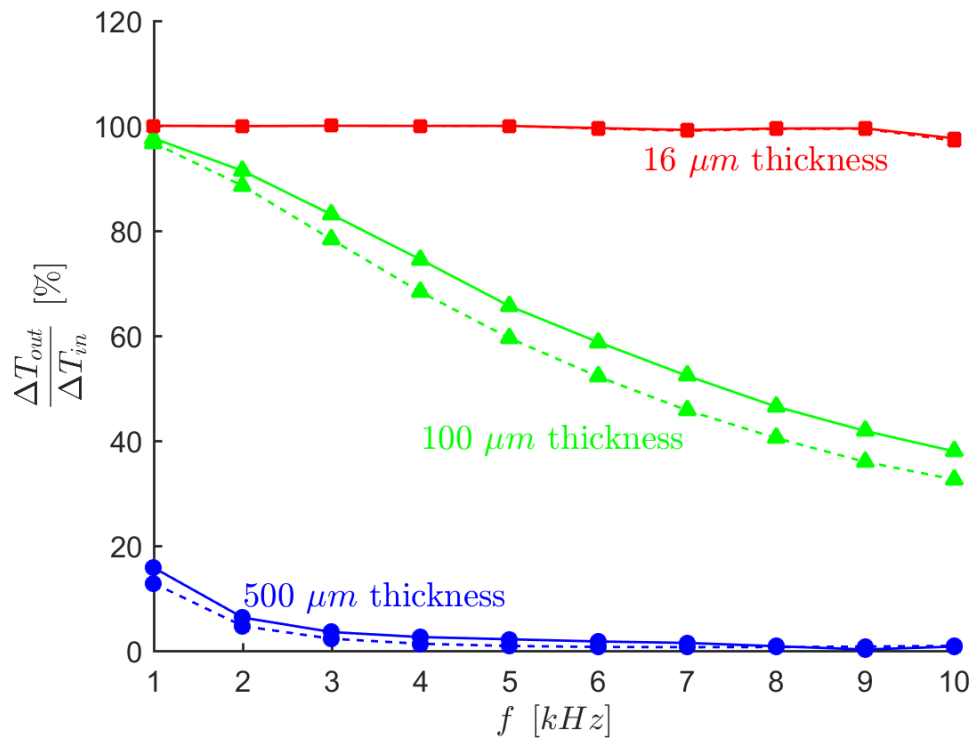


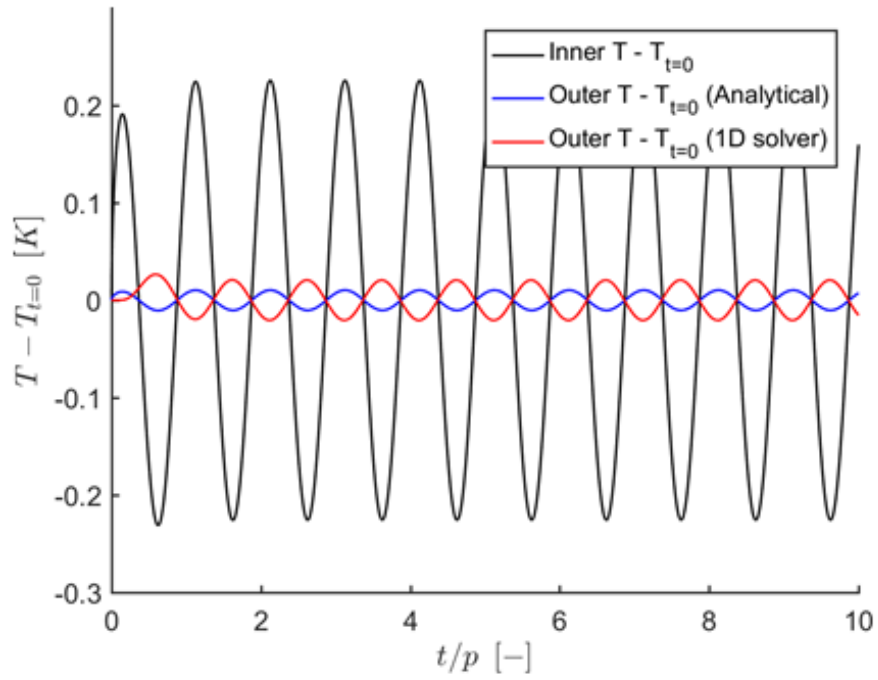
Figure 5-9: Temperature fluctuation damping through Aluminum (dashed lines) and Copper (solid lines) for different thicknesses and frequencies.

Data corresponding to a thick casing ( $0.5\ \text{cm}$ ) are not given in Figure 5-9. This is due to the fact that such a high thickness completely dissipates the fluctuations at the outer face for the

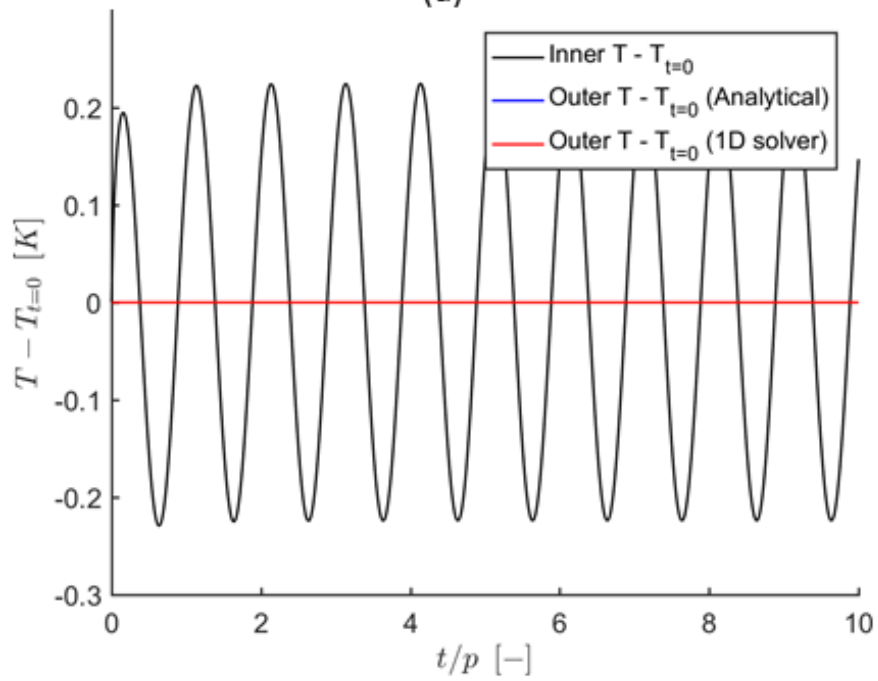
frequencies depicted in that graphic. This case is however analyzed in Figure 5-10(b). Figure 5-10 presents two graphs corresponding to the inner and outer temperature signals retrieved after applying a heat flux boundary condition as the one depicted in Equation (72) on the inner face. In both graphics differential temperature with respect to the initial one (room temperature) is represented against time non-dimensionalized with the period of the fluctuations ( $p$ ). The results shown in Figure 5-10 have been obtained with the analytical solution (blue lines) and the 1D conduction solver (red lines). For the calculation with the 1D solver, the same boundary conditions applied in COMSOL have been imposed.

Figure 5-10(a) shows the significant damping depicted in Figure 5-9 suffered by the temperature signal as it travels through the thickness of the material, Al in this case. Another important effect shown at Figure 5-10(a) is the phase lag added to the signal when travelling through the material. This accounts to approximately  $180^\circ$ , as shown by the data from the 1D solver. Such phase shift cannot be predicted by the analytical solution. This phase lag just described increases with thickness of the casing. However, its full evolution has not been shown for the sake of simplicity. Figure 5-10(b) shows the analogous data to that of Figure 5-10(a), corresponding this time to the thickest casing considered ( $0.5\text{ cm}$ ). In this case, it acts as a semi-infinite solid. As a consequence, the temperature fluctuations appearing at the face when oscillatory heat flux is imposed are completely damped through the material.

The results obtained for Cu are similar to those depicted for Al in Figure 5-10. For the  $0.5\text{ mm}$  thickness case (Figure 5-10(a)), has a lower damping as it can be inferred from Figure 5-9 and it also presents a phase lag between the temperature signals of the two faces of the material. Similarly, for the  $0.5\text{ cm}$  case, Cu also behaves as a semi-infinite solid, damping all temperature fluctuations through the thickness.



(a)



(b)

Figure 5-10. Inner and outer  $T$  vs time signals for a frequency of 1 kHz (a) Al, 500  $\mu\text{m}$  thickness and (b) Al 0.5 cm thickness

#### 5.1.1.2 Practical Implementation

Regarding the feasibility of experimentally implementing inverse methodologies to retrieve rotor overtip casing heat flux, other aspects have been considered: material choice and operational limits of different configurations.

The material choice has been guided by the ability to retrieve the high frequency phenomena previously studied. In order to do that, the damping suffered by the fluctuations through the thickness of the material needs to be minimized. For that, high thermal diffusivity is required. This was, together with their availability, the main reason for choosing Al and Cu for the present study. They have thermal diffusivities of  $8.27 \times 10^{-5} \text{ m}^2/\text{s}$  and  $1.058 \times 10^{-4} \text{ m}^2/\text{s}$ , respectively.

From these two materials studied, Cu has shown a superior performance capturing high frequency phenomena. This is assessed in terms of the lower damping suffered by fluctuating temperature signal through the thickness of this material (see Figure 5-9). Therefore, this would be the preferred material. In addition to that, the study presents that a thickness as small as possible is desired in order to capture phenomena occurring at frequencies as high as possible. Hence, from the cases studied, the lowest thickness ( $16 \mu\text{m}$ ) is the preferred one.

In addition to this, the time limits the different test objects studied could withstand in the high temperature environment of the turbine have been analyzed. This has been done through numerical simulations also with the commercial finite elements solver COMSOL. Convective heat flux data obtained from CFD simulations at engine-like conditions with isothermal walls has been imposed as boundary conditions of plates of the materials and thicknesses considered. Then, with this heat flux applied, the material life time has been evaluated. For Al, these times range from 0.1 to 26 seconds for the thinnest and thickest cases, respectively. For Cu, these times range from 0.3 to 53 seconds.

### 5.1.2 Prediction of the Upstream Conditions Based on IHTM

Inverse methods were conceived to predict unknown parameters or quantities in form of a number or a function based on the solution of the problem. Starting from this statement we evaluated the possibility to predict the variation of the averaged total quantities upstream of the rotor blade, considering constant the other geometrical and thermal properties of the system. In the studied case we have evaluated variations in the total pressure upstream of the rotor blade. An analysis of how the heat flux through the casing varies at different levels of pressure has been made. Pressures of 80%, 90%, 110%, and 120% of the total design point pressure were assessed. Figure 5-11 represents the increase of heat flux observed when we increase the pressure upstream of the blade. This linear relation can be captured with the inverse methodology and then using the outer temperature measurements we can calibrate the model to predict the pressure in the test section. Using the same data in steady state represented in Figure 5-11 we predict a similar linear behavior using the temperature measurements and the inverse procedure.



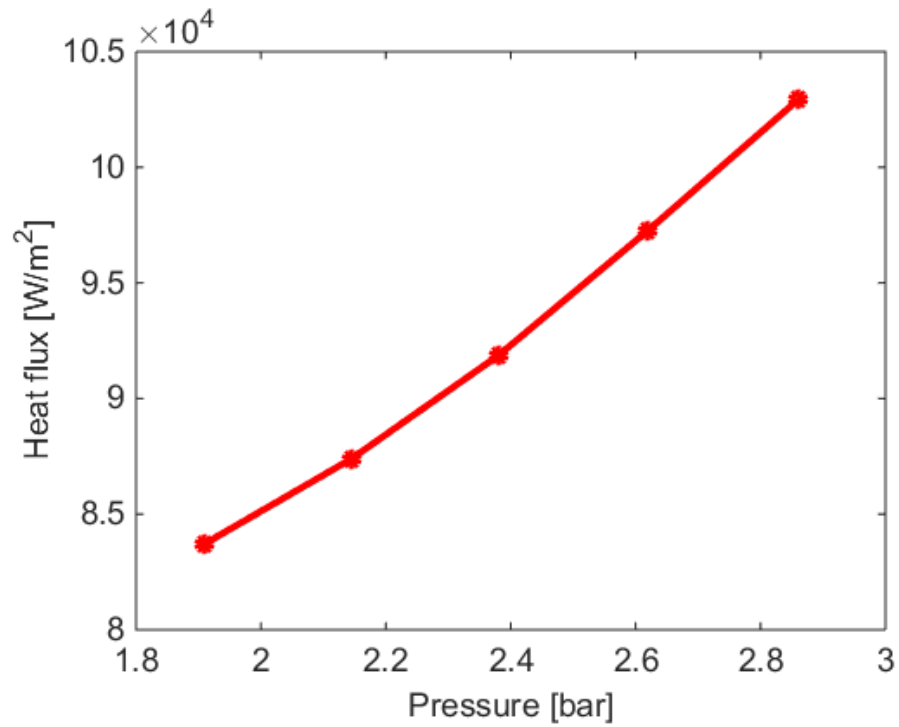


Figure 5-11. Averaged heat flux evolution at different upstream pressure conditions.

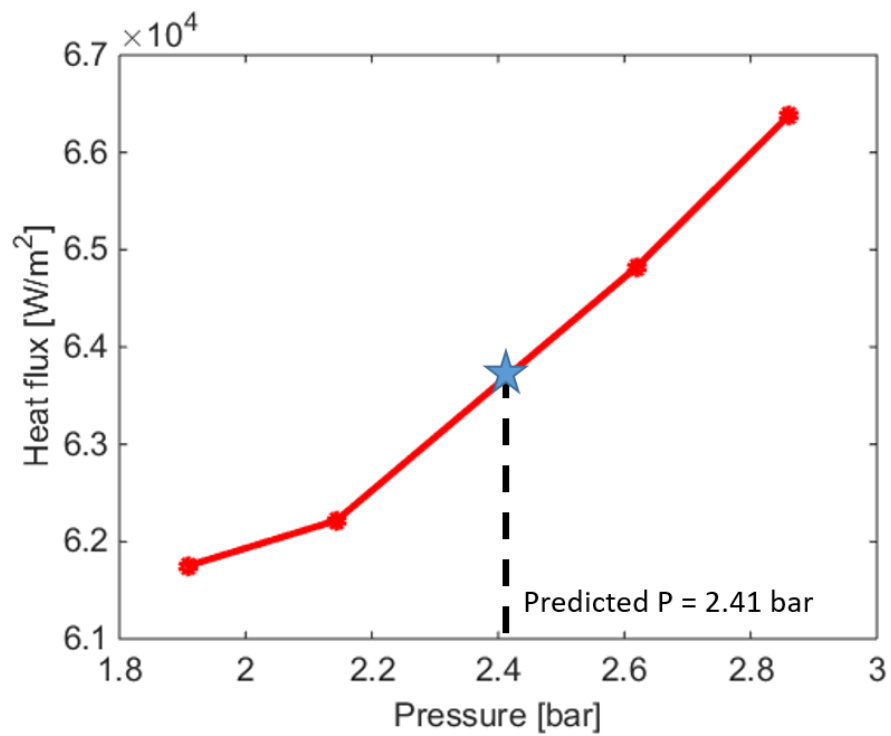


Figure 5-12. Pressure prediction based on the inverse heat transfer procedure.

We could predict the baseline pressure with the data from the other data points, as shown in the Figure 5-12. Even though the values are not exactly the same, since the inverse method cannot accurately predict the values of the heat flux in transient evolution, the trends are representative and they can be used to establish a relation with the total quantities.

In order to get the predicted pressure, we have computed the heat flux using the inverse method for the baseline case. Only the last time steps were taken in order to perform the calculation since in the first timesteps there is more disagreement between the input and the computed data. This is one of the reasons why the values of the heat flux are smaller than in the Figure 5-11. The predicted value of the pressure using this technique is 2.41 bar when the simulation was run at 2.38 bar. We can conclude that we can estimate the pressure with an accuracy higher than the 2% using a linear approximation.

This methodology can be extended to the estimation of other quantities such as total temperature with a previous calibration of the relationship between heat flux and predicted quantity.

## 5.2 Experimental Evaluation of the IHTM in Turbine Casing

The experimental implementation of this technique would consist of placing a layer of a conductive material on the inner face of one of the optical access windows of the facility. For this a new wind tunnel with optical access for turbine research was designed. The characteristics of this unique wind tunnel are detailed below.

### 5.2.1 Blowdown Wind Tunnel Design

The facility was conceived to operate in a wide range of Re and Mach numbers. The control of the Re number is related to the operational limits of pressure and temperature. The test section inlet pressure ranges from 0.5 to 6 bar, while the temperature can vary between 270K and 700K.

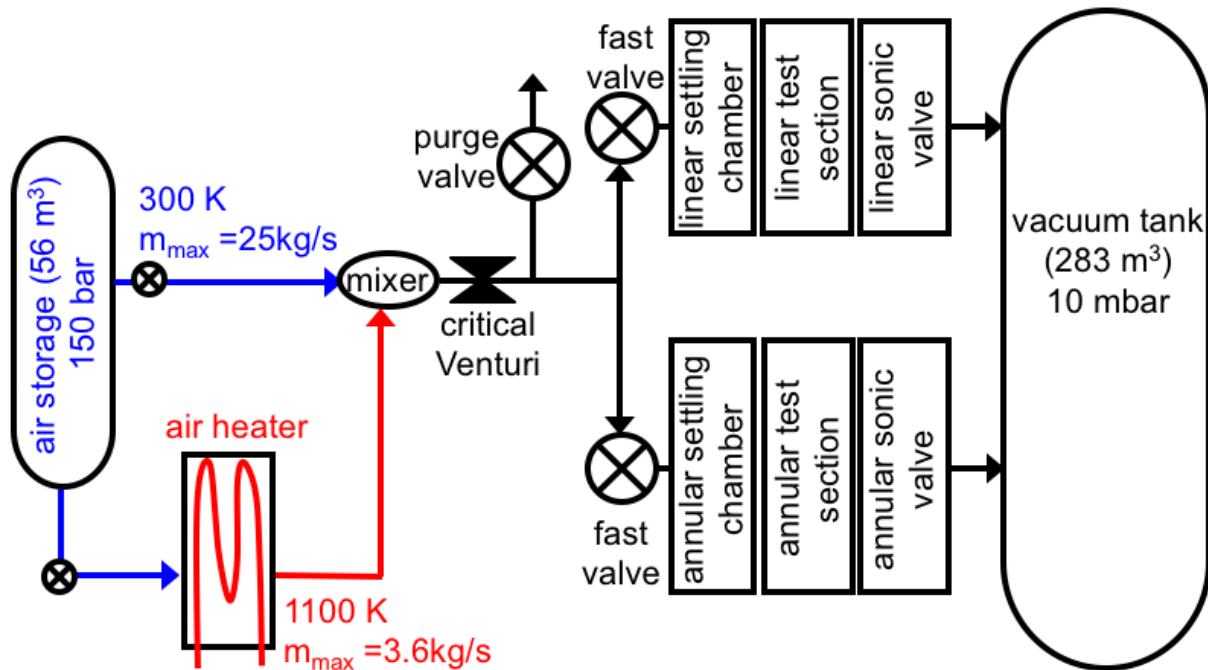


Figure 5-13. Schematic of the layout of the Purdue Experimental Turbine Aerothermal Laboratory.

Figure 5-13 sketches the wind tunnel facility, with the high pressure air storage providing pressurized dry ambient temperature air at 150 bar.

Initially, all valves are closed. We begin the test diverting warm flow to the mixer, which combines the cold with the hot stream. Along the cold and hot pipes, control valves are used to regulate the pressure level and mass flow into the mixer, which serves to adjust the flow temperature. While the temperature is being adjusted, the massflow is purged to the atmosphere through the purge valve.

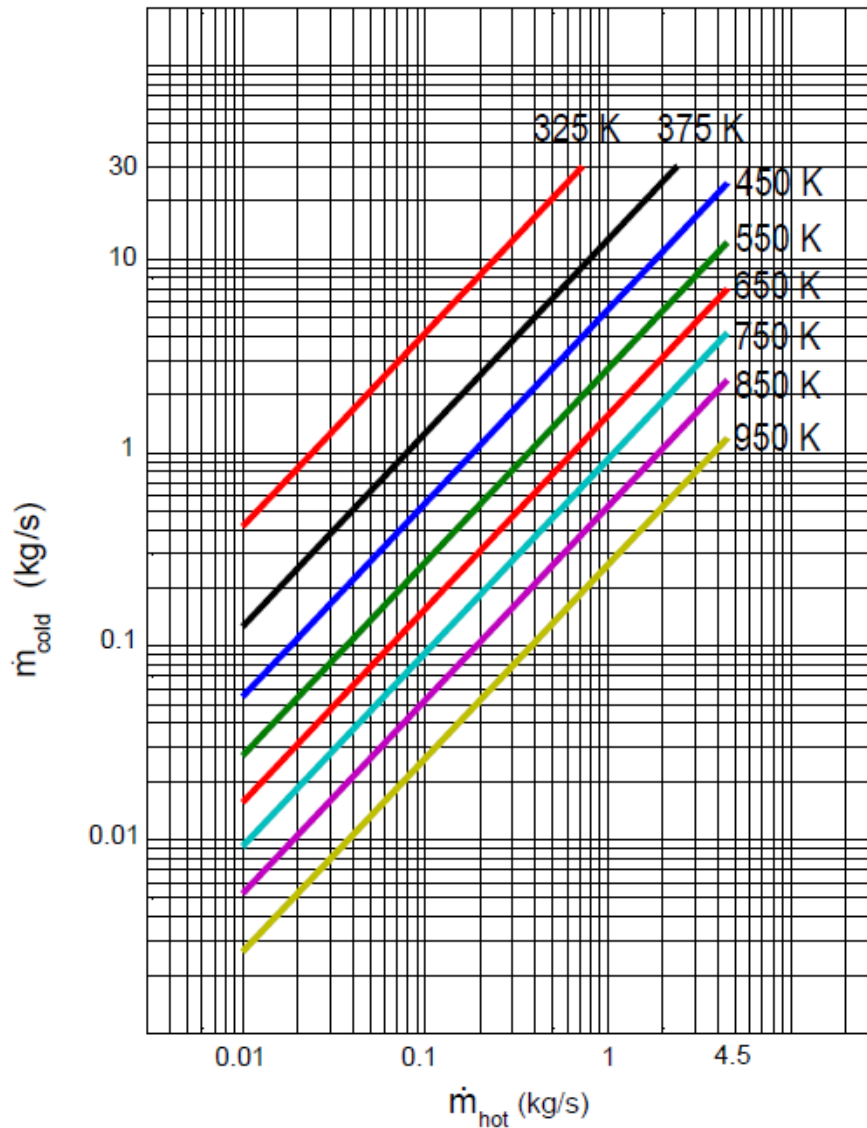


Figure 5-14 . Temperature achieved after the mixer with several hot to cold flow ratios.

The conditioning of the flow upstream of the test rig requires the mixing of a hot stream of air at 1100 K with a cold stream of air at 300 K. The thermal mixing of both streams allows to prepare the flow in a range of temperatures from 350 K to 950 K and total mass flow rates from 1 to 30 kg/s. A T-junction between a main pipe driving the cold stream and a branch pipe that drives the hot stream was chosen as design solution for mixing both air flows. The turbulent nature of these streams promotes a more efficient thermal mixing downstream of the junction, which is favored

by the presence of long straight sections ( $L > 20D$ ) and several  $90^\circ$  elbows that drive the flow to the test section.

Figure 5-14 depicts the range of temperatures that we can achieved in the test section when we mix different massflows of cold air and hot air. The performance of the mixer is the limitation, together with the NTU that the heater can provide to the flow, of the maximum temperature that we can get in the test section. Therefore extensive calculations to compute this limiting temperature and the uniformity of the temperature after the mixing have been performed.

In order to assess the mixing performance of this configuration, a numerical model of the T-junction and downstream piping has been elaborated. A fully structured mesh is created, sufficiently refined in the walls in order to reproduce  $y^+$  values in the range  $1 < y^+ < 30$ . Turbulence has been modeled using a URANS k- $\omega$  SST method with unsteady second order discretization scheme. A density-based solver is employed, using an ideal-gas model for air as working fluid. Static and dynamic pressure fields have been analyzed in order to validate the solution against Idelchik correlations for pressure losses in T-junctions.

Different combinations of hot and cold mass flow rates have been simulated, in order to reproduce a wide range of operating scenarios. The resulting momentum ratios of the main and branch flows allow to classify the mixing pattern of the intruding hot air flow as impinging jet, deflected jet or wall jet. These configurations lead to the formation of a horseshoe vortex downstream of the junction or hairpin vortices, any of them boosting thermal mixing of the flow. Once these vortices disappear, the radial turbulent diffusion of the flow also acts positively towards thermal homogenization of the flow. Finally, the dean vortices that appear when the flow enters in a  $90^\circ$  elbow further enhance thermal mixing, owing to the strong radial velocity components induced by the centrifugal forces.

Figure 5-15 presents an evaluation of the mixing downstream of the junction using as an indicator the maximum local temperature difference. 3.5 m downstream of the junction. Starting from a maximum difference of 800 K, differences between 3.6 and 21.1 K have been predicted, for four different operating conditions.

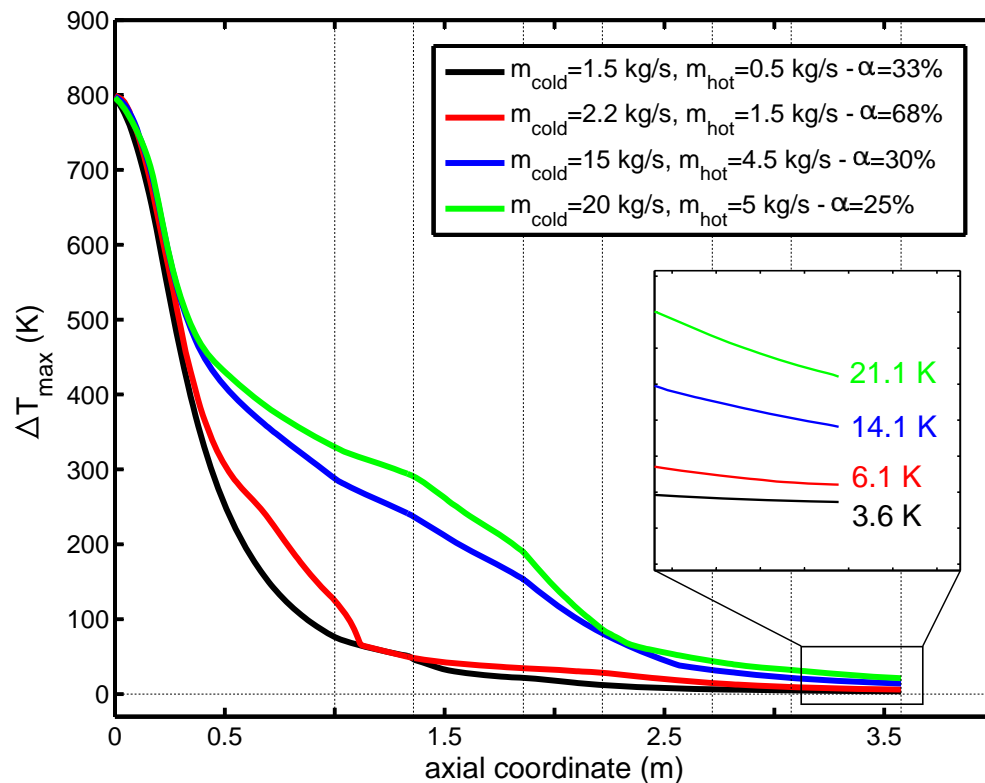


Figure 5-15. Min-max temperature difference along the length of the piping downstream of the mixer.

Once the steady performance of the mixer has been guaranteed, the high pressure control valve is regulated to set the intended massflow. When the operational pressure and temperature are achieved, the fast actuated butterfly valve is triggered, creating a step in temperature. This fast actuated butterfly valve (0.25m diameter ANSI300) upstream of the settling chamber, is prompted by a Kinetrol actuator. The sealing in the valve is bubble tight, to prevent leakage between the high

pressure line and the test section at vacuum conditions. In order to ensure tightness for the hot flow operation, at temperatures around 700 K, special alloys seals were selected.

The flow is discharged to the settling chamber, designed to provide uniform flow conditions to the test section. Downstream of each test section (linear and annular) a sonic valve is used to set the pressure within the test sections, in subsonic operation. The blowdown is working at matched conditions, or steady pressure when the mass flow provided by the upstream high pressure valves matches the mass flow set in the test section. In supersonic operation the sonic valve is fully opened. To allow low Reynolds number testing, the test section and vacuum tank are all set at sub-atmospheric conditions. When operating at sub-atmospheric conditions, the test concludes once the sonic valve gets unchoked due to the filling up of the vacuum tank. The vacuum pump to achieve 10 mbar is the DuraVane Lubricated rotary vane pump, provided by Dekker Vacuum Technologies.

### 5.2.2 Facility Calibration Strategy

The calibration is performed by checking different non-dimensional quantities: Reynolds and Mach number. Based on massflow continuity and isentropic relations, envelopes for both Mach and Reynolds are obtained for different the ranges of pressure, temperature, and mass flow, as shown in the Figure 5-16. The discontinuity on both contours represents the choking limit of the sonic valve. The purpose of the calibration is to characterize the response of the facility to the control parameters and be able to reach accurately each one of the points inside the envelope by setting the correct massflow and sonic throat of the wind tunnel.

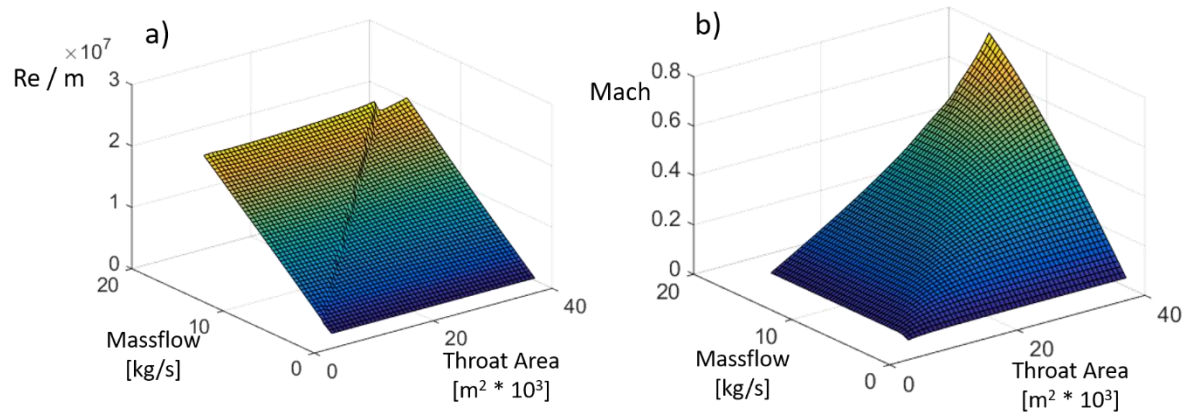


Figure 5-16. a) Reynolds number per meter and b) Mach number maps achieved in the test section in all the span of the sonic valve and with a maximum massflow of 15 kg/s.

The calibration of the linear test section is performed in three successive steps. First, the selection of the number of points to test, providing a reasonable uncertainty in the prediction of the complete envelope. Then, a total number of experimental points is chosen based on the shape of the Mach and Reynolds maps considering a second order model. Once the number of points is decided, a Kriging interpolation method is developed and coupled with a Genetic Algorithm optimizer in order to choose the location of the testing points inside of the envelope, minimizing the Root Mean Squared Error (RMSE) of every point inside the envelope. The cloud of the testing points obtained with this optimization is assessed and compared with a structured array of the same number of points. Finally, we test the points in the experimental facility and compare the results with the numerical solution. Based on the empirical results we can modify the numerical models to fit the Kriging interpolated map extracted from the experiments.

The selection of the calibration points is carried out taking into account the model used to predict the behavior of the wind tunnel [161][162]. The number of points needed to build a  $d^{\text{th}}$ -order model is directly related with the number of independent variables, the tolerance for interference errors



and the uncertainty of the estimated values [160]. The minimum number of points for a specified tolerance is defined by the Eq. (74).

$$N = \frac{(d + k)!}{d! k!} (t_\alpha + t_\beta)^2 \frac{\sigma^2}{\gamma^2} \quad (74)$$

In this equation,  $d$  represents the order of the model,  $k$  is the number of independent variables,  $t_\alpha$  and  $t_\beta$  are the t-statistics related with the Type I and Type II errors,  $\sigma$  is the estimated standard deviation of the measurements and  $\gamma$  is the precision requirement. Therefore, in order to facilitate the feasibility of the experimental calibration we need to find a balance between the desired precision and the limited number of points.

As an approximation we have used a 2nd order model, with  $k=2$  variables, the massflow through the test section and the sonic valve area. The t-statistics type I and type II ( $t_\alpha$  and  $t_\beta$ ) are extracted from the tables of the t-student distribution with a probability of error of 0.02 and 0.05, respectively. The standard deviation of the data taking into account the accuracy of the measurements is estimated around  $9 \times 10^4$  for the Reynolds number per meter and 0.011 for the Mach number. Doubling the precision requirement of the measurements accuracy, the number of experiments is about 40 for both non-dimensional numbers. Since both, Reynolds and Mach envelopes are irregular due to the status of the sonic valve, we implemented a meta-model based in a Kriging interpolation to compute the different quantities [163].

The Kriging model is a model with an infinite number of degrees, which implies that the obtained precision in the different quantities is highly dependent on the location of the points inside of the surface. As a consequence, we can only use the Equation (74) as an initial approximation. The purpose of the Genetic Algorithm coupled with the Kriging interpolation is to minimize the error (RMSE) of the surfaces with respect to the meta-model created with the determined number of

points. After choosing the amount of points, their location inside of the design space is optimized using a Kriging methodology developed in Matlab. The limiting values that we have used for  $c_0$  and  $a_0$  are 30 and 300 respectively to minimize the effect of the location of the points with respect to the mean level.

The Kriging interpolation is coupled with a Genetic Algorithm optimization. This optimization was performed during 80 generations with 25 individuals per generation. The genetic algorithm is programmed in the Optimization Toolbox in Matlab and was executed with parallel processing to optimize the computational time. The objective function is the square of the error of every point in the evaluated surface of Mach and Reynolds. The optimization is performed simultaneously in both targeted surfaces, weighting the error of each of the non-dimensional representations. For safety reasons, there were regions that were penalized during the optimization through the implementation of constraints. For instance, the operational points within the test section pressures over 5 bar were penalized in the objective function and all the selected points fall outside of this region of the envelope. At the same time, the maximum massflow tested is 15kg/s in the current configuration to guarantee a safe operation.

The selection of the order of magnitude number of points was based in the Equation (74) to give a statistical sense assuming a second order function. Using the Kriging interpolation meta-model, we are not imposing anymore a second order function and therefore we evaluated the Root Mean Squared Error (RMSE) of the complete model when we use different number of points. Similarly to a grid sensitivity evaluation, the RMSE between all the points of the real model and the Kriging meta-model for Mach number and Reynolds number was assessed for 20, 36 and 50 points of measurement. Figure 5-17c) depicts the evolution of the error for both quantities, and shows the targeted errors we could tolerate, of 0.015 for the Mach and  $5 \times 10^5$ . There is a trade-off between

the number of points we could test and the error we could admit, and therefore we decided to perform 36 experiments for which the Mach number is well below the error limit and for the Reynolds it is close enough. Figure 5-17a) and b) represents the comparison between the surface generated by the physical model of the facility (in color) and the surface generated by the Kriging interpolation method (in white mesh) for the Reynolds number per unit length and the Mach number respectively. We can observe that the agreement between model and meta-model is accurate for the selection of the points of the optimization, introducing a larger difference outside of the testing envelope where the pressure is higher than 5bar.

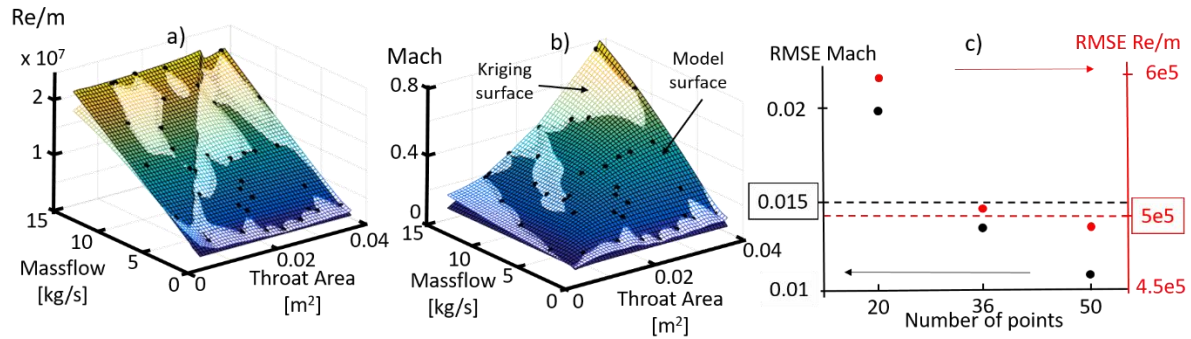


Figure 5-17. a) Comparison between the Re/m map and the Kriging meta-model in function of the massflow and the throat area with the representation of the points resulted from the optimization methodology. b) Comparison between the Mach number map and the Kriging meta-model in function of the massflow and the throat area with the representation of the points resulted from the optimization methodology. c) Root mean squared error of the Mach number and Re/m number using 20, 36 and 50 points in the Kriging interpolation optimization methodology.

In order to verify that we get an optimized solution with the sampling resulted from the optimization we have compared the solution with a Latin Hypercube sampling [164]. The number of points for both cases is 36. In the case of the Latin Hypercube we have created a grid of 7x6 points, where we have eliminated all the 6 points that falls inside of the high pressure region (pressure over 5 bar). Table 5-2 shows the comparison between the different RMSE obtained with

the different sampling approach, being the Kriging interpolation around 30% more accurate than the Latin Hypercube sampling.

Table 5-2. Root Mean Square Error (RMSE) relative to the two non-dimensional numbers using the different sampling distributions.

	<b>Latin Hypercube Sampling</b>	<b>Kriging interpolation Optimization</b>
<b>Mach number RMSE</b>	0.0173	0.0135
<b>Reynolds number (/m) RMSE</b>	$7.54 \times 10^5$	$5.17 \times 10^5$

Figure 5-18 shows a more detailed comparison between the errors in the Reynolds per unit length (b)) and the Mach numbers (c)). Figure 5-18 a) shows the location of the different points for both sampling strategies. We can observe how the Latin Hypercube sampling has a more organized pattern than the solution of the optimization. The points that are located next to the pressure limit have a great effect in the calculation of the error and therefore, the Kriging interpolation optimization has located four points in the surroundings that using the Latin Hypercube sampling we could not locate. Figure 5-18 b) and c) show how the error is located mainly in the high pressure region and it is nearly negligible in the center of the surface.

Once the optimization is performed and the results numerical results have been verified, the next step consists in the experimental characterization of the facility using the optimized points.

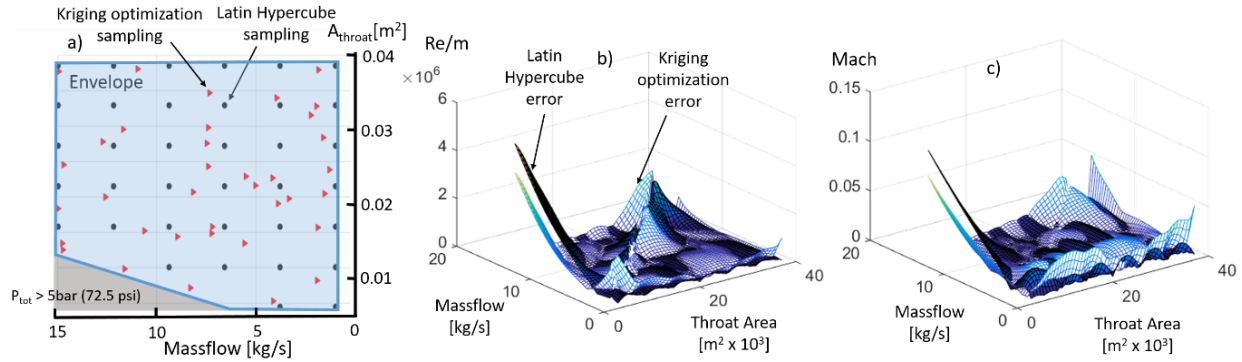


Figure 5-18. a) Sampling comparison between the Kriging optimization result and the Latin Hypercube approach. b)  $Re/m$  error comparison between the surface generated with the Latin Hypercube sampling and the Kriging interpolation optimization. c) Mach error comparison between the surface generated with the Latin Hypercube sampling and the Kriging interpolation optimization.

### 5.2.3 Annular Test Section Design

The annular test section was designed with two casings to allow testing additive manufacturing components in a wide range of pressures, while preserving the structural integrity. The external casing in carbon steel is designed to withstand the pressure difference between the test section and the atmosphere. Whereas the inner casing defines the particular turbine endwalls under investigation. In the current design the hub to tip radius ratio is 0.85, representative of small engine cores, with an outer radius of 420 mm. The aerodynamic design goals were to minimize the blockage of the instrumentation on the flow field, and to maximize the modularity to study vane / rotor rows alone, and their interactions. To minimize the blockage of the aerodynamic probes, the test section was scaled up considerably to the maximum allowable mass flow in the Zucrow laboratory, at engine-like conditions. Additionally, the large size will allow to maximize the spatial resolution of the measurement techniques, which should serve to reveal new phenomena, and reduce the uncertainty in cavity measurements. Furthermore, the test section was designed to allow future research on combustor interactions, and consequently, modularity was prioritized.

Figure 5-19a shows an axial cut of the annular test section, and the four measuring locations. The inlet component replicates a contraction similar to a combustion chamber, to allow testing of combustion chamber emulators. The vane row is mounted on a disc that can be fixed or rotated, as a pre-swirler to the rotor row. This allows to perform rotor measurements with an upstream wake generator, which requires a small electrical generator to absorb the power from the moving “stator row”. This turning pre-swirler can be designed with the adequate geometry to induce vane wakes and secondary flows similar to the actual turbine stage, while respecting the engine-like reduced frequency. At supersonic velocities this pre-swirler would generate shock waves, to characterize the shock airfoil interactions (shock-rotor, and shock-vane interactions). The rotor row is mounted on bearings to allow the rotation, but the movement will be actually constrained with a load cell. Therefore, we will monitor the tangential force directly using the reading from this load cell, and hence the torque.

2D Unsteady Reynolds Averaged Navier-Stokes simulations were performed to evaluate the boundary layer along the annular test section. Axisymmetric computations were performed using Ansys Fluent, with the Spalart-Almaras turbulence model. The computational domain comprised 827,426 cells, from half of the settling chamber until the sonic throat only with the endwalls. Figure 5-19b shows the velocity profile at two axial locations, at the vane leading edge and at the rotor leading edge. Owing to the inlet contraction, the boundary layer is less than the 5% of the blade height at the vane leading edge, and 10% at the rotor.

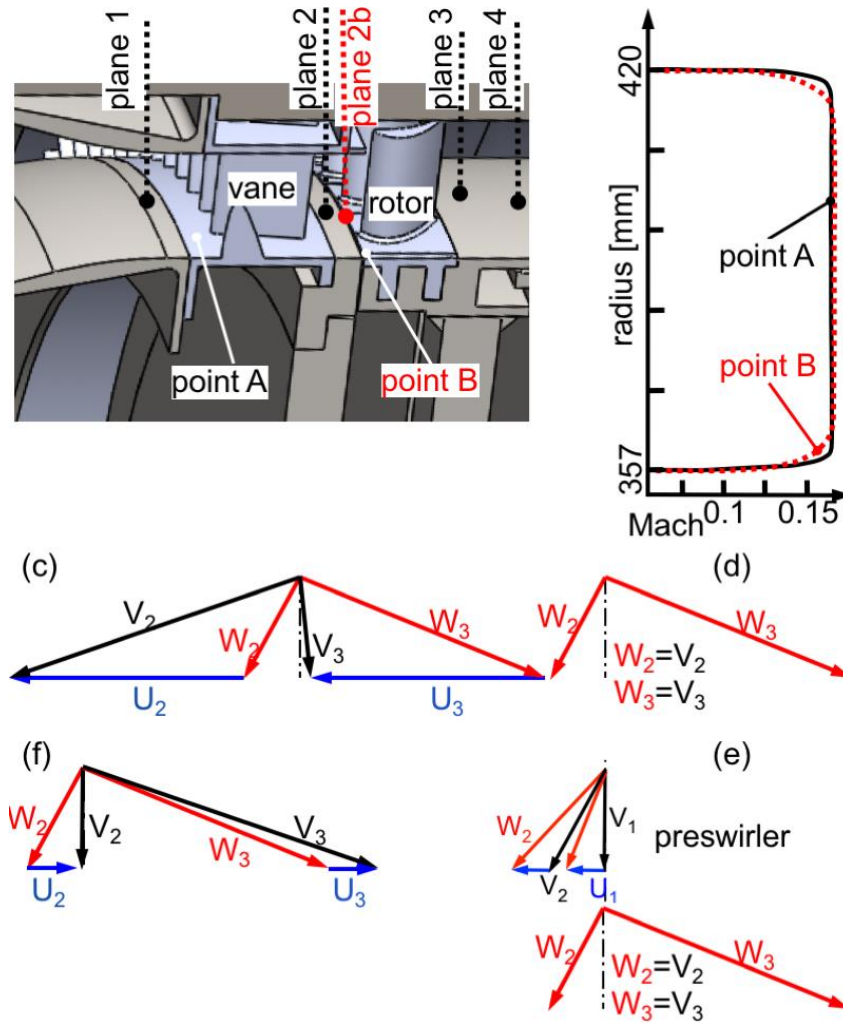


Figure 5-19. a) Annular test section measurement planes. b) Velocity profile at two axial locations. c) Stage velocity triangles. d) Absolute-relative velocities of a rotor row with a pre-swirler; e) Velocity triangle in a stationary rotor row with rotating pre-swirler; f) Reverse rotation.

Traditionally, turbine stages are tested and results compared with CFD following this sequence: 1) linear cascade testing of the vane; 2) linear cascade testing of the blade; 3) annular cascade testing of the vane; 4) rotor is added to the annular cascade and tested in rotation. The comparison between CFD and experiments is typically straight forward for phases 1-3. However, when moving to phase 4, there are multiple effects which obfuscate the agreement between experiments and CFD, namely rotational effects, the interaction between the stator and the rotor, the effect of the cavity at the

stator rim-rotor platform and tip clearance effects. In the present facility we propose to perform annular cascade testing of the vane, and of the rotor separately, including then a device to characterize the unsteadiness at several frequencies in a controlled environment. The actual velocity triangle of the rotor is displayed in Figure 5-19-c. A first option, sketched in Figure 5-19-d, is to mount a stationary pre-swirler, to provide the relative inlet angle to the stationary rotor row. In this way, if we are assessing a rotor row, we use the absolute velocity of the flow as if it would be the relative velocity ( $V_2=W_2$ ,  $V_3=W_3$ ). Typical modern designs would require a turning of about 20 deg. An alternative option would be to use a rotating pre-swirler, as shown in Figure 5-19-e. Due to the rotation, the turning of the flow will increase, which will imply a decrease of the turning of the pre-swirler to keep the same  $W_2$  angle. This implies that little power would be required to be absorbed from this pre-swirler. In all these experiments the rotor torque would be precisely monitored by a load cell. Figure 5-19-f shows another concept, reverse rotation, which allows to replicate the rotor inlet velocity without any upstream stator, i.e. the rotor inlet absolute velocity is axial, which also requires small rotational speeds. However, reverse rotation would not allow to replicate the radial distribution of the static pressure, unless we would investigate rotors with zero relative inlet angle all along the radius.

The modularity in the design of the test section allows the implementation of pioneering turbine concepts, i.e. supersonic turbines [165] and bladeless turbines [166]. To achieve supersonic flows, the inlet contraction shown in Figure 5-19-a will be replaced by a converging-diverging nozzle.

To perform optical measurements through the casings, two sets of windows were required, across the external and inner casing. Figure 5-20-a shows the four windows at different azimuthal positions around the annulus and the multiple 1in and half-an-inch fitting holes needed to fully characterize the flowfield with optical measurement techniques. The inner window is thinner,



around 10 mm, and curved in the inner wall to respect the flow path and minimize the effect of its presence in the flow. The outer window purpose is to preserve the structural integrity of the wind tunnel, thicker and flat. The windows are located right above the rotor blades and extended downstream and upstream of the turbine more than 1.5 times the axial chord. This extension provides access to all the casing instrumentation and supports.

Figure 5-20c-d shows different configurations that can be implemented in the modular annular test section. By changing the components upstream of the stator or rotor rows, we can test in subsonic (Figure 5-20c) and in supersonic conditions (Figure 5-20d).

Figure 5-21 shows the operational Mach and Re number range in the annular test section, based on the vane outlet flow conditions, an axial chord of 60 mm, and a flow direction of 72 deg. The outer diameter at the vane exit is 0.84 m, and the vane airfoil radial span is 63 mm, to scale up small core axial turbines. The dashed lines represent the maximum and minimum Re numbers achievable in the test section at each Mach number. The dotted line represents the minimum Re number that can be attained exhausting directly to the atmosphere. Any point intended to be tested below this line is achieved using the vacuum system. With the range of mass flow provided and the current test section geometry, supersonic velocities may be reached up to Mach 1.3, and axial Mach numbers of about 0.42.

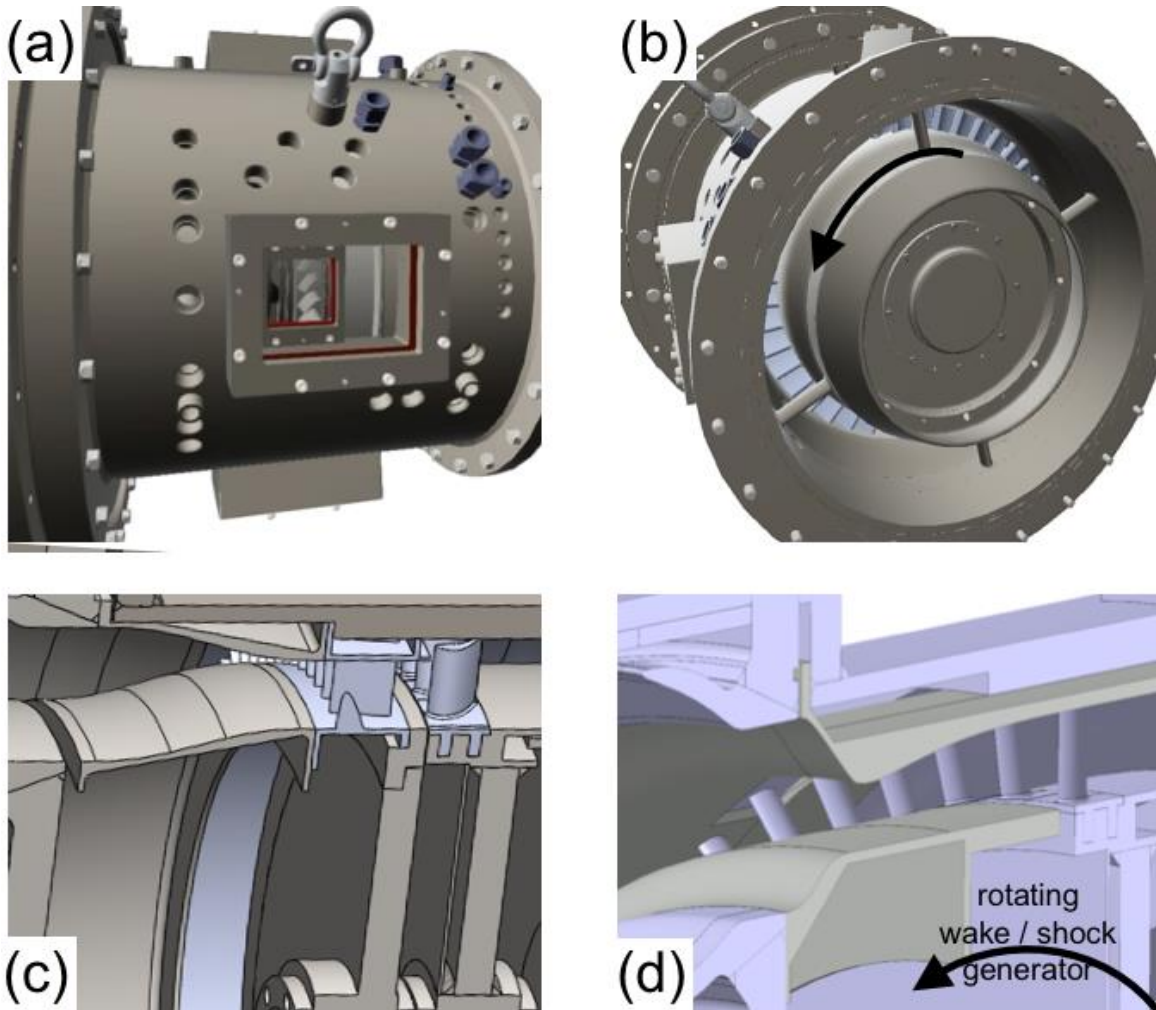


Figure 5-20. Annular test section: a) Overall layout of the optical windows; b) frontal view of the test section; c) meridional view; d) supersonic configuration.

In Figure 5-21-left, we included six different operating points, in the transonic range (Mach 0.9 and Mach 1.1) located along the maximum Re number line (A at  $2.5 \cdot 10^6$  and B at  $2.6 \cdot 10^6$ ), minimum Re number line (C at  $144 \cdot 10^3$  and D at  $151 \cdot 10^3$ ) and the vacuum limit line (E and F). Additionally, the figure also includes data from other turbine facilities. Figure 5-21-right lists the pressures, temperature, massflow, and test duration of the previously specified conditions. Each Re number and Mach number can actually be achieved at various flow temperatures. Therefore, we could independently select the  $T_{\text{gas}}/T_{\text{metal}}$  for high pressure as well as for low pressure turbines.

The test duration of all the points presented in Figure 5-21-right was calculated considering exhaust to the vacuum tank. Blowing to the atmosphere, the experimental time would increase one order of magnitude for the points A, B, E and F. Note that the maximum pressure needed to achieve the maximum Re number is  $2.8 \cdot 10^5$  Pa.

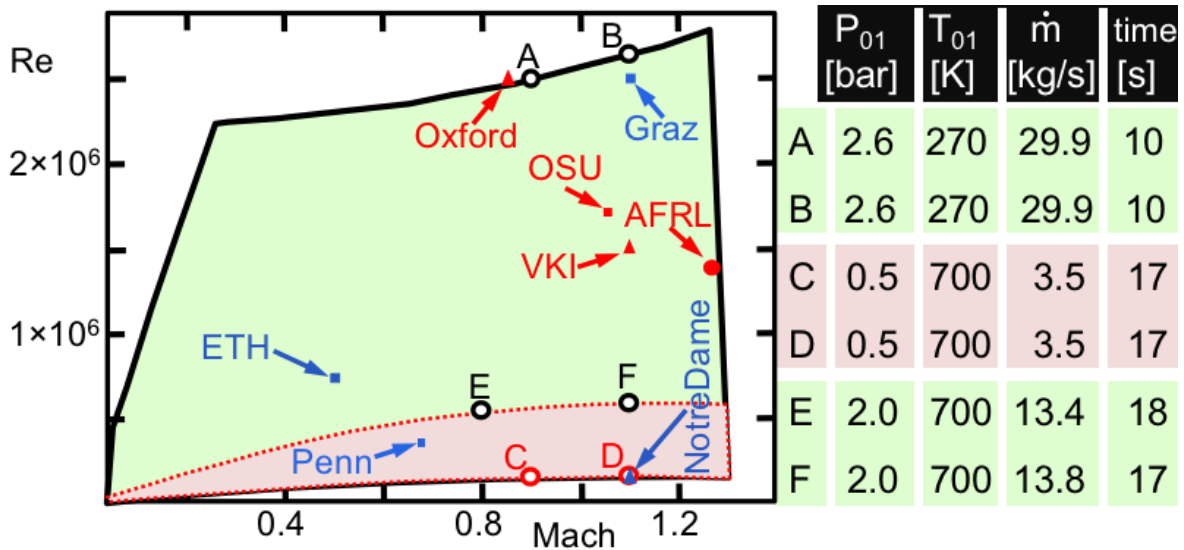


Figure 5-21. Left) Mach-Re limits in subsonic operation. Right) Operational range in subsonic conditions.

To achieve supersonic operation a convergent-divergent nozzle, shown in Figure 5-20-d, was designed using the Method of Characteristics for the supersonic part and Bezier curves for the converging part, preserving the curvature along the transition between both methods and the throat. Figure 5-22 shows the available range of operation of the facility in supersonic operation, with a maximum available mass flow of 30 kg/s. In Figure 5-22-left we included six different operating points at Mach 2 and 3.2 considering that vane outlet Mach number with a turning of only 12 deg. and the same axial chord than in the subsonic case for the calculation of the Re number. Figure 5-22-right lists the pressure, temperature, massflow and test duration. The maximum achievable Reynolds number is most restricted at low Mach numbers, the

minimum achievable Re number is  $119 \cdot 10^3$  at Mach 2 (test C), and  $62 \cdot 10^3$  at Mach 3.2 (condition D). The area inside the dashed line represents tests performed while exhausting to the vacuum tank. The maximum pressure that can cover the entire range is 4 bar and the temperature oscillates between ambient temperature and 700K.

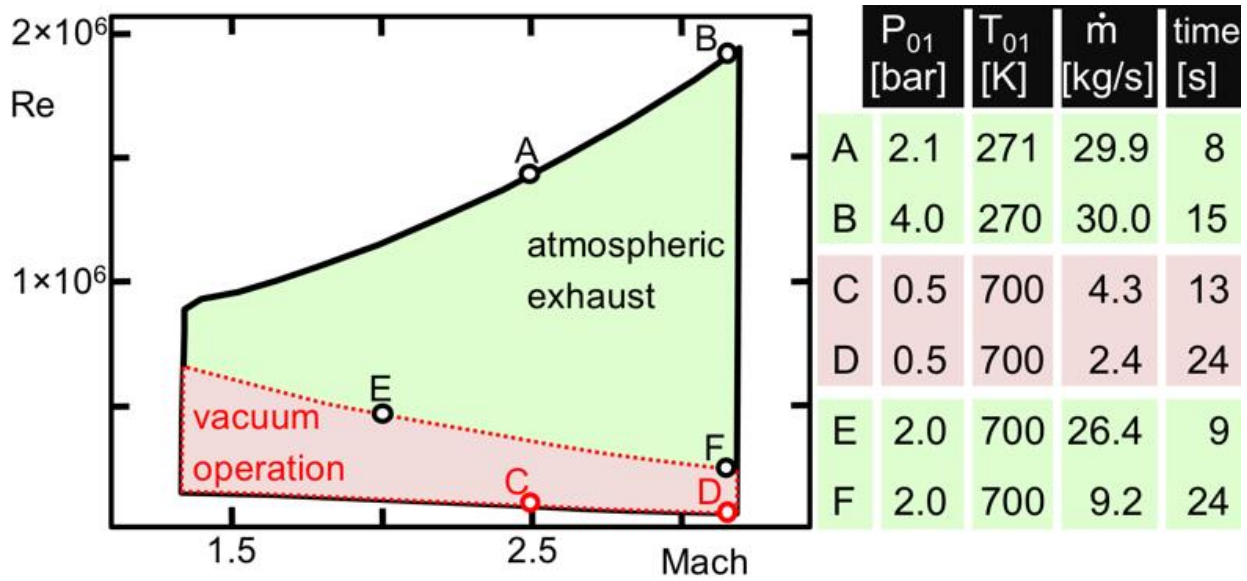


Figure 5-22. Left) Mach-Re limits in supersonic operation. Right) Operational range in supersonic conditions.

#### 5.2.4 Infrared Thermography Experimental Setup

The annular cascade was specifically designed for the use of optical measurement techniques. The optical access of the annular cascade is utilized in experimentally validating the inverse heat transfer methodology in gas turbine applications. The experiment is conducted in the test section without airfoils, so only the contraction of the endwalls provides spatial gradients of heat flux. The purpose of the experiment is to measure the temperature in the intake of the high pressure turbine, where it is extremely difficult to implement instrumentation, and using the inverse methodology, retrieve the conditions in the inner flow path. This allows for non-invasive flowfield measurements and allows for measurements in the turbine which previously would have been nearly impossible.

to instrument. Figure 5-23 shows the meridional cut of the test section where the experiment was performed. This test section does not contain any moving part and the flow is completely axial. Therefore, in this case the spatial gradients are minimal and the experiment is focused in the computation of the flow temperature and massflow.

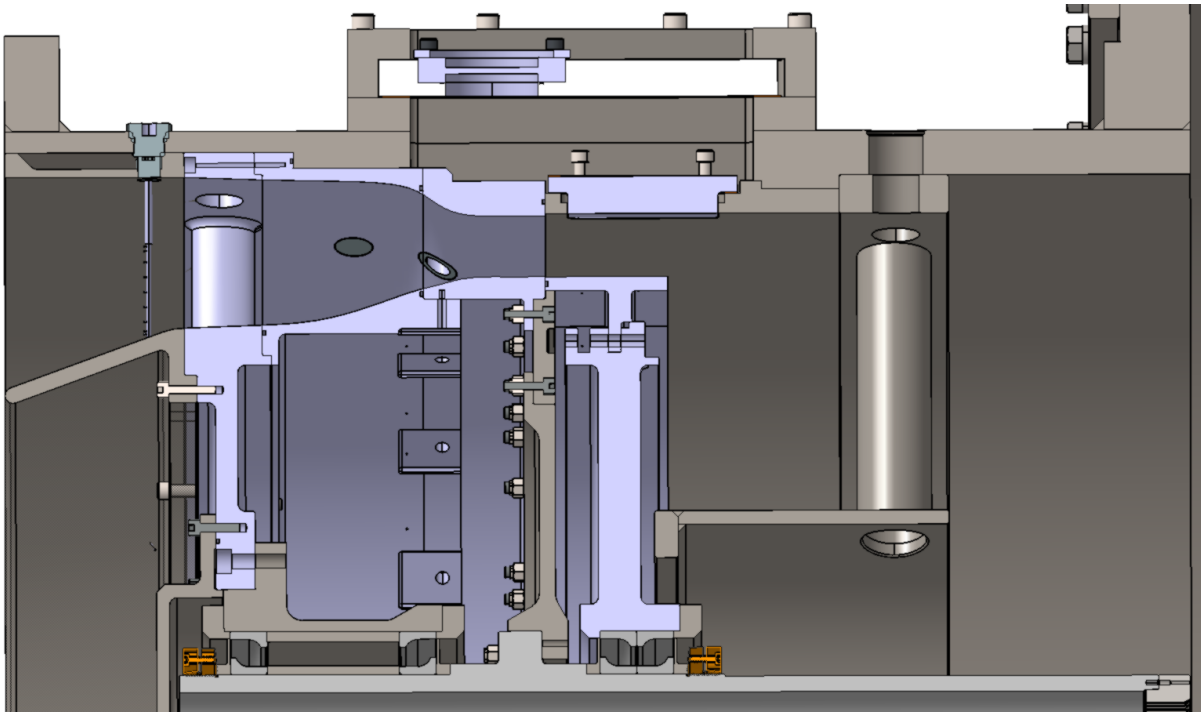


Figure 5-23. Meridional cut of the annular test section under investigation.

To experimentally validate the proposed methodology, one of the windows was modified to hold a smaller infrared transparent window that was installed in the outer casing in order to measure the temperature in the inner casing.

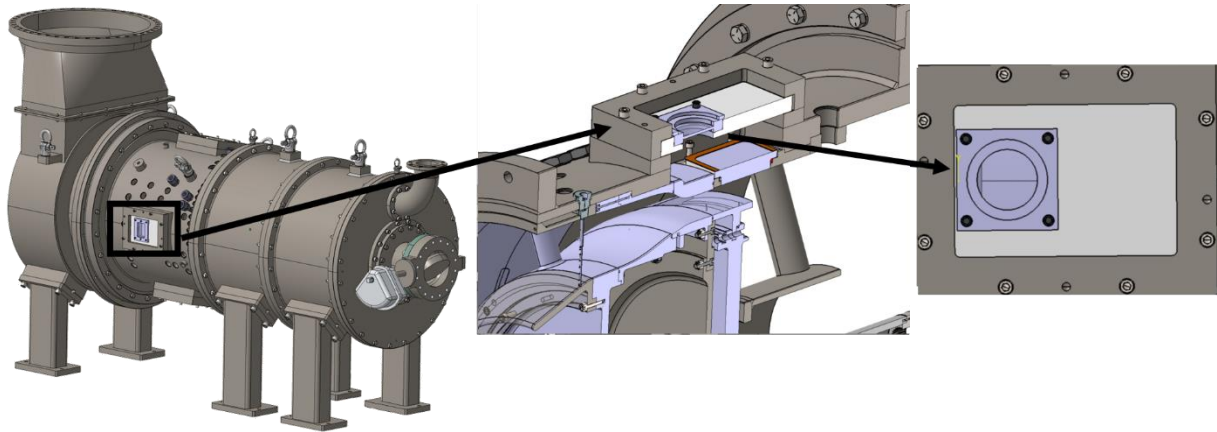


Figure 5-24. Infrared access in the turbine annular cascade to perform infrared thermography of the inner casing of the rotor.

Figure 5-24 shows the details of the modifications required in the wind tunnel to measure temperature in the inner casing. The camera is located outside of the facility protected from possible vibrations of the wind tunnel and the targeted frequency is 10 Hz. In this experiment, in order to validate the heat flux through the casing, more sensors need to be added in the inner surface of the inner casing. With the measurements taken on the inner surface with surface thermocouples and on the outer casing with the infrared camera, we can compute the heat flux through the casing with a 1D calculation, estimating the thermal properties of the material.

#### 5.2.4.1 Instrumentation

The test section is fully instrumented with pressure taps, a pressure probe, a pressure rake, two temperature probes and a temperature rake. These instruments provide the information needed to know the conditions of the flow. The metal temperature is monitored using RTDs all around the casing in the outer and inner endwalls in the same axial locations where the pressure taps are located. There are measurements in three different axial locations along the test section.

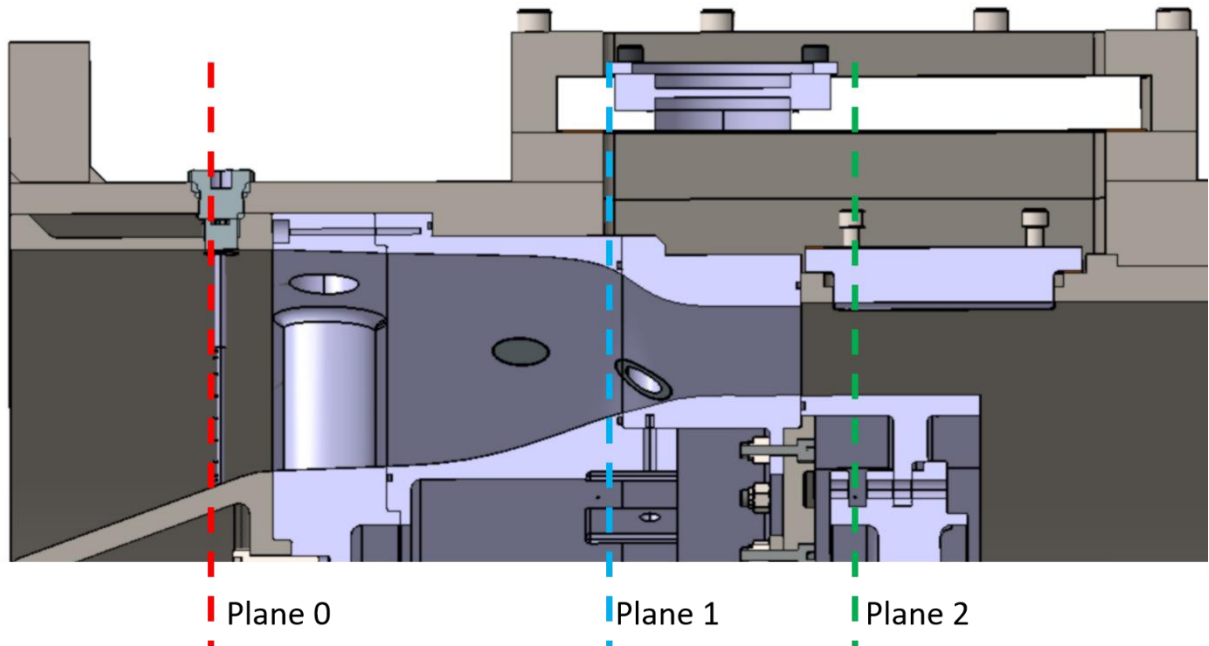


Figure 5-25. Measurement planes in the experimental setup of the annular the test section.

Figure 5-25 depicts the location of the planes where the instrumentation was placed. In plane 0, upstream of the last contraction (which is where the infrared camera is used) there are two temperature probes and one total pressure probe as shown in the Figure 5-26. In plane 1, the windows in the outer endwall are used to place the instrumentation, while in the inner endwall there are 22 pressure taps and 8 RTDs in the outer surface of the contraction, (placed like this so that they are not in the flowpath). In the outer ring, 4 pressure taps and 4 RTDs were placed through one of the windows. Another window was equipped with 4 more RTDs in plane 1, a total pressure rake, and a total temperature rake to measure the uniformity of the flow in the radial direction. In Figure 5-26, the rakes are depicted as well as the insert in which they have been placed in the upstream location of the external window. Plane 2 is located downstream more than 2 inches downstream of the plane 1 and there is no contraction in the annulus at this point. As in plane 1 the four external windows were used to place the instrumentation of the outer endwall while the



inner endwall was not instrumented. All of this instrumentation is used to check the uniformity of the flow in the annulus and to determine the radial pressure and temperature profiles at a desired location. This location corresponds to where the temperature measurements are being taken for the inverse method validation with IR cameras. This is to say that the instrumentation in the endwalls is not used directly in the computation and validation of the inverse methodology, rather it is used to ensure flow uniformity and determine radial profiles at the location of the IR camera; while the IR camera measurements are directly used in the validation of the inverse methodology.

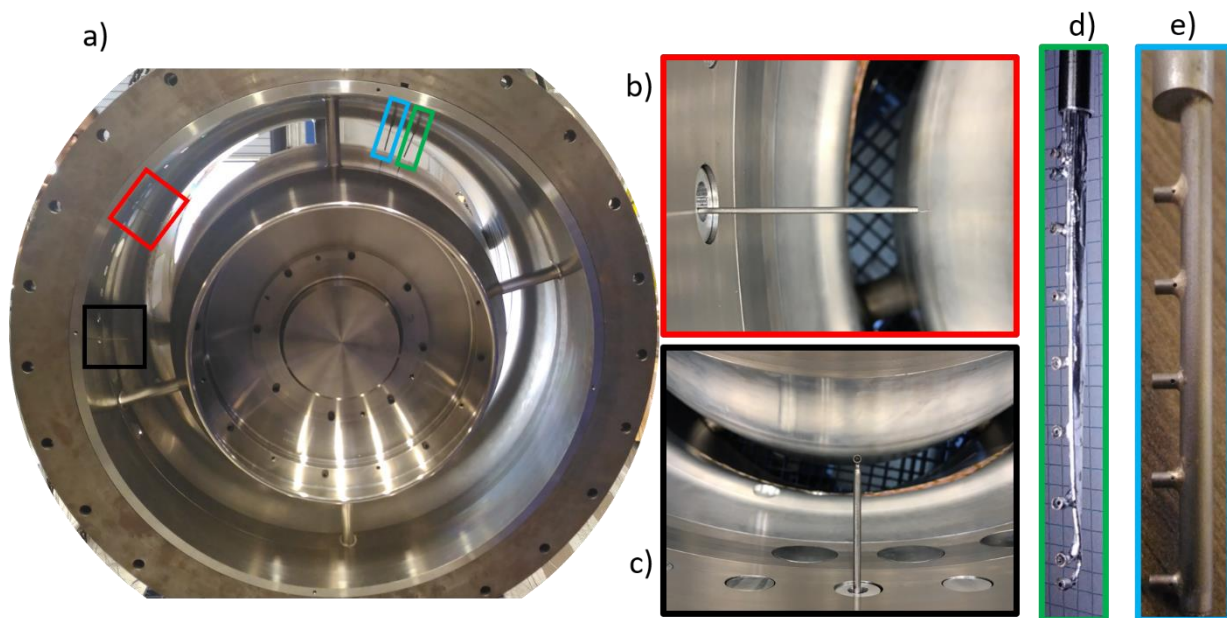


Figure 5-26. a) Instrumented annular test section ready to be set into the wind tunnel. b) Detail of the thermocouple probe already in the test section. c) Detail of the total pressure probe already in the test section. d) Total pressure rake and e) Total temperature rake.

Together with the flow and uniformity instrumentation, surface thermocouples were used to measure the temperature of the endwall temperature and a FLIR Infrared camera was used to monitor the temperature of the outer casing of the inner annulus. One of the external windows was adapted to hold a Calcium Fluoride IR window. Through this transparent window the inner casing temperature can be measured, but a previous calibration needs to be performed to account for the



transmissivity of the window. The material of the window was carefully chosen based on the range of metal temperatures that we were expecting during the experiment and it is detailed in the Appendix D. Figure 5-27 shows the surface thermocouples located in 8 different axial location between the plane 1 and the plane 2 of measurements and right under the location where the infrared camera is taken measurements. They are scattered such that there is no interference between thermocouples and the flow.

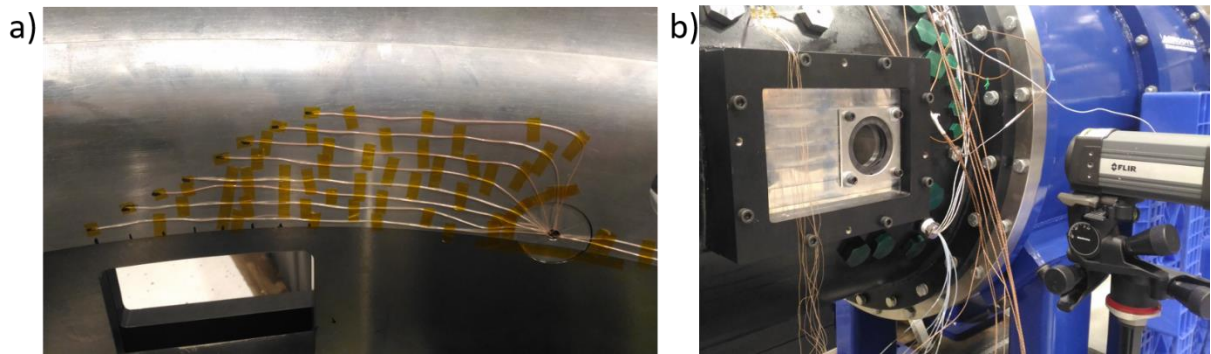


Figure 5-27. Instrumentation used for the validation of the inverse heat transfer methodology composed by a) surface thermocouples in the inner surface of the measured intake and b) Infrared camera configuration to measure the outer temperature of the same turbine intake.

Figure 5-27 also shows the outer configuration of the experimental setup with the IR transparent window and the FLIR Infrared camera. The IR camera was located outside of the test bed of the facility to minimize the vibrations that may occur during the blowdown experiment through the facility. Additionally, the outer surface of the inner casing, where we take the IR temperature data, was painted with a layer of graphite. The aluminum has a high reflectivity coefficient and this modifies the real value of the temperature that we measure with the IR camera. This effect is even more significant when dealing with curved surfaces such as the ones we are dealing with in the inner casing. To remedy this a layer of graphite paint was applied in the region of the inner casing where the measurements were taken. Figure 5-28 shows the test section already in its final position and completely instrumented.

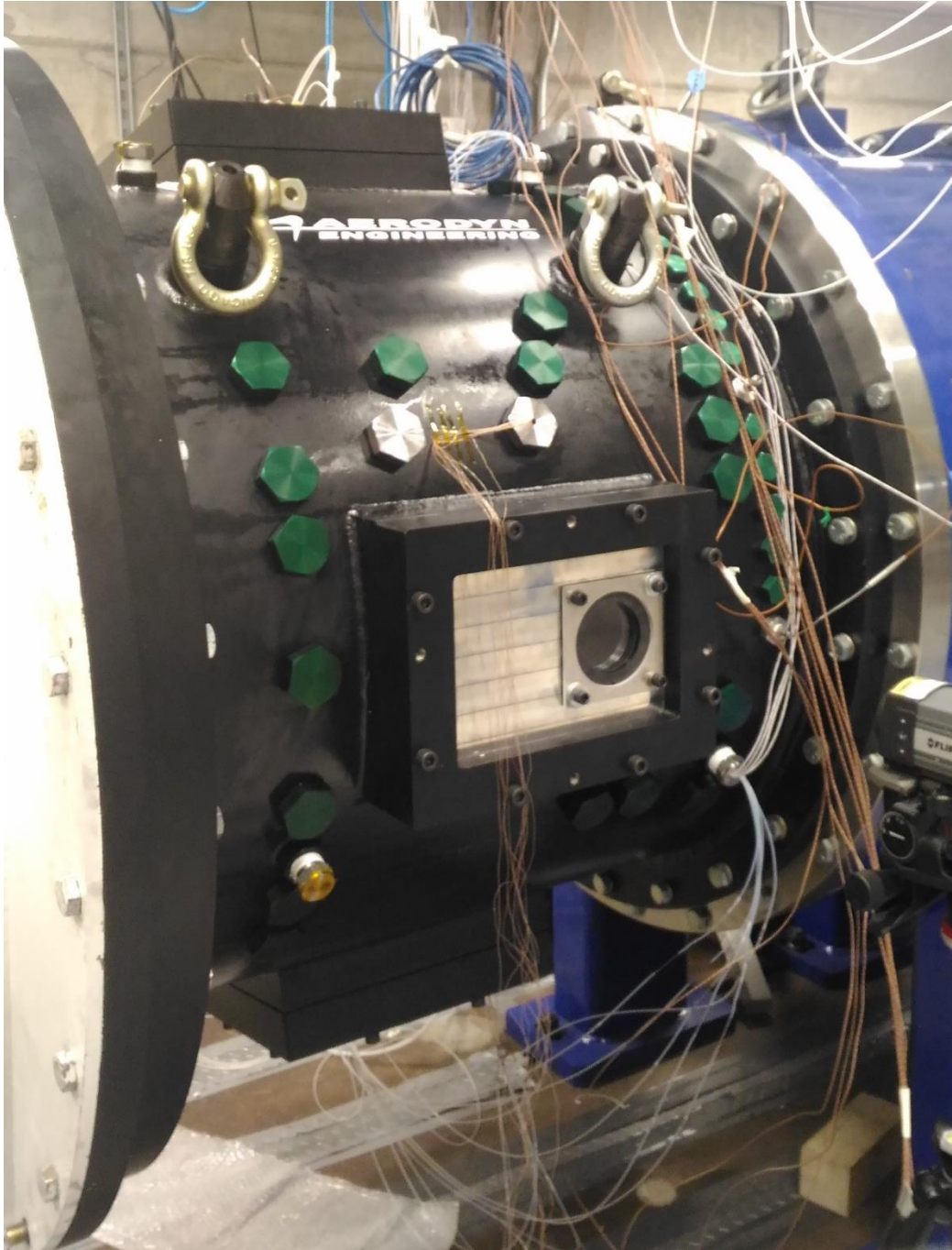


Figure 5-28. Test section instrumented, installed and ready for the experiments.

To summarize, during this experimental campaign, 90 sensors and measurement devices were distributed around the annular stationary test section to ensure uniformity of temperature and

pressure around the annulus and to measure the temperature needed to compute the inverse method and the validation of the methodology.

#### 5.2.5 Experimental campaign

In this experimental campaign, we have analyzed 5 different experiments in which we have modified the massflow and the input temperature in the test section. The procedure followed in each one of the experiments is as follows:

1- Heater starting phase: the heater should reach the intended temperature in order to perform the experiment. For this phase the annular butterfly valve is closed and the purge valve is open. This is done to keep a large gas to wall temperature ratio; allowing us to perform the heat transfer experiments. At this stage, we are blowing low levels of massflow ( $\sim 1\text{lb/s}$ ) while the heater reaches steady state. In this phase all the air is dumped to atmosphere through the purge line. The temperature is slowly increased to achieve the desired inlet temperature at the venture, and once steady state is reached we proceed to the next phase.

2- Massflow adjustment: Next the massflow is increased (with the purge line remaining open and the annular line closed). The heater automatically adapts the fuel in order to heat up the flow to the set temperature. The temperature is set by the test operator and he has to take into account the thermal losses through the piping and therefore the temperature in the test section is lower than the set temperature. These losses depend on the level of massflow and the ambient temperature.

3- Experiment starting: Once the conditions of temperature and massflow are stable, the experiment can start by opening the annular line and then quickly closing the purge line. The massflow is measured by the venturi and directed through the annular test section for the duration of the experiment (2 minutes in this case).

4- Experiment shut-down: Once we complete the intended time of the experiment and we have taken the needed data, we open the purge valve and close the annular valve to finish the experiment.

Then, we can lower the massflow to shut down the facility.

The experiments that were evaluated in this doctoral thesis are contained below in Table 5-3.

Table 5-3. Turbine application experimental campaign tests.

<b>Experiment Name</b>	<b>Temperature [F] in the heater</b>	<b>Massflow [lb/s]</b>
<b>Experiment 1</b>	300	9
<b>Experiment 2</b>	400	9
<b>Experiment 3</b>	500	9
<b>Experiment 4</b>	500	6
<b>Experiment 5</b>	500	12

The baseline case is experiment 3. In these experiments we independently vary the two variables (massflow and temperature) that we can vary in the current configuration of the wind tunnel. The sonic valve downstream of the test section is not used in this experimental campaign; and the variation of total pressure is coupled with the variation of massflow.

Following the aforementioned procedure, the temperature of the flow passing through the test section is complex to control, therefore as observed in the results in Appendix E, the temperature measured by the temperature probe located in the plane 0 is not stable for the different experiments. Instead the main objective is to have a stable gas to wall temperature ratio during the experiment as shown in Figure 5-29.

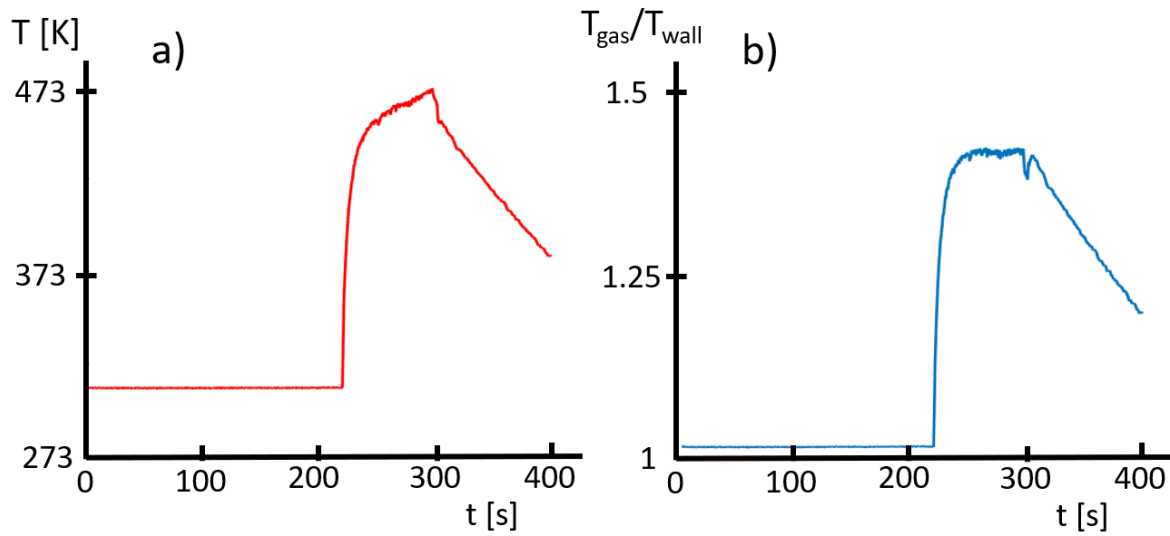


Figure 5-29. a) Gas temperature measured by one of the total pressure probes in the test section during the baseline experiment and b) gas to wall temperature ratio during the same experiment.

Figure 5-29 shows the flow temperature in our baseline case and the uniformity of the gas to wall temperature ratio during the experiment. In the baseline case this ratio is around 1.42 during the experiment (the wall temperature increases at the same rate as the gas temperature during the experiment).

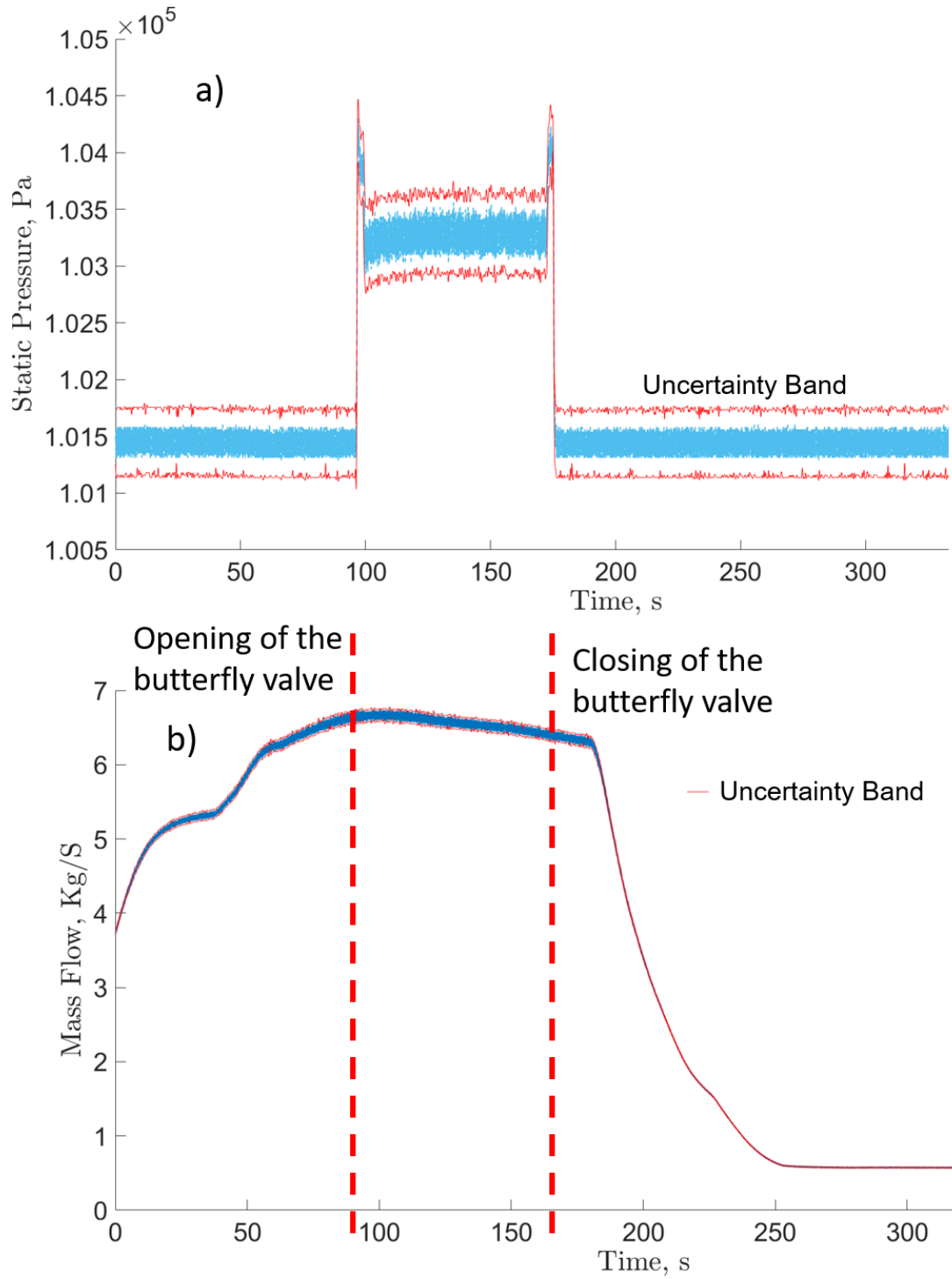


Figure 5-30. a) Total pressure measurement in the annular test section in plane 1 during the experiment 5. b) Massflow measurement during the same experiment in the venturi located upstream of the test section.

Figure 5-30 shows the total pressure and massflow during the experiment. As there is no sonic point downstream of the test section, the pressure and the massflow are coupled. The massflow represented in the figure, is measured in the critical flow venturi upstream of the purge line, while the pressure is measured with the total pressure probe in the test section. The figure shows when the annular valve was opened at the beginning of the experiment and closed at the end of the experiment.

As discussed earlier, one of the necessary steps that needs to be performed for the validation experiments is to check the uniformity of massflow and temperature in the circumferential direction. The uniformity will allow for the inverse methods to be validated in the annular test section. Figure 5-31 depicts the measurements of the different pressure taps around the inner and outer casing in the plane 1 and plane 2. We observe that the measurements fall one on top of each other in all the cases and therefore we can conclude that the flow is uniformly distributed around the whole annulus; allowing us to use the experiments to validate the inverse method. In all these pressure and massflow measurements, the uncertainty is represented with the red bands shown in the figures. The uncertainty is associated to each sensor at every time step of the sensor and is based on the calibration of each sensor.

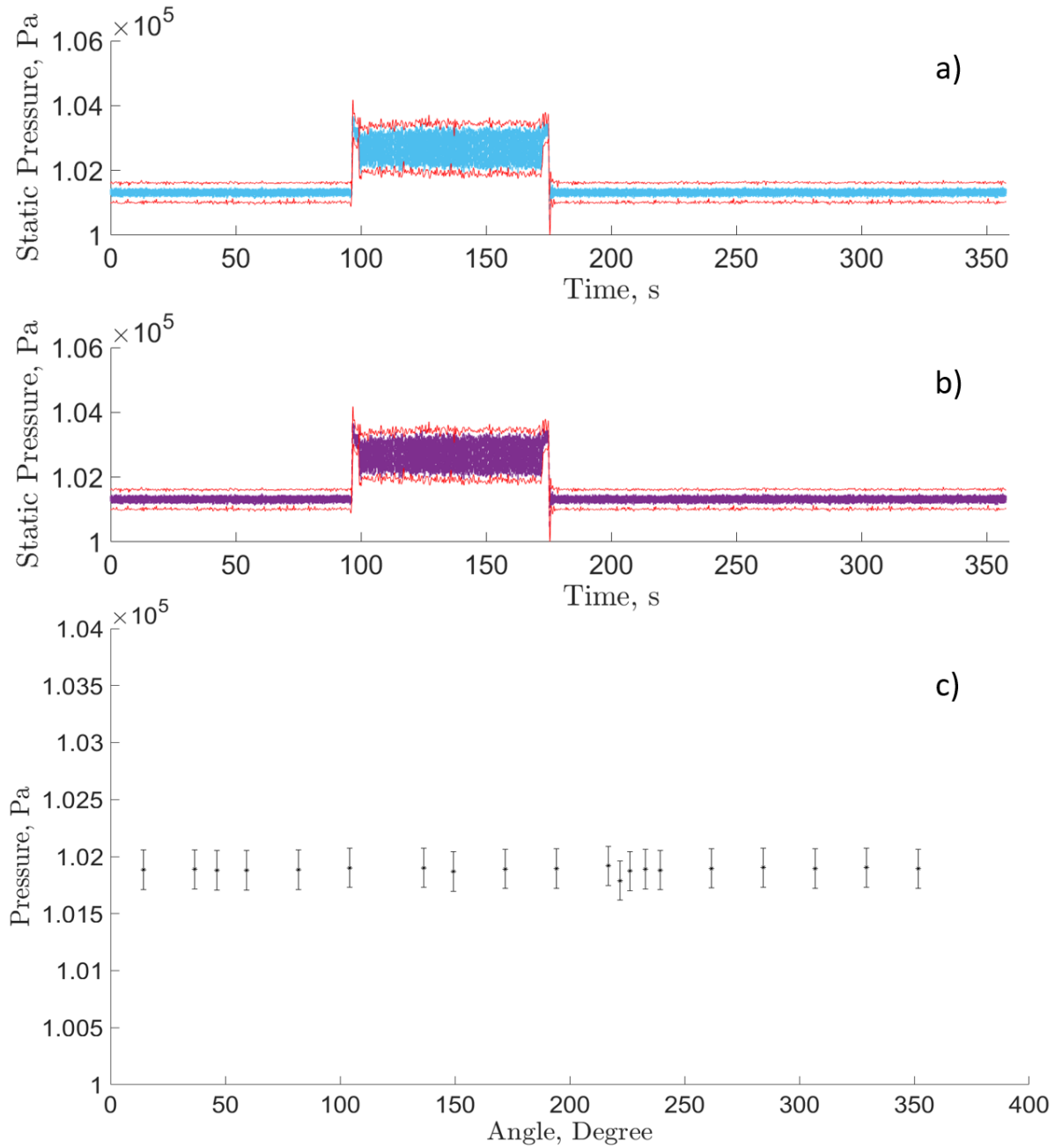


Figure 5-31. a) Static pressure readings in the plane 1 in the hub of the flowpath. b) Static pressure readings in the plane 2 in the shroud of the flowpath. c) Uniformity in the circumferential direction of the static pressure in the hub of the plane 1.

Regarding the wall temperature distribution, the readings of the surface thermocouples within the flow path are compared with each other. As observed in the Figure 5-32 two surface thermocouples



were positioned at the same axial location as thermocouples 1 and 6; but they were placed at different circumferential directions.

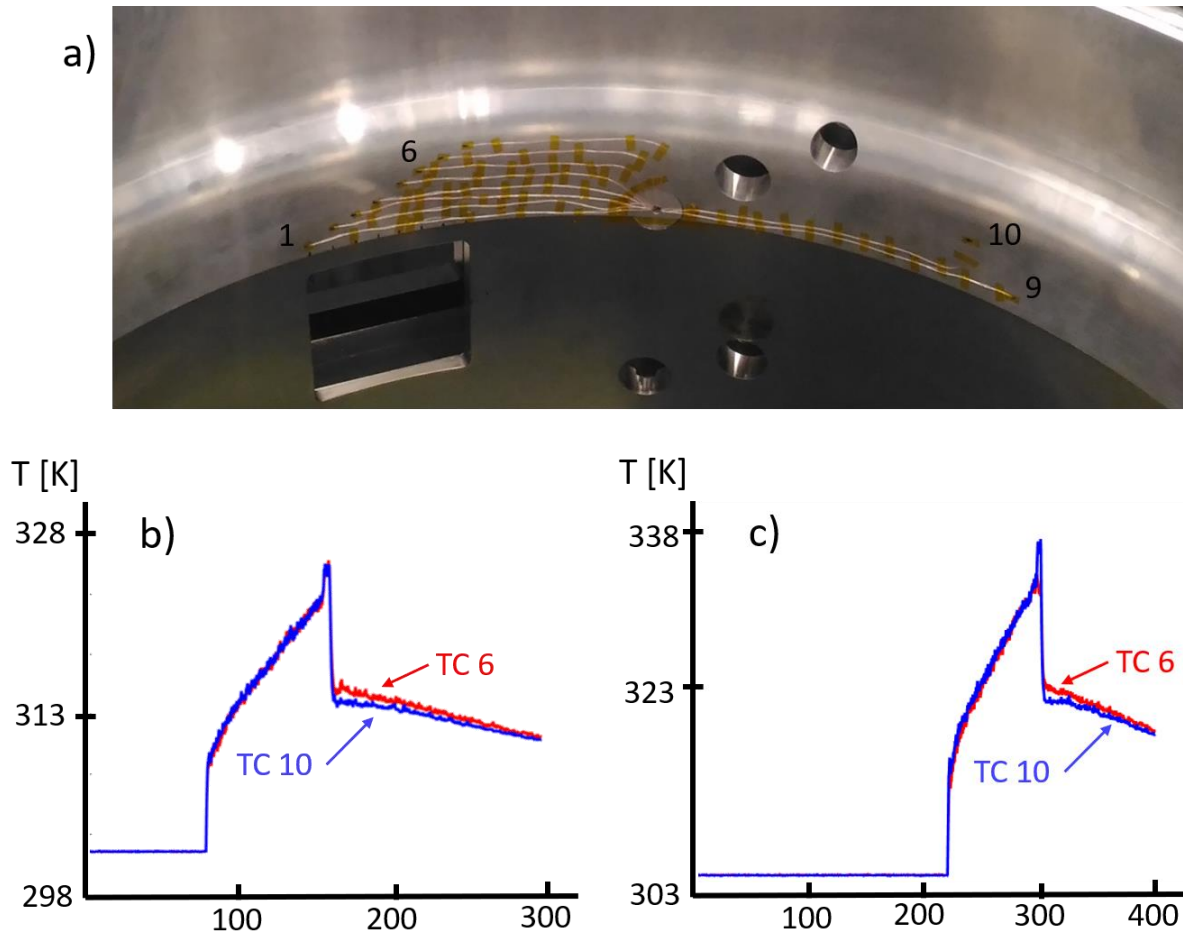


Figure 5-32. a) Surface thermocouples located inside of the test section. b) Temperature comparison between the Thermocouple 6 and the thermocouple 10 located in the same axial position in the experiment 1. c) Temperature comparison between the thermocouple 6 and the thermocouple 10 located in the same axial position in the baseline case.

Figure 5-32 shows the temperature along the experiment 1 and 3 of the two of the thermocouples located in the same axial position. Based off of the similarity between these thermocouple readings at different circumferential locations we conclude that the thermal distribution is uniform in the circumferential direction.

For the validation of the inverse methodology we use the measurements of the surface thermocouples that are located in the inner part of the window and the measurements taken with the infrared camera. In order to compute the heat flux using the Digital Filter Methodology, the only information needed is the temperature gathered with the infrared camera. The temperature monitored with the surface thermocouples is used together with the infrared thermography to directly compute the heat flux and is then compared with the results of the inverse solution.

### 5.2.6 Digital Filter Method Validation

In order to run the inverse method in the inner casing of the facility a model of the casing is needed. The inner casing model was designed in Catia based on the prints and drawings of the part. Then the model was imported into Comsol where finite element thermal computation is performed. We did not use the whole annulus since only we are measuring in the sector of the annulus where we have the outer window. The ring was cut on the borders of this window and periodic boundary conditions were set in the meridional cuts.

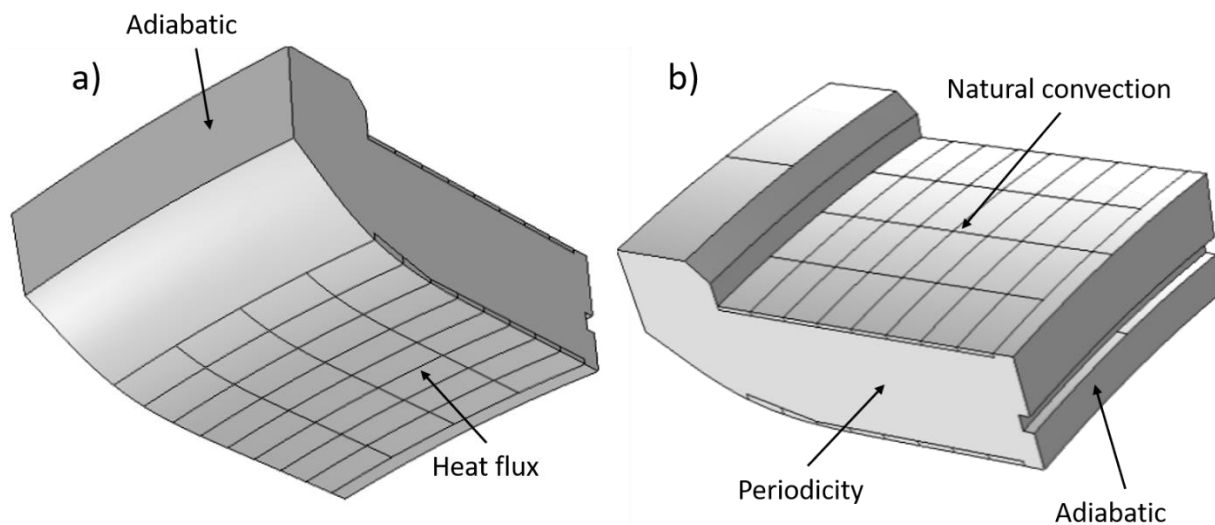


Figure 5-33. Comsol model with the boundary conditions applied during the calculation.

Figure 5-33 depicts the CAD model used in the calculation of the heat flux. We have included all the geometric features that may influence the behavior of the heat flux in this complex 3D geometry. As it can be observed, the top surface and the bottom surface has been divided in rectangles as is required for the inverse computation. The 8x4 array of surfaces is located in both, the inner and the outer surface of the flow path, with 8 divisions in the axial direction of the flow and 4 divisions in the circumferential direction. The temperature measured with the surface thermocouples correspond to the 8 different axial locations of the centers of the divisions. Therefore, the measurements taken in each one of the inner surface thermocouples is then used in the different axial locations in order to retrieve the heat flux. The circumferential direction is assumed to be uniform. Therefore, the same temperature taken in one axial location is extrapolated to the other 4 circumferential locations and we assume that the heat flux is the same all along the circumferential direction. This is assessed with the uniformity in the temperatures that we have observed in the Figure 5-31.

In order to validate the methodology, we need to compute the heat flux through the solid. For this step, we used a Crank-Nicolson 1D in-house conductive heat transfer code [129]. In this computation, in order to get the heat flux, we need to provide the temperatures readings at both sides of the slab of material we are computing as well as the thermal properties of the material and the thickness of the slab. Figure 5-34 shows the readings of the different thermocouples located in the flow path during one of the experiments. We observe that the temperature increases differently depending on the axial location, which effects the calculation of the heat flux. The temperature of the wall increases considerably during the experiment and it takes a while to reach steady state conditions, as observed in Figure 5-34.

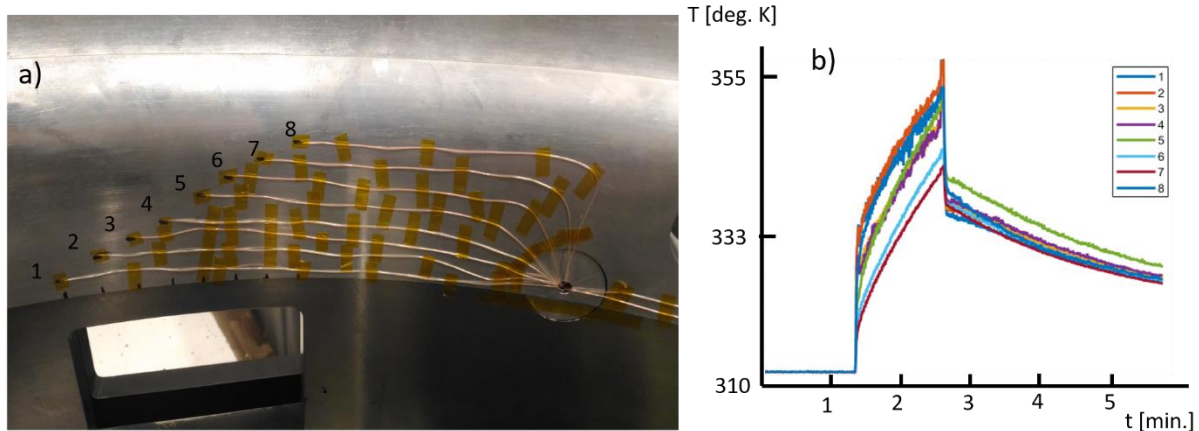


Figure 5-34. a) Surface thermocouples in the inner flowpath and b) inner metal temperature in the different axial locations over the measured surface.

The measurements on the outer surface are made with the infrared camera. In order to keep a uniform emissivity on the whole surface, the surface was coated with graphite paint. The infrared measurements were taken with the camera outside of the wind tunnel. To do this, one of the external windows was adapted in order to hold a Calcium Fluoride window. The camera needs to be calibrated with the window before taking the measurements. For this, a thermal stage painted with the same graphite temperature was used. Figure 5-35 shows the setup for the calibration of the camera with the window. The temperature that we are measuring is known and set by the thermal stage and the emissivity received by the camera can be calibrated for the graphite coating. Once we measure the set temperature we add the window between the thermal stage and the camera, which modifies the measured temperature. Then in the camera the emissivity is adjusted to match the measured temperature.

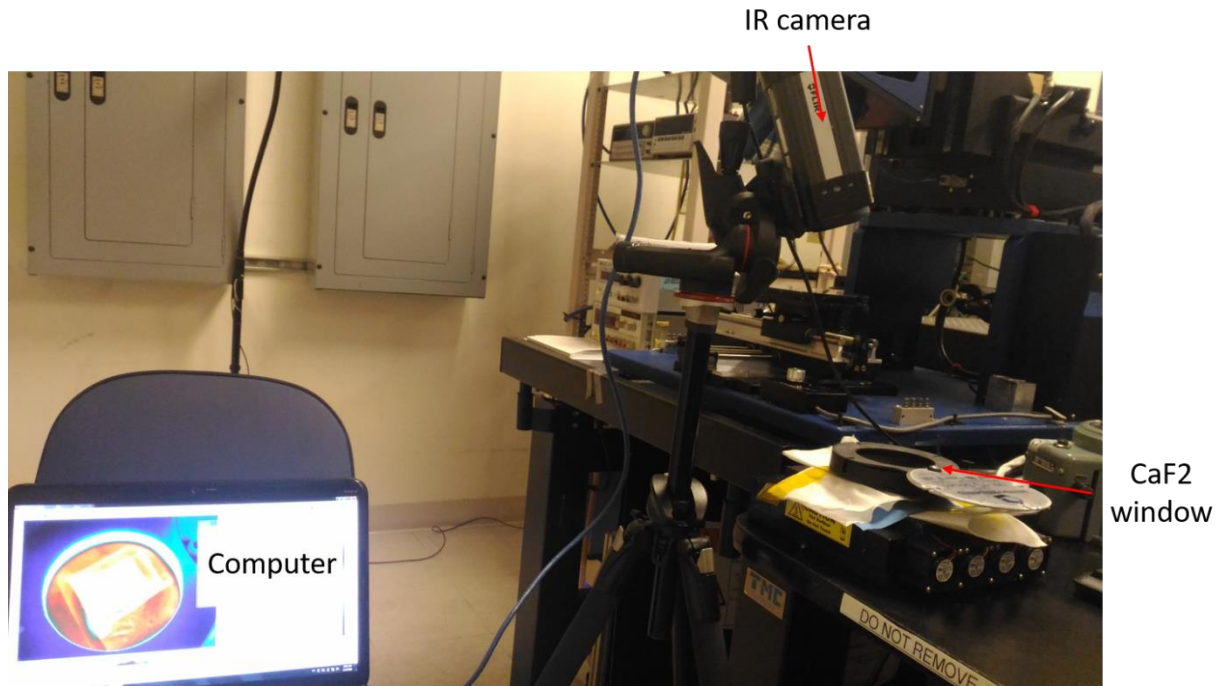


Figure 5-35. Calibration IR camera and IR transparent window set up.

Figure 5-35 shows part of the setup used to calibrate the IR camera with the  $\text{CaF}_2$  window. After the calibration, we setup the experiment in the wind tunnel and we run the different experiments. Figure 5-36 gathers some of the images from the IR camera at different timesteps during one of the experiments. All the data obtained in the five different experiments can be found in the Appendix E.

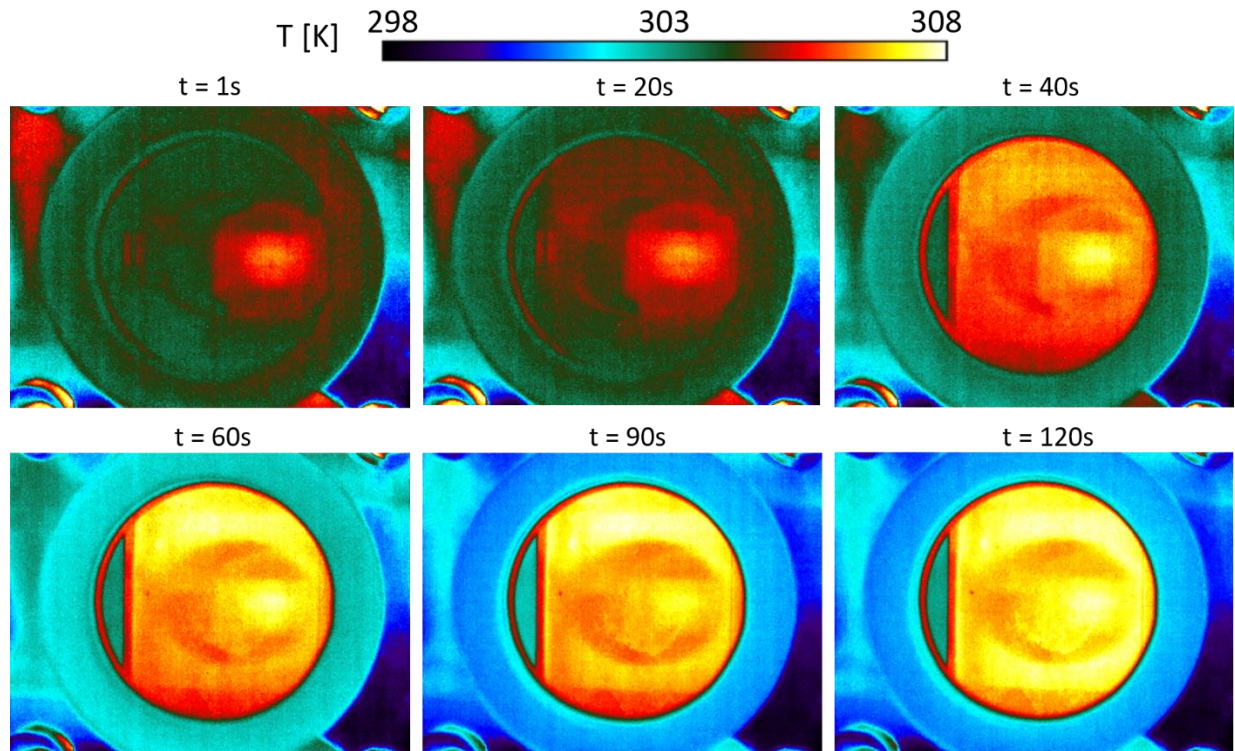


Figure 5-36. IR images taken during the experiment 1.

Extracting the data from the thermal images we observe that the temperature varies slightly in the axial direction; with higher temperatures upstream and lower temperatures downstream. Regarding the behavior in time we observe that the temperature increases during the experiment, with a time delay due to the thickness of the aluminum piece as shown in the Figure 5-37.



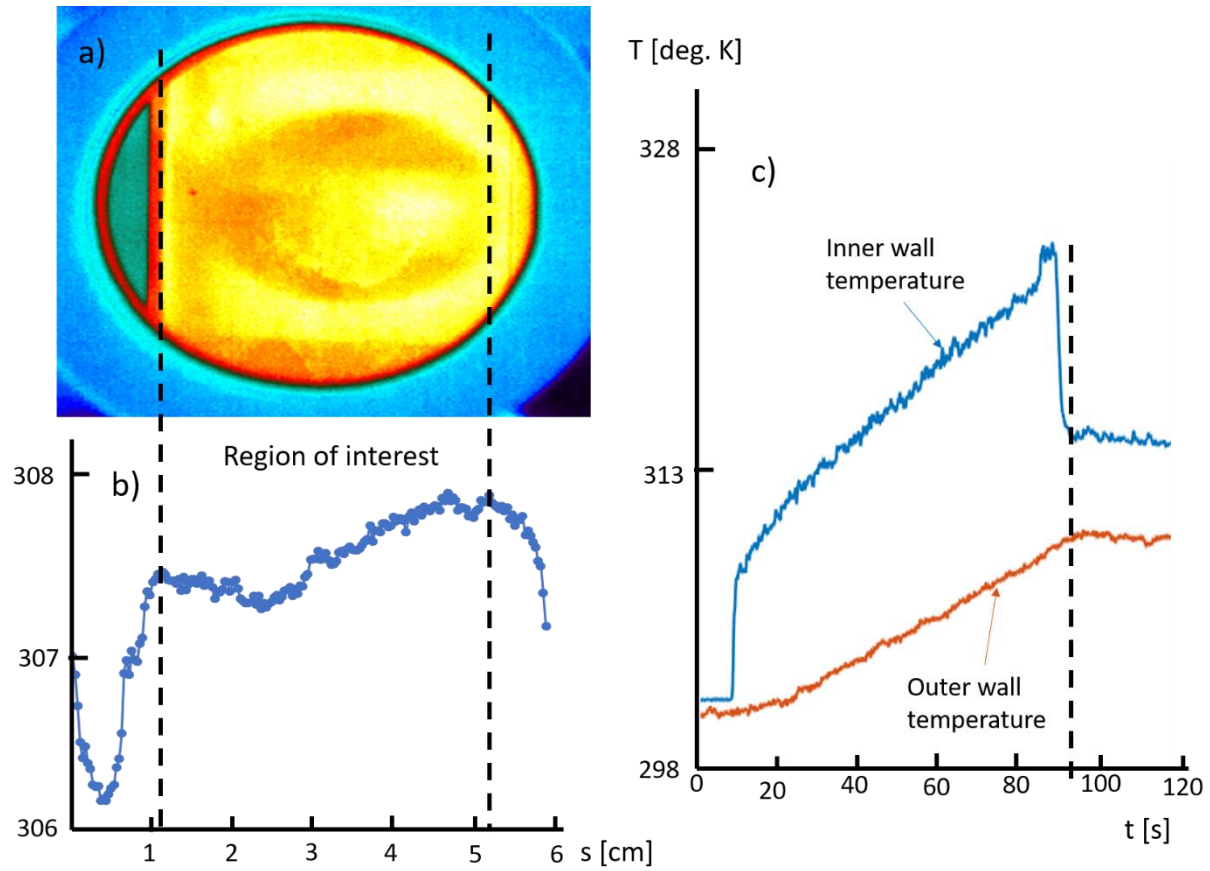


Figure 5-37. a) IR image of the region of interest. b) Spatial behavior of the temperature in the region inside the window. c) Temperature measured in the inner and outer surface of the shroud, used to compute the heat flux with the 1D heat conduction code.

This information over time is fed into the 1D code in order to compute the heat flux. This code is able to compute the temperature through the whole slab in space and time as it is depicted in the Figure 5-38 and compute the heat flux. For the baseline experiment the heat flux in both interfaces are calculated and represented in Figure 5-38.

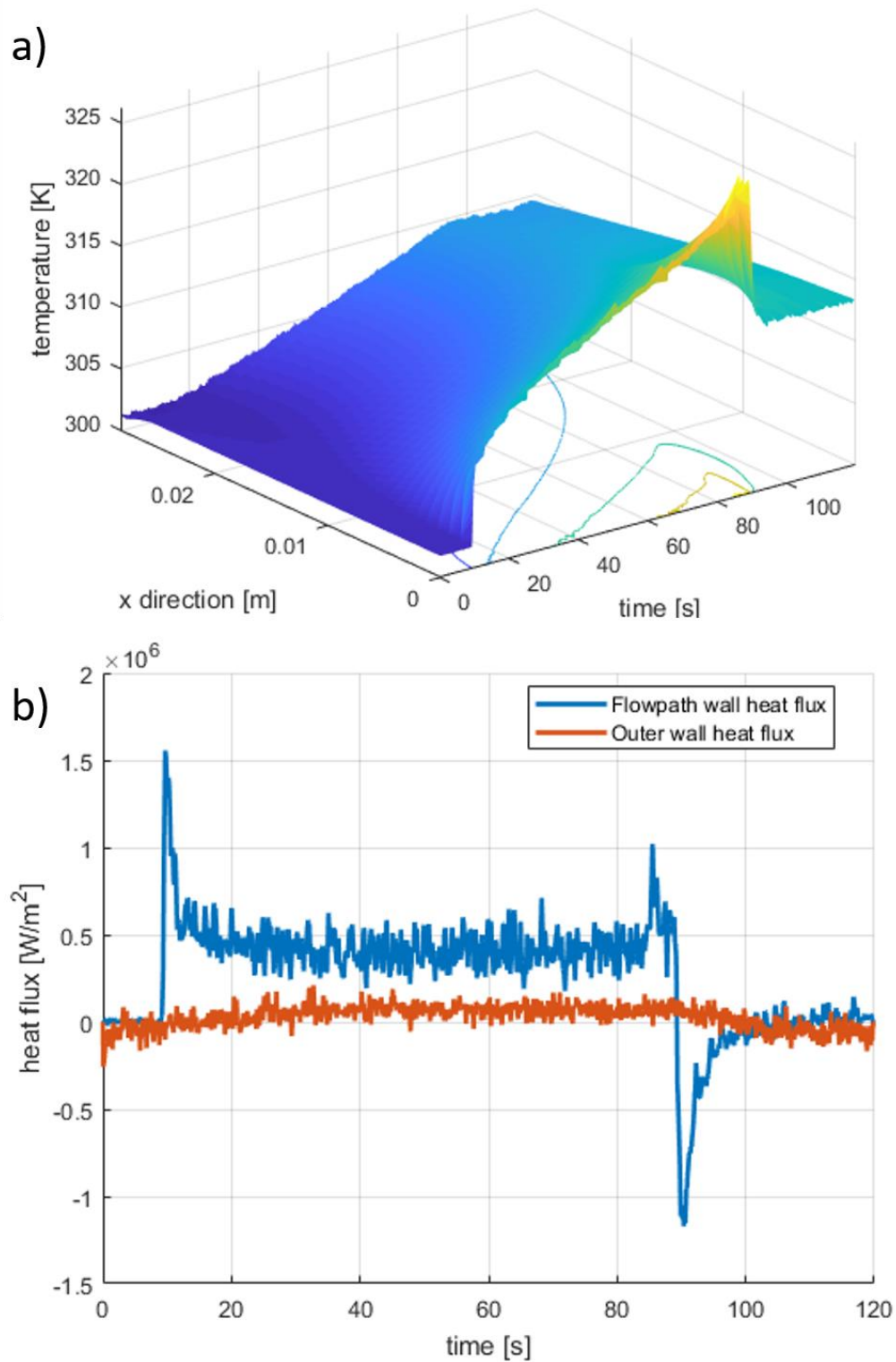


Figure 5-38. a) Temperature map in time and space for the calculation of the 1D heat conduction with the thermocouples in location 1. b) Heat flux computed with the 1D heat conduction code with the temperature from the thermocouple at location 1.



The heat fluxes for the inner surface are the ones we are retrieving with the inverse methodology. Only the information of the infrared camera was used by the Digital Filter Methodology to compute the heat flux. In this case we do not expect large gradients in the spatial domain, but we expect large gradients in the time domain. For this reason, the regularization term in time is large, limiting the gradients in the spatial domain and the regularization coefficient in time is small to allow for rapid changes. Figure 5-39 shows the comparison between the computed heat flux with the inverse method and the heat flux that were experienced in the wind tunnel. The retrieved heat flux matches the imposed heat flux in terms of magnitude and time behavior. As demonstrated in a previous section regarding the frequency retrieval, the thickness and the diffusivity of the material act like a filter for the high frequencies. As a result, the sudden increase of heat flux that can be seen at the beginning and end of the experiment is not captured by the inverse method. Since the method is not able to predict the large temporal excitations of heat flux, the behavior of the calculated heat flux is much smoother than the real heat flux. Additionally, the heat flux calculated by the inverse method starts to rise before the real time of opening of the valve; and the inverse method prematurely predicts the end of the experiment with a smaller gradient than in reality. In this evaluation of the method we are focused on the value of the heat flux during the steady operation of the experiment.

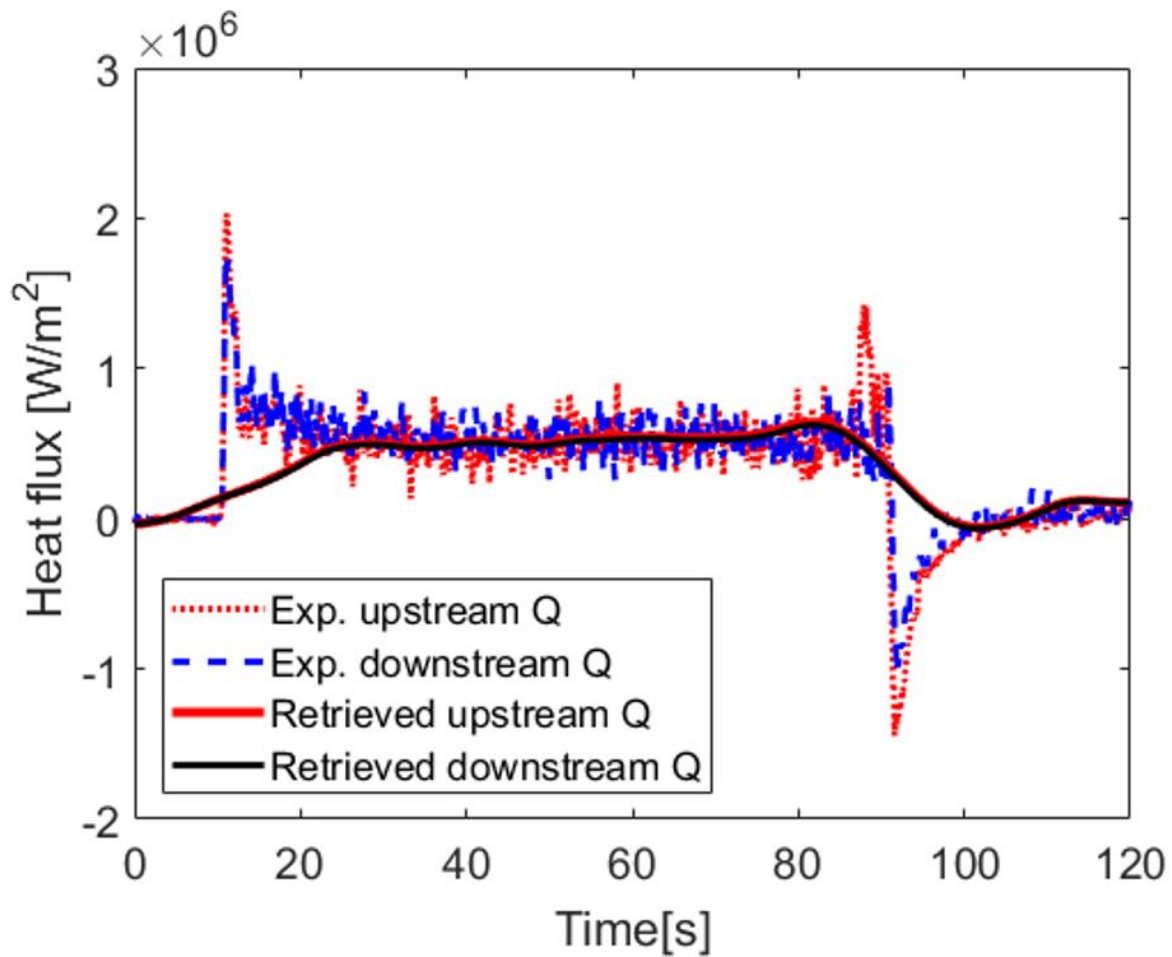


Figure 5-39. Comparison between the heat flux computed by the inverse heat conduction method and the heat flux through the casing.

We performed this calculation for each of the experiments and extracted the heat flux for each case. The heat fluxes were constant across the different experiments, instead the massflow and temperatures were varied across experimental runs. In the wind tunnel operation it is easier to control the massflow by actuating the valve than to control the temperature in the test section. This is because the thermal losses through the pipes bringing hot flow from the external heater to the test section vary greatly depending on the pressure and massflow conditions, as well as the thermal history of the experimental campaign. Due to the thermal history developing in the pipes, the

temperature in the test section for the first test of the day (when the pipes start at ambient temperature) is different from the second or third test of the same day (when the pipes are already heated up). This is why we chose to run the experiments at constant heat fluxes and vary the massflow and temperature in the test section. Figure 5-40 shows the comparison between the computed heat flux and the imposed heat flux in two different points of the casing.

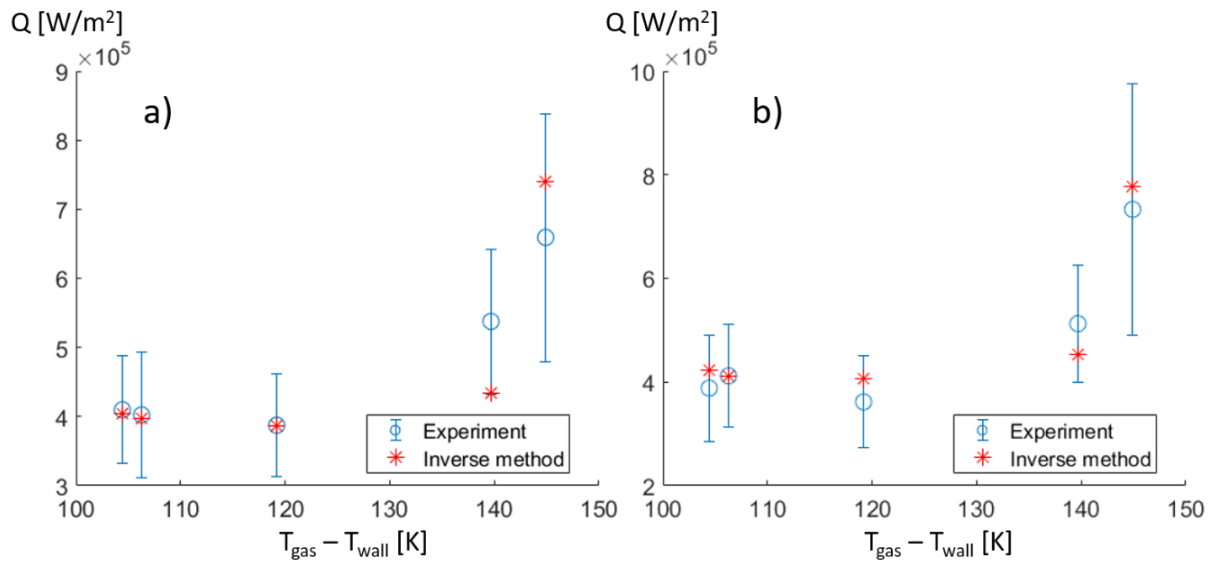


Figure 5-40. a) Heat flux comparison between the inverse method solution and the imposed heat flux in the upstream axial location in function of the difference between the gas temperature and the wall temperature. b) Heat flux comparison between the inverse method solution and the imposed heat flux in the downstream axial location in function of the difference between the gas temperature and the wall temperature.

Due to the difficulty in maintaining the temperature level, we observe that the temperature varies from experiment to experiment and there is no a clear trend in the value of heat flux with respect to the difference between the gas temperature and the metal temperature. This was observed as well in the evaluation of the heat flux with respect to the gas to wall temperature ratio as shown in Figure 5-41. There is not a large range of gas to wall temperature ratios analyzed in this experiment, but as observed in this section, there are constant values of this ratio through the whole

experiment. As the ratios do not differ in a large range amongst each other there is not a clear trend in the value of heat flux with respect to this ratio. The same is observed when we plot the heat flux with respect to the convective heat transfer coefficient computed based on the inlet total temperature in Figure 5-42.

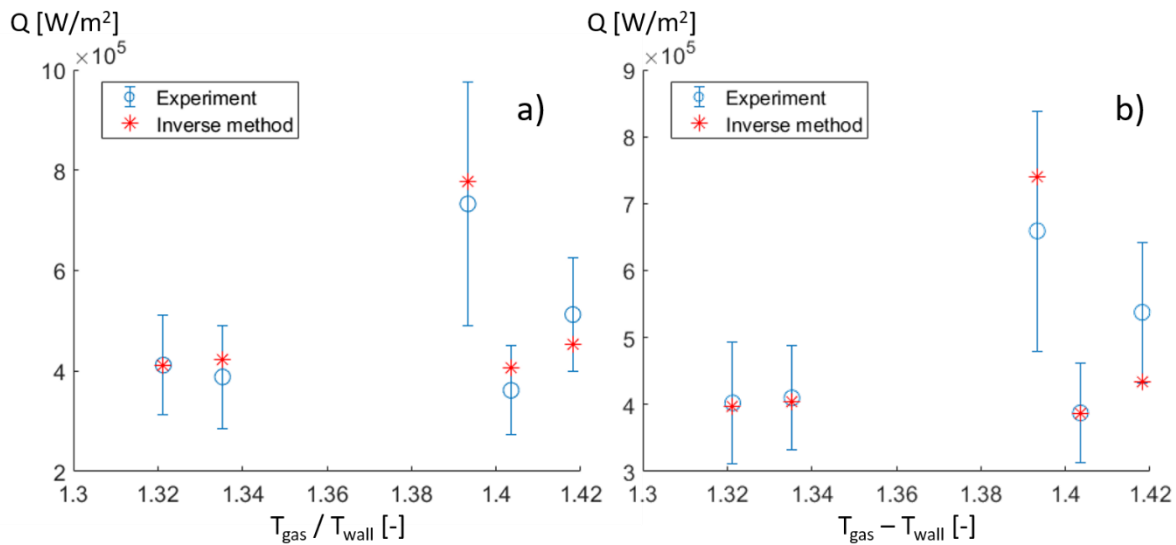


Figure 5-41. a) Heat flux comparison between the inverse method solution and the imposed heat flux in the upstream axial location in function of the gas to wall temperature ratio. b) Heat flux comparison between the inverse method solution and the imposed heat flux in the downstream axial location in function of the gas to wall temperature ratio.

The convective heat transfer coefficient was computed based on the temperature difference between the gas temperature and the metal temperature and the computed heat flux. Representing the heat flux as a function of the massflow, shows a clear trend that can be predicted by the inverse methodology as shown in the Figure 5-43.

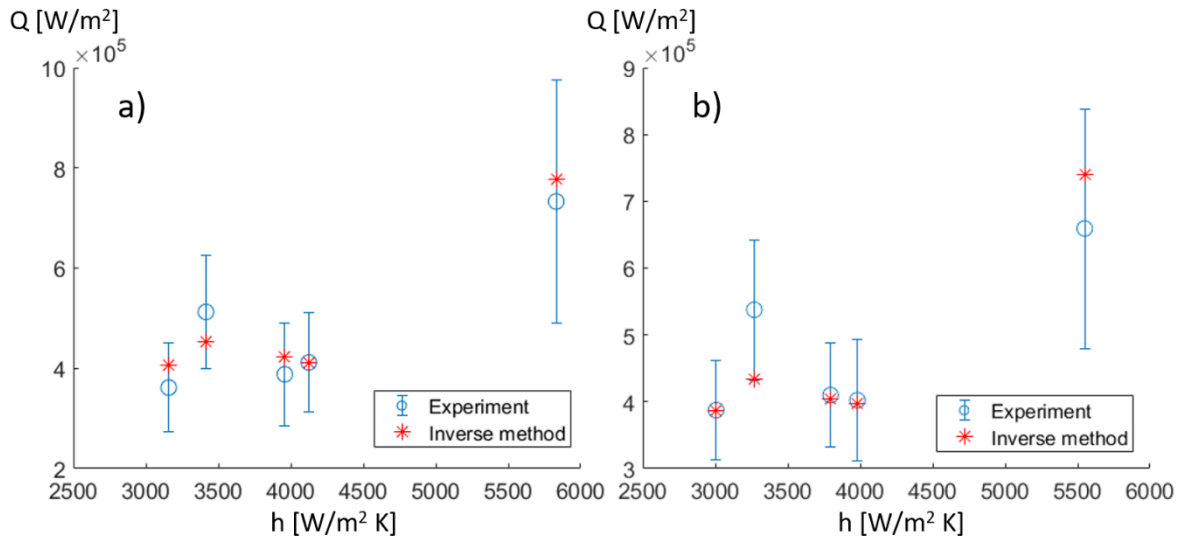


Figure 5-42.a) Heat flux comparison between the inverse method solution and the imposed heat flux in the upstream axial location in function of the convective heat transfer coefficient. b) Heat flux comparison between the inverse method solution and the imposed heat flux in the downstream axial location in function of the convective heat transfer coefficient.

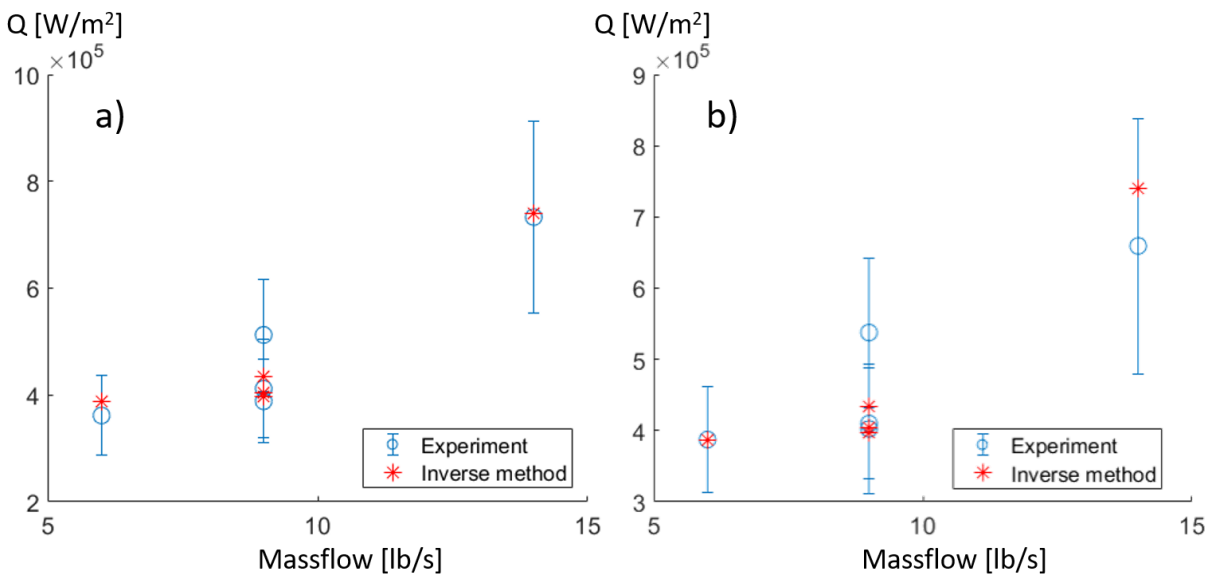


Figure 5-43. a) Heat flux comparison between the inverse method solution and the imposed heat flux in the upstream axial location in function of the massflow. b) Heat flux comparison between the inverse method solution and the imposed heat flux in the downstream axial location in function of the massflow.

### 5.3 Conclusions

In this chapter, the inverse methodologies have been applied to a macroscale field. The gas turbine application is a field where the inverse methodologies can be useful because of the harsh conditions that the sensors must withstand if they are located in the flowpath. In this application, we measure the temperature outside of the engine and using inverse methodologies we retrieve the heat flux through the engine casing. As expected, the heat flux varies with the conditions of the flow, so based on the temperature outside, we can retrieve the flow conditions using inverse methodologies. Based on the analysis performed in this chapter, we draw the following conclusions:

- A numerical analysis was performed coupling CFD with the Digital Filter inverse methodology in a conjugate heat transfer calculation. Based on this analysis, we observe that the method cannot predict with accuracy the behavior in time of the heat flux, but it can retrieve the mean value of given heat flux as well as the spatial distribution of heat flux since the spatial gradient in this macroscale application is more defined.
- The methodology is used to retrieve the inlet conditions of the flow which affect the heat flux through the casing. A numerical assessment of the methodology was used varying the upstream pressure conditions of the flow. The methodology could retrieve the upstream pressure measuring only the outer temperature of the casing with an error below 3%.
- A numerical analysis of the frequency content of the heat flux was performed as well. In this case the objective was to know the limiting factors of the inverse methodology to retrieve the blade passing frequency in case the measurement is performed in the outer rotor casing. The results reveal that the thickness of the solid acts as a low pass filter to the fluctuations of heat flux, therefore unless we are dealing with a very thin layer of metal and a very conductive material, the inverse method cannot predict blade passing frequency since everything is damped through the casing.

- The same situation is observed when we try to obtain the tip gap in the rotor using the same methodology. The flow features are so complex when varying the tip gap, that it is difficult to relate the tip gap with the heat transfer through the casing. In this case, it is not only varying in terms of magnitude but also in terms of location of the hotspots, since the flow morphology changes drastically for tight tip gaps.
- An annular cascade wind tunnel was designed and developed with emphasis in optical measurement techniques. This cascade can target large ranges of Re numbers and Mach Numbers (from subsonic to supersonic). This annular test section was used for the experimental validation of the inverse heat transfer method for the gas turbine application.
- An experimental validation of the Digital Filter Method in the gas turbine application was performed with good agreement between the imposed heat flux and the computed heat flux at different conditions of massflow and temperature of the flow. The experiments were performed in the inlet of a high pressure gas turbine and the methodology could retrieve the heat flux through the casing for the different cases. It is observed a clear trend of increase of heat flux with the increase of massflow and therefore this can be predicted using the inverse methodology. At different inlet temperatures, the heat flux did not vary, maybe because the difference in the temperatures was insufficient and the results were inconclusive based on the performed experiments.

## CHAPTER 6. CONCLUSIONS

The present doctoral research aimed to further develop some of the existing inverse methodologies and its implementation into two different engineering fields where it can be a breakthrough technology. These areas are the microelectronic packaging field and the gas turbine field.

Through the work performed in this doctoral research two inverse methodologies have been developed and improved with respect to the state-of-the-art in applied inverse heat transfer methodologies, these two methods were assessed in terms of robustness and computational efficiency and they were applied to the two different fields aforementioned.

Regarding the development and analysis of the inverse methods, this work has demonstrated the following aspects:

- Inverse methods are applicable to different fields. In heat transfer, they have been developed to determine unknown parameters such as heat flux distribution.
- Based on how the sensitivity parameter varies, some of the inverse methodologies are more attractive and robust than others. The sensitivity parameter is used by all methods in order to compute the unknown parameters.
- The Conjugate Gradient Method and the Digital Filter method were developed. Both methodologies can predict the imposed heat flux for simple cases analyzed using numerical models. The Conjugate Gradient Method is more precise, and the Digital Filter Method is much faster.
- The Conjugate Gradient Method converges slowly using as objective function the difference between the measured temperature and the computed temperature. Given the



iterative nature of the procedure, and based on model with a grid of a million cells, the computation can take days on a computer of 64 GB of RAM memory and 12 cores.

- An improvement of the CGM has been implemented based on a sequential estimation. Sequential estimation improves the computational efficiency of the method, but makes it more unstable for low number of future timesteps.
- The Digital Filter Method is a non-iterative procedure based on the solution to a system of equations which is ill-conditioned. The solution is highly dependent on the regularization terms in time and space that need to be included in order to improve the ill-condition nature of the system of equations. The solution takes seconds in the same computer that for the CGM takes days.
- An improvement of the DFM has been implemented, in order to include non-linearity of temperature dependent thermal properties and convection into the equation. This correction does not increase the time to solve the system of equations and it keeps the non-iterative nature of the DFM.
- The uncertainty associated to these methodologies is below 10% for all the analyzed cases and experimental validations.
- The following figure summarizes different aspects of the developed methodologies based on the numerical analysis.

	Conjugate Gradient Method		Digital Filter Method
	Whole domain	Sequential	
Iterative	Yes	Yes	No
Computational Efficiency	—	—	+++
Robustness	+++	+	—
Flexibility	—	—	+++
Precision	++	+++	+
Uncertainty	5.9%	5.9%	4.6%

Figure 6-1. Comparison summary of the different analyzed methodologies.

In the microscale application, the conclusions drawn through the numerical assessment and the experimental validation are:

- At the microscale, the spatial gradients are small and therefore all the methods based on the computation of gradients, such as all deterministic optimization methods, fail in the computation of the spatial location of the heat sources.
- The Conjugate Gradient Method is a gradient-based methodology and, therefore, have problems in predicting sudden changes of heat flux in space and time. The methodology was assessed numerically providing good agreement for simple and smooth changes of heat flux in time, but failing to capture the spatial gradients due to the small spatial gradients.

- The Digital Filter Method is the recommended method for this application. Not only for its flexibility but also for its accuracy of the results and its computational efficiency. It predicts the magnitude, the location, and the temporal behavior of the imposed heat flux.
- The methodology, if optimized to increase the computational efficiency, can be applied in real time and this makes it suitable for active thermal management of microelectronics.
- The number and location of the sensors inside of the microchip can be optimized using inverse methods. For this application of the inverse method, a Genetic Algorithm optimization combined with a Kriging interpolation method was developed.

Regarding the gas turbine application, the inverse method analysis demonstrated:

- That based on the numerical assessment, the method cannot predict with accuracy the behavior in time of the heat flux, but it can retrieve the mean value of given heat flux as well as the spatial distribution of heat flux since the spatial gradient in this macroscale application is more defined.
- The methodology can retrieve the inlet conditions of the flow. The methodology could retrieve the upstream pressure measuring only the outer temperature of the casing with an error below 3%.
- The thickness of the solid acts as a low pass filter to the fluctuations of heat flux, therefore unless we are dealing with a very thin layer of metal and a very conductive material, the inverse method cannot predict blade passing frequency since the frequency content is damped through the casing.
- The flow features are complex when varying the tip gap. The heat flux is not only varying in terms of magnitude but also in terms of location of the hotspots, since the flow

morphology changes drastically for tight tip gaps. Therefore the prediction of tip gaps using inverse methodologies is limited and needs more assessment.

- There is a good agreement between the imposed heat flux and the computed heat flux at different conditions of massflow and temperature in the experimental validation.
- The heat flux increases with increasing massflow and, therefore, this can be predicted using the inverse methodology. At different inlet temperatures, the heat flux did not vary, because the difference in the temperatures was insufficient and the results were inconclusive based on the performed experiments.

This doctoral research covered the development and application of inverse heat transfer methodologies, through simplified numerical analysis to experimental validations in each one of the applications. Throughout this project, the inverse methodologies were evaluated and improved with satisfactory results in their implementation in micro and macro-scale problems. Guidelines and recommendations about the best practice and methodology were identified given the application and the needs of each user. New insights into the inverse heat transfer problems were provided increasing the current state-of-the-art in the application of these methodologies in real engineering problems such as microelectronics and gas turbine development and monitoring.

## REFERENCES

- [1] Hadamard, Jacques (1902). “*Sur les problèmes aux dérivées partielles et leur signification physique*”. Princeton University, Bulletin. pp. 49–52.
- [2] Newton, I. , "In [experimental] philosophy particular propositions are inferred from the phenomena and afterwards rendered general by induction": "*Principia*", Book 3, General Scholium, at p.392 in Volume 2 of Andrew Motte's English translation published 1729.
- [3] Ambartsumian, Rouben V. "A life in astrophysics. Selected papers of Viktor A. Ambartsumian". *Astrophysics*. 41 (4): 328–330. doi:10.1007/BF02894658.
- [4] Tikhonov, A. N. and Arsenin, V. Y., “*Solution of Ill-Posed Problems*”, Winston & Sons, Washington, DC, 1977.
- [5] Ambartsumian, V. A. (1929). “*On the Relationship between the Solution and the Resolvent of the Integral Equation of the Radiative Balance*”. *Zeitschrift für Physik*, 52(3-4), 263-267.
- [6] Beck, J. V., Blackwell, B., St. Clair, C. R. Jr., “*Inverse heat Conduction. Ill-Posed Problems*”. A Wiley-Interscience Publication, N. Y., 308 pp.
- [7] Beck, J. V. and Arnold K. J., *Parameter Estimation in Engineering and Science*, Wiley, New York, 1977.
- [8] Jurkowsky, T., Jarny, Y. and Delaunay, D. "Estimation of Thermal Conductivity of Thermoplastics under Molding Conditions: an Apparatus and an Inverse Algorithm". *Int. J. Heat Mass Transfer*. 40. 4169-4181.

- [9] Alifanov, O. M, and Tryanin, A. P., "*Determination of the Coefficient of Internal Heat Exchange and the Effective Thermal Conductivity of a Porous Solid on the Basis of a Non-stationary Experiment*", J. Eng. Phys., 48(3), 356-365, 1985.
- [10] Alifanov, O. M., Artyukhin, E. and Romyantsev, A., "*Extreme Methods for Solving Ill-Posed Problems with Applications to Inverse Heat Transfer Problems*", Begell House, New York, 1995.
- [11] Artyukhin, E. A., "*Reconstruction of the Thermal Conductivity Coefficient from the Solution of the Nonlinear Inverse Problem*", J. Eng. Phys., 41(4), 1054-1058, 1981.
- [12] Dantas, L. and Orlande, H. R. B., "*A Function Estimation Approach for Determining Temperature-Dependent Thermophysical Properties*", Inverse Problems in Engineering, 3, 261-279, 1996.
- [13] Ho, C. H. and Ozisik, M. N., "*An Inverse Radiation Problem*", Int. J, Heat and Mass Transfer, 32, 335-341, 1989
- [14] Rupert Jr., N., Raynaud, M. and Sacadura, J. F., "*A Method for the Solution of the Coupled Inverse Heat Conduction-Radiation Problem*", ASME J Heat Transfer, 118, 10-17, 1996.
- [15] Li, H. Y. and Ozisik, M. N., "*Inverse Radiation Problem for Simultaneous Estimation of Temperature Profile and Surface Reflectivity*", J. Thermophysics and Heat Transfer, 7, 88-93, 1993.
- [16] Bokar, J. and Ozisik, M. N., "*An Inverse Problem for the Estimation of Radiation Temperature Source Term in a Sphere*", Inv. Problems in Engineering, 1, 191-205, 1995.

- [17] Zabaras, N. and Ngugen, T. H., "*Control of the Freezing Interface Morphology in Solidification Processes in the Presence of Natural Convection*", Int. J Num. Meth. Eng., 38, 1555- 1578, 1995.
- [18] Zabaras, N. and Yang, G., "*A Functional Optimization Formulation and Implementation of an Inverse Natural Convection Problem*". Comput. Methods Appl. Mech. Engrg., 144,245-274, 1997.
- [19] Yang, G. and Zabaras, N., "*An Adjoint Method for the Inverse Design of Solidification Processes with Natural Convection*", Int. J. Num Meth. Eng., 42, 1121-1 144, 1998.
- [20] Machado, H. A., Orlande, H. R. B., "*Inverse Analysis of Estimating the Timewise and Spacewise Variation of the Wall Heat Flux in a Parallel Plate Channel*", Int. J Numer. Meth. Heat and Fluid Flow, 7, 696-710, 1997.
- [21] Bokar, J. C. and Ozisik, M. N., "*An Inverse Analysis for Estimating Time Varying Inlet Temperature in Laminar Flow Inside a Parallel Plate Duct*", Int. J. Heat Mass Transfer, 38, 39-45, 1995.
- [22] Machado, H.A. and Orlande, H.R.B., "*Inverse Problem of Estimating the Heat Flux to a Non-Newtonian Fluid in a Parallel Plate Channel*", RBCM, J. Braz. Soc. Mech. Sciences, 20, 5 1-6 1, 1998,
- [23] Huang. C. H., Ozisik, M. N., and Sawaf, B. "*Conjugate Gradient Method for Determining Unknown Contact Conductance during Metal Casting*", Int. J. Heat Mass Transfer, 35. 1779- 1789, 1992.
- [24] Ozisik. M. N., Orlande, H. R. B., Hector. L.G. and Anyalebechi, P.N., "*Inverse Problem of Estimating Interface Conductance During Solidification via Conjugate Gradient Method*", J. Materials Proc. Manufact. Science, 1,2 13-225, 1992.

- [25] Orlande, H. R. B. and Ozisik , M . N., "*Inverse Problem of Estimating Interface Conductance Between Periodically Contacting Surfaces*", J. Thermophysics and Heat Transfer. 7, 3 19-325, 1993.
- [26] Orlande, H. R. B. and Ozisik, M. N., "*Determination of the Reaction Function in a Reaction-Diffusion Parabolic Problem*," J. Heat Transfer, 116, 1041-1044, 1994.
- [27] Brizaut, J.S., Delaunay, D., Gamier, B. and Jarny, Y., "*Implementation of an Inverse Method for Identification of Reticulation Kinetics from Temperature Measurements on a Thick Sample*", Int. J Heat Mass Transfer, 36, 4039-4097, 1993.
- [28] Dulikravich, G. S. and Martin, T. J., "*Inverse Shape and Boundary Condition Problems and Optimization in Heat Conduction*", Chapter 10 in Advances in Numerical Heat Transfer, 1, 38 1-426, Minkowycz, W. J. and Sparrow, E. M. (eds.), Taylor and Francis, 1996.
- [29] Huang, C.H. and Chiang, C.C., "*Shape Identification Problem in Estimating Geometry of Multiple Cavities*", AIAA J. Therm. and Heat Transfer, 12,270-277, 1998.
- [30] Ozisik, M. Necati, Orlande R. B. Helcio, "*Inverse heat transfer: fundamentals and applications*. CRC Press, 2000.
- [31] Bergman, Theodore L., and Frank P. Incropera."Fundamentals of heat and mass transfer." John Wiley & Sons, 2011.
- [32] Stolz, G., Jr., "*Numerical Solutions to an Inverse Problem of Heat Conduction for Simple Shapes*", J. Heat transfer 82, 20-26, (1960).
- [33] Keanini R.G., Ling X., Cherukuri H.P., "*A modified sequential function specification finite element-based method for parabolic inverse heat conduction problems*", Comput. Mech. 36 (2) (2005) 117–128.



- [34] Giedt, W. H., "*The Determination of Transient Temperatures and Heat Transfer at a Gas-metal Interface Applied to a 40-mm Gun Barrel*", Jet Propulsion, 25, 158-162, 1955.
- [35] Masket, A. V. and Vastano A. C., "*Interior Value Problems of Mathematics Physics, Part II. Heat Conduction*", American Journal of Physics, 30, 796-803, 1962.
- [36] Sabherwal, K. C., "*An Inverse Problem of Transient Heat Conduction*", Indian J. of Pure and Applied Physics, 3, 397-398, 1965.
- [37] Beck, J. V., "*Surface Heat Flux Determination Using an Integral Method*", Nuclear Engineering and Design, 7, 170- 178, 1968.
- [38] Abramovich, B. G. and Trofimov, V. S., "*Integral Form of the Inverse Heat Conduction Problem for a Hollow Cylinder*", High Temp. (USSR), 17,552-554, 1979.
- [39] Hills, R. G., Mulholland, G. P., and Matthews, L. K., "*The Application of the Backus-Gilbert Method to the Inverse Heat Conduction Problem in Composite Media*", ASME Paper No. 82-HT-26, 1982.
- [40] Hills, R. G, and Mulholland, G. P., "*The Accuracy and Resolving Power of One-Dimensional Transient Inverse Heat Conduction Theory as Applied to Discrete and Inaccurate Measurements*" International Journal Heat and Mass Transfer, 22.8 (1979): 1221-1229.
- [41] Temkin, A. G., "Integral Solutions of Inverse Heat Conduction Problems", Heat Transfer Sov. Res., 10, 20-32, 1978.
- [42] Burggraf, O. R., "*An Exact Solution of the Inverse Problem in Heat Conduction Theory and Applications*", J. Heat Transfer, 86C, 373-382, 1964.
- [43] Makhin, J. A. and Shmukin, A. A., "*Inverse Problems of Unsteady Heat Conduction*", Heat Transfer - Sov. Res., 5, 160- 165, 1973.

- [44] Langford, D., *"New Analytical Solutions of the One-Dimensional Heat Equation for Temperature and Heat Flow Rate Both Prescribed at the Same Fixed Boundary (with Applications to the Phase Change Problem)"*, Quarterly of Applied Mathematics, 24, 3 15-322, 1976.
- [45] Koverlyano, V. A., *"Inverse Problem of Non-Steady Thermal Conductivity"*, Teplojzika Vysokikh Temp., 5, 141-148, 1967.
- [46] Mulholland, G. P. and San Martin, R. L., *"Indirect Thermal Sensing in Composite Media"*, Int. J. Heat Mass Transfer, f 6, 1056- 1060, 1973.
- [47] Mulholland. G. P., Gupta, B. P., and San Martin, R. L., *"Inverse Problem of Heat Conduction in Composite Media"*, ASME Paper No. 75-WA/HT- 83, 1975.
- [48] Frank, I., *"An Application of Least Squares Method to the Solution of the Inverse Problem of Heat Conduction"*, J. Heat Transfer, 8, 378-379, 1963.
- [49] Murio, D. A., *"The Mollification Method and the Numerical Solution of an Inverse Heat Conduction Problem"*, SIAMJ. Sci. Star. Comput. 2, 17-34, 1981.
- [50] Murio, D. A., *"The Mollification Method and the Numerical Solution of the Inverse Heat Conduction Problem by Finite Difference"*, Comput. Math. Appl., 17, 1385-1 896, 1989.
- [51] Murio, D. A, *"The Mollification Method and the Numerical Solution of Ill-Posed Problems"*, Wiley Inter-science, New York, 1993.
- [52] Weber, C. F., *"Analysis and Solution of the Ill-posed Inverse Heat Conduction Problem"*, Int. J. Heat Mass Transfer, 24. 1783- 1792, 1981.
- [53] Novikov, N. A., *"Hyperbolic Equation of Thermal Conductivity: Solution of the Direct and Inverse Problems for a Semi-Infinite Bar"*, J. Eng. Physics, 35, 1253-1257, 1978.

- [54] Novikov, A., *"Solution of the Linear One-Dimensional Inverse Heat-Conduction Problem on the Basis of a Hyperbolic Equation"*, J. Eng. Phys., 40(6). 1093- 1098, 1981.
- [55] Matsevityi, Y.M. and Multanovskii, A. V., *"Pointwise Identification of Thermophysical Characteristics"*, J. Eng. Phys., 49(6), 1392-1 397, 1986.
- [56] Alifanov, O. M., *"Solution of an Inverse Problem of Heat-Conduction by Iterative Methods"*, J. Eng. Phys., 26(4), 47 1-476, 1974.
- [57] Alifanov, O. M. and Kerov, N. V., *"Determination of External Thermal Load Parameters by Solving the Two-Dimensional Inverse Heat-Conduction Problem"*, J. Eng. Phys., 41(4), 1049- 1053, 1981.
- [58] Alifanov, O. M. and Mikhailov, V. V., *"Solution of the Overdetermined Inverse Problem of Thermal Conductivity Involving Inaccurate Data"*, High Temperature, 23(1), 112-1 17, 1985.
- [59] Artyukhin, E.A. and Nenarokomov, A.V., *"Coefficient Inverse Heat Conduction Problem"*, J. Eng. Phys., 53, 1085- 1090, 1988.
- [60] Artyukhin, E. A., *"Iterative Algorithms for Estimating Temperature Dependent Thermophysical Characteristics"*, 1<sup>st</sup> International Conference on Inverse Problems in Engineering - Proceedings, 10 1 108, Palm Coast, F1, 1993.
- [61] Artyukhin, E. A. and Rumyantsev, S. V., *"Descent Steps in Gradient Methods of Solution of Inverse Heat Conduction Problems"*, J. Eng. Phys., 39,865-868, 1981.
- [62] Colaço, M. J., Orlande, H. R., & Dulikravich, G. S. (2006). *"Inverse and optimization problems in heat transfer."* Journal of the Brazilian Society of Mechanical Sciences and Engineering, 28(1), 1-24.

- [63] Bailleul, J. L., Delaunay, D. and Jamy, Y., "*Optimal Thermal Processing of Composite Materials: An Inverse Algorithm and Its Experimental Validation*", 11<sup>th</sup> International Heat Transfer Conference, 5, 87-92, Kyongju, Korea, 1998.
- [64] Alencar Jr., J.P., Orlande, H.R.B. and Ozisik, M.N., "A Generalized Coordinates Approach for the Solution of Inverse Heat Conduction Problems", 11<sup>th</sup> International Heat Transfer Conference, 7, 53-58, Kyongju, Korea, 1998.
- [65] Carvalho, R.N., Orlande, H.R.B. and Ozisik, M.N., "Estimation of the Boundary Heat Flux in Grinding via the Conjugate Gradient Method", Heat Transfer Engr., (to appear), 2000.
- [66] Colaço, M.J. and Orlande, H.R.B., "A Comparison of Different Versions of the Conjugate Gradient Method of Function Estimation", Num. Heat Transfer - Part A, (to appear), 1999.
- [67] Chen, Tsung-Chien, and Pan-Chio Tuan. "*Input estimation method including finite-element scheme for solving inverse heat conduction problems.*" Numerical Heat Transfer, Part B 47.3 (2005): 277-290.
- [68] Banim RS, Tierney MJ, Brett PN. "*The estimation of fluid temperatures through an inverse heat conduction technique*", Numerical Heat Transfer Part A, 2000; 37:465–76.
- [69] M. Monde, M. Kosaka, Y. Mitsutake, "*Simple measurement of thermal diffusivity and thermal conductivity using inverse solution for one-dimensional heat conduction*", International Journal of Heat and Mass Transfer, 53 (2010), pp. 5343-5349.
- [70] Luchesi, Vanda M., and Reginaldo T. Coelho. "*An inverse method to estimate the moving heat source in machining process.*" Applied Thermal Engineering 45 (2012): 64-78.
- [71] Tikhonov, A. N., "*Solution of Incorrectly Formulated Problems and the Regularization Method*", Soviet Math. Dokl. , 4(4), 1035- 1038, 1963.

- [72] Tikhonov, A. N., *"Regularization of Incorrectly Posed Problems"*, Soviet Math. Dokl. , 4(6), 1624- 1627, 1963.
- [73] Tikhonov, A. N., *"Inverse Problems in Heat Conduction"*, J. Eng. Phys., 29(1), 816-820, 1975.
- [74] Busby, H. R. and Trujillo, D. M., *"Numerical Solution of a Two Dimensional Inverse Heat Conduction Problems"*, Int. J. Num. Meth. Eng., 21,349-359, 1985.
- [75] Trujillo, D. M. and Busby, H. R., *"Practical Inverse Analysis in Engineering"*, CRC Press, Boca Raton, 1997.
- [76] Bialecki, R.A., Kassab, A.J. and Ostrowski, Z., 2003, *"Application of the proper orthogonal decomposition in steady state inverse problems"*. In: M. Tanaka (Ed.) Inverse Problems in Engineering Mechanics IV (Amsterdam: Elsevier BV), pp. 3–12.
- [77] Ostrowski Z., Bialecki R. A. & Kassab A. J., *"Solving inverse heat conduction problems using trained POD-RBF network inverse method,"* Inverse Problems in Science and Engineering, 16:1, 39-54,2008. DOI: 10.1080/17415970701198290.
- [78] Ostrowski, Z., Bialecki, R.A. and Kassab, A.J., 2005, *"Estimation of constant thermal conductivity by use of proper orthogonal decomposition"* Computational Mechanics, 37(1), 52–59.
- [79] Fic, A., Bialecki, R.A, Kassab, A.J., 2005, *"Solving transient nonlinear heat conduction problems by proper orthogonal decomposition and the finite-element method"*, Numerical Heat Transfer Part B, 48(2), 103–124.
- [80] Alifanov, O. M. *"Inverse heat transfer problems"*. Springer Science & Business Media, 2012.

- [81] Marquardt, D. W., "An Algorithm for Least Squares Estimation of Nonlinear Parameters", J, Soc. Ind. Appl. Math, 11, 431-441, 1963.
- [82] Beck, J. V., "Criteria for comparison of methods of Solution of the Inverse Heat Conduction Problem", Nuclear Engineering and Design, 53, 11-22, 1979.
- [83] Levenberg, K., "A Method for the Solution of Certain Non-linear Problems in Least-Squares", Quart. Appl. Math, 2, 164-168, 1944.
- [84] Alifanov, O. M., "Determination of Heat Loads from a Solution of the Nonlinear Inverse Problem." High Temperature. 15. 498-504. 1977.
- [85] Bard, Y. B., *Nonlinear Parameter Estimation*, Acad. Press, New York, 1974.
- [86] Dennis, J. and Schnabel, R., *Numerical Methods for Unconstrained Optimization and Nonlinear Equations*, Prentice Hall, 1983.
- [87] Beyer, W. H. Ed., "Handbook of Tables for Probability and Statistics," 2<sup>nd</sup> ed., The Chemical Rubber Co., Cleveland, OH, 1968, p.484.
- [88] H. Najafi, K.A. Woodbury, J.V. Beck, "A filter based solution for inverse heat conduction problems in multi-layer mediums", Int. J. Heat Mass Transfer, 83, (April 2015) 710–720.
- [89] H. Najafi, K.A. Woodbury, J.V. Beck, "Real time solution for inverse heat conduction problems in a two-dimensional plate with multiple heat fluxes at the surface", Int. J. Heat Mass Transfer, 91, (September 2015) 1148-1156.
- [90] J. Blum, W. Marquardt, "An optimal solution to inverse heat conduction problems based on frequency domain interpretation and observers", Numer. Heat Transfer Part B Fundam. 32 (4) (1997) 453–478.

- [91] K.D. Cole, J.V. Beck, A. Haji-Sheikh, B. Litkouhi, *"Heat conduction using green's functions,"* Series in Computational and Physical Processes in Mechanics and Thermal Sciences, Taylor & Francis Group, 2010.
- [92] Fernandes A.P., Guimarães G., *"Heat conduction analytical solutions to be applied in boundary conditions obtained from discrete data,"* J. Energy Power Eng. 7 (2013) 1527–1532.
- [93] Fernandes, A. P., dos Santos, M. B., & Guimarães, G. (2015). *"An analytical transfer function method to solve inverse heat conduction problems"*. Applied Mathematical Modelling, 39(22), 6897-6914.
- [94] Dulikravich, G. S. and Martin, T. J., 1996, *"Inverse Shape and Boundary Condition Problems and Optimization in Heat Conduction"*, Chapter 10 in Advances in Numerical Heat Transfer, 1, 381-426, Minkowycz, W. J. and Sparrow, E. M. (eds.), Taylor and Francis.
- [95] Woodbury, K., 2002, *"Inverse Engineering Handbook"*, CRC Press, Boca Raton.
- [96] Denisov, A. M., 1999, *"Elements of the Theory of Inverse Problems"*, VSP, Netherlands.
- [97] Zubelli, J. P., 1999, *"An Introduction to Inverse Problems: Examples, Methods and Questions"*, Institute of Pure and Applied Mathematics, Rio de Janeiro, Brazil.
- [98] Wang, Y., Yagola, A.G. and Yang, C., 2011. *"Optimization and regularization for computational inverse problems and applications,"* Beijing:: Higher Education Press.
- [99] Ramm, A. G., Shivakumar, P.N. and Strauss, A. V. (eds.), 2000, *"Operator Theory and Applications"*, Amer. Math. Soc., Providence.
- [100] Byrne, C.L., 2014. *"Iterative Optimization in Inverse Problems,"* Chapman and Hall/CRC.

- [101] Kurpisz, K. and Nowak, A. J., 1995, *“Inverse Thermal Problems”*, WIT Press, Southampton, UK.
- [102] Yagola A. G., Kochikov, I.V., Kuramshina, G. M. and Pentin, Y. A., 1999, *“Inverse Problems of Vibrational Spectroscopy”*, VSP, Netherlands.
- [103] Bard, Y. B., 1974, *“Nonlinear Parameter Estimation”*, Acad. Press, New York.
- [104] Broyden, C.G., *“A Class of Methods for Solving Nonlinear Simultaneous Equations”*, 1965, Math. Comp., vol. 19, pp. 577-593.
- [105] Broyden, C.G., 1967, *“Quasi-Newton Methods and Their Applications to Function Minimization”*, Math. Comp., vol. 21, pp. 368-380.
- [106] Fletcher, R. and Powell, M.J.D., 1963, *“A Rapidly Convergent Descent Method for Minimization”*, Computer J., vol. 6, pp. 163-168.
- [107] Davidon, W. C. (1959). *“VARIABLE METRIC METHOD FOR MINIMIZATION”* (No. ANL-5990). Argonne National Lab., Lemont, III.
- [108] Ozisik, M. N., *Heat Conduction*, 2nd ed., Wiley, New York, 1993.
- [109] Huang, C. H. and Ozisik, M. N., "Optimal Regularization Method to Determine the Strength of a Plane Surface Heat Source", Int. J. Heat and Fluid Flow, 12, 173-178, 1991.
- [110] Weber, Charles F. *Analysis and solution of the ill-posed inverse heat conduction problem*. International Journal of Heat and Mass Transfer 24.11 (1981): 1783-1792.
- [111] K.J. Dowding, J.V. Beck, *“A sequential gradient method for the inverse heat conduction problems,”* J. Heat Transfer 121 (1999) 300–306.
- [112] Goldberg, D. E., *“Genetic Algorithms in Search, Optimization and Machine Learning,”* Addison Wesley, Reading, MA, 1989.



- [113] Deb, K., 2002, "*Multi-Objective Optimization Using Evolutionary Algorithms*", John Wiley & Sons.
- [114] Mishra SC, Roy HK. "*Solving transient conduction–radiation problems using the lattice Boltzmann method and the finite volume method*". J. Comput. Phys., 2007, 223:89–107.
- [115] Das, R., Mishra, S. C., Ajith, M., & Uppaluri, R., "*An inverse analysis of a transient 2-D conduction–radiation problem using the lattice Boltzmann method and the finite volume method coupled with the genetic algorithm.*" Journal of Quantitative Spectroscopy and Radiative Transfer 109.11 (2008): 2060-2077.
- [116] Storn, R. and Price, K.V., 1996, "*Minimizing the Real Function of the ICEC'96 Contest by Differential Evolution*", IEEE Conf. on Evolutionary Computation, pp. 842-844.
- [117] Eberhart, R., Shi, Y. and Kennedy, J., 2001, "*Swarm Intelligence*", Morgan Kaufmann.
- [118] Kennedy, J. and Eberhart, R.C., 1995, "*Particle Swarm Optimization*", Proceedings of the 1995 IEEE International Conference on Neural Networks, vol. 4, pp. 1942-1948.
- [119] Naka, S., Yura, T.G. and Fukuyama, T., 2001, "*Practical Distribution State Estimation using Hybrid Particle Swarm Optimization*", Proceedings IEEE Power Engineering Society, Winter Meeting, Columbus, Ohio, January 28-February 1st.
- [120] Corana, A., Marchesi, M., Martini, C. and Ridella, S., 1987, "*Minimizing Multimodal Functions of Continuous Variables with the Simulated Annealing Algorithm*", ACM Transactions on Mathematical Software, vol. 13, pp. 262-280.
- [121] Goffe, W.L., Ferrier, G.D. and Rogers, J., 1994, "*Global Optimization of Statistical Functions with Simulated Annealing*", Journal of Econometrics, vol. 60, pp. 65-99.
- [122] Colaço, M.J., Dulikravich, G.S. and Martin, T. J., 2003a, "*Optimization of Wall Electrodes for Electro-Hydrodynamic Control of Natural Convection Effects during*

- Solidification*”, In: ASME International Mechanical Engineering Congress & Exposition, Washington, DC, November.
- [123] Colaço, M.J., Dulikravich, G.S. and Martin, T. J., 2004, “*Optimization of Wall Electrodes for Electro-Hydrodynamic Control of Natural Convection Effects During Solidification*”, Materials and Manufacturing Processes, Vol. 19, No. 4, pp. 719-736.
- [124] Dulikravich, G.S., Colaço, M.J., Martin, T.J. and Lee, S., 2003b, “*An Inverse Method Allowing User-Specified Layout of Magnetized Micro-Fibers in Solidifying Composites*”, Journal of Composite Materials, vol. 37, no. 15, pp. 1351-1365.
- [125] Dulikravich, G.S., Colaço, M.J., Dennis, B.H., Martin, T.J. and Lee, S., 2004, “*Optimization of Intensities, and Orientations of Magnets Controlling Melt Flow during Solidification*”, Materials and Manufacturing Processes, vol. 19, iss. 4, pp. 695-718
- [126] Neto, F. D. M., and da Silva Neto, A. J. (2012). “*An introduction to inverse problems with applications*”, Springer Science & Business Media.
- [127] Andreoli V, G. Cuadrado D, Paniagua G. “*Prediction of the Turbine Tip Convective Heat Flux Using Discrete Green Functions*”. ASME. Turbo Expo: Power for Land, Sea, and Air, Volume 5B: Heat Transfer ():V05BT22A011. doi:10.1115/GT2017-64080.
- [128] Sieverding, C. H., Arts, T., Denos, R., & Martelli, F. (1996). “*Investigation of the flow field downstream of a turbine trailing edge cooled nozzle guide vane*”. Journal of Turbomachinery, 118(2), 291-300.
- [129] Saavedra, J., Paniagua, G. and Saracoglu, B.H., 2017. “*Experimental Characterization of the Vane Heat Flux Under Pulsating Trailing-Edge Blowing*”, Journal of Turbomachinery, 139(061004).

- [130] Jarny Y, Ozisik MN, Bardon JP. "*A general optimization method using adjoint equation for solving multidimensional inverse heat conduction*". International Journal of Heat and Mass Transfer. 1991; 34(11):2911–919.
- [131] Sousa, Jorge Fernandes Lopes, et al. "*Three-dimensional (3D) inverse heat flux evaluation based on infrared thermography.*" Quantitative InfraRed Thermography Journal 9.2 (2012): 177-191.
- [132] Sousa, J., et al. "*Inverse heat flux evaluation using conjugate gradient methods from infrared imaging.*" 11th International Conference on Quantitative Infrared Thermography. 2012.
- [133] Huang, Cheng-Hung, and Shao-Pei Wang. "*A three-dimensional inverse heat conduction problem in estimating surface heat flux by conjugate gradient method.*" International Journal of Heat and Mass Transfer 42.18 (1999): 3387-3403.
- [134] Kleijnen, Jack PC. "*Kriging metamodeling in simulation: A review.*" European journal of operational research 192.3 (2009): 707-716.
- [135] Jalali, Hamed, Inneke Van Nieuwenhuyse, and Victor Picheny. "*Comparison of Kriging-based algorithms for simulation optimization with heterogeneous noise.*" European Journal of Operational Research 261.1 (2017): 279-301.
- [136] Clark, Isobel. "*Practical kriging in three dimensions.*" Computers & Geosciences 3.1 (1977): 173-180.
- [137] Venturelli, Giovanni, Ernesto Benini, and Łukasz Łaniewski-WoŃk. "*A Kriging-assisted Multiobjective Evolutionary Algorithm.*" Applied Soft Computing (2017).

- [138] Khademi, Gholamreza, and Paknoosh Karimaghaee. *"Hybrid FDG optimization method and kriging interpolator to optimize well locations."* Journal of Petroleum Exploration and Production Technology 6.2 (2016): 191-200.
- [139] Chiles, Jean-Paul, and Pierre Delfiner. *"Geostatistics: modeling spatial uncertainty"*. Vol. 497. John Wiley & Sons, 2009.
- [140] Denton, J.D., 1993. *"Loss Mechanisms in Turbomachines"*, Journal of Turbomachinery, Vol. 115, pp. 621-656.
- [141] Zhang, Q., O'Dowd, D. O., He, L., Wheeler, A. P. S., Ligrani, P. M., and Cheong, B. C. Y., 2011, *"Overtip shock wave structure and its impact on turbine blade tip heat transfer,"* Journal of Turbomachinery, 133(4), 041001.
- [142] Krishnababu, S. K., Newton, P. J., Dawes, W. N., Lock, G. D., Hodson, H. P., Hannis, J., and Whitney, C., 2009, *"Aerothermal Investigations of Tip Leakage Flow in Axial Flow Turbines—Part I: Effect of Tip Geometry and Tip Clearance Gap,"* Journal of Turbomachinery, 131(1), 011006.
- [143] De Maesschalck, C., Lavagnoli, S., Paniagua, G., and Vinha, N., 2014, *"Aerothermodynamics of tight rotor tip clearance flows in high-speed unshrouded turbines,"* Applied Thermal Engineering, 65(1), 343-351.
- [144] Thorpe, S. J., Yoshino, S., Thomas, G. A., Ainsworth, R. W., and Harvey, N. W., 2005, *"Blade-tip heat transfer in a transonic turbine,"* Proceedings of the Institution of Mechanical Engineers, Part A: Journal of Power and Energy, 219(6), 421-430.
- [145] Lavagnoli, S., Paniagua, G., De Maesschalck, C., and Yasa, T., 2013, *"Analysis of the unsteady overtip casing heat transfer in a high speed turbine,"* Journal of Turbomachinery, 135(3), 031027.

- [146] Polanka, M. D., Hoying, D. A., Meininger, M., and MacArthur, C. D., 2002, “*Turbine Tip and Shroud Heat Transfer and Loading: Part A—Parameter Effects Including Reynolds Number, Pressure Ratio, and Gas to Metal Temperature Ratio,*” ASME Turbo Expo 2002: Power for Land, Sea, and Air (pp. 219-230). American Society of Mechanical Engineers.
- [147] Shyam, V., Ameri, A., and Chen, J. P., 2012. “*Analysis of Unsteady Tip and Endwall Heat Transfer in a Highly Loaded Transonic Turbine Stage,*” Journal of Turbomachinery, 134(4), 041022.
- [148] Lavagnoli, S., De Maesschalck, C., and Paniagua, G., 2015, “*Uncertainty analysis of adiabatic wall temperature measurements in turbine experiments,*” Applied Thermal Engineering, 82, 170-181.
- [149] Lavagnoli, S., Paniagua, G., Tulkens, M. and Steiner, A., 2012. “*High-fidelity rotor gap measurements in a short-duration turbine rig*”, Mechanical Systems and Signal Processing, Vol. 27, pp. 590-603.
- [150] Demeulenaere, A. and Van den Braembussche, R., 1998. “Three-Dimensional Inverse Method for Turbomachinery Blading Design”, Journal of Turbomachinery, Vol. 120, pp. 247-255.
- [151] De Vito, L., Van den Braembussche, R.A. and Deconinck, H., 2003. “A Novel Two-Dimensional Viscous Inverse Design Method for Turbomachinery Blading”, Journal of Turbomachinery, Vol. 125, pp. 310-316.
- [152] Daneshkhah, K. and Ghaly, W, 2007. “Aerodynamic Inverse Design for Viscous Flow in Turbomachinery Blading”, Journal of Propulsion and Power, Vol. 23(4), pp. 814-820.

- [153] Hahn, David W., and M. Necati Özişik. *"Use of Duhamel's Theorem."* *Heat Conduction*, Third Edition (2012): 273-299.
- [154] Anderson, A. M., and Moffat, R. J. 1992, "*The adiabatic heat transfer coefficient and the superposition kernel function: Part 1—data for arrays of flatpacks for different flow conditions,*" *Journal of Electronic Packaging*, 114(1), pp. 14-21.
- [155] Vick, B., Beale, J. H., and Frankel, J. I., 1987, "*Integral Equation Solution for Internal Flow Subjected to a Variable Heat Transfer Coefficient,*" *ASME J.*, vol. 109, no. No. 4, pp. pp. 856-860.
- [156] R. J. Moffat, 1997, "*What's new in convective heat transfer?*" *Int. J. Heat Fluid Fl.*, pp. vol. 19, no.2, pp. 90-101.
- [157] Booten, C., and Eaton, J., 2005, "*Discrete Green's Function Measurements in Internal Flows,*" *J. Heat Transfer*, 127, pp. 692–698.
- [158] Booten, C., and Eaton, J., 2007, "*Discrete Green's Function Measurements in a Serpentine Cooling Passage,*" *J. Heat Transfer*, 129, pp. 1686–1696.
- [159] Mukerji, D., and Eaton, J. K., 2005, "*Discrete Green's function measurements in a single passage turbine model,*" *Journal of heat transfer*, 127(4), pp. 366-377.
- [160] Rhode, M.N., Deloach R., "*Hypersonic Wind Tunnel Calibration Using the Modern Design of Experiments,*" *AIAA Paper* 2005-4274.
- [161] Deloach, R., "*Tailoring Wind Tunnel Data Volume Requirements Through the Formal Design of Experiments,*" *AIAA Paper* 98-2884, June 1998.
- [162] Kammeyer, M.E., "*Wind Tunnel Facility Calibrations and Experimental Uncertainty,*" *AIAA Paper* 98-2715, June 1998.

- [163] Montgomery, D.C., *Design and Analysis of Experiments*, 5th ed., John Wiley & Sons, New York, 2001, Chapters 3, 11, 13.
- [164] Helton, J. C., and Davis F. J. "*Latin hypercube sampling and the propagation of uncertainty in analyses of complex systems.*" *Reliability Engineering & System Safety* 81.1 (2003): 23-69.
- [165] Paniagua, G., Iorio, M., Vinha, N., Sousa, J. 2014, "*Design and Analysis of Pioneering High Supersonic Axial Turbines*". *Int. J. Mech. Sci.*, Vol. 89, pp 65–77.
- [166] Vinha N., Paniagua G., Sousa J., Saracoglu B., 2016, "*Axial bladeless turbine suitable for high supersonic flows*". *Journal of Propulsion and Power*. DOI: 10.2514/1.B35818. ISSN: 0748-4658.
- [167] Edmund Optics webpage : <https://www.edmundoptics.fr/resources/application-notes/optics/the-correct-material-for-infrared-applications/>.
- [168] Sound and Vision webpage: <https://www.soundandvision.com/content/eye-color-physics-physiology-page-3>
- [169] D. G. Cuadrado, A. Marconnet, G. Paniagua, "*Inverse Conduction Heat Transfer and Kriging Interpolation Applied to Temperature Sensor Location in Microchips*", *J. of Electronic Packaging*, March 2018, doi: 10.1115/1.4039026.
- [170] D. G. Cuadrado, F. Lozano, V. Andreoli, G. Paniagua, 2019. "*Engine-scalable Rotor Casing Convective Heat Flux Evaluation Using Inverse Heat Transfer Methods*", *Journal of Engineering for Gas Turbines and Power*, 141(1), p. 011012.
- [171] Paniagua, G., Cuadrado, D., Saavedra, J., Andreoli, V., Meyer, T., Solano, J.P., Herrero, R., Meyer, S. and Lawrence, D., 2019. "*Design of the Purdue Experimental Turbine*

- Aerothermal Laboratory for Optical and Surface Aerothermal Measurements.*” Journal of Engineering for Gas Turbines and Power, 141(1), p.012601.
- [172] V. Andreoli, D. G. Cuadrado, G. Paniagua, “*Prediction of the Turbine Tip Convective Heat Flux Using Discrete Green Functions.*” ASME. J. Heat Transfer. 2018;(), doi:10.1115/1.4039182.
- [173] D. G. Cuadrado, J. Saavedra, V. Andreoli, G. Paniagua, “*Experimental Calibration of a High Speed Blowdown Tunnel*”. 2017 ISABE conference No 2017-22636.



## APPENDIX A. UNCERTAINTY ANALYSIS PROCEDURE

While the error is associated to a single observation, the uncertainty is determined for a number of experiments and represents the possible value that the error might have given a confidence interval.

The value of uncertainty always depends upon the confidence level. For a given confidence level, experiments performed with care will result in a reduced uncertainty.

In order to determine a property of interest generally we need to measure several parameters. As the property of interest is a combination of the measured properties, the propagation of error from these properties need to be assessed to know the uncertainty of the property of interest. For that, we use again the concept of sensitivity coefficient. Mathematically, the total uncertainty value of a property A is equivalent to the mathematical exercise of performing a Taylor's series expansion about the true value of A in terms of the parameters it depends upon.

For small values of uncertainty, the higher terms can be neglected, but for large uncertainty values or for highly non-linear dependence of the particular quantity A, second and third derivatives can be considered in the Taylor's expansion.

In the case of the inverse method, we are dealing with small uncertainties of different magnitudes that we can measure: thermal properties of the different materials, the measured temperature which is the input of the method and the thicknesses of the different layers of material.

The procedure we have used consists of a simplification of the mathematical approach since the equation to compute the sensitivity due to uncertainty of each parameter can be tedious. This method is divided in the following steps:

1. All the uncertainties relative to the measured parameters need to be known or assessed, and a mean value for each one of them needs to be assigned. Typically, the mean assigned values are the ones of the baseline analyzed case.
2. The baseline values are used to compute the analyzed quantity (in the inverse method, the heat flux, or mean value of heat flux over time and space).
3. We need to repeat the calculation as many times as different dependent parameters. In each one of these calculations we modify the values of one parameter with the uncertainty of the parameter and we compare with the baseline case.
4. We compute the variation in the analyzed quantity due to the variation of the measured parameter.
5. The total uncertainty of the analyzed parameter will be the root means squares sum of each contribution.

Table A-1. Uncertainty analysis of the heat flux computation using the non-linear inverse method.

Quantity	Absolute input uncertainty	Uncertainty in %	Variation in heat flux relative to mean in %	Sensitivity
Temperature [K]	2.0	0.64	6.35	9.98
k silicon [W/mK]	10	7.69	-0.15	-0.02
$\rho$ silicon [kg/m <sup>3</sup> ]	10	0.43	0.14	0.32
C <sub>p</sub> silicon [J/K kg]	7	0.99	0.30	0.30
k polycrystalline silicon [W/mK]	10	10.00	-1.66	-0.17
$\rho$ polycrystalline silicon [kg/m <sup>3</sup> ]	10	0.43	0.09	0.21
C <sub>p</sub> polycrystalline silicon [J/K kg]	7	1.03	0.15	0.15
thickness silicon [m]	0.00005	5.00	1.97	0.39
thickness polycrystalline silicon [m]	0.00005	10.00	1.97	0.20
Overall Uncertainty in heat flux calculation			<b>7.14</b>	

The sensitivity column contains shows the influence of the measured parameter on the final result of the analyzed parameter. It is calculated by dividing the variation in the analyzed parameter in by the uncertainty of the measured parameter. The larger the sensitivity, the higher Is the effect of the measured parameter. Therefore, in order to decrease uncertainties we should target the reduction of the parameters with high sensitivity.

In the case of the inverse method represented in the example, the temperature measurement plays a big role in the variation of the computed heat flux. The uncertainty due to the measurement in the temperature is more than the 6% of the total 7% of the uncertainty of the methodology. An improvement in the temperature uncertainty would imply a great improvement in the uncertainty of the method.

## APPENDIX B. EXPERIMENTAL DATA IN MICROELECTRONICS APPLICATION

After several numerical assessment of the two different methodologies based on results from a model, we performed twelve different experiments with the microchip in the temperature controlled enclosure. The microchip consists of 25 heaters that can be controlled independently. Different patterns were used to provide a variety of spatial distributions of hot spots in the measured surface.

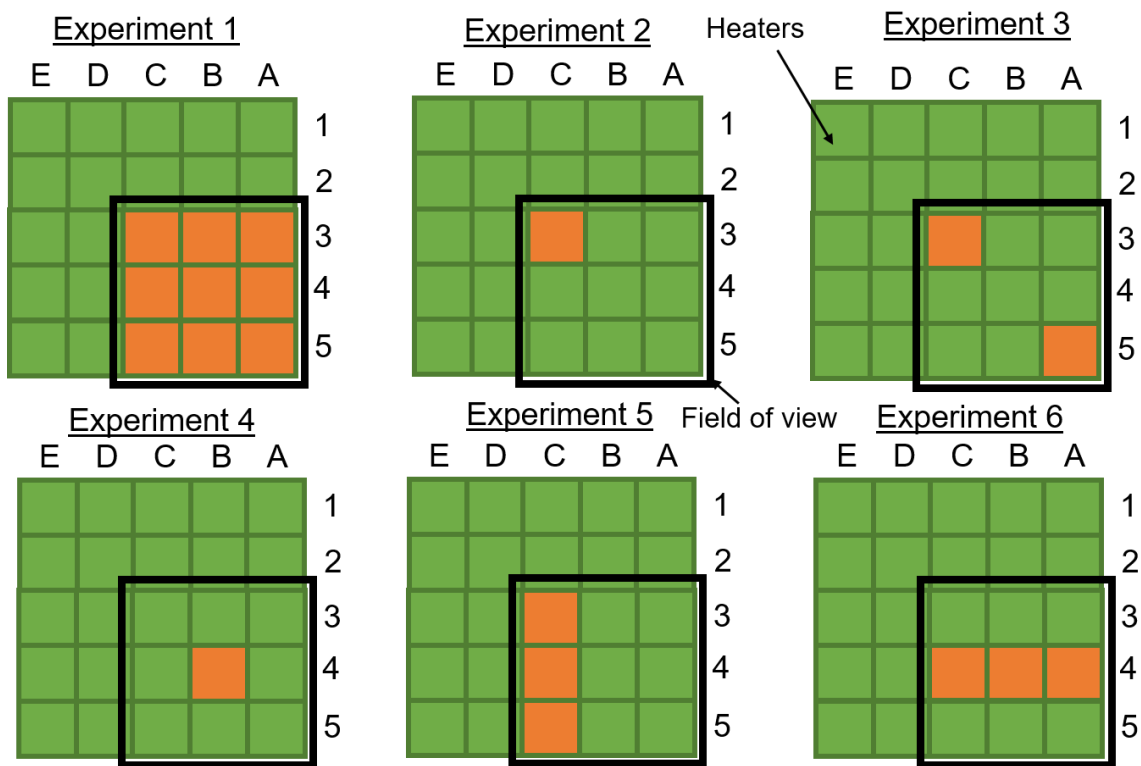


Figure B- 1. Different experiments performed with the 5x5 heaters test article.

The six different patterns were performed in natural convection and in forced convection (therefore, there are twelve experiments). From these experiments, the experiments 1, 3 and 4 were analyzed

by the inverse methodology since with them we can assess all the features where the inverse method can fail: magnitude of the heat flux, time behavior of the heat flux, spatial distribution of the hotspots, and identification of more than one hot spot.

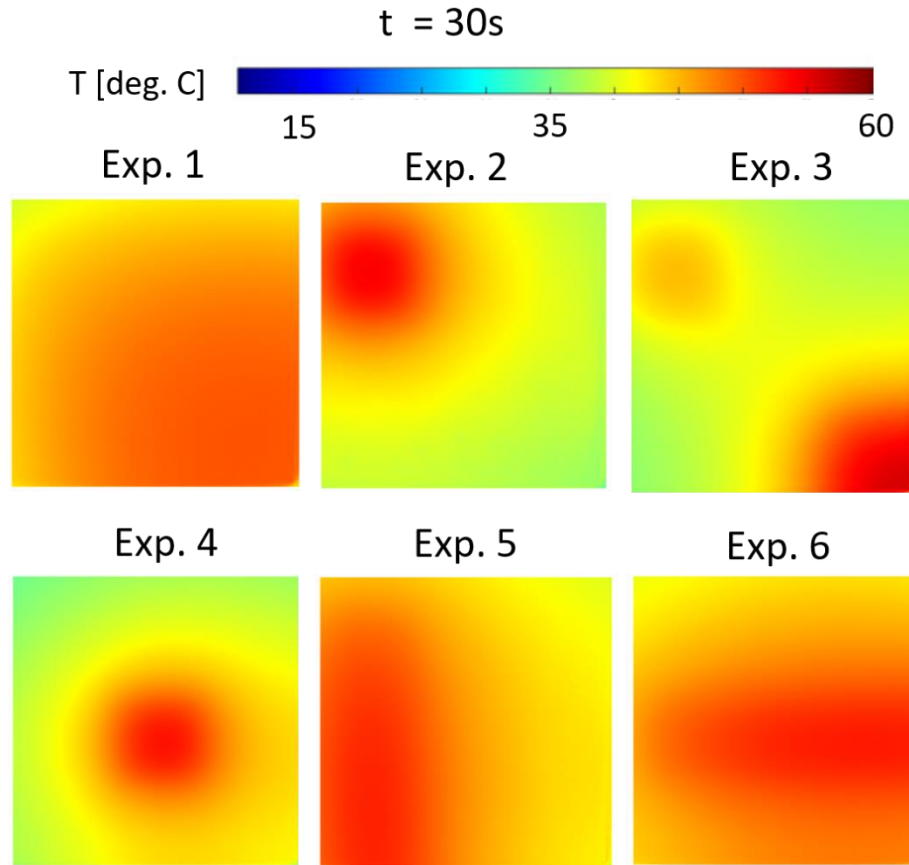


Figure B- 2. Temperature maps for each one of the six experiments under natural convection.

In order to be able to use the methodologies, the pixel size needs to be increased, to decrease the number of sensors. For that we divided the image in squares and computed the mean value of temperature in each square. We evaluated the inverse method with different sizes of the pixel and there is not a large difference of performance once the number of sensors is larger than the number of heat sources that we have to compute.

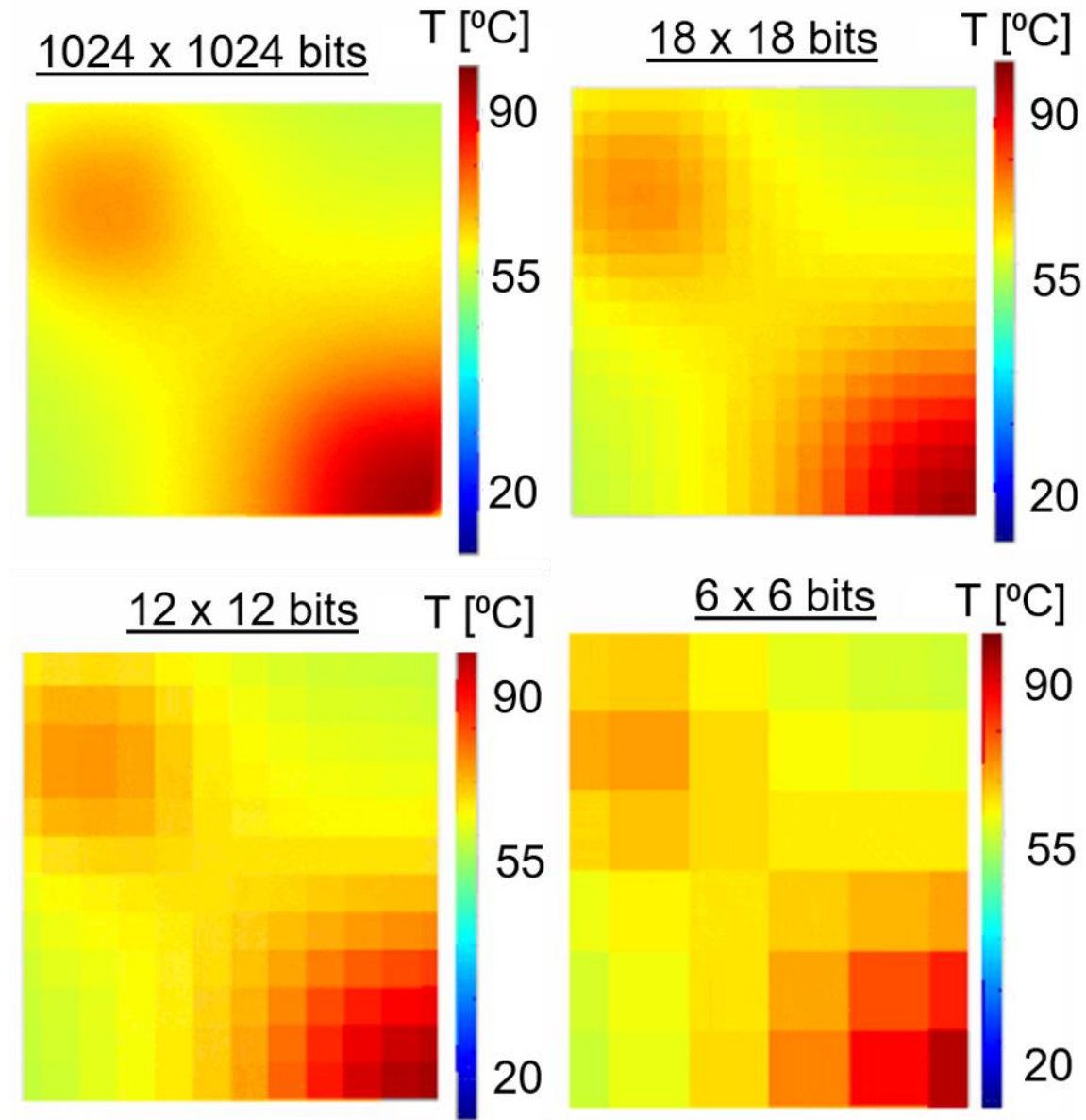


Figure B- 3. Temperature maps of the experiment 3 with different pixel size.

### Experiment 1

This experiment was used to validate the Conjugate Gradient Method and the Digital Filter Method. With this test we are able to track how the methodologies respond regarding the prediction of the magnitude of the heat flux and its behavior in time. The temperature maps over with respect to time are detailed in Figure B- 4.

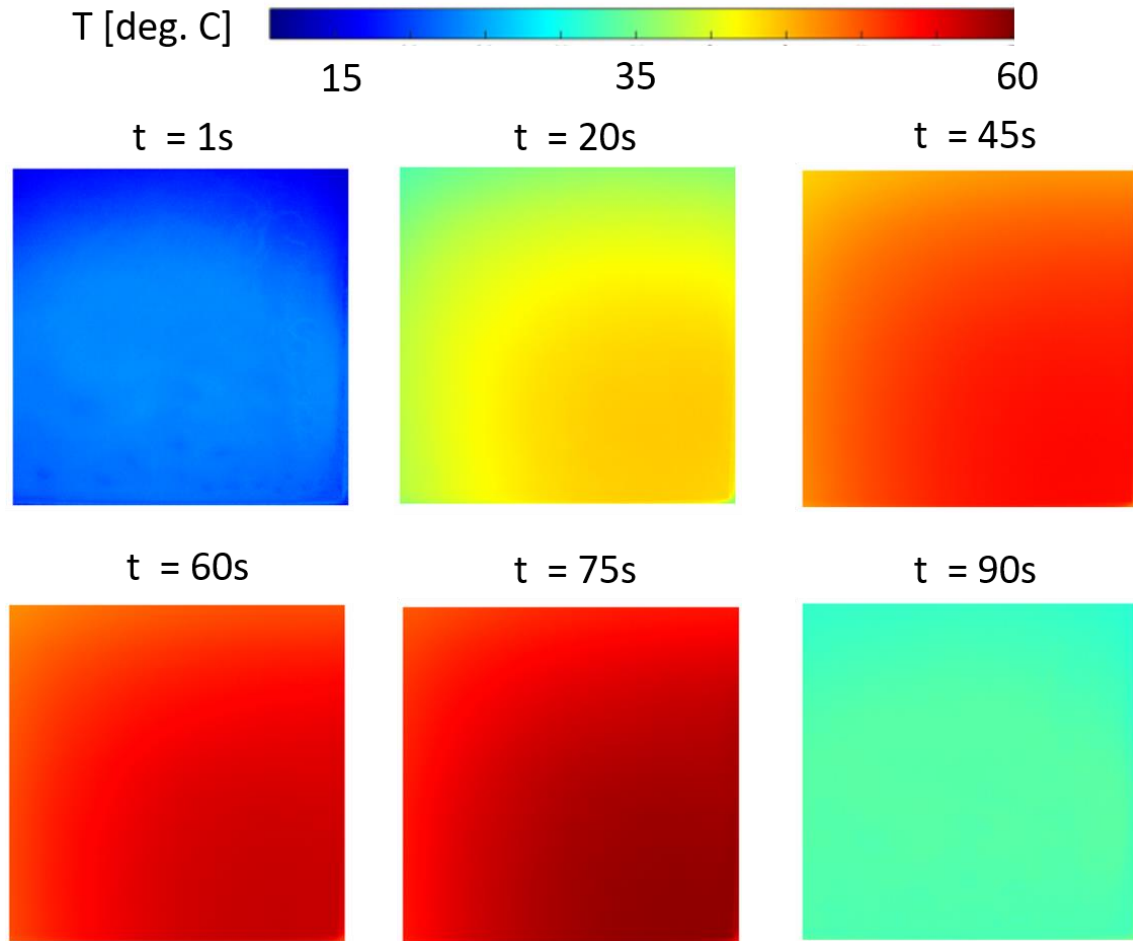


Figure B- 4. Temperature maps at different timesteps during experiment 1.

When we evaluated the experiment 1 using the Conjugate Gradient Method, we observed that we could not reproduce the behavior of the imposed heat flux in terms of magnitude. It takes a lot of time to converge to a reasonable value and the trends in time are predicted (when the heat flux start and when the power is turned off).

The Digital Filter Method with the correction, predicts well the magnitude of the heat flux and the temporal behavior both in the pure conduction analysis using COMSOL Multiphysics and in the Conjugate Heat Transfer analysis performed using ANSYS Fluent.

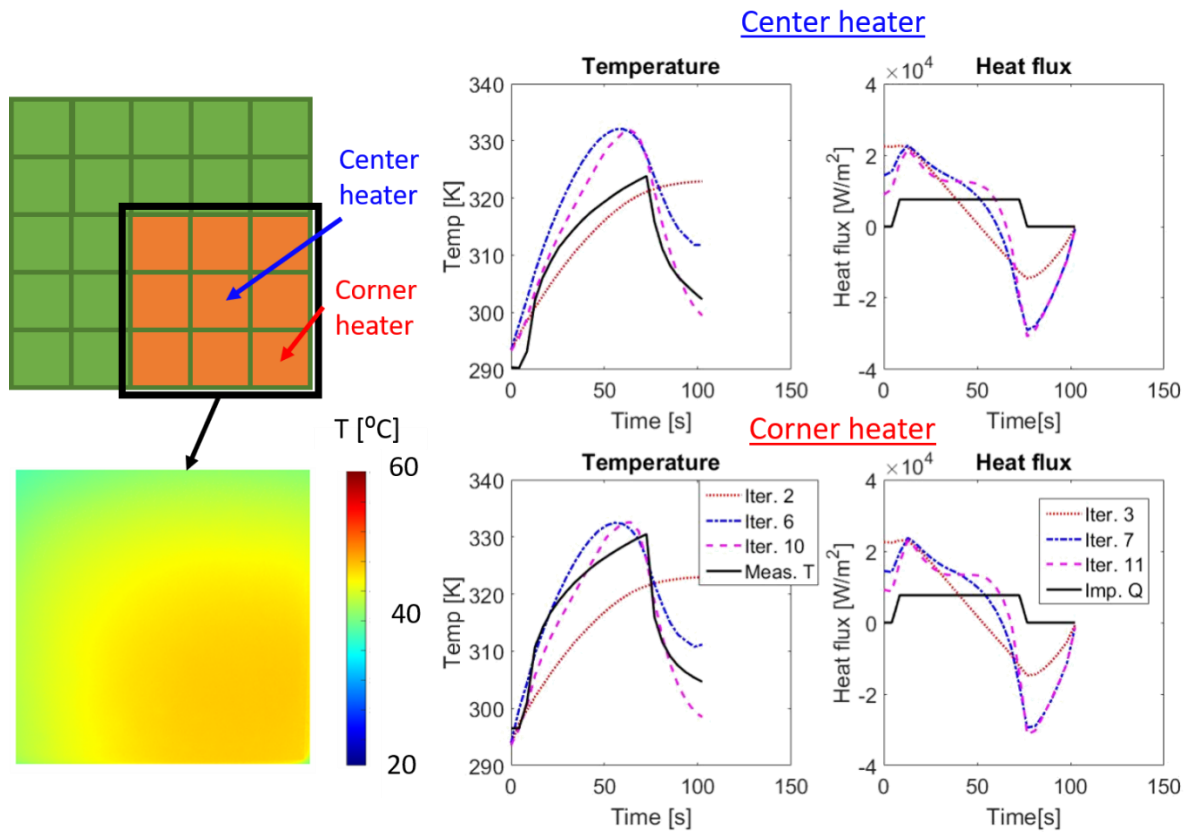


Figure B- 5. Conjugate Gradient Method results using the experimental data from the experiment 1 in two different heaters.



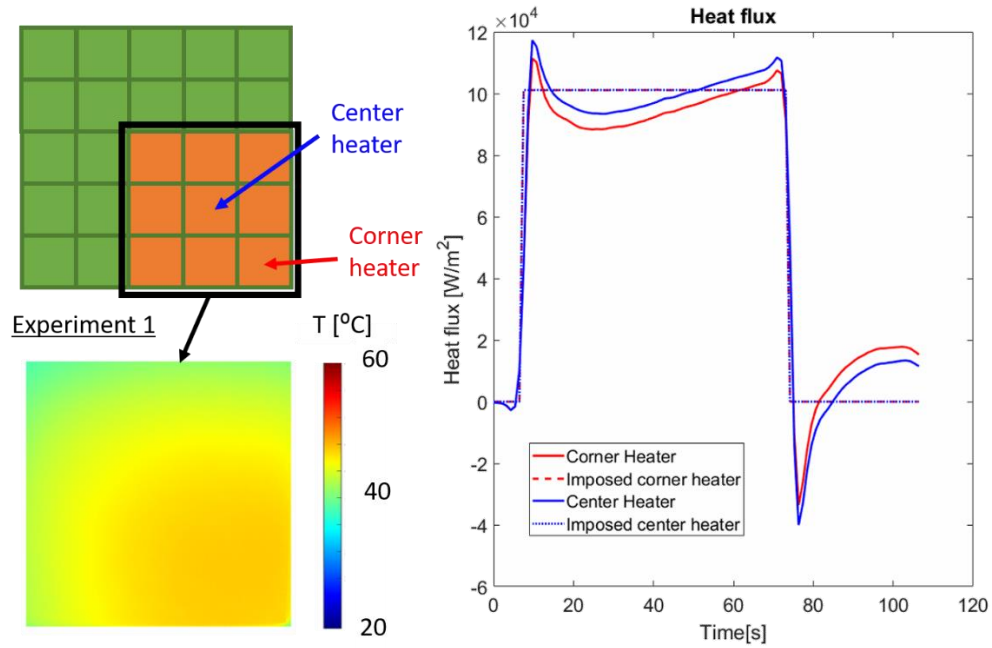


Figure B- 6. Digital Filter Method results using the experimental data from the experiment 1 in natural convection in two different heaters.

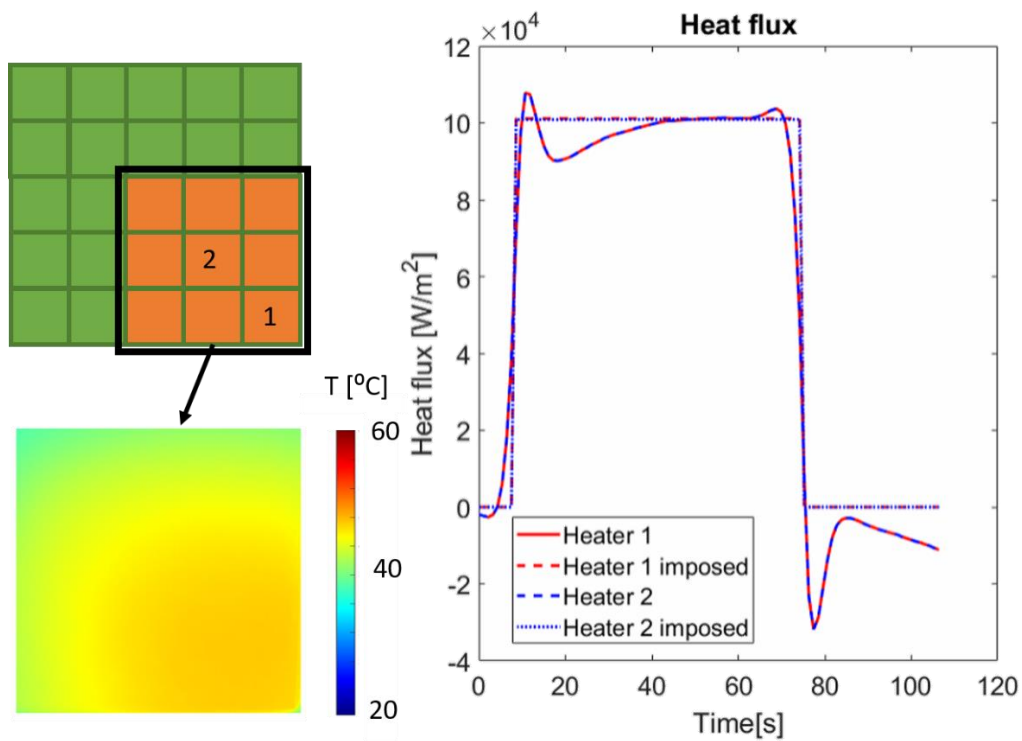


Figure B- 7. Digital Filter Method results using the experimental data from the experiment 1 in forced convection in two different heaters.

#### Experiment 4

This experiment was used to observe if the different methods could predict the location of the heat sources that are activated. This is the most simple experiment to analyze the spatial distribution. We evaluated the results with the CGM, with not a good agreement with the imposed heat flux and the DFM which was able to predict the time, space and magnitude of the heat that was provided to the chip.

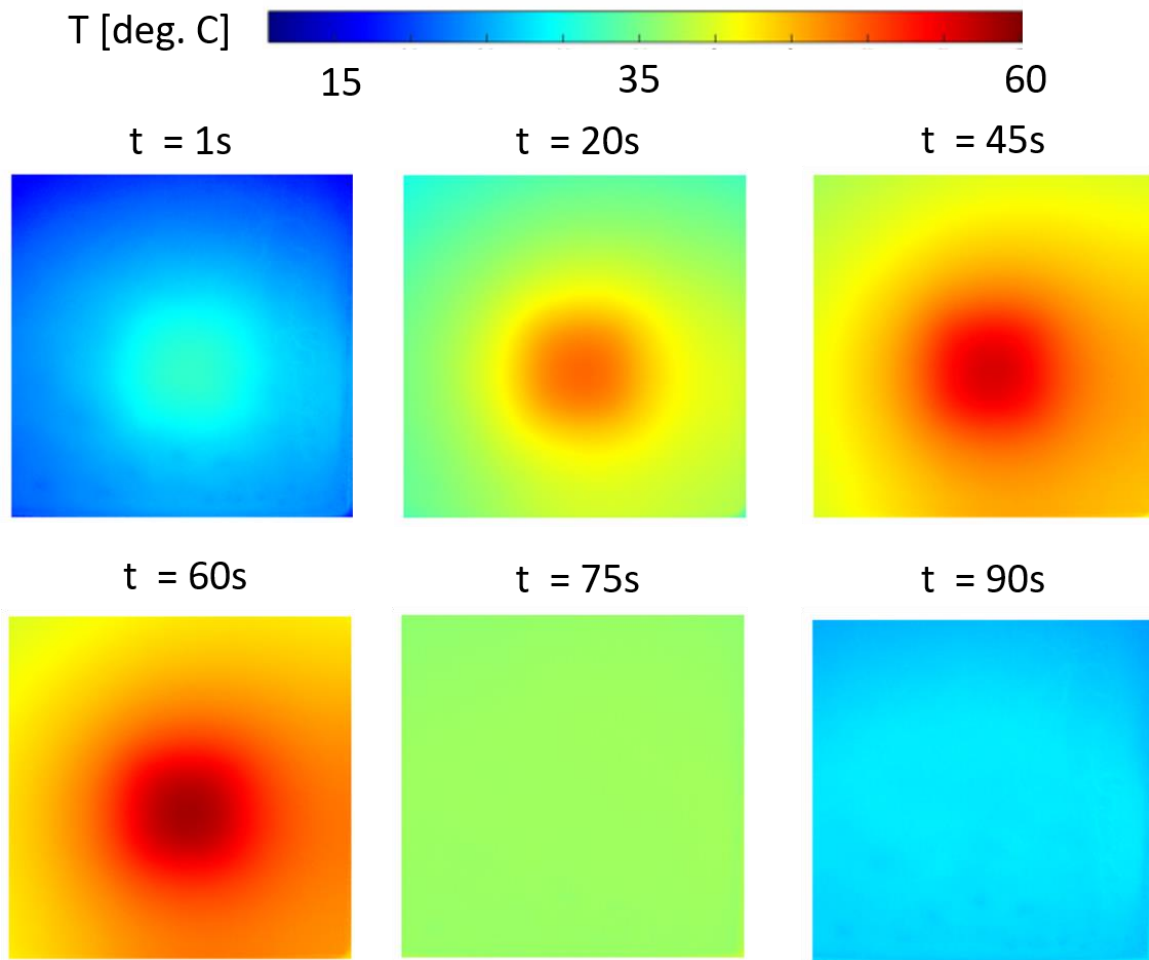


Figure B- 8. Temperature maps at different timesteps during experiment 4.

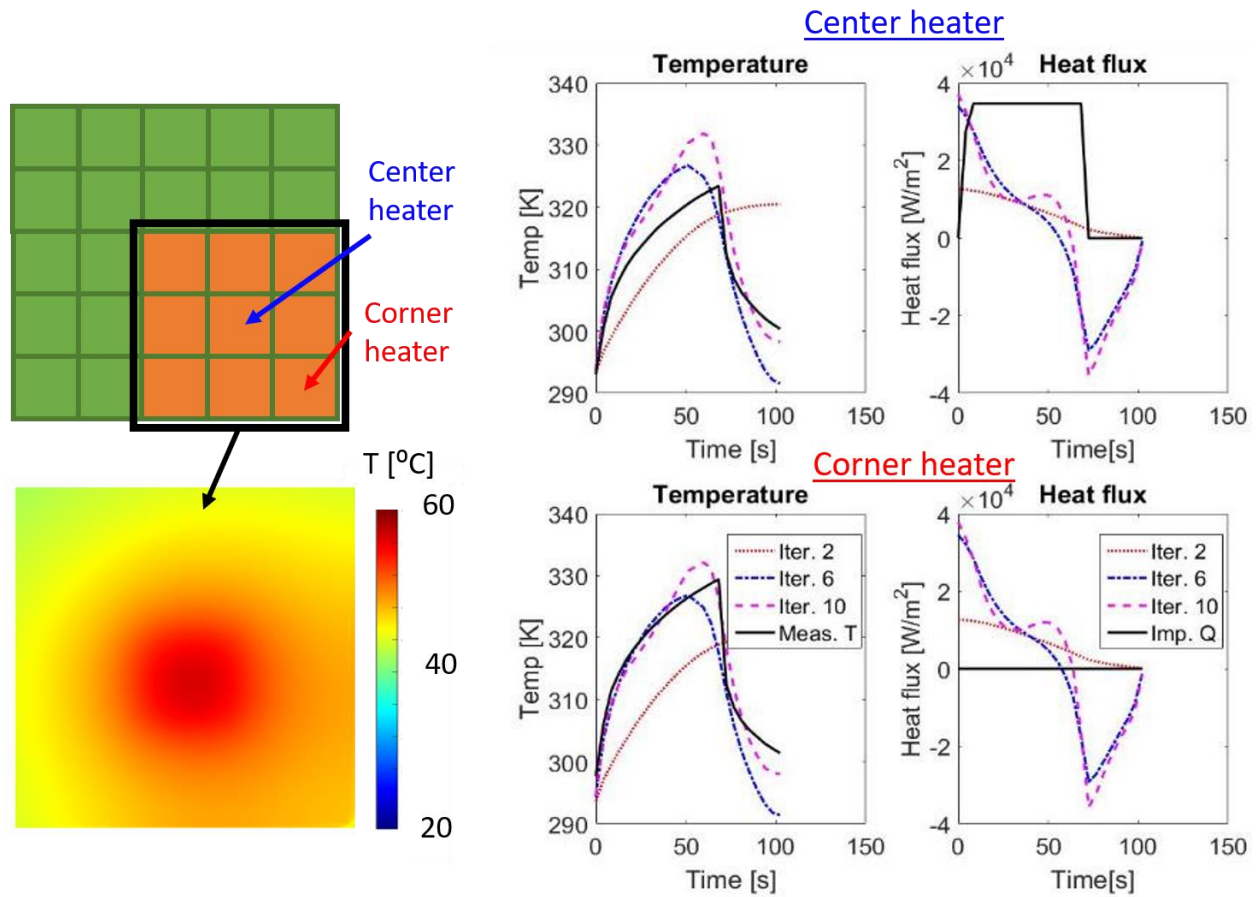


Figure B- 9. Conjugate Gradient Method results using the experimental data from the experiment 4 in two different heaters.

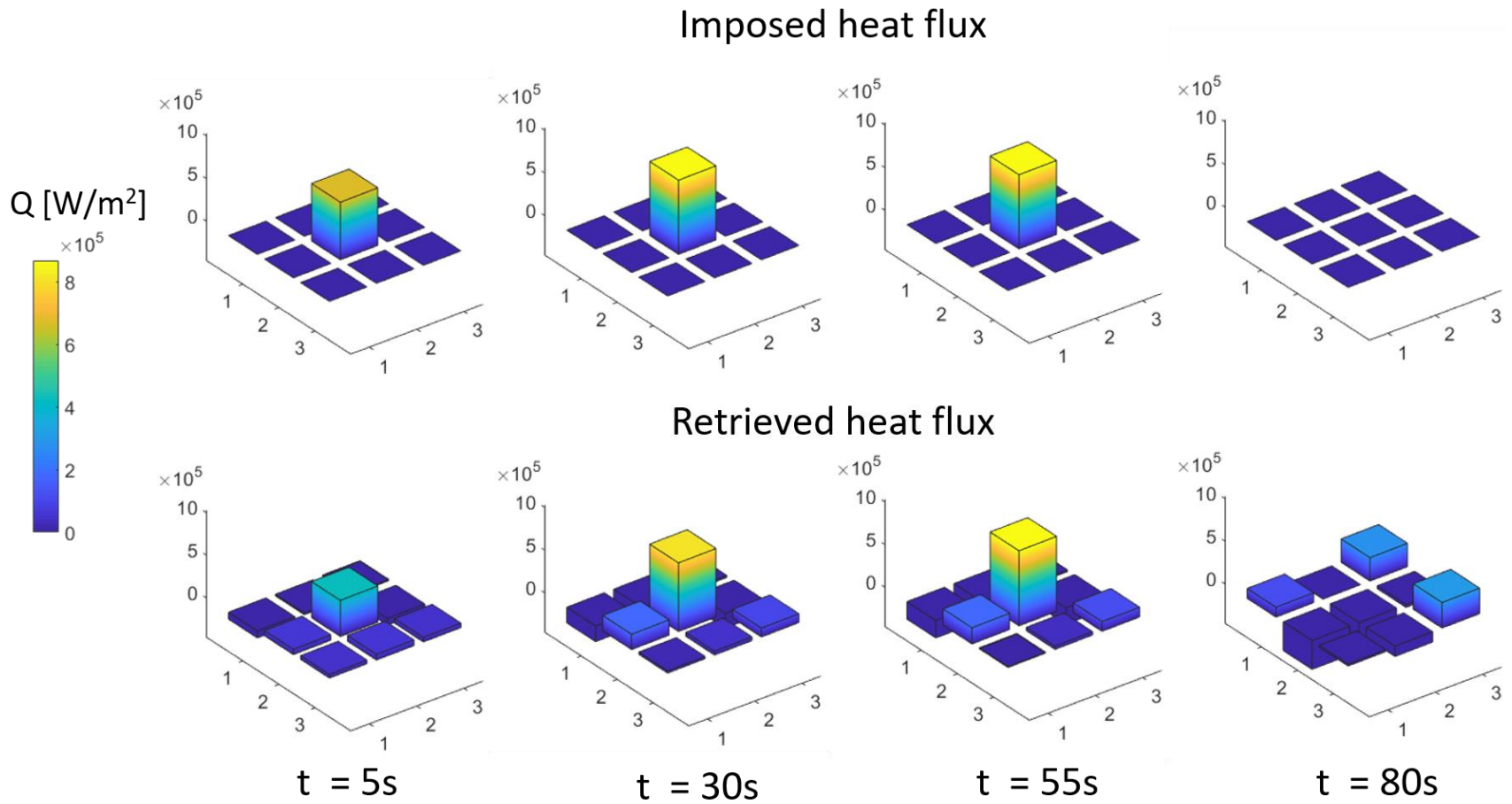


Figure B- 10. Digital Filter Method results using the experimental data from the experiment 4 in natural convection representing the different heaters.

### Experiment 3

We evaluate the case which would be more difficult to compute for the Digital Filter Method, where we have two different hot spots clearly separated. We observe that the inverse method can predict accurately the magnitude of the heat flux, the location of the heaters that are providing power to the system and the time behavior of the heating pattern.

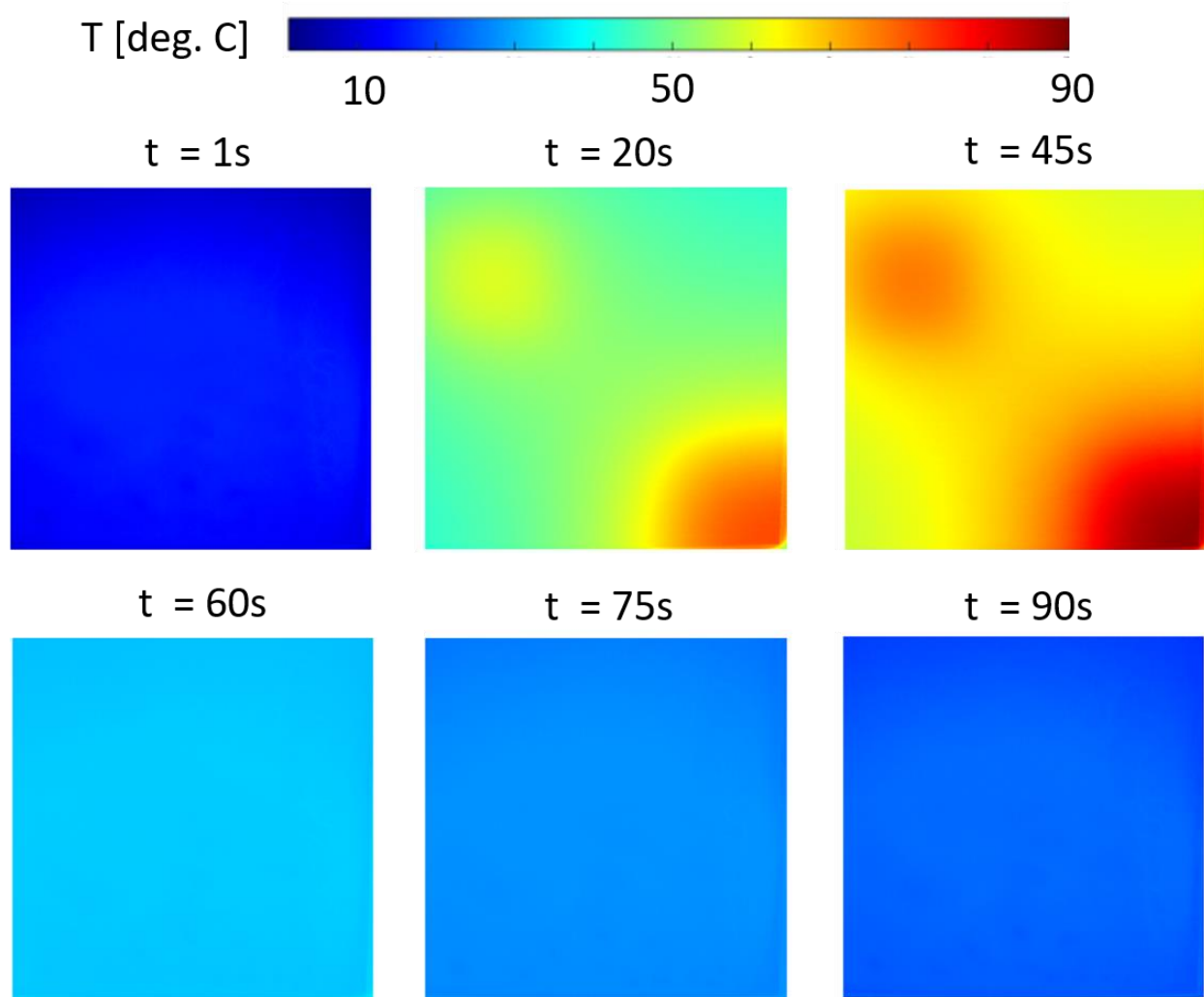


Figure B- 11. Temperature maps at different timesteps during experiment 3.

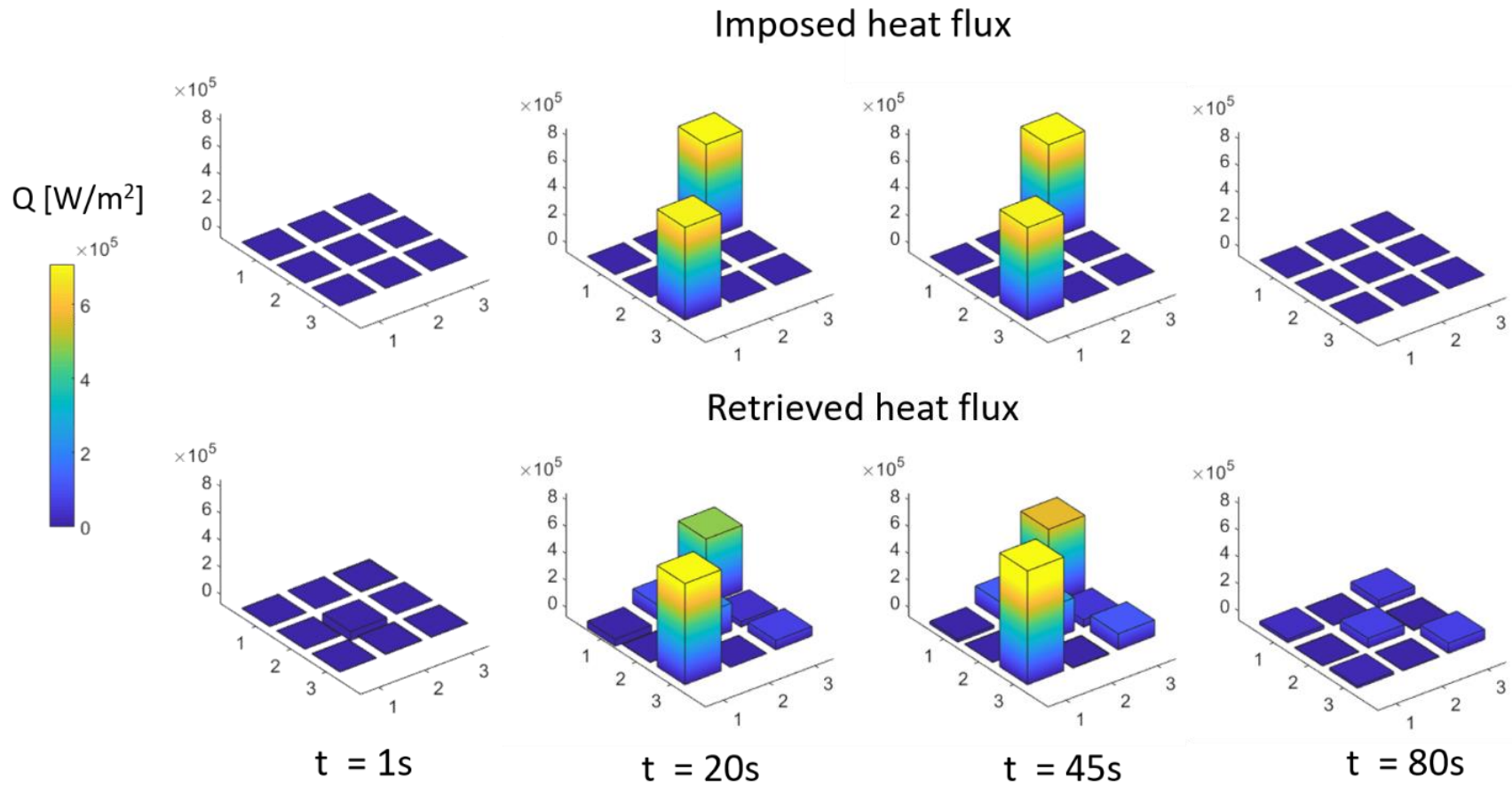


Figure B- 12. Digital Filter Method results using the experimental data from the experiment 3 in natural convection representing the different heaters.

## APPENDIX C. INVERSE METHOD AND KRIGING INTERPOLATION

### OPTIMIZATION MATLAB GUI FOR SIMPLE 3D GEOMETRIES

The work performed regarding the assessment of the inverse methodology in microchips was framed in the Cooling Technologies Research Center (CTRC). One of the objectives of the development of the inverse method in this frame is to make it accessible to all the community. Since the methodology is rather complex, we have developed an interface to make the inverse method easier to run to all the interested members of the consortium.

We have summarized the way this code works in 7 simple steps that we have to follow in the main user interface shown in Figure C- 1.

**Inverse Methodology**

**Step 1: Model setup**

Import CAD

or

Build blocks

Show geometry

**Step 2: Material setup**

Create material

Set material

**Step 3: Mesh**

Extremely fine ▢

Mesh

**Step 4: Heat source surface**

Set heat source

**Step 5: Import temperature data**

Import temperature data

**Step 5: Compute heat flux value**

Compute sensitivity matrix

Regularization term in time

Regularization term in space

Sigma

Compute heat flux

**Step 6: Optimize sensor location and numbers**

Initial number of sensors

Objective goodness of fitting(%)

Run

Figure C- 1. Main user interface

#### Step 1: Model setup

In this step we can choose between import the CAD or to make a simple CAD formed by blocks or parallelepipeds.

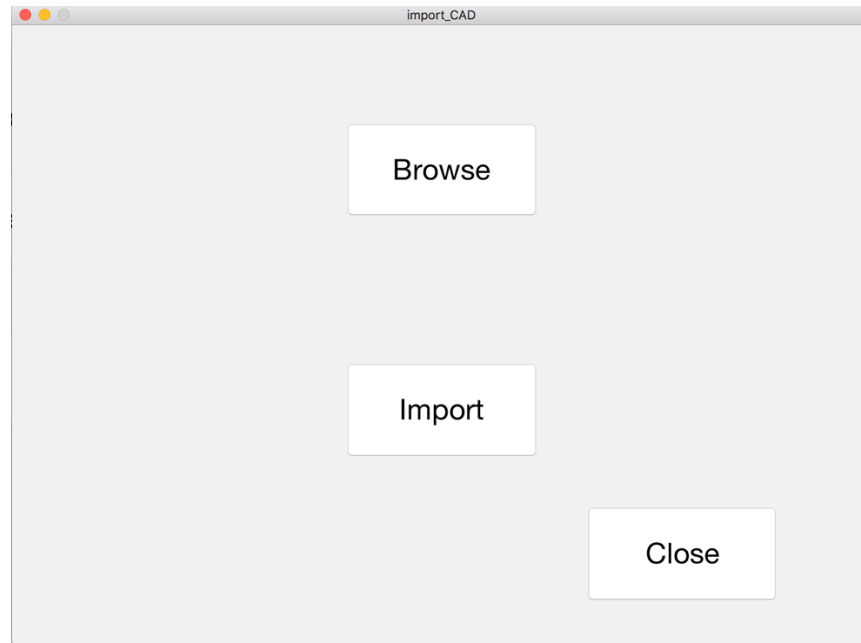


Figure C- 2. Import CAD models.

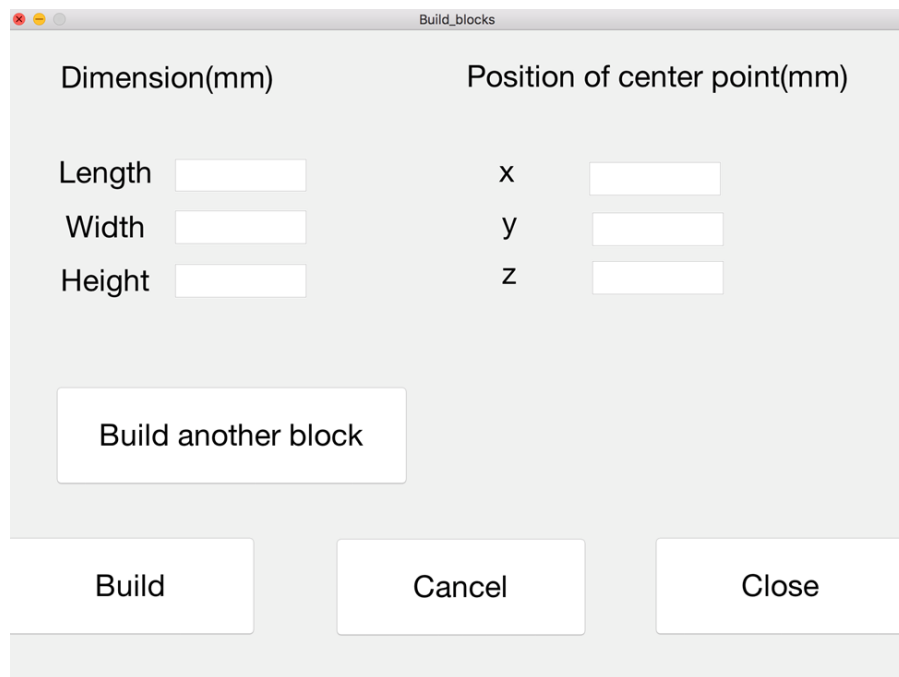


Figure C- 3. Build blocks interface

With these interfaces we can generate the preferred geometry and then with the button of “Show Geometry”, we can see the generated or imported geometry.



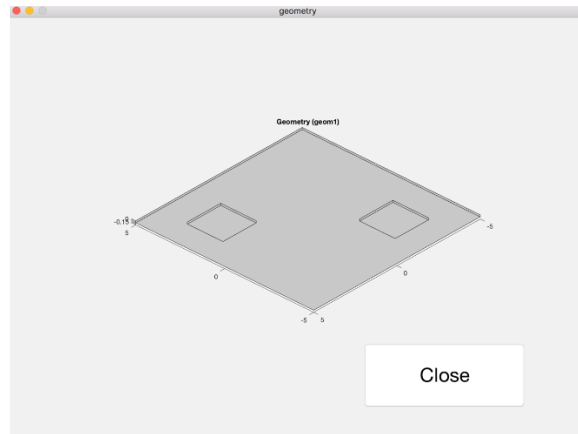


Figure C- 4. Geometry viewer.

### Step 2: Material setup

In the inverse method it is extremely important to set up the materials and their properties in each one of the generated domains. In this step, we can create new materials and assign them to the different domains that are created in our model.

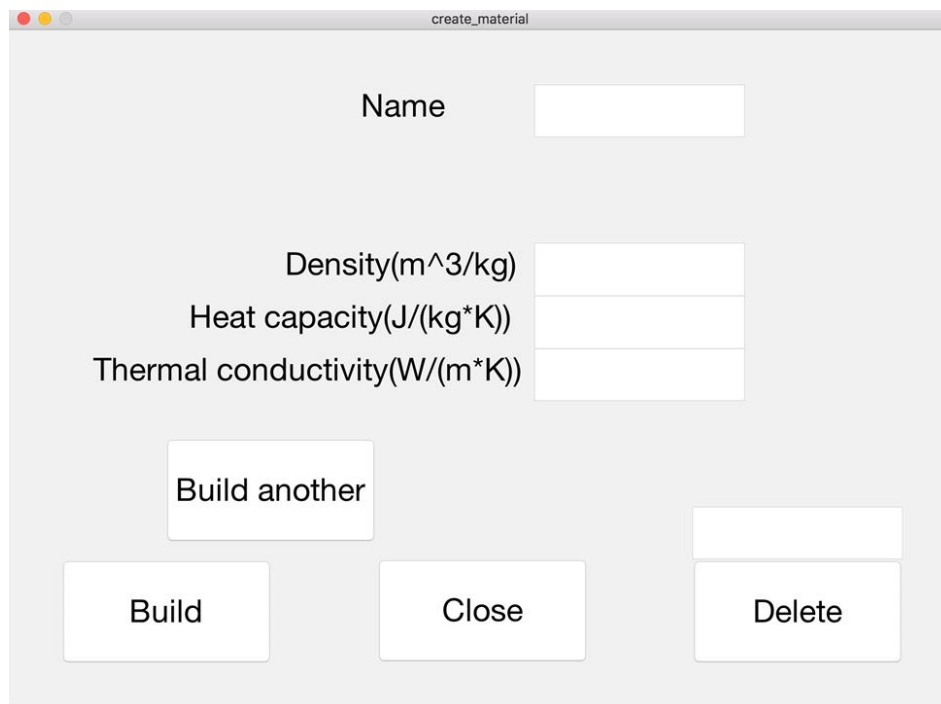


Figure C- 5. Create Materials.

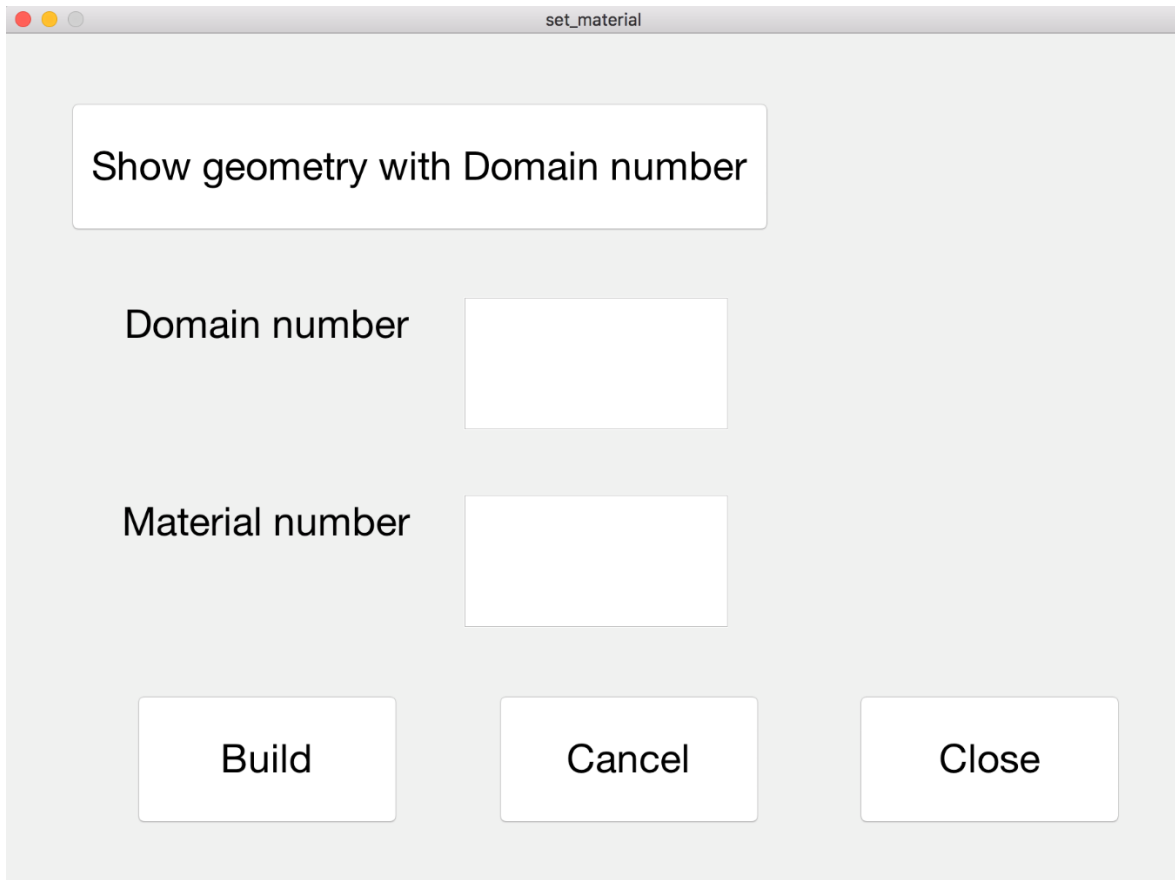


Figure C- 6. Assign materials to the different domains.

### Step 3: Mesh

Once the complete model is defined with the different materials assigned, we proceed to mesh the different domains. We can assign different levels of discretization depending on the accuracy that is needed, the complexity of the 3D domains and the computational power of the machine in which the program is being used.

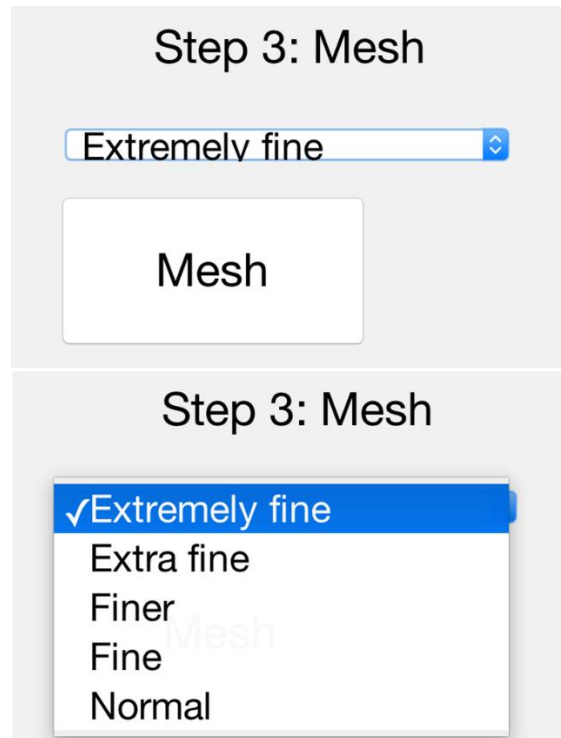


Figure C- 7. Meshing interface.

#### Step 4: Heat source surfaces

In this step we define which surfaces are likely to have the heat flux that we need to compute. This is a necessary step in all the inverse methods: at least we should be able to provide the surfaces where we want that the computation of the heat flux is performed. If we fail in this step, the code will not know where to apply the pulses in order to generate the sensitivity coefficients needed for the inverse computation.

In this step, we can define the surface or surfaces that will have heat flux and the type of boundary condition that needs to be implemented: heat flux in surface or boundary heat source in the surface. The last can be used for surfaces that are inside the domain or between domains.

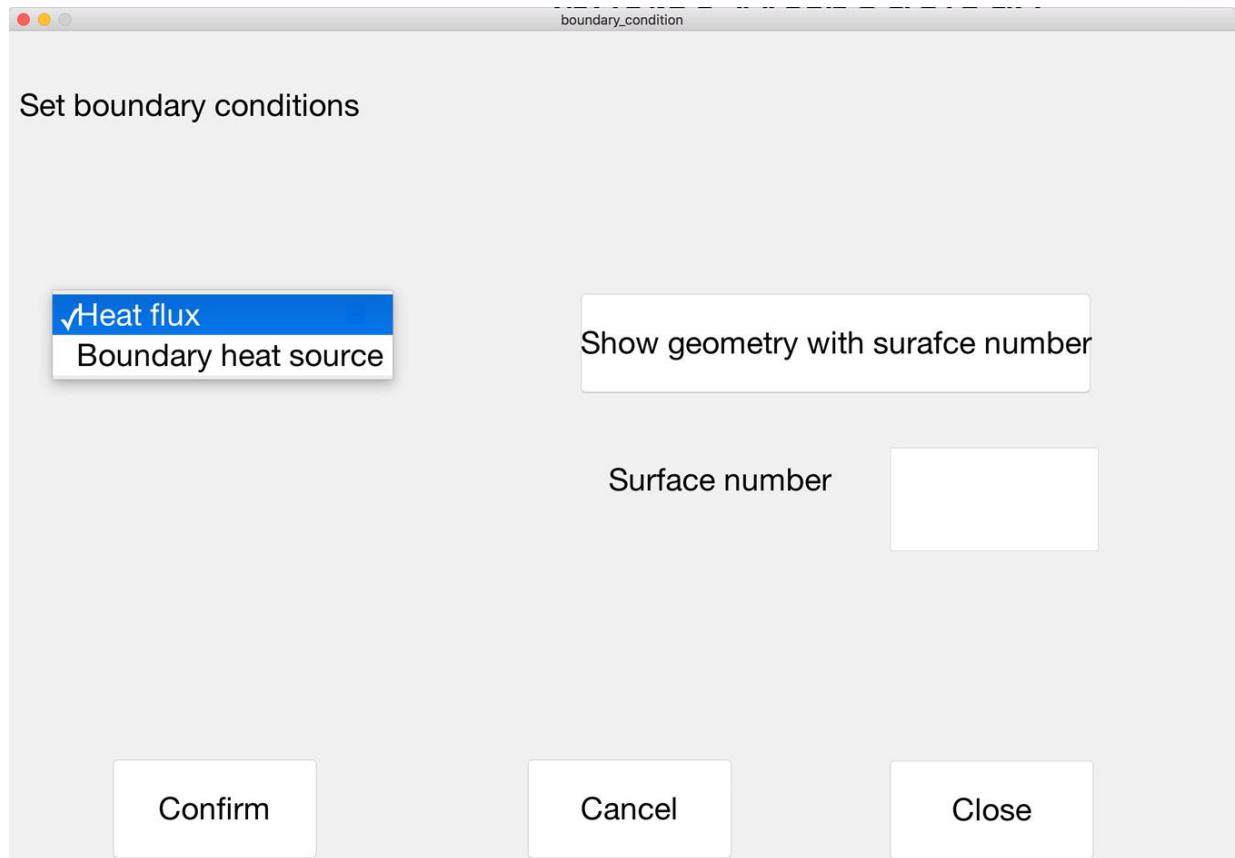


Figure C- 8. Heat flux surfaces interface.

#### Step 5: Import temperature data

In this step we define the surface where we are measuring the temperature and we need to provide a temperature map which needs to be in a .mat format. It should be 3D matrix with the first two dimensions the temperatures in the x and y directions of the sensors or pixels and the third dimension gather the data in time. This step is particularly complicated because the code needs to map the temperature maps over the surface that it is provided by the user. We define as well the timestep that it is needed in the methodology in this step.

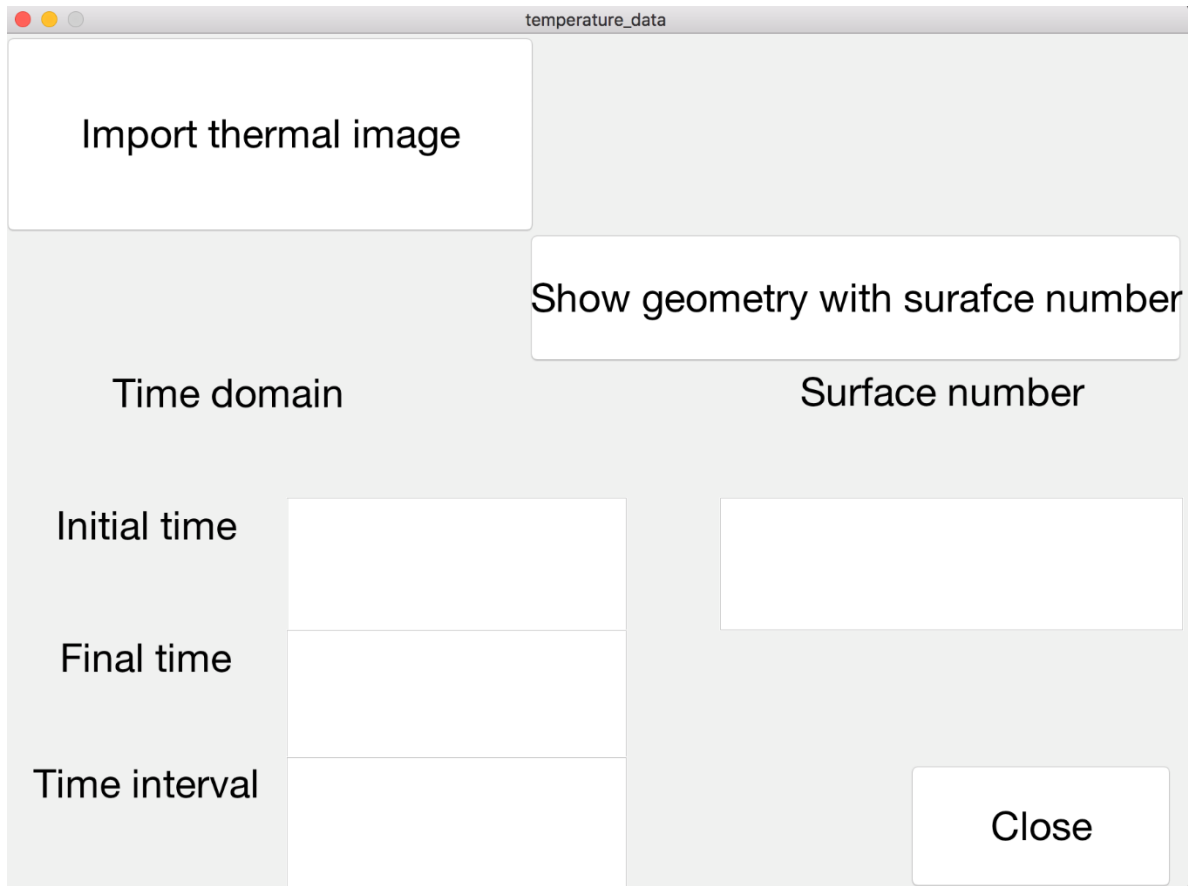


Figure C- 9. Temperature map reading interface.

#### Step 6: Inverse method:

This step is the one where the inverse method is computed. First we have to compute the sensitivity coefficients for which the only information that is needed is the thermal properties of the model, the place where the heat flux are located and the geometry itself. It will run different pulses at different temperatures in order to create a sensitivity matrix that will be connected exclusively to the model that we are analyzing. It is not independent on the temperature that it was input because of the correction for temperature that it has been introduced in a previous section.

Once the matrix of coefficients is defined, we can compute the inverse method and for that we only have to define the regularization terms and the sigma value (to correct for differences in the

thermal properties) and click the button of “Compute Heat Flux”. As quick as seconds, the computation of the heat flux will be performed, since in this case the methodology that has been used is the Digital Filter Method.

**Step 5: Compute heat flux value**

**Compute sensitivity matrix**

Regularization term in time	5e-12
Regularization term in space	5e-12
Sigma	2

**Compute heat flux**

Figure C- 10. Inverse methodology interface.

#### Step 7: Sensor number and location optimization

In this step, we optimize using the Kriging Methodology and a Genetic Algorithm optimization technique the number and the location of the sensors inside of the chip or geometry. For this we need to provide an initial number of sensors and a desired goodness of fit. The optimization will start with the initial number of sensors and if after the optimization the goodness of fit is below the intended value, the code will add another sensors and the optimization will start again.

Finally we will have the final value of the number of sensors, their location and the goodness of fit in terms of temperature that we will be able to get with the optimized number and location of the sensors.

Step 6: Optimize sensor location and numbers

Initial number of sensors

Objective goodness of fitting(%)

Figure C- 11. Kriging Interpolation Optimization interface.

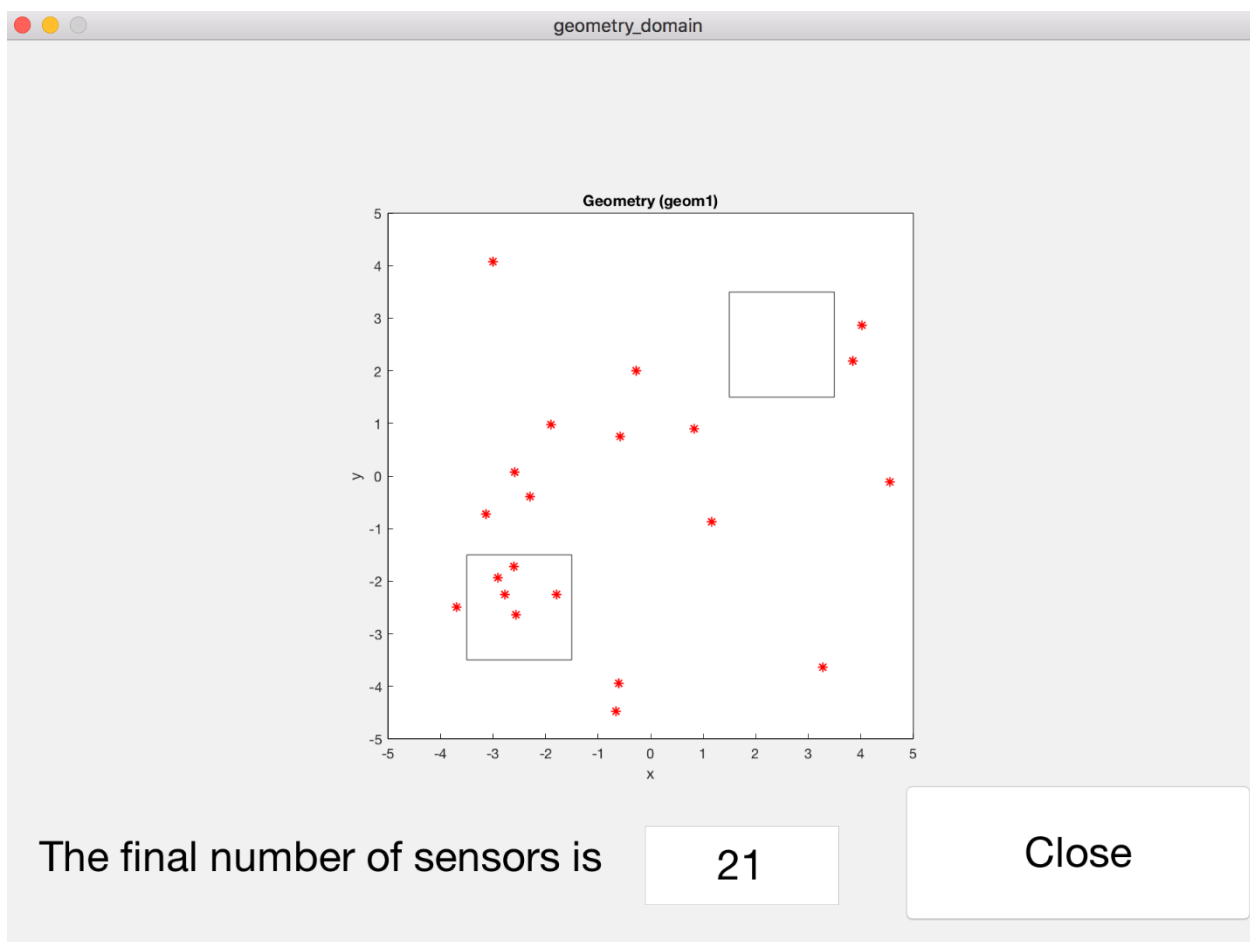


Figure C- 12. Final result with a goodness of fit of 85%.

## **APPENDIX D. INFRARED WINDOW MATERIAL SELECTION**

The selection of the material of the Infrared transparent window is crucial for the measurements intended in the annular test section in the application for gas turbines. In the case of the microelectronics application since the IR microscope has a smaller dimensions and there is no need to be sealed, we decided not to use a window.

In the gas turbine application for safety and for sealing we need to use an IR transparent window. To make the choice of the material we need to consider different aspects of the experiment, such as the metal temperature in which the window is going to be located, the temperature and the pressure inside the chamber that the window is enclosing and the range of temperatures of the surface that needs to be measured.

The first parameter that we looked at is the temperature of the fluid in the chamber. If we want to have temperatures larger than 500K, we need to use ceramic (glass) materials and we have to avoid the plastic windows.

The second requirement is the metal temperature of the surface we are measuring. For that we need to evaluate the wavelength that we are expecting to measure with our infrared camera, which is located in the mid-wave infrared region (3 to 30micrometers of wavelength) as shown in the Figure D- 1. At ambient temperatures the expected wave length is approximately 10micrometers as shown in Figure D- 2.



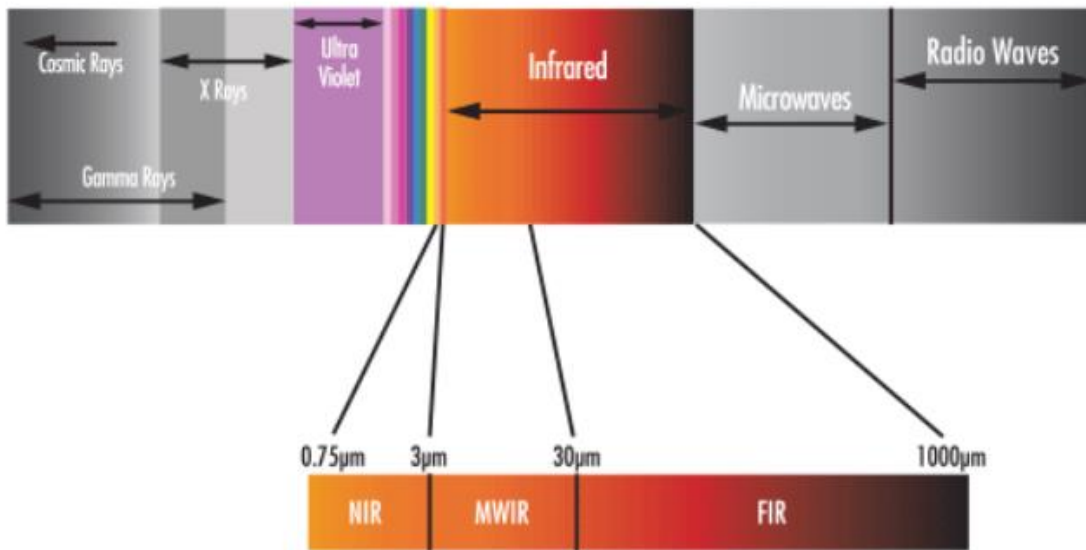


Figure D- 1. Electromagnetic spectrum.[167]

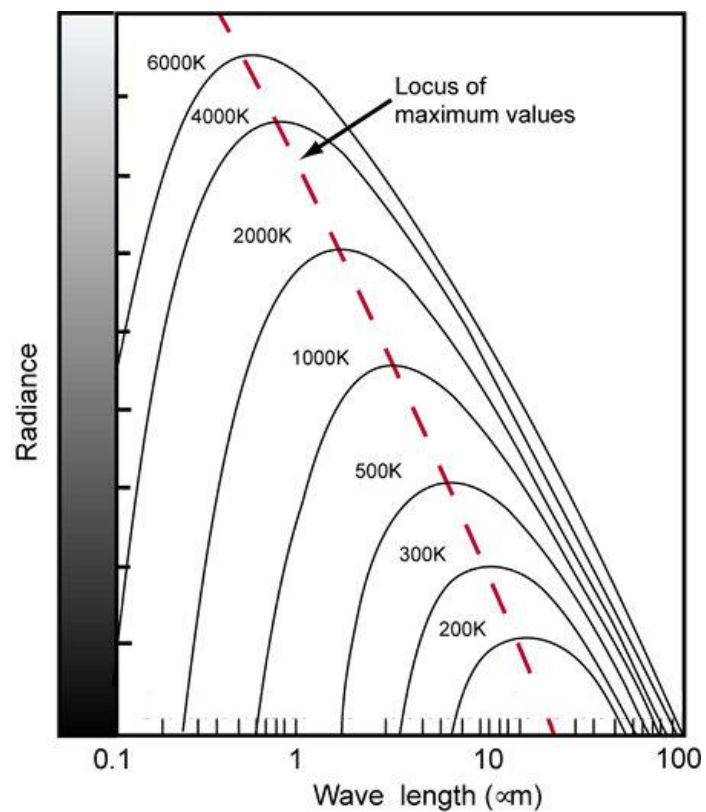


Figure D- 2. Radiance with respect to the temperature [168]. As the temperature of a blackbody increases, the spectral curve shifts toward shorter wavelengths. In this diagram, wavelengths are given in microns ( $\mu\text{m}$ ), which are 1000 times longer than nanometers (nm).

In the mid-wave range the number of materials that can be used is reduced more, since the range is so large that not many materials can fully cover it. Figure D- 3 shows the range of transparency for some of the most common substrates used in Infrared thermography.

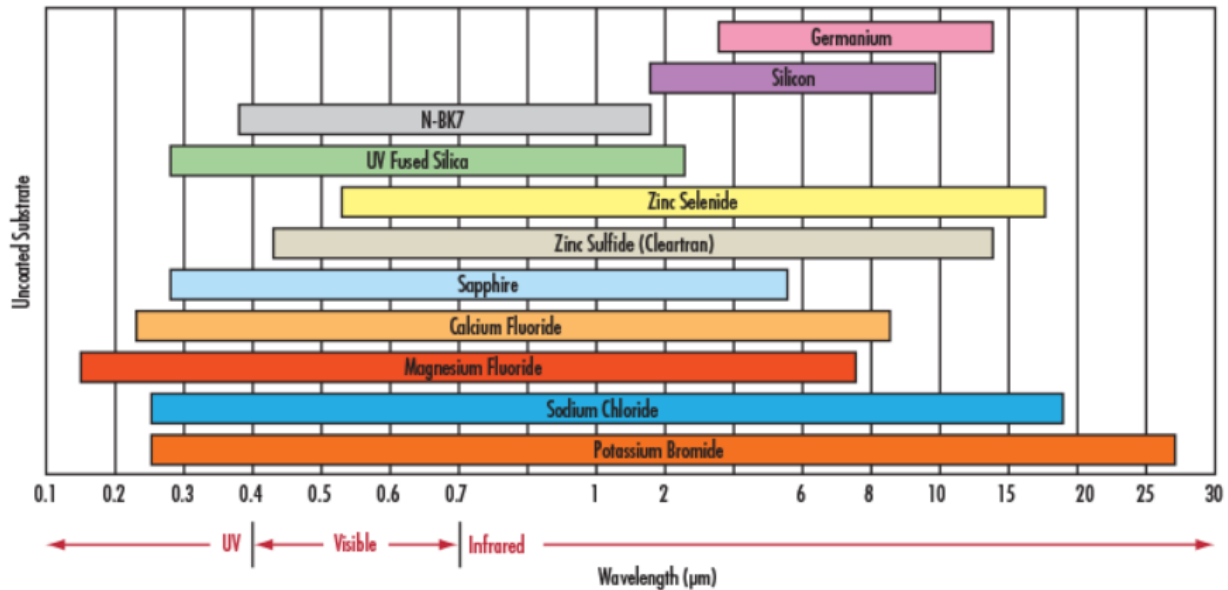


Figure D- 3. Infrared Substrate Comparison[167].

After the first temperature analysis the list of materials was reduced to KBr, NaCl, BaF<sub>2</sub>, ZnSe, ZnS, Germanium, Silicon, CaF<sub>2</sub>.

The last check is the differential pressure that the window should withstand during the blowdown operation. In the experiments performed in this work , the differential pressure is below 1 atmosphere, but the calculation was intended in order to withstand 3 bar of differential pressure. The pressure is directly related with the thickness of the window with respect to the size of the window, and most part of the optical providers have a limited number of thickness that they can provide, unless a custom made window needs to purchased increasing considerably the cost.

Based on the surface that needed to be measured in order to cover the whole axial length where we analyze the heat flux data, the size of the window is 3in diameter. The thickness of the window

needs to be computed based on this requirement. The formula that we have used for this computation is the following:

$$S_{max} = \frac{(k D^2 P)}{4 t^2} \quad (76)$$

where k is a constant, the value for which depends upon whether or not the window is clamped. We use 0.75 for clamped windows and 1.125 for unclamped (See Figure D- 4).  $S_{max}$  is the maximum stress, D is the window diameter under pressure (i.e., the portion of window not supported by the flange as shown in the schematic in Figure D- 4), P is the load, and t is the thickness of the window material.

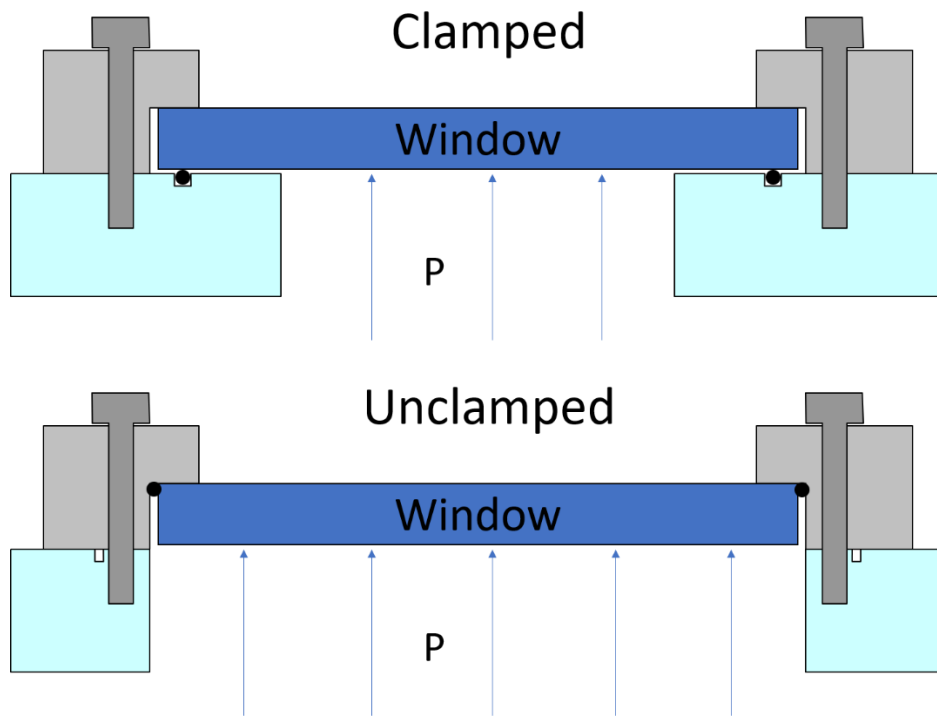


Figure D- 4. Configuration of high pressure windows.

In this experiment we have decided to implement the clamped configuration since it is safer for the window when there is no a strong gradient of pressure across the window, that happens when installing the window and every time that we are not using the wind tunnel.

We use a safety factor in the calculation of the thickness of 2. Using this safety factor and the catalog of available windows of different manufacturers it was decided to use a CaF<sub>2</sub> window of 76mm diameter and 3.5mm thickness. This window is able to withstand a pressure differential of 3 bar.

## APPENDIX E. EXPERIMENTAL DATA IN GAS TURBINE APPLICATION

In the gas turbine application, we run several test at different conditions of temperature and massflow. The following table summarizes all the analyzed tests for this study.

The experiments that were evaluated in this doctoral thesis are contained in the Table E-1.

Table E-1. Turbine application experimental campaign tests.

<b>Experiment Name</b>	<b>Temperature [F] in the heater</b>	<b>Massflow [lb/s]</b>
<b>Experiment 1</b>	300	9
<b>Experiment 2</b>	400	9
<b>Experiment 3</b>	500	9
<b>Experiment 4</b>	500	6
<b>Experiment 5</b>	500	12

The baseline case is the experiment 3 and we vary independently the two variables that we can vary in the current configuration of the wind tunnel (massflow and temperature). The variation of total pressure is coupled with the variation of massflow.

In this appendix we summarize the conditions and the most important results of each one of the experiments that were used to compile all the information displayed in the main body of the doctoral dissertation. We focus in the gas and metal temperatures in the different places that they were measured and the computation of the heat flux that are derived from these measurements.

Finally the Digital Filter Method is used to compute the heat flux based on the temperatures obtained using infrared thermography in the outer surface of the inner casing.

### Experiment 1

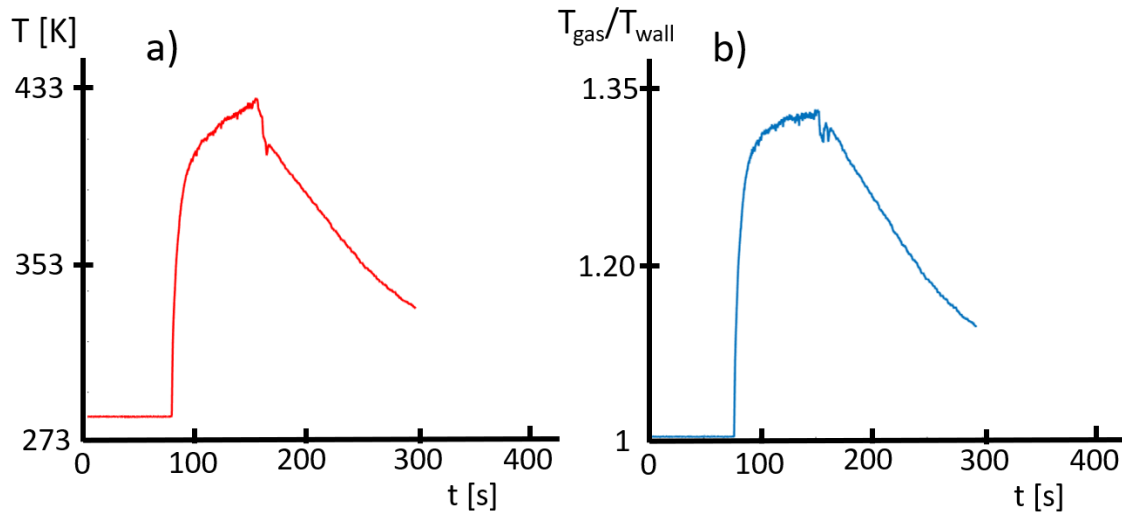


Figure E- 1. a) Gas temperature measured by one of the total pressure probes in the test section during the experiment 1 and b) gas to wall temperature ratio during the same experiment.

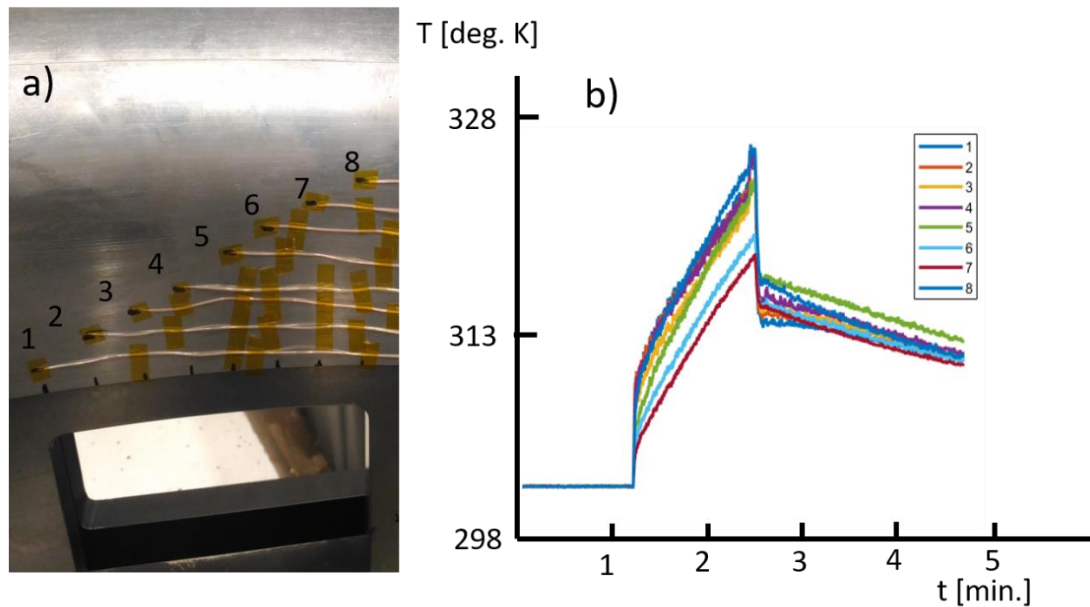


Figure E- 2. a) Surface thermocouples in the inner flowpath and b) inner metal temperature in the different axial locations over the measured surface.

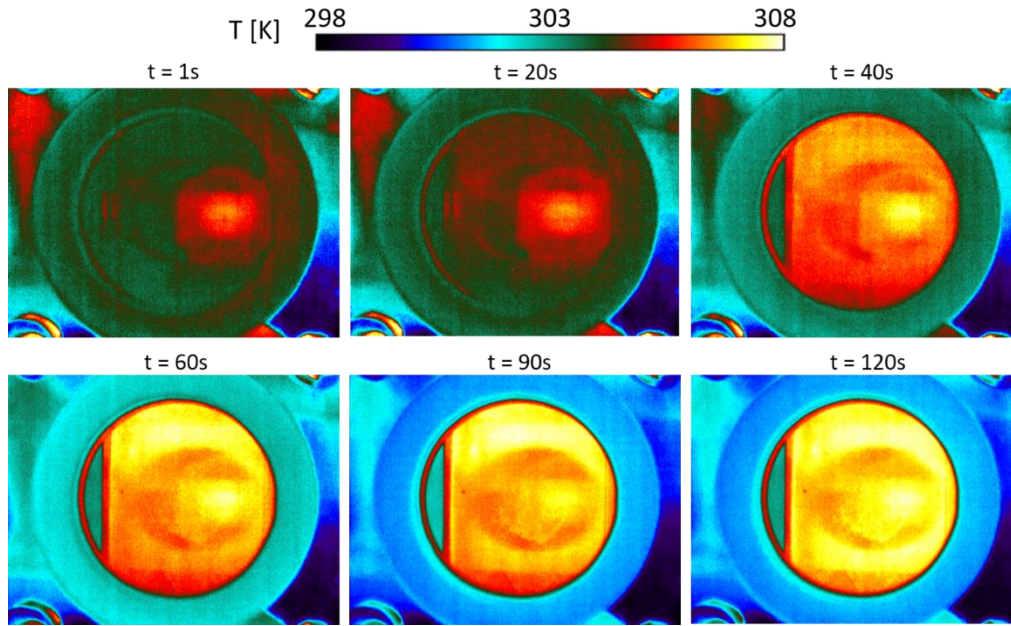


Figure E- 3. IR images taken during the experiment 1.

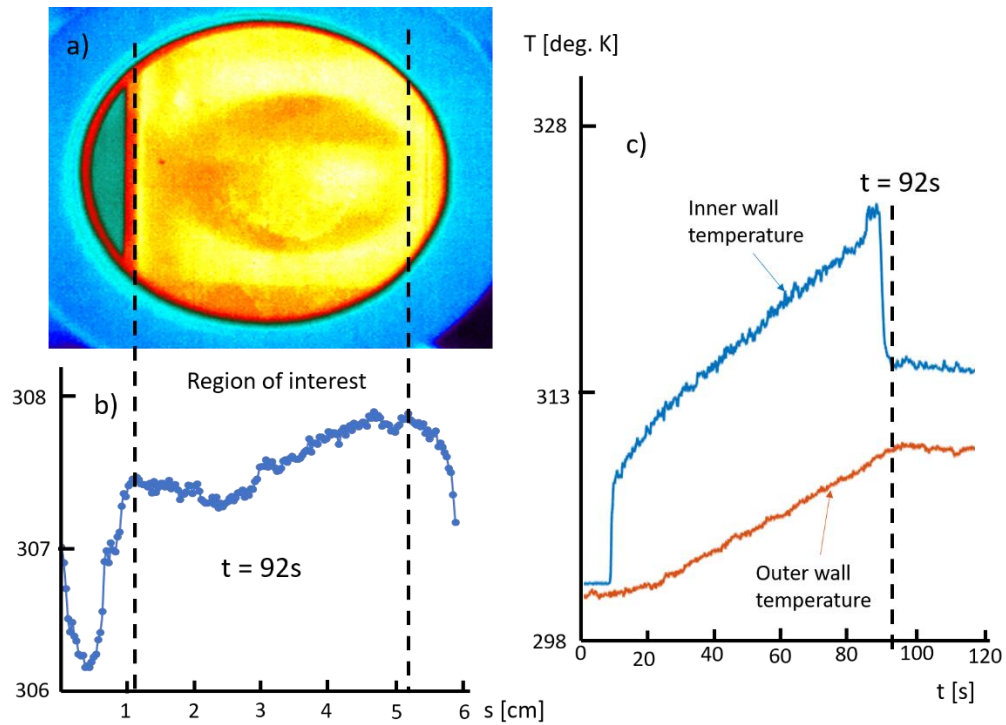


Figure E- 4. a) IR image of the region of interest. b) Spatial behavior of the temperature in the region inside the window. c) Temperature measured in the inner and outer surface of the shroud, used to compute the heat flux with the 1D heat conduction code.

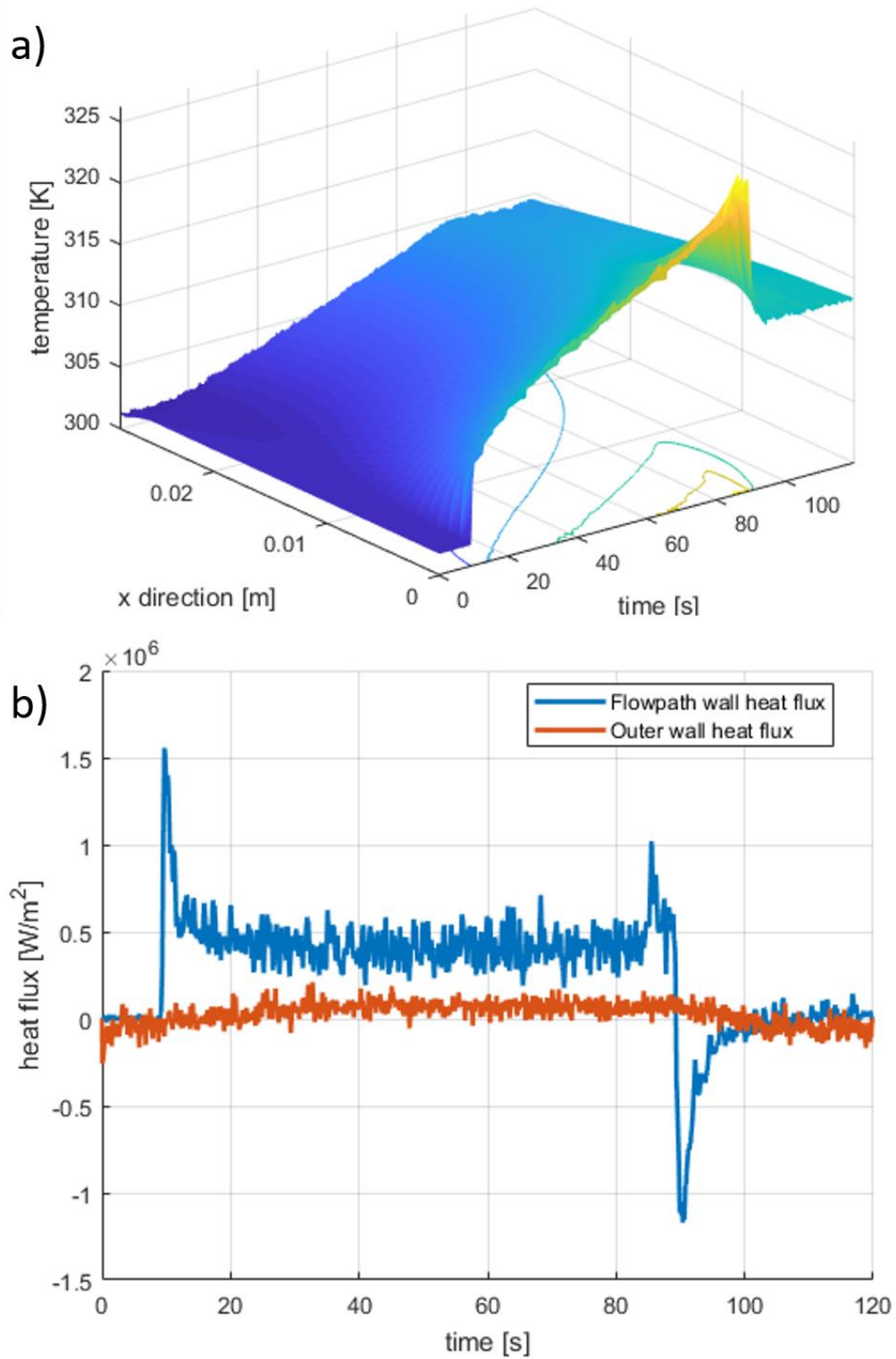


Figure E- 5. a) Temperature map in time and space for the calculation of the 1D heat conduction with the thermocouples in location 1. b) Heat flux computed with the 1D heat conduction code with the temperature from the thermocouple at location 1.



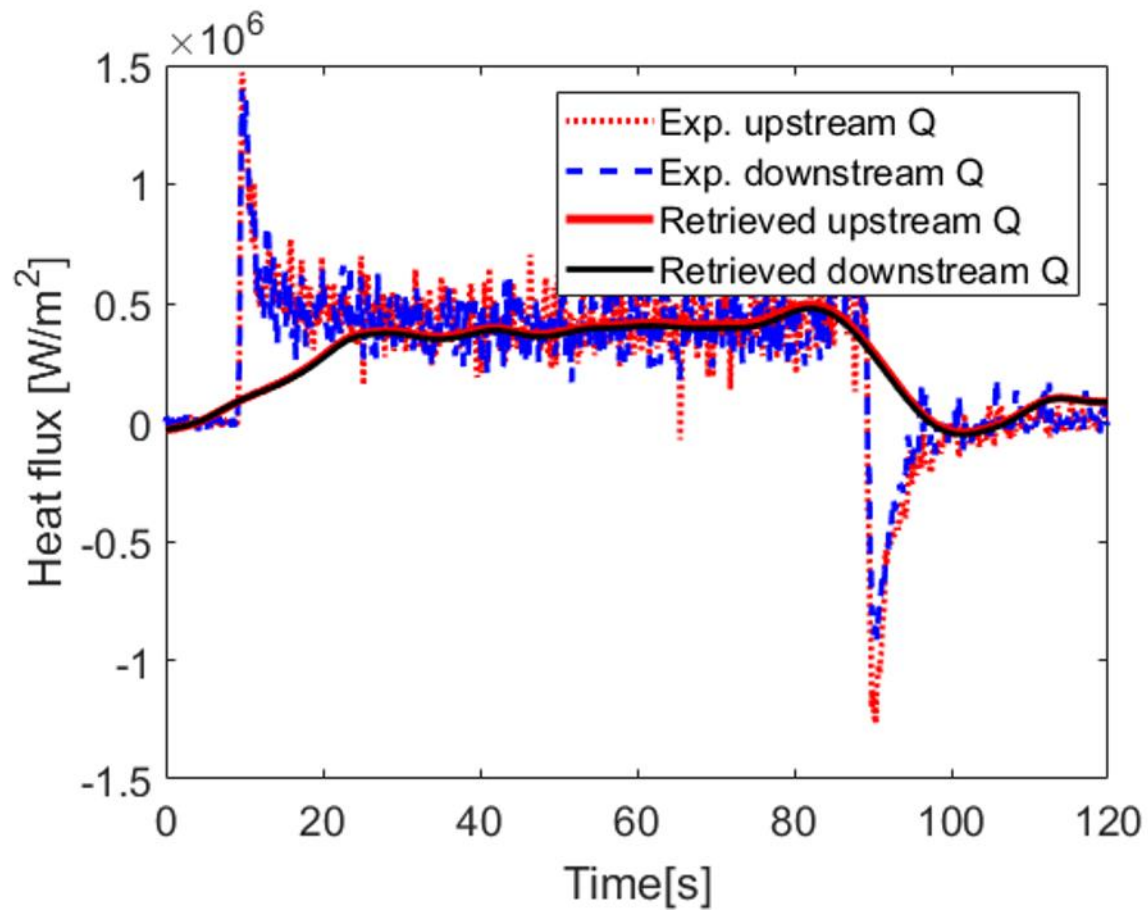


Figure E- 6. Comparison between the heat flux computed by the inverse heat conduction method and the heat flux through the casing.

### Experiment 2

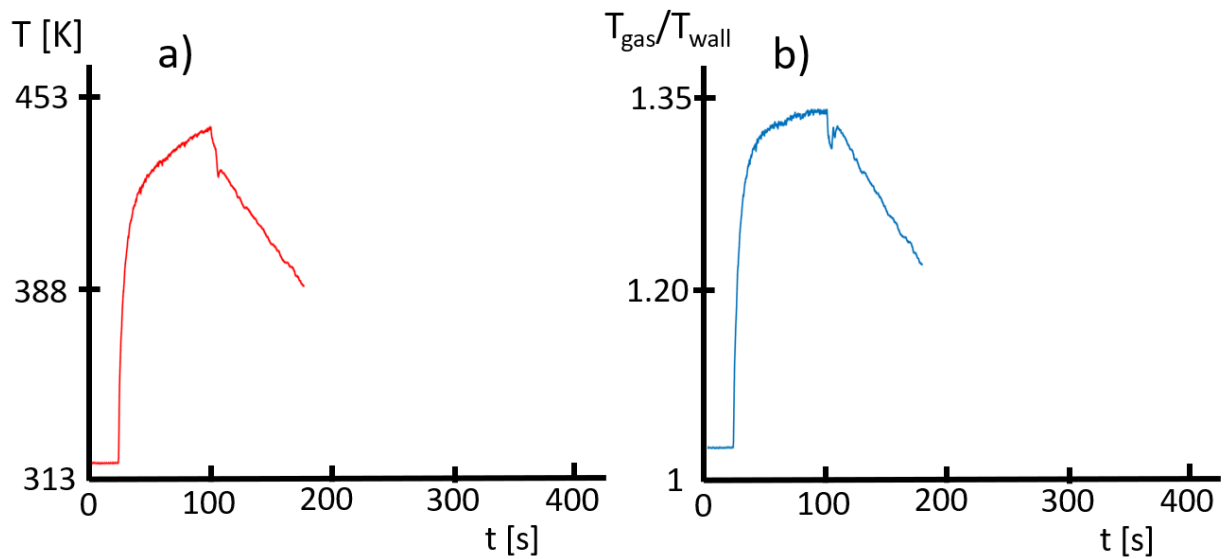


Figure E- 7. a) Gas temperature measured by one of the total pressure probes in the test section during the experiment 2 and b) gas to wall temperature ratio during the same experiment.

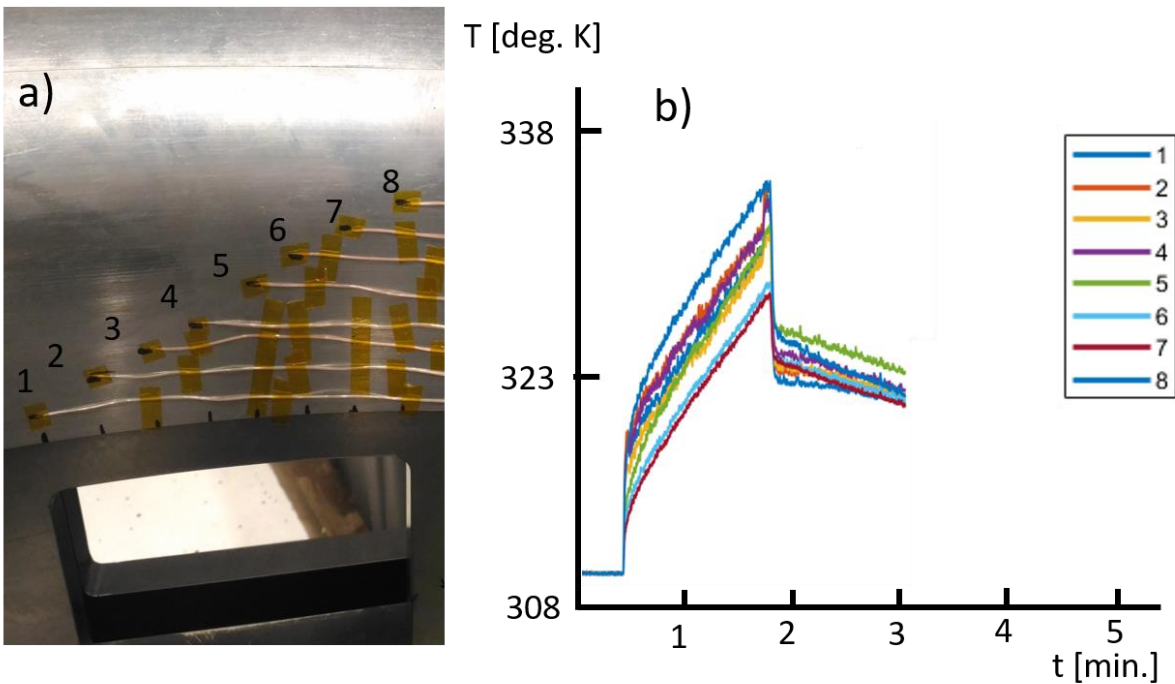


Figure E- 8. a) Surface thermocouples in the inner flowpath and b) inner metal temperature in the different axial locations over the measured surface.

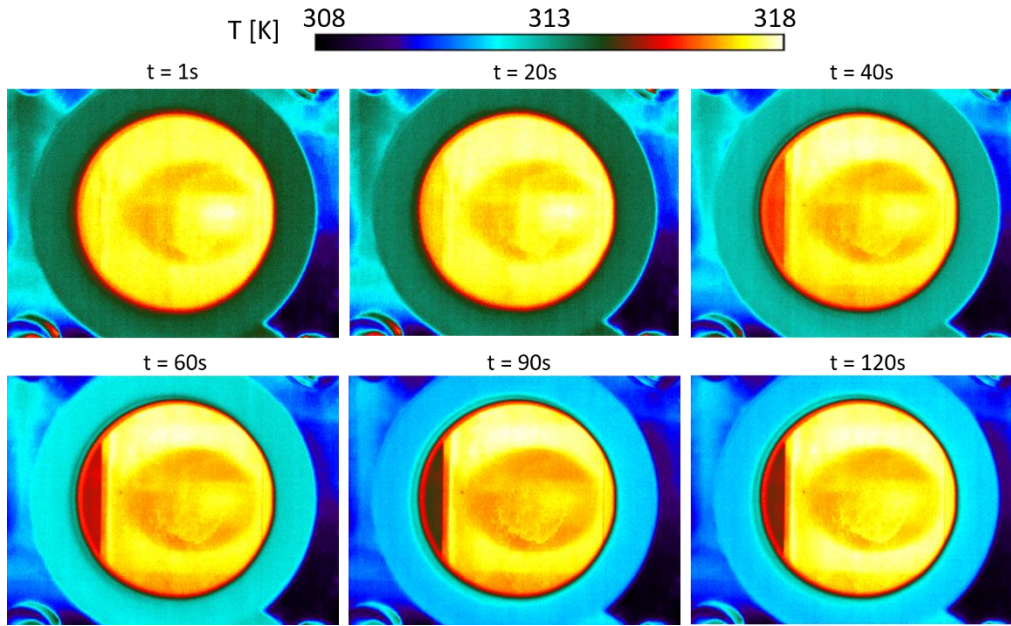


Figure E- 9. IR images taken during the experiment 2.

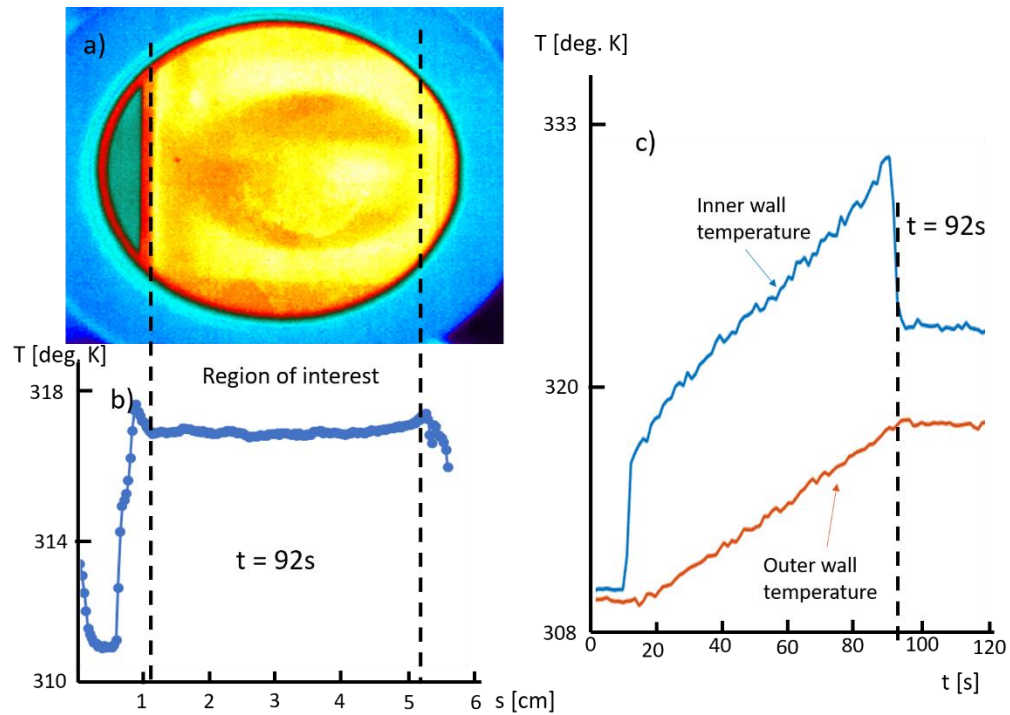


Figure E- 10. a) IR image of the region of interest. b) Spatial behavior of the temperature in the region inside the window. c) Temperature measured in the inner and outer surface of the shroud, used to compute the heat flux with the 1D heat conduction code.

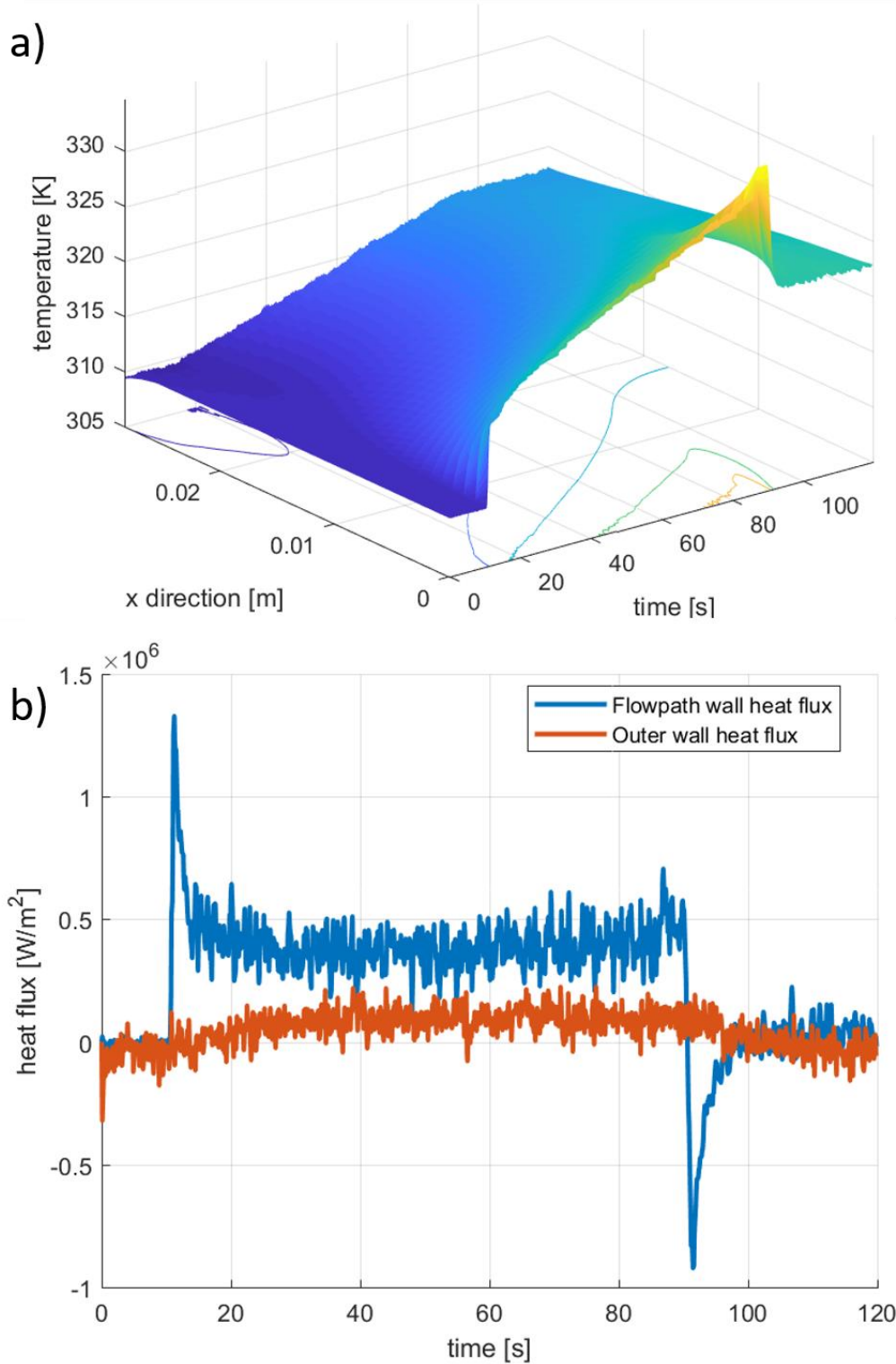


Figure E- 11. a) Temperature map in time and space for the calculation of the 1D heat conduction with the thermocouples in location 1. b) Heat flux computed with the 1D heat conduction code with the temperature from the thermocouple at location 1.

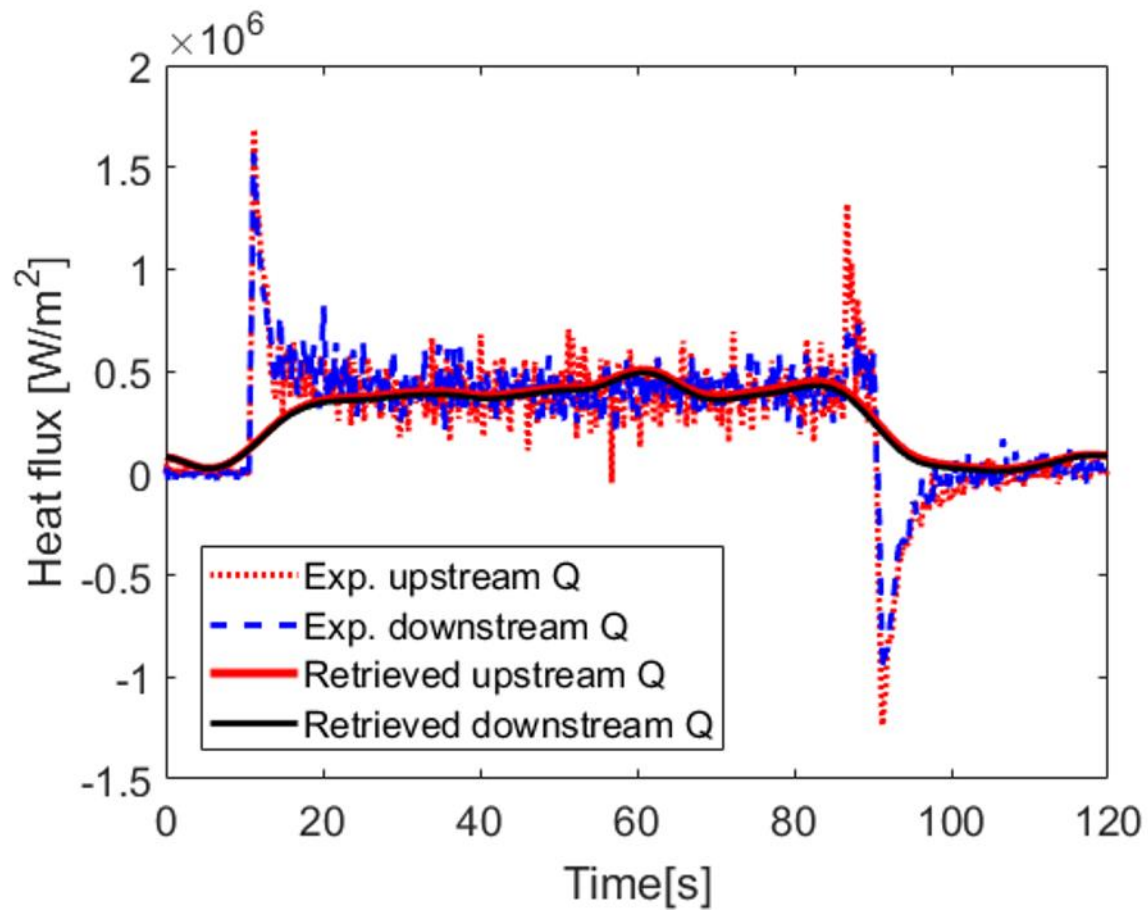


Figure E- 12.Comparison between the heat flux computed by the inverse heat conduction method and the heat flux through the casing.

### Experiment 3 (Baseline)

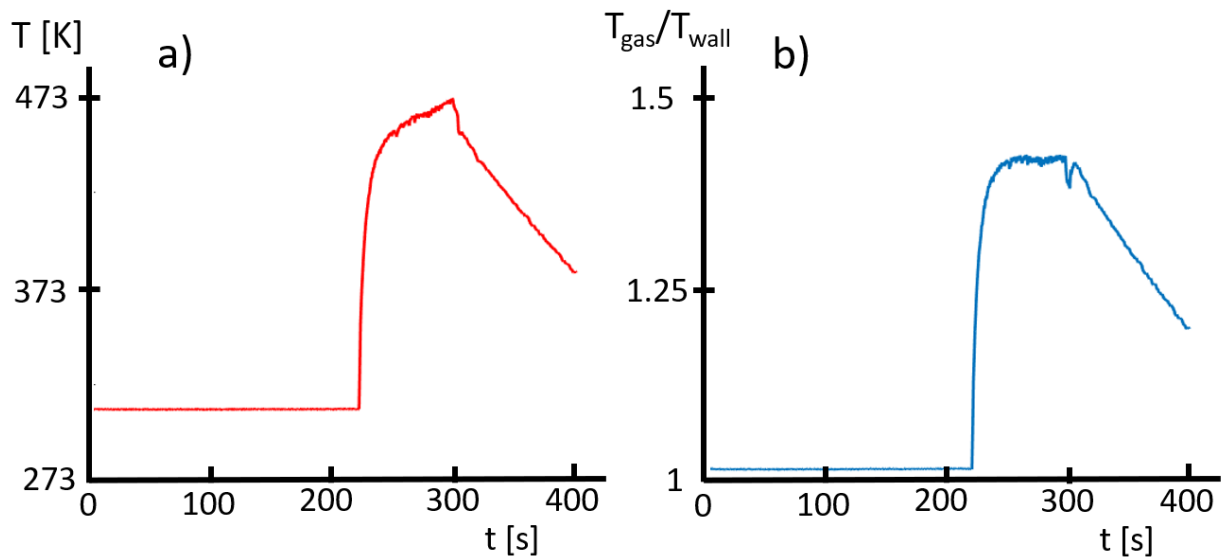


Figure E- 13. a) Gas temperature measured by one of the total pressure probes in the test section during the experiment 3 and b) gas to wall temperature ratio during the same experiment.

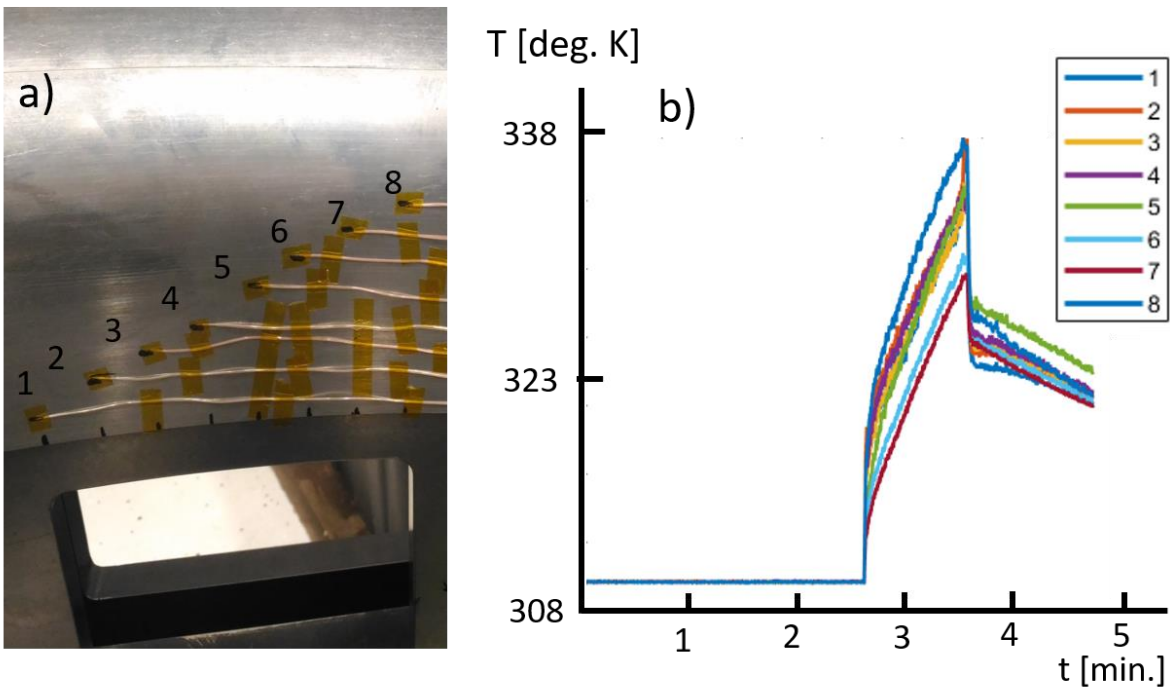


Figure E- 14. a) Surface thermocouples in the inner flowpath and b) inner metal temperature in the different axial locations over the measured surface.



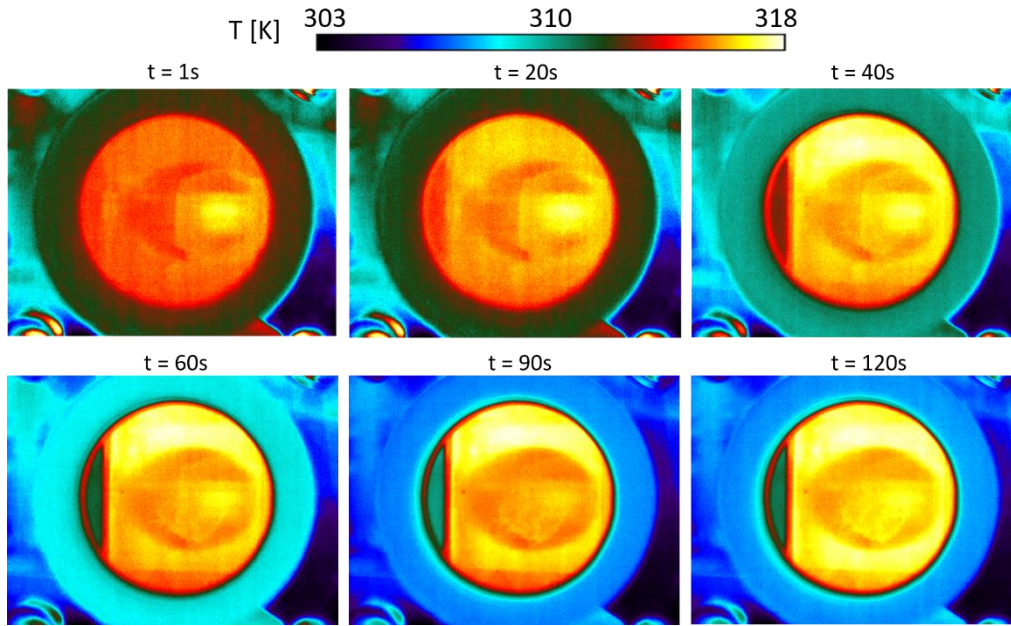


Figure E- 15. IR images taken during the experiment 3.

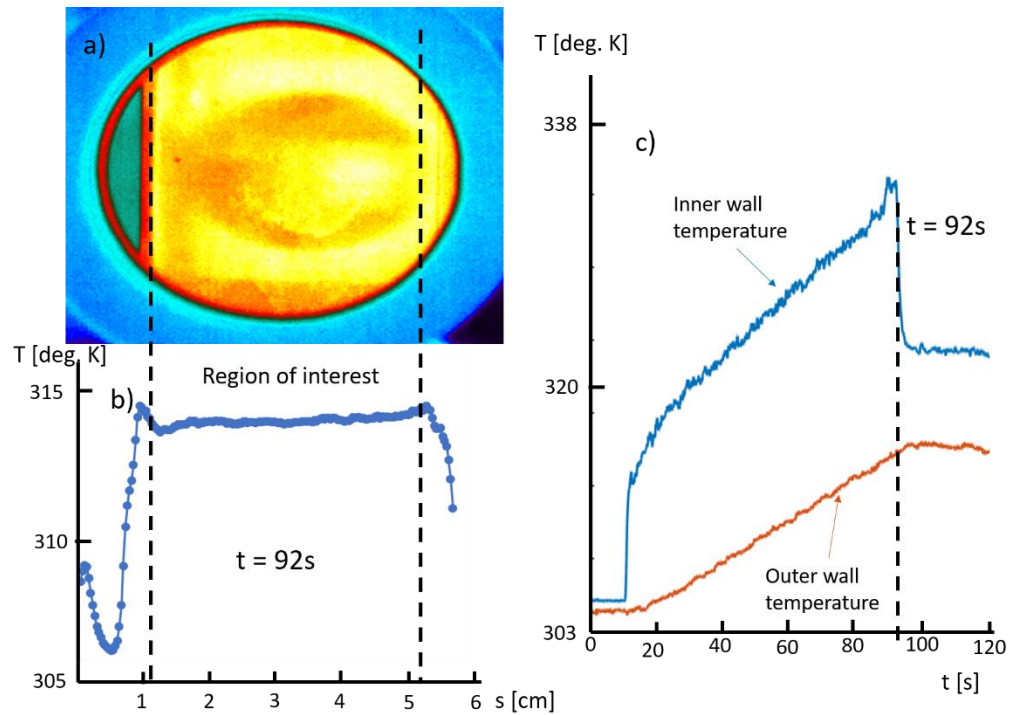


Figure E- 16. a) IR image of the region of interest. b) Spatial behavior of the temperature in the region inside the window. c) Temperature measured in the inner and outer surface of the shroud, used to compute the heat flux with the 1D heat conduction code.

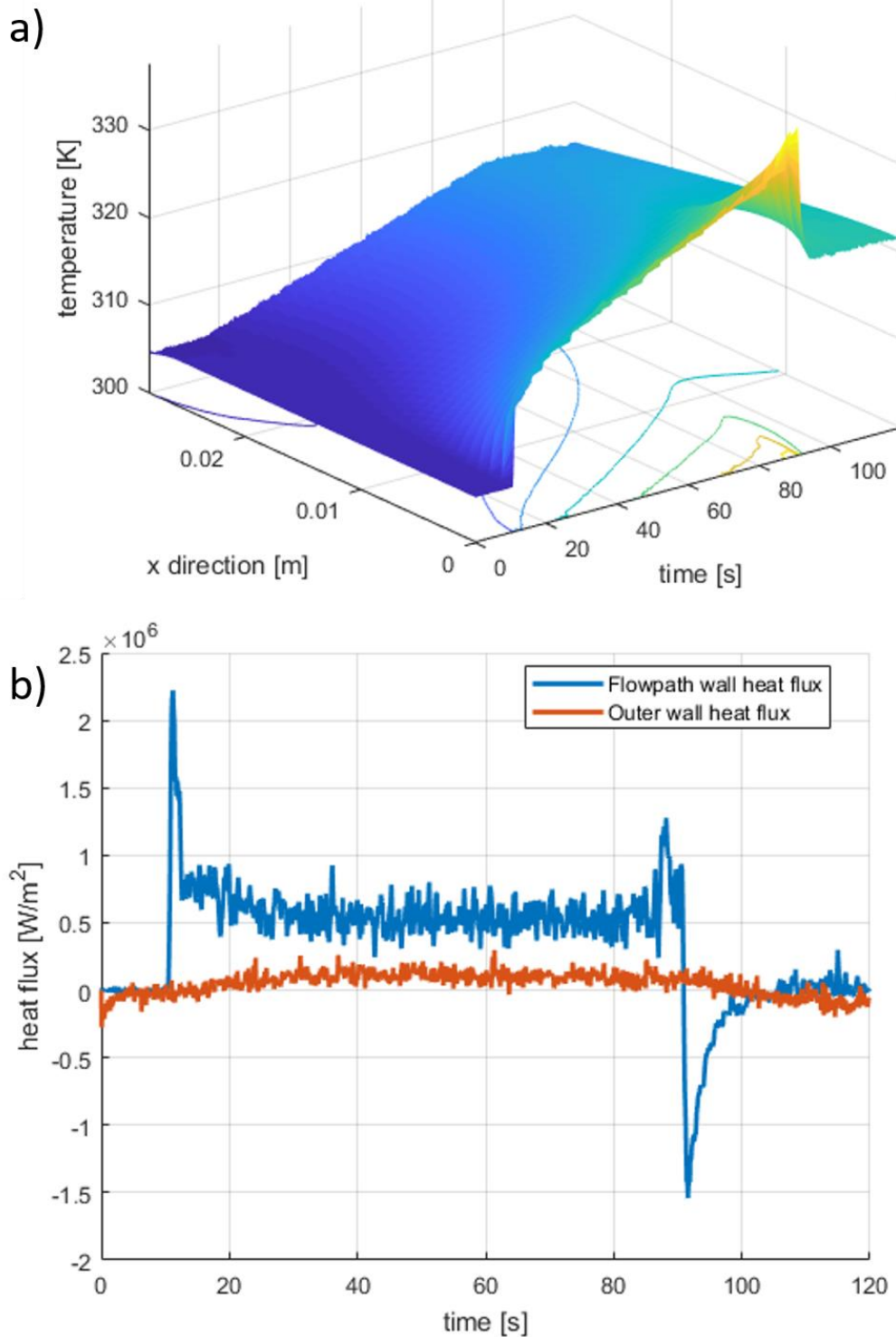


Figure E- 17. a) Temperature map in time and space for the calculation of the 1D heat conduction with the thermocouples in location 1. b) Heat flux computed with the 1D heat conduction code with the temperature from the thermocouple at location 1.



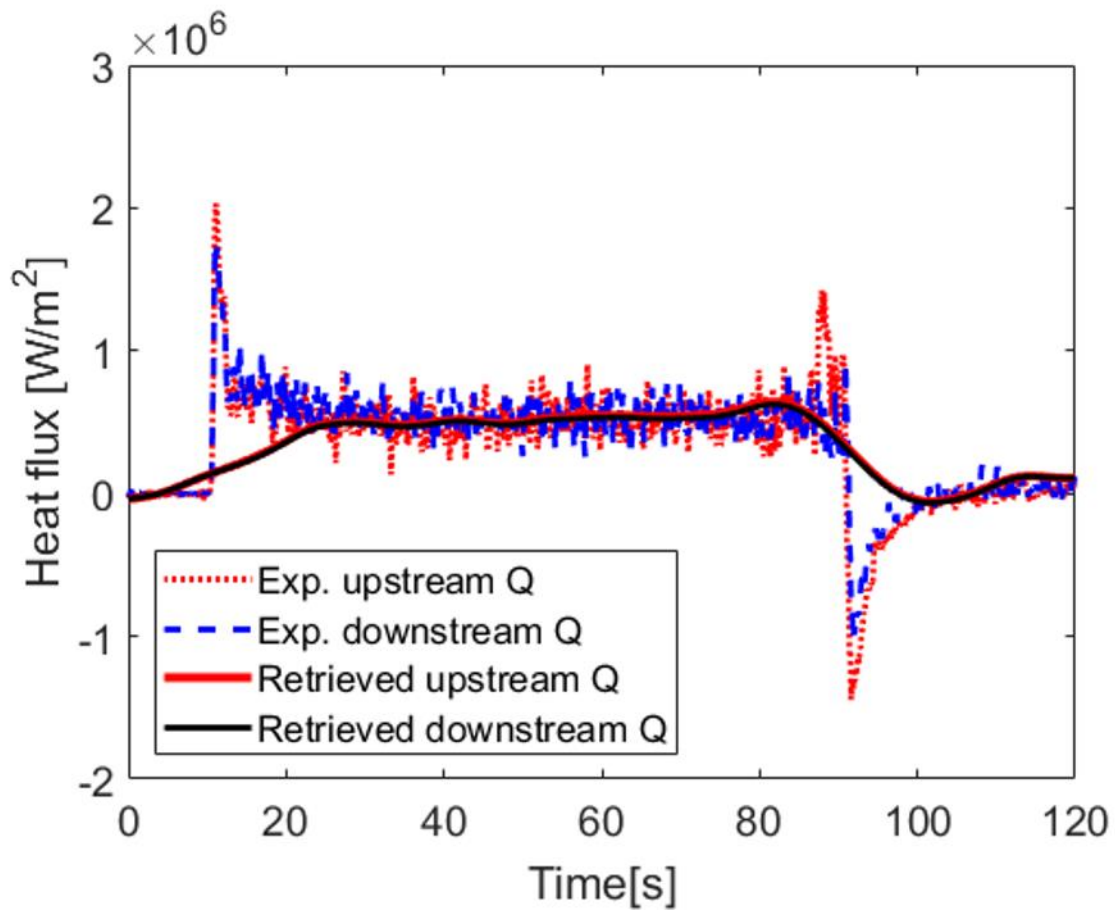


Figure E- 18. Comparison between the heat flux computed by the inverse heat conduction method and the heat flux through the casing.

### Experiment 4

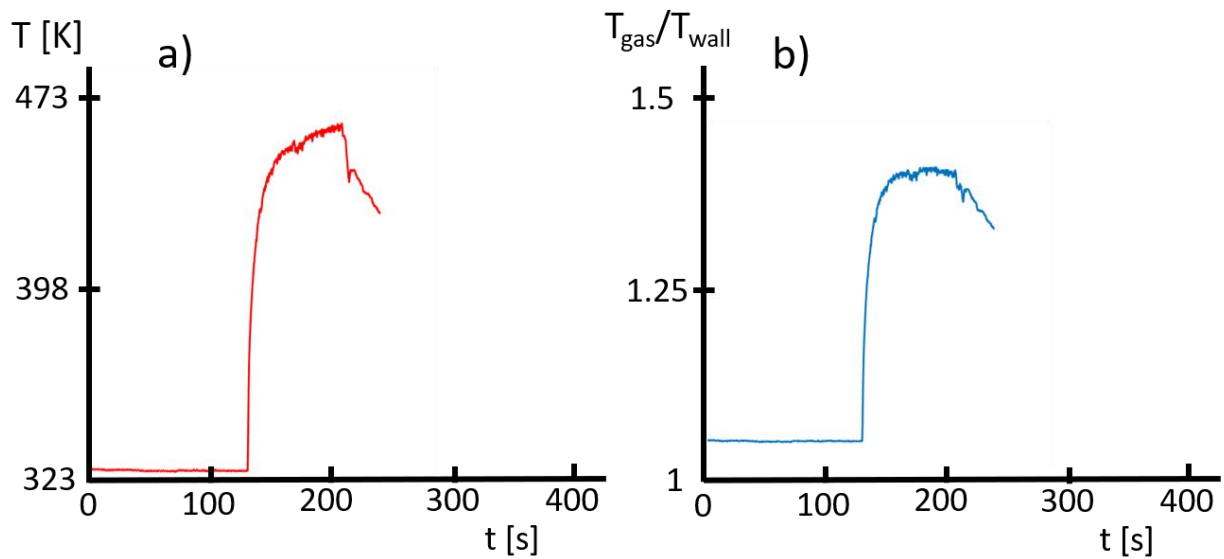


Figure E- 19. a) Gas temperature measured by one of the total pressure probes in the test section during the experiment 4 and b) gas to wall temperature ratio during the same experiment.

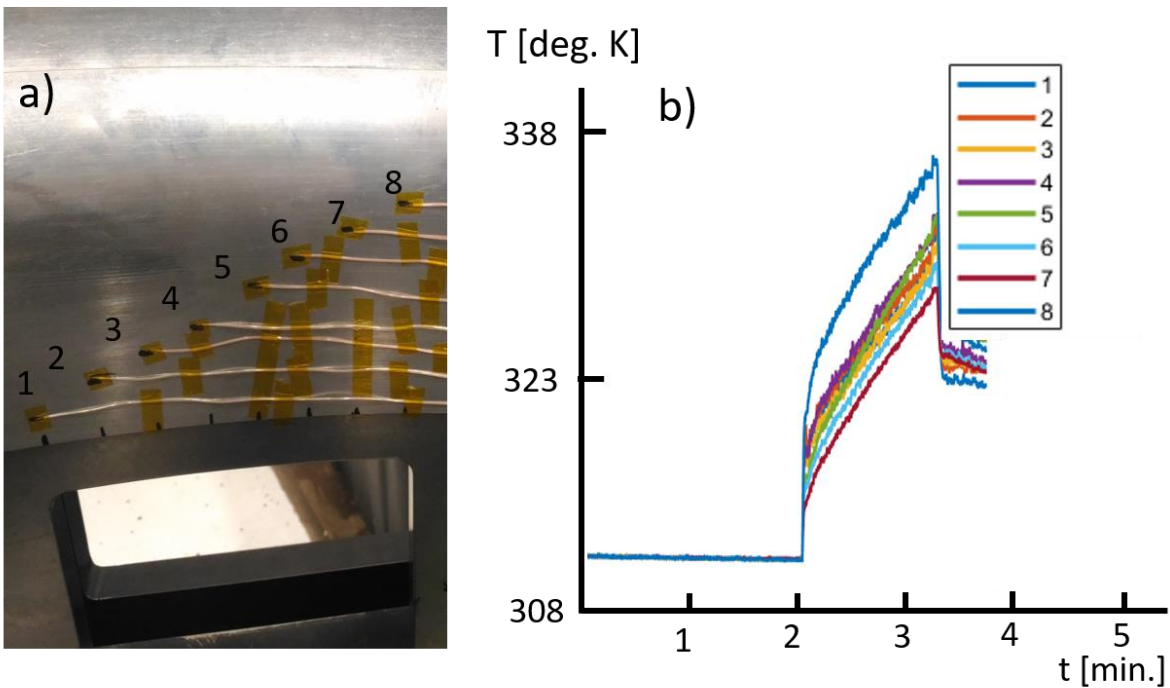


Figure E- 20. a) Surface thermocouples in the inner flowpath and b) inner metal temperature in the different axial locations over the measured surface.

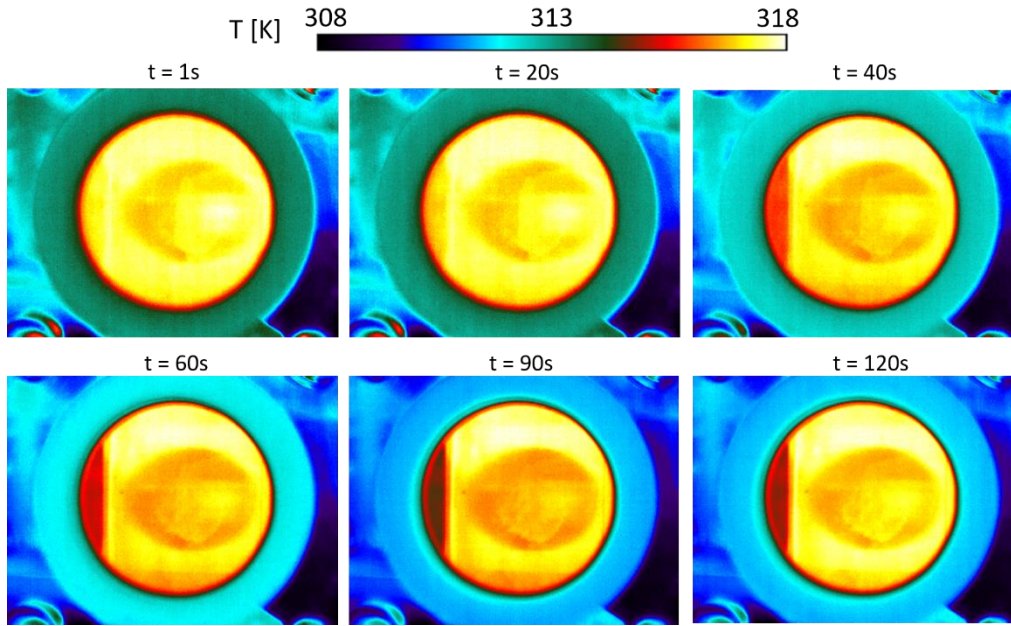


Figure E- 21. IR images taken during the experiment 4.

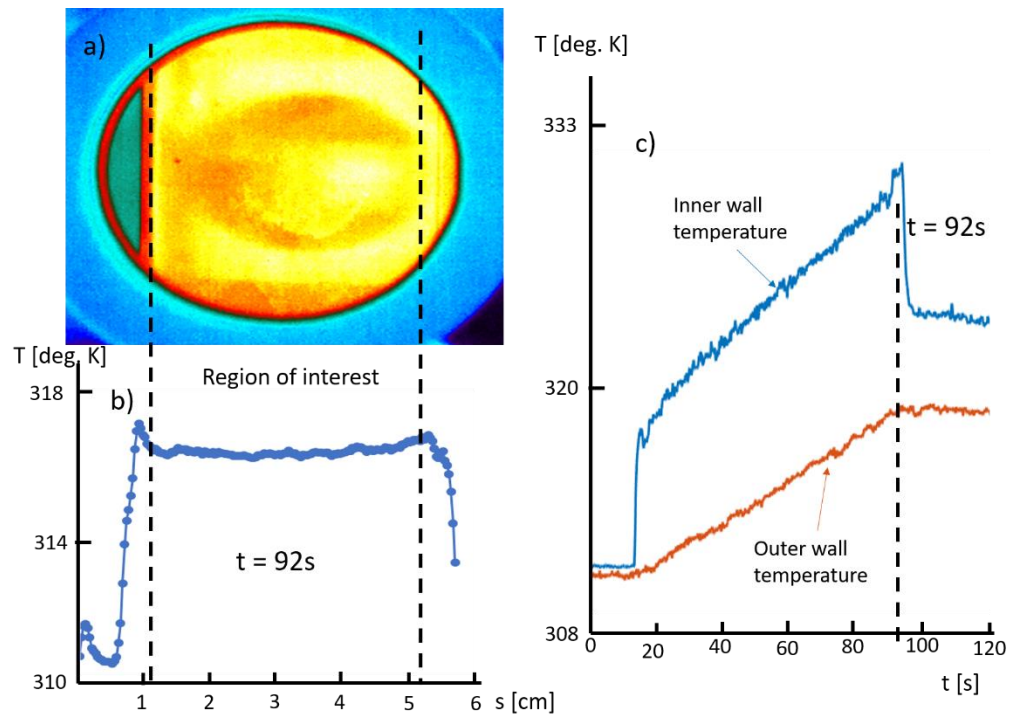


Figure E- 22. a) IR image of the region of interest. b) Spatial behavior of the temperature in the region inside the window. c) Temperature measured in the inner and outer surface of the shroud, used to compute the heat flux with the 1D heat conduction code.

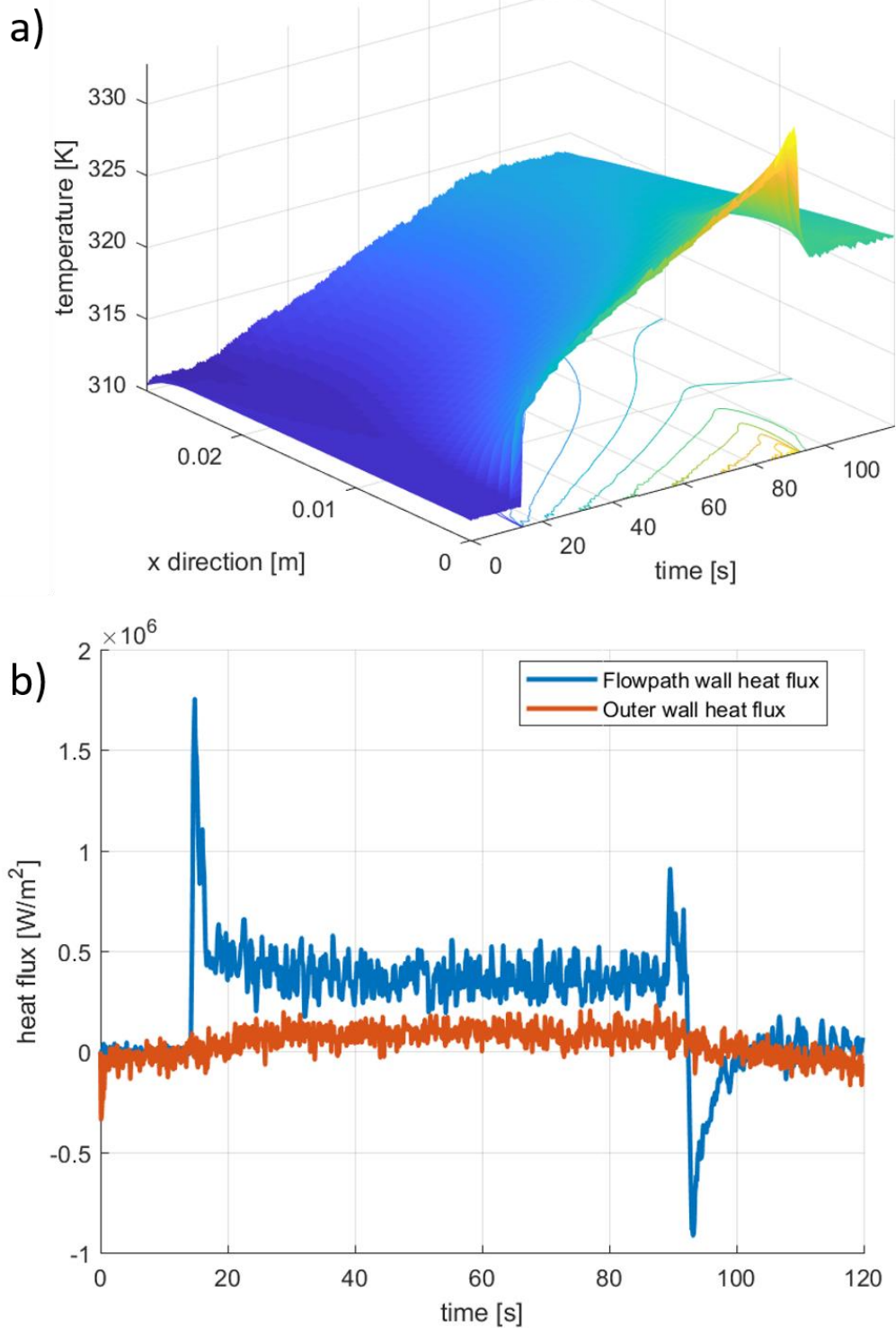


Figure E- 23. a) Temperature map in time and space for the calculation of the 1D heat conduction with the thermocouples in location 1. b) Heat flux computed with the 1D heat conduction code with the temperature from the thermocouple at location 1.

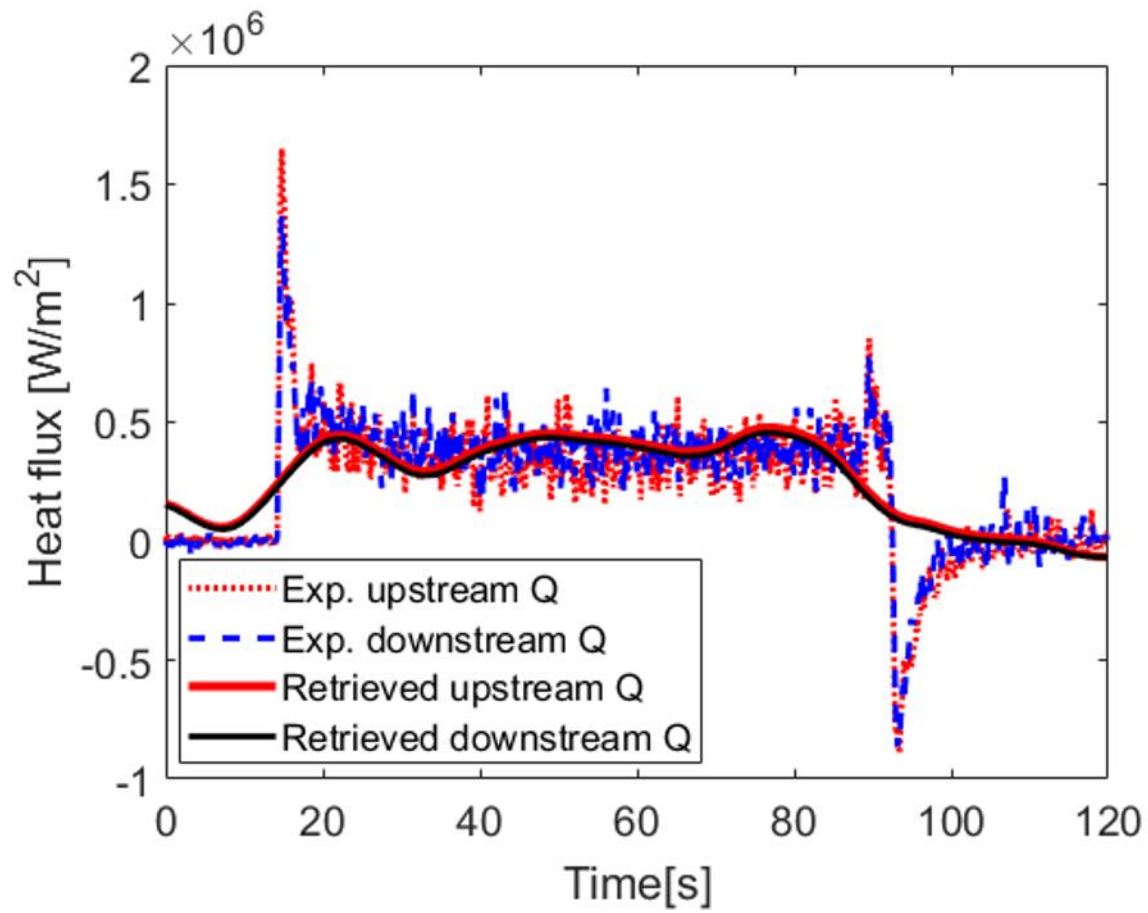


Figure E- 24.Comparison between the heat flux computed by the inverse heat conduction method and the heat flux through the casing.

### Experiment 5

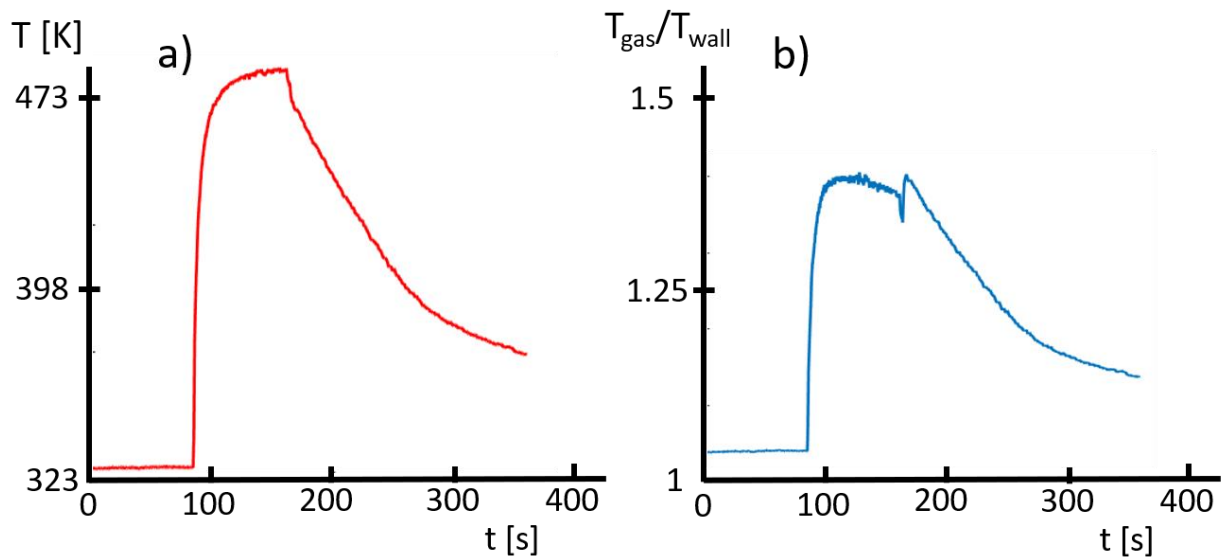


Figure E- 25. a) Gas temperature measured by one of the total pressure probes in the test section during the experiment 5 and b) gas to wall temperature ratio during the same experiment.

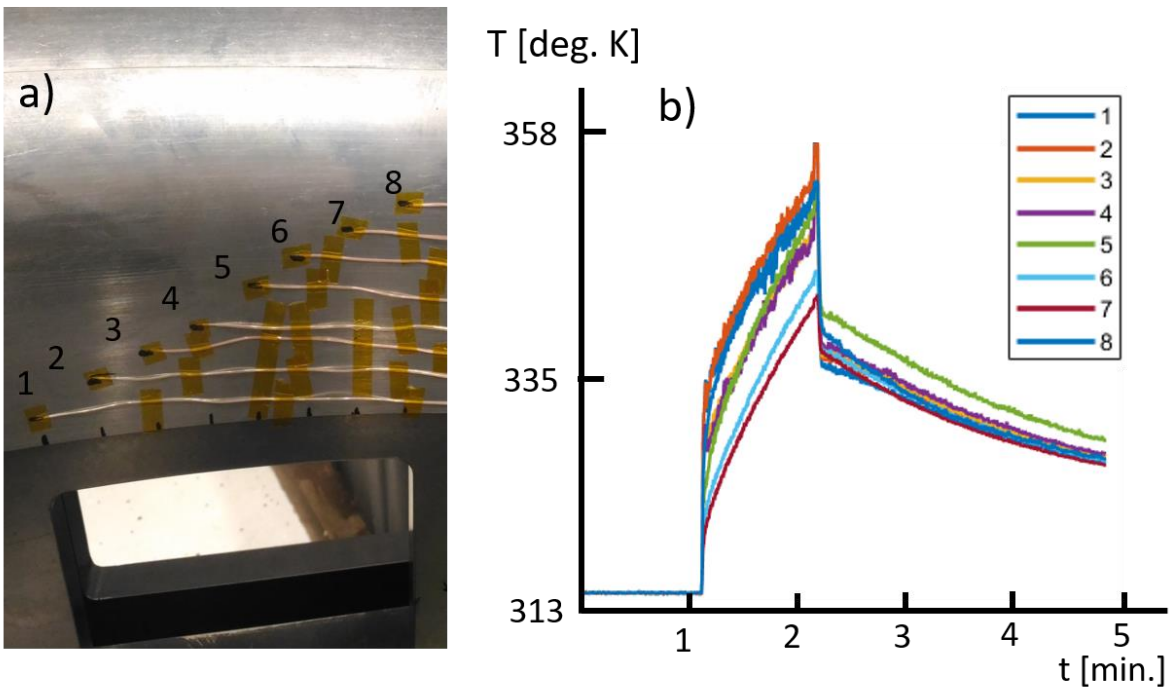


Figure E- 26. a) Surface thermocouples in the inner flowpath and b) inner metal temperature in the different axial locations over the measured surface.



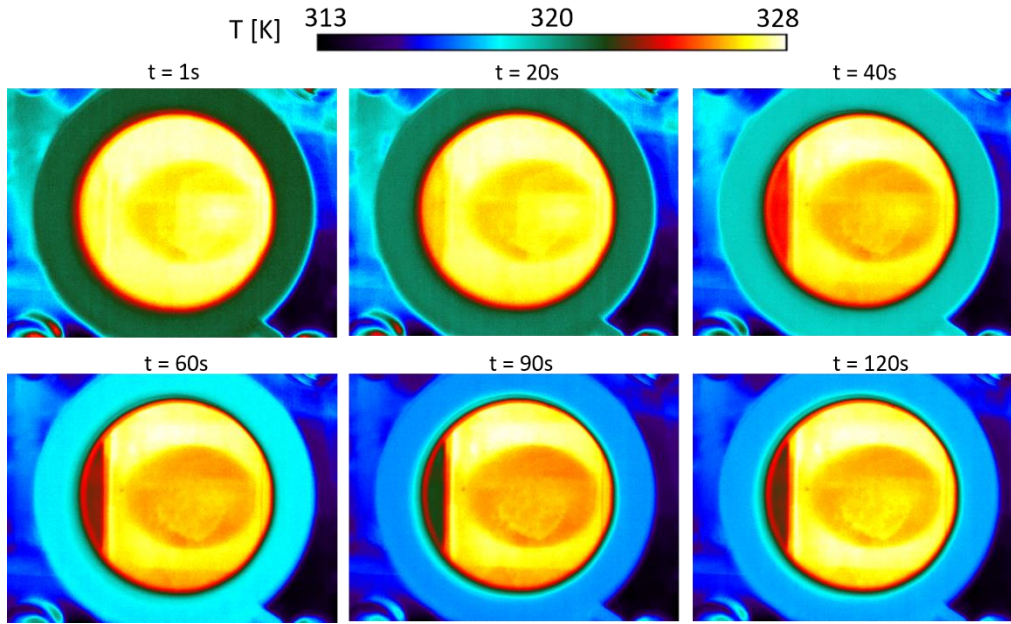


Figure E- 27. IR images taken during the experiment 5.

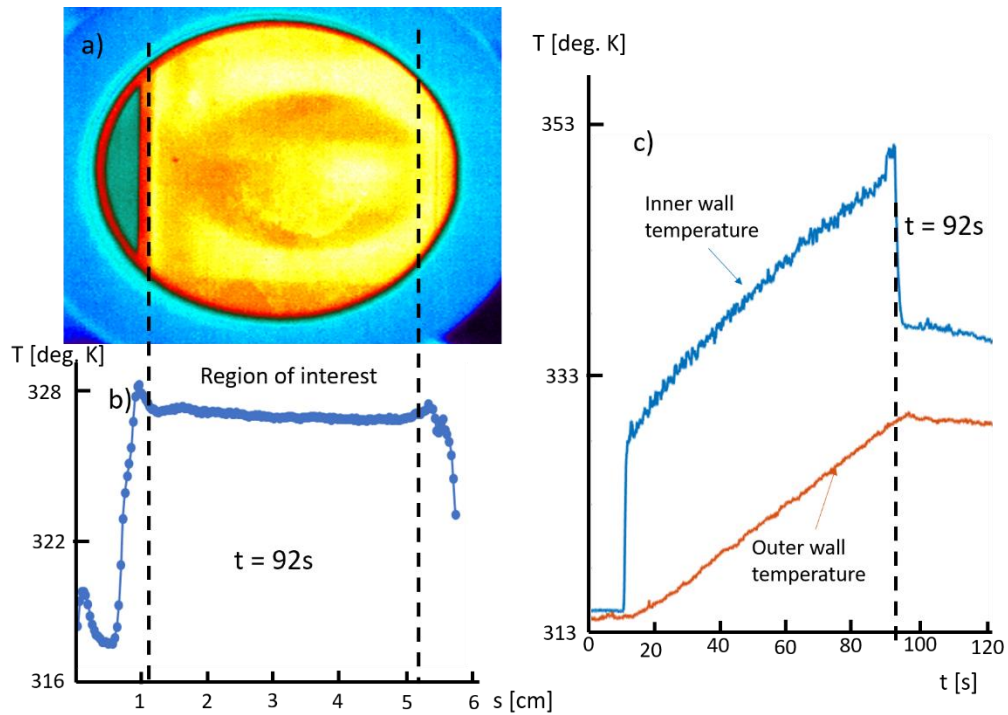


Figure E- 28. a) IR image of the region of interest. b) Spatial behavior of the temperature in the region inside the window. c) Temperature measured in the inner and outer surface of the shroud, used to compute the heat flux with the 1D heat conduction code.

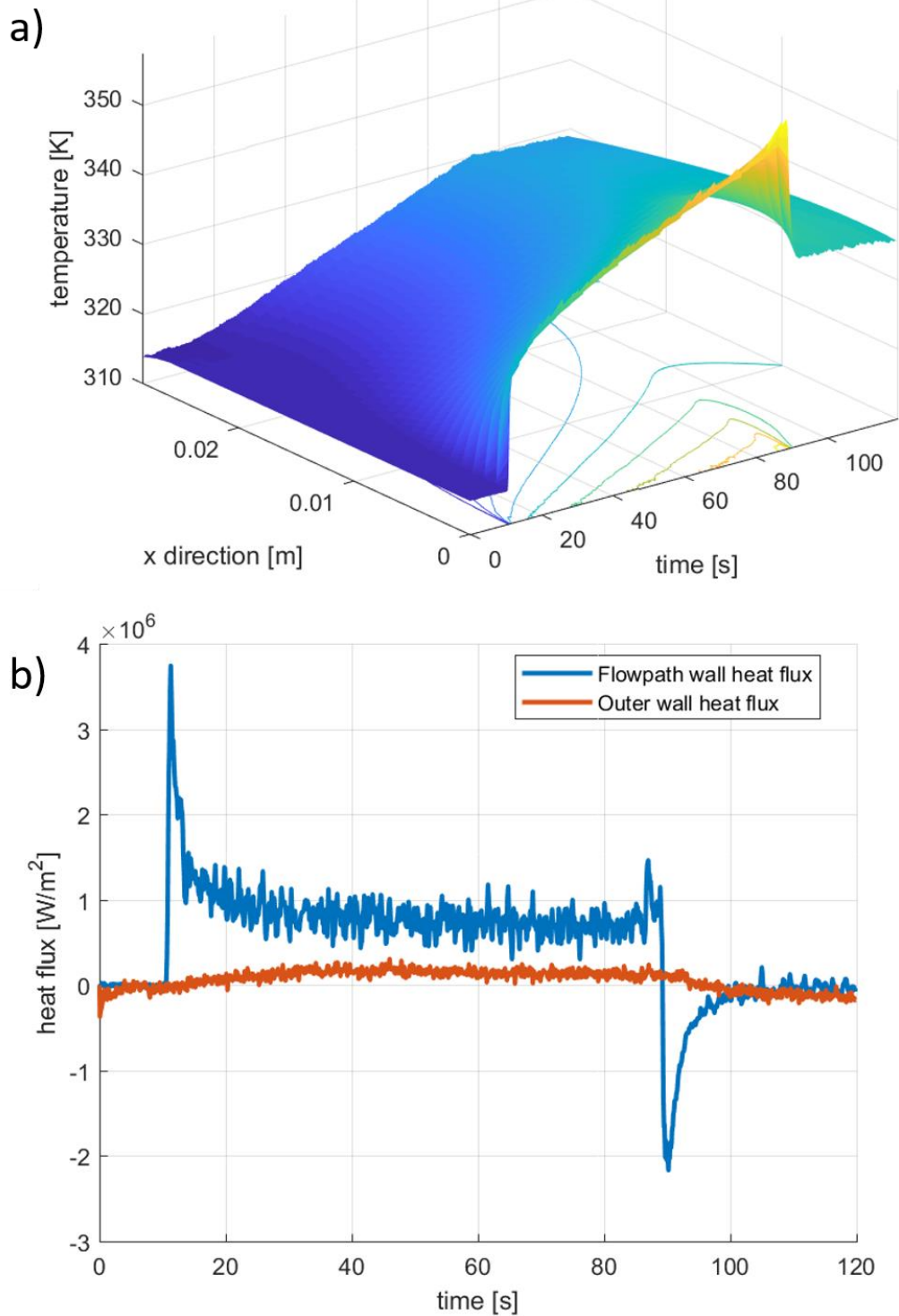


Figure E- 29. a) Temperature map in time and space for the calculation of the 1D heat conduction with the thermocouples in location 1. b) Heat flux computed with the 1D heat conduction code with the temperature from the thermocouple at location 1.



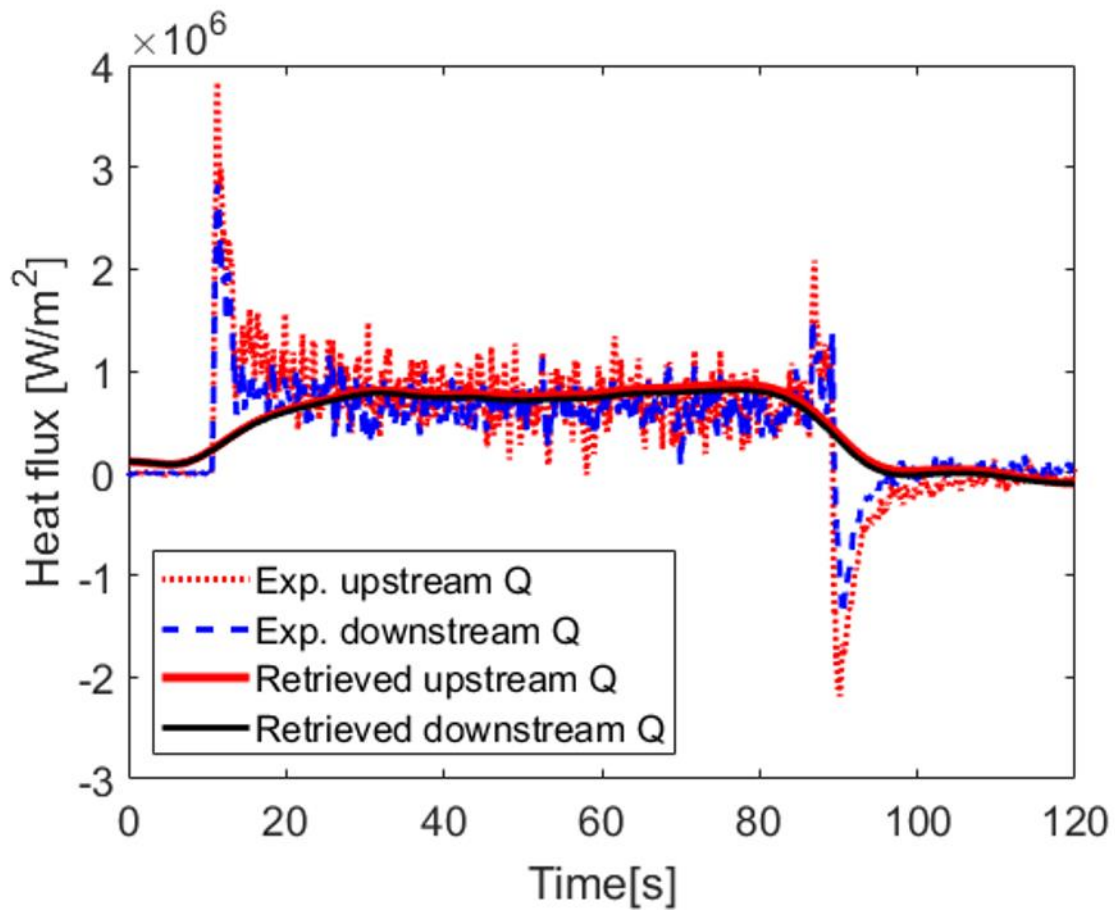


Figure E- 30.Comparison between the heat flux computed by the inverse heat conduction method and the heat flux through the casing.

## VITA

David Gonzalez Cuadrado was born in Leon (Spain) to parents Miguel Angel Gonzalez Garcia and Maria de los Angeles Cuadrado Garcia on December 29<sup>th</sup> 1989. He has an older brother Miguel and he grew up in Serrilla de Torio, a small mountain village in the north of Leon, Spain. He commuted every day to the city, Leon, to study in the Claudio Sanchez Albornoz High School of the mentioned city. Through his high school years, he represented at a national level his region Castilla y Leon, in two Mathematical Olympic competition.

After graduating from high school, he embarked on Aeronautical Engineering undergraduate program in University of Leon. He finished his undergraduate studies as second ranked of his promotion. The last year of his undergraduate program he participated in an Erasmus exchange program in the University Paul Sabatier III in Toulouse where he was ranked first amongst all national and international students. In 2010, he started his graduate studies on Aeronautical Engineering in the Polytechnic University of Valencia. He completed his Master studies in 2013 after completing his Final Master Thesis in the von Karman Institute of Fluid Dynamics in Belgium. He got the Best Project Award in Turbomachinery for his thesis in the design of supersonic wind tunnels. In 2013, he pursued a Master-after-master degree in the von Karman Institute for Fluid Dynamics in Belgium which he completed with honors in 2014, before enrolling at Purdue University as a Mechanical Engineering PhD student. His research aims on turbomachinery design and application of inverse heat transfer methodologies in different fields.

## PUBLICATIONS

### Journal Publications:

- **D. G. Cuadrado**, F. Lozano, V. Andreoli, G. Paniagua, 2019. *"Engine-scalable Rotor Casing Convective Heat Flux Evaluation Using Inverse Heat Transfer Methods"*, Journal of Engineering for Gas Turbines and Power, 141(1), p. 011012.
- Paniagua, G., **Cuadrado, D.**, Saavedra, J., Andreoli, V., Meyer, T., Solano, J.P., Herrero, R., Meyer, S. and Lawrence, D., 2019. *"Design of the Purdue Experimental Turbine Aerothermal Laboratory for Optical and Surface Aerothermal Measurements."* Journal of Engineering for Gas Turbines and Power, 141(1), p.012601.
- V. Andreoli, **D. G. Cuadrado**, G. Paniagua, *"Prediction of the Turbine Tip Convective Heat Flux Using Discrete Green Functions."* ASME. J. Heat Transfer. 2018;(), doi:10.1115/1.4039182.
- **D. G. Cuadrado**, A. Marconnet, G. Paniagua, *"Inverse Conduction Heat Transfer and Kriging Interpolation Applied to Temperature Sensor Location in Microchips"*, J. of Electronic Packaging, March 2018, doi: 10.1115/1.4039026.
- **D. G. Cuadrado**, S. Lavagnoli, G. Paniagua, *"Methodology to correct the magnetic field effect on thin film measurements"*, J. of Engineering for Gas Turbines and Power., Vol. 138, March 2016.

### Conference Publications:

- **D. G. Cuadrado**, F. Lozano, V. Andreoli, G. Paniagua, *"Engine-scalable Rotor Casing Convective Heat Flux Evaluation Using Inverse Heat Transfer Methods"*, 2018 ASME TurboExpo Conference, GT2018-76906.
- **D. G. Cuadrado**, A. Marconnet, G. Paniagua, *"Inverse Conduction Heat Transfer and Kriging Interpolation Applied to Temperature Sensor Location in Microchips"*. ASME 2017 International Technical Conference and Exhibition on Packaging and Integration of Electronic and Photonic Microsystems. doi:10.1115/IPACK2017-74224.
- **D. G. Cuadrado**, J. Saavedra, V. Andreoli, G. Paniagua, *"Experimental Calibration of a High Speed Blowdown Tunnel"*. 2017 ISABE conference No 2017-22636.

- V. Andreoli, **D. G. Cuadrado**, G. Paniagua, "*Prediction of the Turbine Tip Convective Heat Flux Using Discrete Green Functions*". ASME 2017 Turbo Expo: Power for Land, Sea, and Air, Volume 5B: Heat Transfer. doi:10.1115/GT2017-64080.
- **D. G. Cuadrado**, G. Paniagua, "*Discrete Green Functions Approach to predict Convective Heat Transfer*", 2016 XXIII Biennial Symposium on Measuring Techniques in Turbomachinery, Stuttgart.
- G. Paniagua, **D. G. Cuadrado**, J. Saavedra, V. Andreoli, T. Meyer, S. Meyer, D. Lawrence, "*Design of the Purdue Experimental Turbine Aero-thermal Laboratory for optical and surface aero-thermal measurements*", 2016 ASME TurboExpo Conference, GT2016-58101.
- S. Lavagnoli, C. de Maesschalck, V. Andreoli, G. Paniagua, **D. G. Cuadrado**, "*Wind Tunnel Testing of Turbine Blade Tip Flows*", 2016 AIAA Scitech Conference, AIAA 2016-0910.
- **D. G. Cuadrado**, S. Lavagnoli, G. Paniagua, "Methodology to correct the magnetic field effect on thin film measurements", 2015 ASME TurboExpo Conference, GT2015-42715.